Alma Mater Studiorum - Università di Bologna

DOTTORATO DI RICERCA IN

CHIMICA

Ciclo 35

Settore Concorsuale: 03/B1 - FONDAMENTI DELLE SCIENZE CHIMICHE E SISTEMI INORGANICI

Settore Scientifico Disciplinare: CHIM/03 - CHIMICA GENERALE E INORGANICA

STUDY AND CHARACTERIZATION OF POLYMORPHS OF BTBT DERIVATIVES AND THEIR APPLICATION IN ORGANIC ELECTRONICS

Presentata da: Priya Pandey

Coordinatore Dottorato

Luca Prodi

Supervisore

Enrico Modena

Co-supervisore

Lucia Maini

Esame finale anno 2023

Table of content

Acknowledgements

The pursuit of PhD is an enduring adventure. I must admit that it seems like yesterday when I first embarked upon this adventure. This journey of three years was made possible with the support of a lot of people. During all this time, *Prof. Lucia Maini* and *Dr. Enrico Modena* were always present to supervise me and give me the best advice possible. From the first interview to the final thesis submission, I received plenty of moral support from them. Thank you, Lucia and Enrico, for everything!

I would like to give credit to my parents, who always stood beside me, understanding, and supporting my pursuits. They encouraged me on every step of my career, from setting up the foundation to supporting my decision to move far from home to another continent for a Ph.D. They have always been a pillar of my life, which always stood strong to support me. Thank you so much, *Mummy* and *Papa*, for bearing my rants about all the struggles! When it comes to supporting from family, how can I fail to mention my elder brother, who put the idea of becoming a scientific researcher in my mind since my childhood days, always teaching science in the most interesting way possible me, a kid back then, and manifested the love for science in the start. My brother, sister-in-law, and my little joy of happiness, my nephew strengthened me in every way possible. Thank you for this, *Bhai*, *Bhabhi,* and *Aarav*!

During the Ph.D, I had the opportunity to go for two secondments. My first secondment was at Université libre de Bruxelles (ULB) under the supervision of *Prof. Yves Geerts*, who was always present to guide and motivate me. His dynamic attitude towards research intrigued me further to be open to tackling all the challenges during my Ph.D. Yves always gave a prompt response to any of my questions or curiosities with both positive feedback and constructive criticism. I must also thank *Dr. Guillaume Schweicher,* who has been an erudite advisor and taught me new techniques with simplicity. My three months of secondment flew so quickly in the company of a fun research group (friends now) – *Martina, Rahul, Luca, Andrew, Jie, Guangfeng*, and more. Our scientifically-charged discussions over coffee or lunch were illuminating. They all contributed to making my stay in Brussels wonderful, and

I returned to Bologna with improved knowledge, good results, a more positive attitude, and many memories. My second secondment was in Instituto de Ciencia de Materiales de Barcelona (ICMAB-CSIC) under *Prof. Marta Mas-Torrent,* who is a high-spirited advisor, and she always believed in me and inspired me to explore my abilities to a greater extent. Her door was always open to discussion. In ICMAB, *Lamiaa* always stood beside me, helping me in learning new concepts and techniques with her super-positive attitude. With the combination of Marta's supervision and Lamiaa's expertise, I obtained good results from completely new techniques in the field of organic electronics. I perceived something from a lot of people from the institute along with enjoying one of the best companies- *Lamiaa, Adriyan, David, Shaqayeq, Jiali, Lorenzo, Diego* and more. Thanks to all the people from both my secondments. These secondment periods were the greatest time for me in my PhD.

During these three years, many people asked me ''how do you always get calls and visits from so many people, and who are they?'' These amazing people are my friends and too many of them! To start with, *Antik*, who is my closest friend, from my bachelor's and master's degree, also came to Europe for doing Ph.D. not so far from me, in France. He not only motivated me throughout both the previous degrees but also was a constant support during my PhD time. We often discussed about chemistry and complemented each other with our respective fields of research. This journey of Ph.D. was made comfortable because of *Inês,* who is not just my colleague, but also a friend. We enjoyed working together and also bonded after work, with drinks, dinners and discussions and being there for each other in every situation, including the tough time of the pandemic. Thanks to my friends in Bologna, *Nidhi*, *Manish, Kuldeep, and Bhavana* who made me feel at home in Bologna. My friends from master's, bachelor's, and high school, and friends met during PhD, who inspired and cheered me despite the long-distance friendship – *Pranalli, Ayushi, Ritu, Rohan, Aditya V., Aditya G., Udayan, Shubham, Hardik, Kuldeep, Ashish, etc.*, the names are far too many to mention them all. All these people made my journey way easier. Thanks a lot, folks!

I believe that I met the best project colleagues. Us, fifteen early-stage-researchers shared an excellent bond– I am thankful to *Christos, Nemo, Nicholas, Ann Maria, Federico, Marco, Mindaugas, Kripa, Lucia,* and *Alessandro* (also *Rahul, Martina, Inês* and *Lamiaa* again). We worked together and shared our ideas, which helped us to extend our knowledge. The

progress meetings of the project allowed us to come together and discuss elaborately which sometimes solved many scientific problems. I collaborated with *Rahul, Nemo, Marco, Lamiaa, Nicholas, Ann Maria,* and *Federico.* I would like to express profound thanks to them for their contributions, as they amplified my research project with their expertise in respective specializations. We also interacted and boosted our friendships by travelling together.

I would also like to thank *Prof. Dario Braga, Prof. Fabrizia Grepioni, Dr. Simone d'Agostino* and also all the former and current group members of Molecular Crystal Engineering group in Unibo - *Francesco, Inês, Caterina, Alessandra, Cecilia, Marriana, Lucia Casali, Samet, Renren* and *Laura* for their cooperation throughout my PhD.

Finally, I would like to express my heartiest gratitude to the *UHMob project, Polycrystalline, and the University of Bologna*. European Commission-funded H2020-MSCA-UHMob project provided me with the ideal platform for a PhD, combining interdisciplinary fields, companies, and universities with the best brains as Principal investigators. It was always easy to reach out to discuss my ideas and doubts with them and expand my skills in multiple directions. I sincerely thank the Polycrystalline and Molecular Crystal Engineering group in the Department of Chemistry, University of Bologna, who hosted me for PhD and provided all the facilities for carrying out my research smoothly.

Abbreviations

2MX: 2-Methoxyethanol

2PR: 2-Propanol

ABZ: Benzyl Alcohol

ACN: Acetonitrile

AFM: Atomic Force Microscopy

ANI: Anisole

API: Active Pharmaceutical Ingredient

ATR-FTIR: Attenuated Total Reflection-Fourier Transform Infrared

BAMS: Bar-Assisted Meniscus Shearing

BGBC: Bottom gate/bottom contact

BGTC: Bottom gate/top contact

BTBT: [1]Benzothieno[3,2-b][1]benzothiophene

C7-BTBT-C7: diheptylbenzo[b]benzo[4,5]thieno[2,3-d]thiophene

CHF: Chloroform

CLB: Chlorobenzene

CT: Charge Transfer

CVD: Chemical Vapour Deposition

DCM: Dichloromethane

DEC: Diethyl Carbonate

DFT: Density Functional Theory

DitBuC6-BTBT: 2,7-bis(7,7-dimethyloctyl)benzo[b]benzo[4,5]thieno[2,3-d]thiophene

DMA: *N,N*-dimethylacetamide

DMF: *N,N*-dimethylformamide

DMS: Dimethyl Sulfoxide

DMX: 1,2- Dimethoxyethane

DNTT: dinaphtho[2,3-b:2’,3’-f]thieno[3,2-b]thiophene

DSC: Differential Scanning Calorimetry

ETH: Ethanol

H_2O: Water

HOMO: Highest Occupied Molecular Orbital

HPLC: High-Performance Liquid Chromatography

HSM: Hot Stage Microscopy

HT: High Temperature

IE: Ionization Energy

IPA: Isopropyl Acetate

IPE: Isopropyl Ether

LT: Low Temperature

LUMO: Lower Unoccupied Molecular Orbital

MEK: Methyl ethyl Ketone

MPY: 1-Methyl-2-Pyrrolidone

MST: Mesitylene

MTR: Multiple Trap and Release

NMR: Nuclear Magnetic Resonance

NMT: Nitromethane

OEG-BTBT: 2,7-bis(2-(2-methoxyethoxy)ethoxy)benzo[b]benzo[4,5]thieno[2,3-d]thiophene

OFET: Organic Field Effect Transistors

OMN: Octamethyl Naphthalene

OMP: Octamethyl perylene

OMT: Octamethyl Terrylene

OSC: Organic Semiconductors

PCA: Principal Component Analysis

PFBT: Pentafluorobenzenethiol

POM: Polarized Optical Microscope

PS: Polystyrene

PSI: Paul Scherrer Institute

PVD: Physical Vapour Deposition

PXRD: Powder X-ray Diffraction

PXY: p-Xylene

RFID: Radio Frequency Identification

RT: Room Temperature

SAM: Self-Assembled Monolayer

SCXRD: Single-Crystal X-ray Diffraction

SIP: Substrate Induced Phases

SS: Sparingly Soluble

TDPA: Tetradecylphosponic Acid

TGA-EGA: Thermogravimetric Analysis-Evolved Gas Analysis

THF: Tetrahydrofuran thiophene

TLC: Thin Layer Chromatography

TMN: Tetramethyl Naphthalene

TMP: Tetramethyl Perylene

TMT: Tetramethyl Terrylene

TOL: Toluene

VTXRD: Variable-Temperature X-ray Diffraction

Abstract

The perquisites of organic semiconductors (OSCs) in the vivid field of organic electronics have attracted much attention due to the advantages like cost-effectiveness, solution processibility, versatility in material synthesis, and compatibility with a wide range of substrates. A key property in OSCs is charge carrier mobility, which essentially depends on molecular packing, as even the slightest changes or thermal fluctuations in the packing of OSC can significantly impact the mobility. Organic molecules are constructed by weak interactions like van der Waals, which makes the OSCs prone to adopt multiple packing arrangements, thus giving rise to polymorphism. Therefore, polymorph screening in bulk and thin films, and stability assessment of each crystal form are crucial for material development.

This thesis aims to present a systematic study of polymorphism and crystal growth of [1]benzothieno[3,2-b]benzothiophene (BTBT) derivatives functionalized with different side chains. The important role of peripheral side chains has been studied since they can promote different packing arrangements.

The bulk polymorph screening of OSCs was firstly approached with conventional solution mediated recrystallization experiments such as evaporation, slurry maturation, anti-solvent precipitation and desolvation processes. Each of the polymorphs were inspected thoroughly for their relative stability and the kinetics of transformation was evaluated. Secondly, polymorphism in thin films was also investigated for selected OSCs. Non-equilibrium methods like, thermal gradient and solution shearing were employed to examine the nucleation, crystal growth and morphology in controlled crystallization conditions. After careful analysis of crystal phases in bulk and thin films, OFETs have been fabricated by optimizing the manufacturing conditions and the hole mobility values were finally extracted from the transfer curves. The charge transport property of the OSCs tested for OFETs was also supported by the ionization potential and transfer integrals calculation. An attempt to correlate the solid-state structure to electronic properties was carried out. For some of the molecules, mechanical properties have been also investigated, as the response to mechanical stress is highly susceptible to packing arrangements and the intermolecular interaction

energy contributions. Mechanical deformability holds many advantages in OSC devices. For the applications in flexible electronic devices, mechanically flexible active layer of OSC is a plus as the device can withhold any fracture, which increases its durability.

Additionally, in the framework of PhD project, a collaborative research activity was carried out by solving and analysing the crystal structures of molecules from the rylene family. The comparison of crystallographic parameters of polycyclic aromatic hydrocarbons were also accomplished.

Chapter 1

Introduction

Introduction

1. Polymorphism and molecular packing

The term ‘’polymorphism’’ derives from a Greek word meaning ‘’many forms’’. Polymorphism is an important concept in many fields, including chemistry, materials science, and pharmaceuticals, as it has a significant impact on the properties and performance of materials.

The first case of polymorphism was witnessed by Klaproth in 1788, who identified three crystal forms of calcium carbonate.[1] Wöhler & Liebig, in 1832, discovered the first case of polymorphism in an organic compound, benzamide.[2] However, it wasn't until 1938 that the first X-ray diffraction structure of resorcinol polymorphs was reported by Robertson and Ubbelohde.[3] Although the phenomenon was well known, the definition of polymorphism has evolved over time. McCrone, a pioneer in crystallographic work on polymorphism, in 1965 defined polymorphs as ‘’*A polymorph is a solid crystalline phase of a given compound resulting from the possibility of at least two different arrangements of the molecules of that compound in the solid state*’’.[4] He also stated that *“It is at least this author's opinion that every compound has different polymorphic forms, and that, in general, the number of forms known for that compound is proportional to the time and money spent in research on that compound.”* In 1969, Rosenstein & Lamy proposed the definition: ‘’*When a substance can exist in more than one crystalline state it is said to exhibit polymorphism*.’’[5] Later, in 1983, Burger pointed polymorphs as ‘’*If these (solids composed of only one component) can exist in different crystal lattices, then we speak of polymorphism*.’’[6] As criticized by Bernstein, this definition suffered the exclusion of polymorphism in salts and solvates.[7] Further, in 1987, Sharma defined polymorphs as ‘’*Polymorphs means the different crystal forms, belonging to the same or different crystal systems, in which the identical units of the same element or the identical units of the same compound, or the identical ionic formulas or identical repeating units are packed differently*’’.[8] Gavezzotti in 2007 came up with definition consisting of three points: ‘’*Polymorphs are a set of crystals (a) with identical chemical composition; (b) made of molecules with same molecular connectivity, but allowing for different conformations by*

rotation about single bonds, (c) with distinctly different three-dimensional translationally periodic symmetry operations''.[9] This definition clearly described the packing (e.g., Paracetamol[10]) and conformational (e.g., Ritonavir[11]) polymorphism. However, when it comes to tautomerism, the question of whether tautomeric polymorphism should be considered a "real" polymorphism has been the subject of debate in the field of crystallography. To go from one tautomeric form to the other, a chemical bond needs to be broken and reassembled differently. Thus, from our point of view, the compounds which possess different connectivity of atoms of a molecule, may not be regarded as ''real'' polymorphs.

More recently, in 2009, Purohit & Venugopalan, defined polymorphism as: ''*thus it is defined as the ability of a substance to exist as two or more crystalline phases that have different arrangements or conformations of the molecules in the crystal lattice*.''[12]

Based on the definitions, polymorphism can be classified into three main categories: packing polymorphism, conformational polymorphism, and synthon polymorphism.[13–15]

i. **Packing polymorphism**: the molecules can pack or arrange into different three-dimensional structures.
ii. **Conformational polymorphism:** the conformationally flexible molecules fold into different shapes that pack in different three-dimensional structures.
iii. **Synthon polymorphism:** Synthon polymorphism may arise when the competing functional groups adopt different supramolecular synthons and thus forms polymorphs.

In the case of organic semiconductor (OSC) the different crystal structures can exhibit distinct electronic properties, making the polymorphism a critical factor in determining the performance of OSC devices. To optimize the performance of OSCs, it is crucial to understand the relationship between their structure and properties. Thus, by studying the polymorphism of OSCs, scientists can gain insights into the factors that influence their electronic behaviour, paving the way for developing new materials with improved performance and functionality.

1.1 Types of Polymorphism

While it was established that polymorphism is a common phenomenon, further consideration of the relative stability of the forms is also crucial. The relative stability of the polymorphic forms is governed by the free energies, with the thermodynamic phase (most stable) having the lowest energy at given values of T and P, then the other metastable phases (kinetic phases).[13] The stability of the metastable form can vary from a few seconds to several years.[16]

Based on the stability of the solid crystals with respect to temperature and pressure, polymorphism can be categorized into two classes: Monotropic and enantiotropic.[12,17]

(i) Monotropic polymorphism: When only one polymorph is stable at all temperatures below the melting point, with all the other polymorphs being unstable, these polymorphs are termed monotropes.

(ii) Enantiotropic polymorphism: In the enantiotropic system of polymorphism, there are different polymorphs, and each polymorph is stable in a specific range of temperatures.

These polymorphic relationships can be rationalized by the plots reported in Figure 1. An approach to defining the type of relation between two polymorphs is based on the comparison

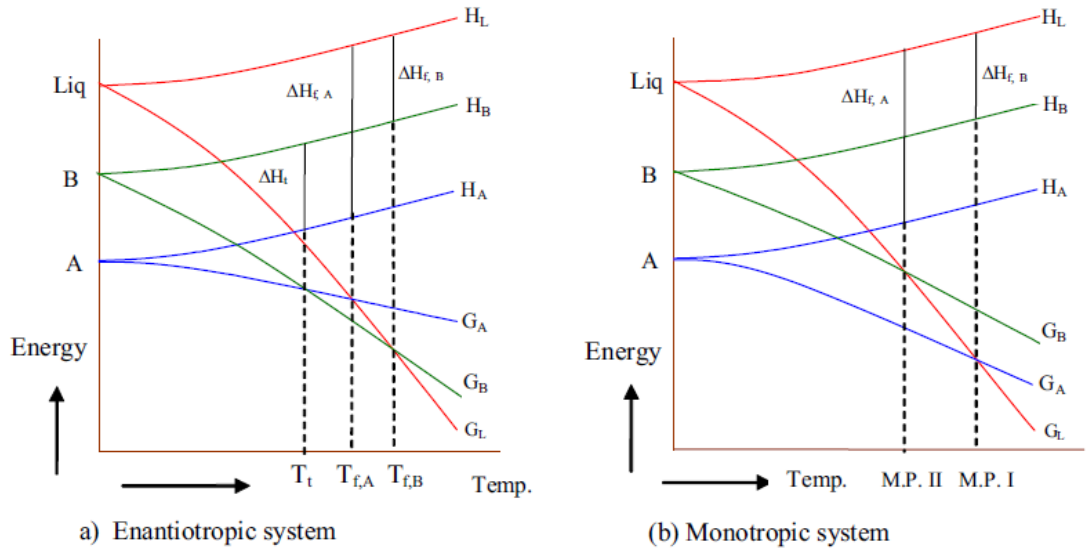

Figure 1 Variation of energy with temperature for enantiotropic and monotropic systems. Curves H_A, H_B and H_L are for enthalpy, whereas $\Delta H_{f,A}$ and $\Delta H_{f,B}$ represent enthalpy of fusion and ΔH_t represents enthalpy of transformation. Image reused from Purohit et al. Resonance volume 14, Article number: 882 (2009).[12] Copyright © 2009, Indian Academy of Sciences.

of their melting temperature and the associated heats of fusion according to the "Burger-Ramberger rules" which states that *''In almost any case, the heat of transition (or the difference in the heats of fusion) is positive for enantiotropic transitions from the low-temperature to the high-temperature form and negative for monotropic transitions.''*.[18] The heat or enthalpy of transition refers to the amount of heat absorbed or released when a substance undergoes a phase transition, such as melting or boiling. Burger-Ramberger postulated that in general, the heat of transition is positive for enantiotropic transitions from the low-temperature to the high-temperature form, because energy is required to break the intermolecular bonds holding the solid in its low-temperature phase and convert it into the high-temperature phase and negative for monotropic transitions because energy is released as the solid transitions to a more stable state. It is also important to note that there may be exceptions depending on the specific properties of the substances involved and the conditions under which the transition occurs.[19]

1.2 Thin film polymorphism

It has been observed that when molecules crystallize on a material surface, they might adopt unique interfacial packing arrangements compared to the bulk, leading to new polymorphic phases, and these phases are referred to as ''thin film phases'' or ''surface induced phases'' or ''substrate induced phases'' (SIPs). These SIPs tend to extend over several molecular layers.[20,21] The rigid substrate support, which acts as the nucleating agent, can propel a different reorganization of the molecules that locally affect the intermolecular orbital overlap.[22]

The physical properties are mediated by the molecular packing arrangements, and any deviation of packing from bulk might have a profound impact on a large range of OSC systems.[23] Therefore, gaining insight into the exact molecular packing in thin films is of utmost importance for a complete understanding and control over the structure-property relationships.

The concept of SIPs emerged quite recently; even if researchers have attempted to understand the science behind the origin of SIPs, some questions remain unanswered, like which type of systems are prone to produce SIPs or the influence of the substrate.[20]

One classic example is a well-known compound of pentacene, which forms different structures and morphologies depending on the growth conditions and, in the case of films, on the type of surface it is deposited on. In bulk, pentacene exhibits two polymorphs- the low temperature (LT) phase and the high temperature (HT) phase. Interestingly, in thin films, two SIP phases are observed in addition to a monolayer structure.[24–26] The difference between pentacene polymorphs can always be related to a change in the tilt of the long molecular axis, as shown in Figure 2.

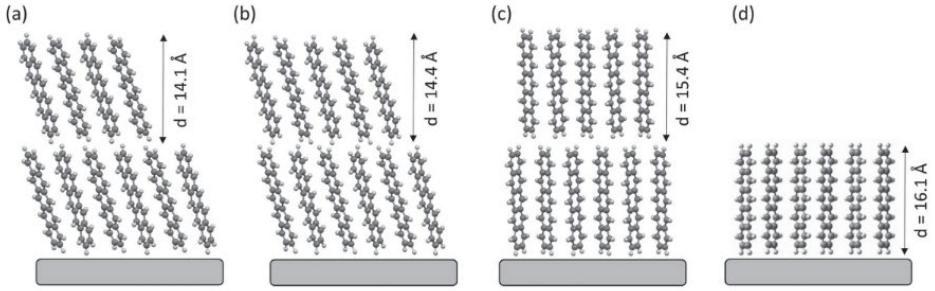

Figure 2 Different packing motifs of pentacene molecules observed in thin films where the precise molecular packing is known: (a) molecules in the bulk (LT) phase with a tilt of ≈24° from the substrate normal, (b) molecules in the bulk (HT) phase with a tilt of ≈21°, (c) molecules in the common 15.4 Å SIP with a less pronounced tilt of ≈3° and (d) upright-standing molecules (0° tilt) in a monolayer. Image reused from Jones et al. Adv. Funct. Mater., 26: 2233-2255 (2016).[20]

2. Crystal growth

Crystals can be considered as ordered supramolecular systems with nearly perfect periodic self-assemblage of millions of molecules, held together by medium- and long-range non-covalent interactions as described by Dunitz [27]. In the solid state, the molecules self-assemble owing to a complex combination of chemical and geometrical factors and a complementary contribution of different intermolecular interactions, like π-π and van der Waals'.[28–31] From the thermodynamic point of view, a stable crystal structure for a molecule is associated with a free energy minimum which is a result of the overall optimization of attractive and repulsive intermolecular interactions of varying strengths. Thus, it is of fundamental importance to understand the nature, strength, and directionalities of the intermolecular interactions.[25] The rational process for designing and constructing fine-tuned functional crystalline materials is referred to as crystal engineering.[30]

Based on a classical interpretation, a crystalline phase is generated as an outcome of molecular aggregation processes in a solution that leads to the formation of nuclei, which procure a certain size for a sufficient time to enable growth into macroscopic crystals. It has to be highlighted that crystallization is still a not-fully-understood process: in the following sections, the nucleation and growth steps are described and elaborated accordingly to traditional crystallization theory.

2.1 Nucleation and crystal growth

In a solution, the formation of a solid depends on several parameters like temperature, supersaturation, chemical composition of the medium, and hydrodynamics. Nucleation is a decisive step in the process of crystallization, and it can occur through two different pathways: classical and nonclassical.[32,33] Classical nucleation pathway is the most commonly observed pathway in crystallization, and thus we focused our further discussion to classical nucleation theory. It involves the formation of a small cluster of atoms or molecules, called a critical nucleus, from the supersaturated solution. This critical nucleus grows as additional atoms or molecules are added to it, forming a stable crystal. This pathway is driven by the

thermodynamic properties of the material and can be described by classical nucleation theory (also see Section 2.2).

In classical nucleation, the nucleus forms when random fluctuations in the material's energy state exceed a certain threshold, and the nucleus grows by capturing additional molecules or atoms from the surrounding material. The review by Karthika *et al.*[32] provides a comprehensive and clear discussion of both classical and nonclassical nucleation theories, which describes that the classical nucleation theory is based on the condensation of vapor to a liquid which can be extended to other liquid–solid equilibrium systems. The free energy change of the system during homogeneous nucleation of a spherical nucleus of radius r is given by:

$$\Delta G = \frac{-4\pi r^3}{3v} KT \ln S + 4\pi r^2 \sigma \qquad \text{Equation } 1^{32}$$

Where, $4\pi r^3/3v$ represents the number of molecules in a cluster of radius r with the volume of a single molecule as v, S = P/P* is the vapor supersaturation ratio and σ is the specific surface energy of the interface between drop and the surrounding vapor. The two terms in Equation 1 have separate dependencies on *r*, as, when *r* is large, ΔG decreases because the first term dominates (it represents the energy decrease upon transition from vapor to liquid) while when *r* is less, ΔG increases because the second term dominates which is associated to the creation of a new surface. Thus, the free energy (ΔG) of formation passes through a

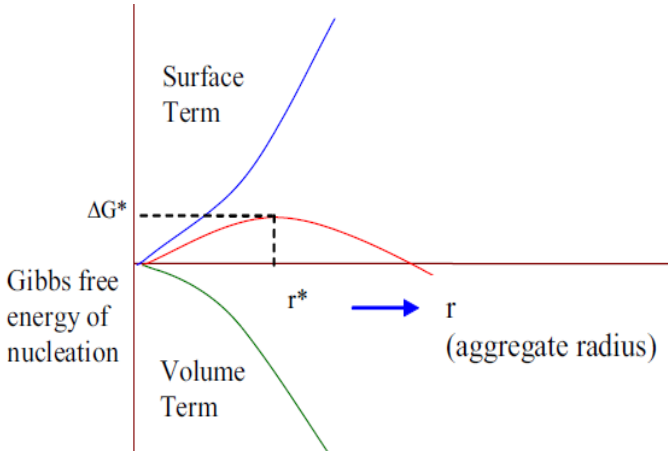

Figure 3 Schematic representation showing the dependence of nucleation barrier ΔG*on the radius r according to classical nucleation theory. The plot shows Gibbs free energy G of molecular aggregates vs. size of the aggregates. The red curve represents total free energy. The activation free energy ΔG* is the free energy at r*. Image reused from Purohit *et al.* Resonance volume 14, Article number: 882 (2009).[12] Copyright © 2009, Indian Academy of Sciences.

maximum = r*, where r* is the radius of a critical nucleus at which the probability of formation of a nucleus goes through a minimum (Figure 3).

The classical nucleation mechanisms can be grouped into two major categories: primary and secondary nucleation.[16,34]

(i) **Primary nucleation** designates all the events of the nucleation which do not involve crystals of the solute already formed. We can further classify primary nucleation into primary homogeneous nucleation, where the nucleation process is independent of any foreign particle, and primary heterogeneous nucleation, where the nucleation occurs thanks to the interaction with foreign particles or substrate.

(ii) **Secondary nucleation** is driven by crystals of solute present in the supersaturated solution and can involve their interaction with external elements like crystallizer walls, stirrers, and other surfaces.

Nucleation is driven by supersaturation and takes place in a metastable region called the metastability zone.[34] The number of molecules necessary to achieve an effective nucleating cluster is inversely proportional to the supersaturation, which means that the probability of nucleation will increase with increased supersaturation. Other important parameters like solubility, the rate at which supersaturation is created, temperature, diffusivity, and the reactivity of surfaces toward nucleation also govern the mechanism of nucleation and growth.[16,35]

Once the nucleation step has been overcome, the nuclei grow into macroscopic crystals during a step called crystal growth. The growth rate of a crystal phase is particularly ruled by multiple external factors like solubility (the higher the solubility, the higher the growth rate), temperature (produces extremely different growth rates), and hydrodynamics (the relative velocity of the solution compared to the crystal).[36]

Nonclassical nucleation pathways, which are rather less commonly observed, occur when the formation of the new phase is not solely governed by thermodynamics but also by kinetic effects such as surface energy and topology. These pathways can involve the formation of

non-spherical nuclei with complex structures, and they often occur in materials that have complex chemical and physical properties. Nonclassical nucleation can occur through the assembly of pre-existing clusters rather than the formation of a critical nucleus.

2.2 Origin of kinetic and thermodynamic phases

It is entrenched that the crystallization process commences with nucleation, which serves as a structural blueprint for the subsequent growth of a particular crystal. In a supersaturated solution, the existence of all the possible crystal forms of the molecule persists, and the system could evolve towards different relaxation paths, hence the crystallization process is regulated by kinetic competition.

Ostwald's rule of stages describes that the crystallization from solution occurs in steps, according to which the initial nucleation results in the appearance of a kinetic phase (thermodynamically least stable) which is most soluble.[37,38] This form may dissolve or transform into a more stable form over time. Subsequently, the most stable form appears at the end of this cycle. In practice, it is possible to isolate each polymorph at different levels of solution supersaturation by attaining precise control over the crystallization process.[39] Furthermore, the thermodynamics of crystallizations can be comprehended by the concept of energy barrier. For example, let us consider a dimorphic system with Polymorph A and Polymorph B, with Polymorph A being more stable (Figure 4). In 1991, Etter presented that during the nucleation process, different clusters (pre-nucleation molecular assemblies) compete for molecules. The concentration of each form of a cluster is determined by the free energy barrier of cluster formation.[40] Moreover, there will be a characteristic value of r_c and ΔG^*_c related to each cluster (according to the Volmer model, the viability of a cluster with mean radius, r, depends on the attainment of the critical cluster size, r_c). Therefore, the first polymorph to crystallize will correspond to the cluster with the lowest free energy barrier (Polymorph B as $\Delta G^*_{c,\,B} < \Delta G^*_{c,\,A}$). Even though the stable Polymorph A has the higher thermodynamic drive to crystallize, Polymorph B nucleates first as it results from the cluster with the fastest growth rate due to the lowest free energy barrier.

Metastable phases featuring 'disappearing polymorphs'- While hovering on the subject of kinetic phases, the classic tale of 'disappearing polymorphs' by Dunitz and Bernstein[41] must

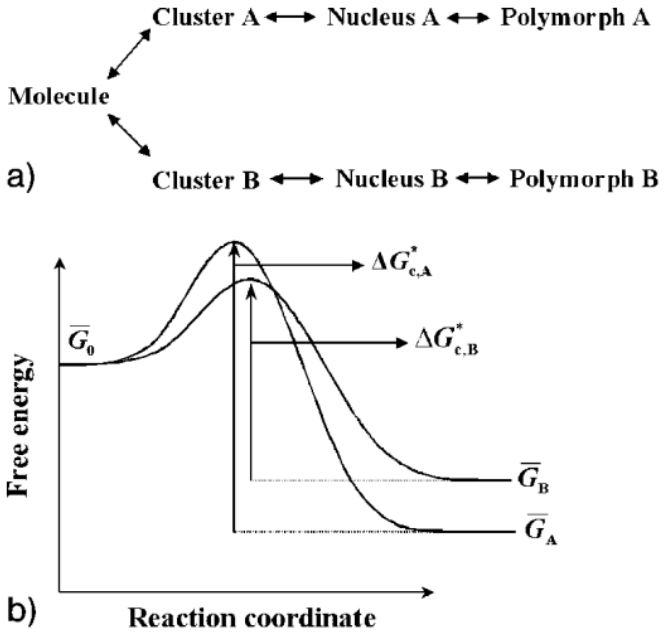

Figure 4 (a) Clusters competing for molecules during crystallization of polymorphs A and B.[31]. (b) Free energy barrier associated with crystallization of polymorphs A and B. $\Delta G^*_{c,A}$ and $\Delta G^*_{c,B}$ are the activation free energies.[13] Image reused from Lohani et al.[11] Copyright © 2006 Wiley-VCH Verlag GmbH & Co. KGaA.

be highlighted. They reported several cases of metastable phase that crystallized and recrystallized until the thermodynamic phase appeared. After the crystallization of the thermodynamic phase, the metastable phases became dramatically unstable and ceased to exist. Moreover, the crystals of the thermodynamic stable phase acted like planetary seeds, which prevented the further attainment of the metastable phase. However, they concluded the article with the sentence: ''In any case, we believe that once a particular polymorph has been obtained, it is always possible to obtain it again; it is only a matter of finding the right experimental conditions." which is open to the possibility make the polymorph to reappear.

2.3 Crystallization methods used to explore the polymorphic landscape.

Crystallization is a chemical process that involves solid or liquid, or gas, whether individually or together, to separate a homogeneous solid substance having a three-dimensional atomic arrangement. Multiple techniques can be employed depending on the chemical process. Dhanaraj *et al.*[42] illustrated all the conventional techniques in detail that can be adopted for performing crystallization. Some of the common techniques are briefly reported as follows:[43]

Solution crystallization: The crystallization of an organic compound after being dissolved in a solvent is known as solution crystallization. This is the most common method for obtaining crystals. This can be performed at desired experimental conditions, like controlling the temperature and pressure. Upon the crystallization initiation, the concentration in the solution may vary in different pathways depending on the process parameters.

- ***Precipitation by gradient temperature:*** Using this method, it is likely to obtain crystals by cooling down a saturated solution with a controlled rate; it can be slow cooling or crash cooling.
- ***Antisolvent crystallization:*** This method is widely used for polymorph control and yield improvement. The organic compound is dissolved in a solvent where it is soluble, and then an anti-solvent is added to decrease the solubility. The selection of solvent type and temperature variations can help to control the resultant crystal form.
- ***Slurry maturation:*** Performing slurry experiments can prove to be advantageous for obtaining a thermodynamically stable form. Slurry experiments usually take days to weeks and can be monitored at intermediate checkpoints. Although this method is not likely to provide well-growth single crystals since the solution is under constant stirring, the most stable form is usually obtained. The slurry can also be performed by solvent mixtures and at high temperatures to induce the isolation of different polymorphs (enantiotropic forms).
- ***Solvothermal method:*** As the term suggests, the crystallization with the solvothermal method is performed using a solvent at elevated temperatures. The process is carried out in a closed vessel (autoclave with Teflon lining) where the saturated solution is filled. The solvent selected should be one in which the solubility is sparing but finite. The autoclave is placed inside an oven, and the temperature is set above the boiling point of the solvent. The increased temperatures increase the vapour pressure hence the solubility. However, one of the major drawbacks is the amount of material required for making the solution saturated for good solvent: the use of solvent mixtures with antisolvent can help to reduce the amount requested.

Melt crystallization: Melt growth of crystals is undoubtedly the most widespread method of growing large single crystals at relatively high growth rates. If the decomposition of an organic compound doesn't occur upon heating and melting, the crystallization can be performed by melt cooling. Melt cooling is preferred when solution evaporation leads to solvent inclusion or co-crystal formation.

Sublimation: Sublimation refers to crystallization from vapour. When it is possible to sublime the solid directly into the vapour (vacuum), crystals are deposited when the vapour is chilled by a cold surface. If the vapour pressure of the molecule is suitably high, the sublimation method can be employed for the recrystallization experiment. One of the pros of sublimation is that the sublimation enables the separation of a volatile organic molecule in a purer form. The crystals can be isolated by keeping the condenser at a lower temperature compared to the temperature of vaporization. For cooling, no artificial refrigeration is required. However, the vapour pressures of most organic molecules are too low for this technique to be used.

Mechanochemistry: This is a technique used to obtain crystals of molecules with poor solubility at ambient conditions. Upon neat grinding, the heat generated can induce local melting at the interface, and that can cause the nucleation of a new phase. Sometimes solvent-assisted grinding or kneading is also performed to increase the rate of nucleation. However, this technique cannot yield good-quality single crystals.[43]

3. The rise of organic semiconductor materials

The vivid field of organic electronics has gained much attention in the past few decades. Organic semiconductors (OSCs) attained recognition in the early 1940s. However, extensive research was propelled during the 1960s. Owing to their great possibilities and versatility for a wide range of applications, including portable solar cells, curved television screens, biochemical sensors, flexible light sources, radio frequency identification (RFID) tags, and smartphone displays, OSCs have proven to be an asset in multiple directions of organic electronics.[44] One of the major benefits of using organic semiconductors (OSCs) is the tuneable chemical and physical properties of the OSCs by efficient design strategies and polymorphism control. Furthermore, the OSCs are advantageous due to their high solution processibility, which offers the possibility to fabricate cost-effective and flexible devices.[45] Particularly, in the field of organic field effect transistors (OFETs), the operation principle relies on the transfer of charge carriers. Charge carrier mobility, which is the ability to transport electrical charges (defined as the derivative of the drift velocity of the charge carrier (cm s^{-1}) with respect to the applied electric field (V cm^{-1})), is a property intrinsic to a material, and it depends on its structure at the molecular and supramolecular level.[46] The charge transport in OSCs is greatly governed by intermolecular interactions and π-orbital overlap, which indicates the sensitivity of charge transport depending on the molecular structural arrangements. Since in small organic molecules, the dominant interactions are van der Waals and weak electrostatic interactions, the possibility of the molecules to self-assemble in multiple packing arrangements becomes quite high, and therefore, polymorphism comes into play. As previously discussed, each polymorph of a molecule can exhibit different physical properties. Thus, it is crucial to have a thorough understanding of the polymorphic phases, their respective crystal structures, and relative stabilities for digging deep into the structure-electronic property relationship. For example, the dependence of the charge carrier mobility on the crystal packing can be observed in the research of TIPS-pentacene thin film transistors, where one of the polymorphs exhibits the hole mobility of 1 $cm^2V^{-1}s^{-1}$ whereas the other polymorph yielded the high mobility of 11 $cm^2V^{-1}s^{-1}$. There are plenty of other examples like Pentacene,[47–50] Rubrene,[51–54] 5,11-bis((triethylsilyl)ethynyl)anthra[2,3-b:6,7-b']dithiophene (TES-ADT),[50,55–57] BTBTs,[22,46,58–65] dinaphtho[2,3-b:2',3'-f]thieno[3,2-b]thiophene (DNTT),[66–68]

etc. in the literature where drastic differences in the charge carrier mobility were observed for different polymorphs of the compounds. However, the references are far too many to cite them all. Reviews by Chung *et al.,*[44] Anthony,[50] and Schweicher *et al.*[22] discussed the wide landscape of molecules that have been studied elaborately in the context of crystal packing and charge transport.

3.1 Types of molecular packing motifs in organic semiconductor molecules

The structural features of a molecular crystal can be described in terms of motifs or patterns of interactions. Packing motifs are the patterns of the orientation of molecules with respect to one another in the crystal structures.[69] Comprehensive research on the packing motif of molecular crystals has been performed formerly, and it led to five major possible packing motifs in organic crystals (Figure 5).

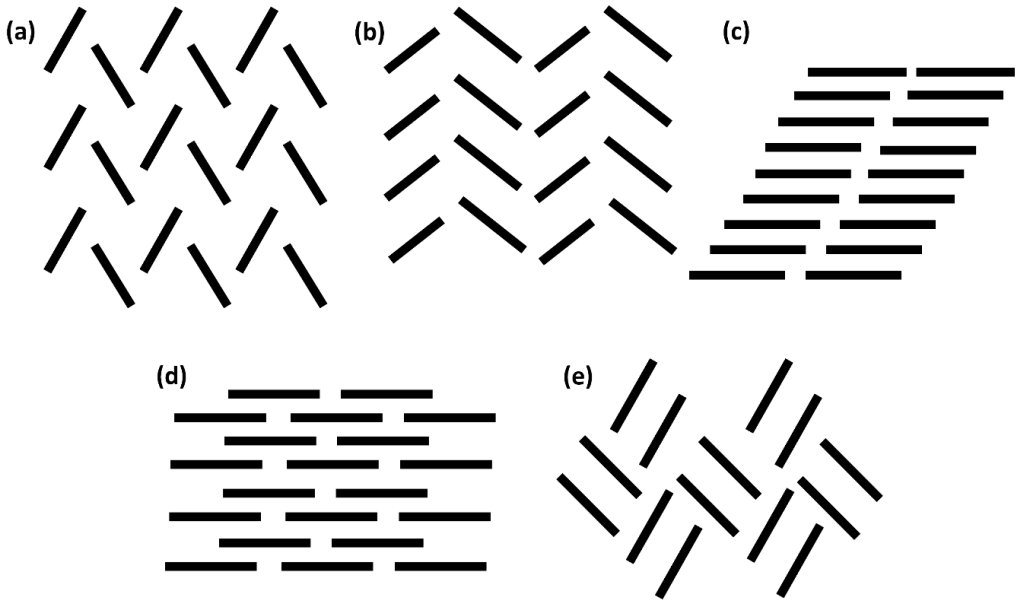

Figure 5 Molecular packing motifs in crystals. (a) Typical herringbone (face-to-edge) without π –π overlap, (b) herringbone packing with π – π overlaps between adjacent molecules; (c) lamellar motif, 1D π -stacking; (d) lamellar motif, 2D π -stacking and (e) sandwich herringbone.

(a) Typical herringbone (C—H···π) without the π- π overlap between neighbouring molecules,[70] is typically characterized by an edge-to-face packing of molecules.

(b) Slipped π-stacking or non-classical herringbone packing with π- π overlap between neighbouring molecules.[71]

(c) **One dimensional (1D) π-stacking**, lamellar packing[72] characterized by columnar face-to-face packing of molecules with columns angled relative to one another.

(d) **Two-dimensional (2D) π-stacking**, lamellar packing.[73,74] characterized by columnar face-to-face packing of molecules with columns parallel to one another.

(e) **Sandwich herringbone**, characterized by pairs of molecules packed face-to-face and with the pairs packing edge-to-face with other pairs.

The first detailed study of packing motifs was thoroughly discussed in 1989 by Desiraju and Gavezzoti[75] when they suggested the crystal structures of polycyclic aromatic hydrocarbons.

However, recently some studies with an emphasis on structural and packing descriptors have been reported.[76] For a refined and elaborative understanding of the molecular packing arrangement, the packing descriptors might describe the rigid core of organic molecules more accurately. Crystal packing features like the angles of tilting of the aromatic core in the stacking direction, the sliding/shifting of the molecule in long and short axes, pitch and roll angles, etc., can be investigated to give guidelines for predicting the most likely packing family. These descriptors guide the understanding of the nature of packing motifs which compliments the traditional well-defined definitions of the packing motifs.

The descriptors and packing arrangements largely govern critically the overall physical properties like electrical, mechanical, or optical properties, discussed in later sections.

3.2 [1]Benzothieno[3,2-b][1]benzothiophene (BTBT) derivatives

Aiming for the application in OFETs, selecting a molecule with high solution processibility and chemical stability is essential. Numerous research groups have extensively studied the [1]Benzothieno[3,2-b][1]benzothiophene (BTBT) π-conjugated molecules and their derivatives with bulky and linear chains more recently (Figure 6).

BTBT systems present a promising core structure for air-stable organic semiconductors.[77] The derivatives of BTBT are composed of fused thiophenes and benzene rings, which introduce a

rigid and planar π-conjugated system. Such chemical structure leads to a large intermolecular orbital overlap in solid state elucidating their high charge-carrier mobility.[78]

Minemawari *et al.*[79] investigated the crystal packing arrangements of a series of BTBT with alkylated side chains, and it was observed that layered herringbone packing prevails in all the systems. Ruzie *et al.* reported a thorough study of five novel BTBT derivatives with aliphatic side chains (alkyl, ether and thioether chains). They illustrated the influence of intrinsic structural factors that regulate the final electronic property, and thus pointed out the significance of effective design strategies.[46]

Effect of BTBT derivatives with symmetrical bulky substituents like di-iPr, di-tBu and di-tTMS groups in crystal packing, polymorphic transition pathways, transfer integrals and charge transport have also been reported by multiple research groups.[63,80,81] The highest mobility observed among the bulky group substituted BTBT systems was recorded in ditBu-BTBT with mobility as high as 17 $cm^2V^{-1}s^{-1}$.[63]

In our work, we continued to explore the BTBT derivatives with different functionalization to investigate extensively the polymorphism, the crystal structure and finally the electronic performances in manufactured devices.[82]

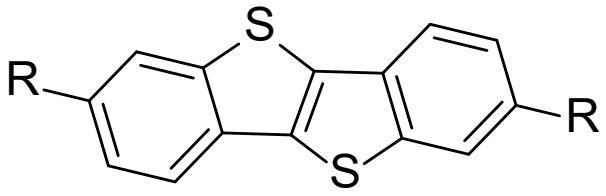

Figure 6 Molecular structure of BTBT with substitutions (R) present at -2 and -7 positions in the core, where R= alkyl chain or bulky group.

3.3 Charge transport

Charge transfer originates with the transfer of charge carriers between individual molecules. However, to comprehend how the charge transfer takes place, we require elaborate knowledge of the electronic structure of the organic molecule. Organic molecular systems consist of carbon atom backbones with sp^2 hybridised atomic orbitals of adjoining carbon atoms that overlap, resulting in bonding σ and antibonding σ* molecular orbitals. The remaining atomic p_z orbitals overlap to a lesser degree, so that the resulting molecular π and π* orbitals are less bonding or antibonding, thereby, yielding the frontier orbitals of the

molecule. All the bonding orbitals up to the highest occupied molecular orbital (HOMO) are filled with two electrons (antiparallel spin), at the ground state. While lower unoccupied molecular orbital (LUMO) onwards, is empty. For the occurrence of charge transport in organic molecules, there has to be charge on the molecular unit, which is achieved either by the addition of an electron on the antibonding orbital or by the removal of an electron from the bonding orbital.[83]

The vicinity of the atomic units within the structures governs the width of the energy band. There are various models of charge transfer theories such as the classic band-like model for single crystal materials (disorder-free OSCs), the mobility edge model and multiple trap and release (MTR) for polycrystalline material with a low extent of structural disorder, the hopping model for highly disordered or amorphous material, and finally Marcus charge transfer (CT) model, which is considered commonly, since in many OSCs electron or hole transport along the polymeric backbone would require reorganization energy and also the polarization effect exists.[84]

Equation 2[84] is the Marcus equation illustrating the rate of electron transfer k_{ET}.

$$k_{ET} = \left(\frac{4\pi^2}{h}\right) \frac{t^2}{(4\pi\lambda T)^{1/2}} e^{(-\lambda/4kT)} \qquad \text{Equation 2}$$

Where, h is the Plank's constant, λ is the reorganizational energy, and t is the transfer integral.

The transfer integrals of the neighbouring molecules indicate the wave function overlap of the implicated orbitals.

It can be highlighted that the efficiency of the charge transfer of an organic molecule is determined by slow reorganizational energy combined with a large transfer integral.[85] Although, there are several other factors - such as molecular packing, temperature, pressure, disorder, impurities, electric field, doping, dielectric, etc. - that influence the charge transport and thus the mobility, [22,85]

4. Organic field effect transistors

4.1 Methods of deposition

The performance of an OFET device greatly depends on surface engineering, which, for example, includes the type of substrate used, surface modification techniques and surface coating methods. The surface coating method requires the deposition of an OSC thin film layer on the surface of the substrate, which is responsible for altering the properties of the surface. This means that different deposition techniques can result in different surface properties like surface morphology, microstructure, throughput, electrical and optical properties, and hardness.[86,87]

There are several methods of deposition like Physical Vapour Deposition (PVD), Chemical Vapour Deposition (CVD), solution-phase deposition, and molten state deposition. In this chapter we will focus on a few deposition techniques selected and used in the present work.

PVD describes the deposition processes that require condensation of the vaporized solid material on top of the surface of the solid material under a partial vacuum condition.[88,89] Deposition by PVD process usually leads to film thickness in the range of a few nanometres to a thousandth of nanometres. There are different types of PVD depositions, like vacuum evaporation, ion plating, arc vapour deposition, and sputtering. For example, in thermal or vacuum deposition, at first, the vapour is formed by subjecting the target material to a very high temperature by subliming, this ejected vapour is then transferred to the substrate via vacuum, and at last, the condensation of the vapour takes place which results in a solid thin film.[90]

Solution-phase deposition consists of an array of solution processing techniques for thin film deposition such as-

(i) Drop casting: Drop casting involves casting the OSC solution onto the target substrate followed by subsequent evaporation of the solvent. After the evaporation, either crystals or a thin film is obtained, depending on the self-organising ability of the OSC.

(ii) **Spin coating:** Spin coating is the most commonly used technique as a one-step deposition with uniform thickness. Once the solution is dropped onto a substrate, the substrate is accelerated to a high angular velocity to simultaneously spread the solution and evaporate the solvent. The acceleration, solution viscosity and concentration govern thickness.

4.1.1 Solution shearing deposition

Solution shearing deposition technique has gained attention more recently as it is a highly versatile method where a movable top bar/blade drags an OSC ink droplet over a temperature-controlled substrate using Bar-Assisted Meniscus Shearing (BAMS), as shown in Figure 7.[91]

This technique allows tuning the basic parameters like substrate temperature and the substrate dragging speed. The substrate temperature is selected based on the boiling point of the ink solution used to control the crystallization rate, while the nucleation and crystal growth are influenced by the coating speed. These parameters are highly crucial for the kinetics and thermodynamics of crystallization. Apart from this, other parameters like ink formulation, substrate type and surface treatments can also be modified. All these parameters are interrelated and have a key role in the final thin film phase and morphology, which eventually impacts the device performance.[23]

Figure 7 Schematic representation of Bar-assisted meniscus grinding (BAMS)

By modulating these parameters, one can control the crystallization process and induce high-performing devices. Furthermore, the ink formulation can be modified additionally with OSC blends with polymers, and other parameters combined with the previous ones comes into play like the polymer binder nature, its molecular weight, and the OSC: polymer binder ratio. Typically, the device performance is expected to increase with the addition of polymer binder

as during the deposition there is vertical phase separation, where polymer remains on the bottom and the organic semiconductor crystallises on the top. This results in a reduction of the interfacial charge trap density and an enhancement of the device stability.[92,93]

With all the possibilities to tune and optimize the deposition parameters, this method has proven to be promising to obtain high-performing thin film devices at low cost and large throughput as it is compatible with roll-to-roll manufacturing.

4.1.2 Deposition from the melt by thermal gradient

A plethora of deposition methods like spin-coating, drop casting, dip coating, inkjet printing, zone casting, spray coating, stamping, blade coating, etc., have been extensively used.[91] Over the years solution shearing and vapour deposition (as discussed above) have emerged to produce uniform and aligned thin films. However, thin film production from the melt is still less explored comparatively.[91] Directional crystallization using the thermal gradient technique is well-known in the inorganic semiconductor industry. However, in the mid-1970s, Lovinger *et al*.[94–96] proved that this method led to the formation of a unique nucleus and allowed the growth of highly oriented polymer chains. More recently, the use of thermal gradient also expanded to organic small molecules to study the faceted growth of the crystals, liquid crystal phases and emergence of new non-equilibrium polymorphs due to controlled conditions of crystallization.[97,98]

The thermal gradient technique makes it possible to restrict the crystallization in 2-dimension (2D) by allowing the formation of a macroscopically flat crystal front. Uniformly distributed films (thickness in µm range) are formed by sandwiching the material between two glass slides to avoid dewetting of the melt. Then, the sandwiched glass slides are translated at a constant pulling rate (µm s^{-1}). As the sample approaches the cold stage, in situ nucleation and growth of the crystals are observed by a Polarized Optical Microscope (POM). The setup shown in Figure 8 consists of two distinct heating stages separated by a gap (usually 2-2.5 mm). One heating stage is set at the temperature above the melting point (T_h) and the other stage is at a temperature below the crystallization point (T_c) of the molecule in concern. This whole setup can be displaced with controlled pulling velocities.

Nucleation and kinetics play a decisive role in the crystallization process.[99–101] With the aid of the thermal gradient technique, we can produce films from the melt by tailoring the conditions responsible for nucleation and growth, like the temperature of hot and cold stages, pulling rate of the substrate, the cooling rate, etc.

For molecules crystallizing from the melt using directional crystallization, decoupling of nucleation (triggered by a thermal gradient) and growth (triggered by sample displacement) is possible, and the conditions of crystallizations lead to the production of highly textured thin films with the uniaxial in-plane alignment of crystallites. Another major advantage is that since the crystallization conditions can be controlled, thus polymorph-selective crystallization can be performed.

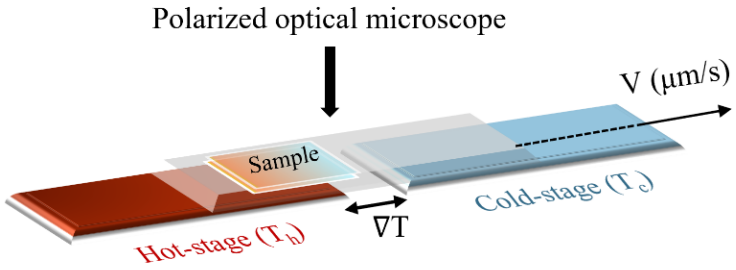

Figure 8 Schematic representation of thermal gradient setup.

4.2 Transistor measurement theory

The major components of a OFET device are (i) the active layer of OSC, deposited by either of the methods described in Section 4.1, (ii) the dielectric layer and (iii) three conducting electrodes, gate (G), source (S) and drain (D). Figure 9 depicts different geometries that can be considered for the device set-up.

The function of the source and drain electrodes is to inject and fetch charge carriers to and from the semiconductor. For p-type semiconductors, the source and the drain are made of high-work function metals (usually Au, but also Pd, Pt, and Ni or some conducting polymers).

Due to the application of gate voltage, the charge injection, and the formation of conducting channel in the OSC takes place. While on the application of the drain voltage, the charge migration across the organic layer and collection at the drain electrode happens. Dealing with

organic molecules, these charge-transport properties depend on the structural packing and the degree of order in the solid state.[102]

Parameter extraction: For comparing the performances of OSC materials, a reliable, albeit reproducible extraction of mobility and threshold voltage from the current-voltage (I-V) characteristics of the transistor is imperative. As the drain current (I_D), depends on two independent voltages- the gate voltage (V_G) and the drain voltage (V_D)-the I-V curves can be plotted in two different ways: transfer characteristics, where I_D is plotted as a function of V_G, for a given V_D; and output characteristics, where I_D is plotted as a function of V_D, for a given V_G.

Equation 3 indicates the plotting of the square root of saturation current versus gate voltage, which would result in a straight line. The slope of the straight line gives mobility, while threshold voltage is obtained by extrapolation of the line to zero current.

$$\sqrt{I_D} = \sqrt{\frac{W}{2L}C_i\mu}(V_G - V_T) \qquad \text{Equation 3}$$

Where, I_D drain current in saturation regime, V_G is the gate voltage, V_T is the threshold voltage, W is the channel width, L is the channel length, and C_i the capacitance (per unit area) of the dielectric and μ is the carrier mobility.

However, in a real device, there are two challenges while mobility extraction- gate-voltage-dependent mobility and contact resistance, due to which the actual curve is not a straight line and it gets upward curvature. Therefore, for such a curve, both the extracted mobility and the threshold voltage critically depend on the voltage range used for the linear fitting. The downward curvature of transfer characteristics is observed due to contact resistance, which

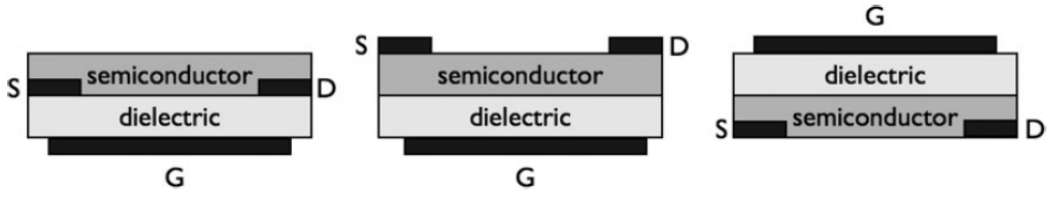

Figure 9 Three popular organic-transistor geometries. From left to right: bottom gate, bottom contacts (BG-BC); bottom gate, top contacts (BG-TC); top gate, bottom contacts (TG-BC). S: source; D: drain; G: gate. Image reused from Braga *et al.*[103]

tends to limit the available current out of the device. In the end, both these effects tend to compensate one another and thus the final transfer curve looks close to a straight line.[103]

Nonetheless, there are plenty of other factors which play crucial roles and influence the mobility and threshold voltage, and there is ample scope for discussion, however, we hereby limit the consideration until the parameter extraction.

5. Objective of this work

My Ph.D. is a part of the project Ultra-high Charge Carrier Mobility to Elucidate Transport Mechanisms in Molecular Semiconductors (UHMob), which is a European Training Network (ETN) funded by Horizon 2020 project and Marie Sklodowska-Curie Action. The objective of UHMob project is to gain a fundamental understanding of charge transport mechanisms in molecular semiconductors. To attain this goal, 15 early-stage-researchers (ESRs), have conducted complementary studies in diverse research domains.

In this framework, as one of the ESRs, the core objective of my project was:

- to determine the number and the relative stability of polymorphs of selected molecular semiconductors
- identification of molecular features and crystal growth conditions favouring robustness against polymorphism
- solving and analysing crystal structures of organic molecular semiconductors

Furthermore, the secondment training goals of the project were designed:

- to explore if forced non-equilibrium conditions using the thermal gradient technique allow obtaining new polymorphs, not observed with more traditional methods. The secondment was hosted by Université Libre de Bruxelles (ULB)
- to use solution-shearing processing techniques to explore the occurrence of non-equilibrium polymorphs and also fabricate OFETs to evaluate the charge transport properties of the molecular semiconductors. The secondment was hosted by Instituto de Ciencia de Materiales de Barcelona (ICMAB-CSIC).

In addition to acquire scientific knowledge and technical skills in solid-state characterizations and device fabrication, the Ph.D. project was also aimed to develop transferable skills like networking, collaboration, and project management.

6. References

1 M. H. Klaproth, *Bergmannische J*, 1798, 294–299.
2 Wöhler and Liebig, *Ann. Phar.*, 1832, **3**, 249–282.
3 A. R. UBBELOHDE and J. M. ROBERTSON, *Nature*, 1937, **140**, 239.
4 W. McCrone, *Polymorphism, Interscience, New York*, 1965, **Chapter 8, 2**, 725–767.
5 S. Rosenstein and P. P. Lamy, *Am. J. Hosp. Pharm.*, 1969, **26**, 598–601.
6 A. Burger, *in Top. Pharm. Sci., Proc. Int. Congr. Pharm. Sci. F.I.P. 43rd, Elsevier*, 1983, 347.
7 J. Bernstein, *Polymorphism in Molecular Crystals*, OUP Oxford, 2002.
8 B. D. Sharma, *J. Chem. Educ.*, 1987, **64**, 404–407.
9 A. Gavezzotti, *J. Pharm. Sci.*, 2007, **96**, 2232–2241.
10 P. Espeau, R. Céolin, J. Tamarit, M. Perrin, J. Gauchi and F. Leveiller, *J. Pharm. Sci.*, 2005, **94**, 524–539.
11 J. Bauer, S. Spanton, R. Henry, J. Quick, W. Dziki, W. Porter and J. Morris, *Pharm. Res.*, 2001, **18**, 859–866.
12 R. Purohit and P. Venugopalan, *Resonance*, 2009, **14**, 882–893.
13 S. Lohani and D. J. W. Grant, *Polymorphism: in the Pharmaceutical Industry*, 2006, 21–42.
14 K. B. Raju, S. Ranjan, V. S. Vishnu, M. Bhattacharya, B. Bhattacharya, A. K. Mukhopadhyay and C. M. Reddy, *Cryst. Growth Des.*, 2018, **18**, 3927–3937.
15 J. P. Brog, C. L. Chanez, A. Crochet and K. M. Fromm, *RSC Adv.*, 2013, **3**, 16905–16931.
16 D. Mangin, F. Puel and S. Veesler, *Org. Process Res. Dev.*, 2009, **13**, 1241–1253.
17 R. J. Davey, *Cryst. Growth Des.*, 2002, **2**, 675–676.
18 A. Burger and R. Ramberger, *Microchimica Acta*, 1979, **72**, 273–316.
19 N. Zencirci, T. Gelbrich, D. C. Apperley, R. K. Harris, V. Kahlenberg and U. J. Griesser, *Cryst. Growth Des.*, 2010, **10**, 302–313.
20 A. O. F. Jones, B. Chattopadhyay, Y. H. Geerts and R. Resel, *Adv. Funct. Mater.*, 2016, **26**, 2233–2255.
21 T. Salzillo and A. Brillante, *Adv. Mater. Interfaces*, 2022, **9**, 2200815.
22 G. Schweicher, Y. Olivier, V. Lemaur and Y. H. Geerts, *Isr. J. Chem.*, 2014, **54**, 595–620.
23 S. Riera-Galindo, A. Tamayo and M. Mas-Torrent, *ACS Omega*, 2018, **3**, 2329–2339.
24 C. C. Mattheus, A. B. Dros, J. Baas, G. T. Oostergetel, A. Meetsma, J. L. de Boer and T. T. M. Palstra, *Synth. Met.*, 2003, **138**, 475–481.
25 N. Koch, A. Gerlach, S. Duhm, H. Glowatzki, G. Heimel, A. Vollmer, Y. Sakamoto, T. Suzuki, J. Zegenhagen, J. P. Rabe and F. Schreiber, *J. Am. Chem. Soc.*, 2008, **130**, 7300–7304.
26 C. D. Dimitrakopoulos, A. R. Brown and A. Pomp, *J. Appl. Phys.*, 1996, **80**, 2501.
27 J. D. Dunitz, *Pure Appl. Chem.*, 1991, **63**, 177–185.
28 G. R. Desiraju, *J. Chem. Sci., 2010 122:5*, 2010, **122**, 667–675.
29 R. Taylor, *CrystEngComm.*, 2014, **16**, 6852–6865.
30 D. Braga, F. Grepioni, L. Maini and S. d'Agostino, *Eur. J. Inorg. Chem.*, 2018, **2018**, 3597–3605.

31 A. Nangia and G. R. Desiraju, in *Design of Organic Solids*, eds. E. Weber, Y. Aoyama, M. R. Caira, G. R. Desiraju, J. P. Glusker, A. D. Hamilton, R. E. Meléndez and A. Nangia, Springer Berlin Heidelberg, Berlin, Heidelberg, 1998, pp. 57–95.

32 S. Karthika, T. K. Radhakrishnan and P. Kalaichelvi, *Cryst. Growth Des.*, 2016, **16**, 6663–6681.

33 H. Cölfen, *Crystals,* 2020, **10**(2), 61.

34 R. Lacmann, A. Herden and Ch. Mayer, *Chem. Eng. Technol.*, 1999, **22**, 279–289.

35 N. Rodríguez-hornedo and D. Murphy, *J. Pharm. Sci.*, 1999, **88**, 651–660.

36 F. E. Rosenberger, *Fundamentals of Crystal Growth I*, Springer Berlin Heidelberg, Berlin, Heidelberg, 1979, vol. 5.

37 A. Y. Lee, D. Erdemir and A. S. Myerson, *Annu. Rev. Chem. Biomol. Eng.*, 2011, **2**, 259–280.

38 R. A. Van Santen, *J. Phys. Chem.*, 1984, **88**, 5768–5769.

39 M. R. Caira, in *Design of Organic Solids*, eds. E. Weber, Y. Aoyama, M. R. Caira, G. R. Desiraju, J. P. Glusker, A. D. Hamilton, R. E. Meléndez and A. Nangia, Springer Berlin Heidelberg, Berlin, Heidelberg, 1998, pp. 163–208.

40 Margaret C. Etter, *J. Phys. Chem.*, 1991, **95**, 4602.

41 J. D. Dunitz and J. Bernstein, *Acc. Chem. Res.*, 1995, **28**, 193–200.

42 G. Dhanaraj, K. Byrappa, V. (Vish,) Prasad and M. Dudley, *Springer Handbook of Crystal Growth*, 2010, 3–16.

43 G. R. Desiraju, J. J. Vittal and A. Ramanan, *Crystal Engineering*, Co-Published with Indian Institute of Science (IISc), Bangalore, India, 2011.

44 H. Chung and Y. Diao, *J. Mater. Chem. C*, 2016, **4**, 3915–3933.

45 M. Mas-Torrent and C. Rovira, *Chem. Rev.*, 2011, **111**, 4833–4856.

46 C. Ruzié, J. Karpinska, A. Laurent, L. Sanguinet, S. Hunter, T. D. Anthopoulos, V. Lemaur, J. Cornil, A. R. Kennedy, O. Fenwick, P. Samorì, G. Schweicher, B. Chattopadhyay and Y. H. Geerts, *J. Mater. Chem. C*, 2016, **4**, 4863–4879.

47 R. Ruiz, D. Choudhary, B. Nickel, T. Toccoli, K. C. Chang, A. C. Mayer, P. Clancy, J. M. Blakely, R. L. Headrick, S. Iannotta and G. G. Malliaras, *Chem. Mater.*, 2004, **16**, 4497–4508.

48 C. M. Duffy, J. W. Andreasen, D. W. Breiby, M. M. Nielsen, M. Ando, T. Minakata and H. Sirringhaus, *Chem. Mater.*, 2008, **20**, 7252–7259.

49 J. A. Lim, H. S. Lee, W. H. Lee and K. Cho, *Adv. Funct. Mater.*, 2009, **19**, 1515–1525.

50 J. E. Anthony, *Chem Rev*, 2006, **106**, 5028–5048.

51 Y. Chen, B. Lee, H. T. Yi, S. S. Lee, M. M. Payne, S. Pola, C. H. Kuo, Y. L. Loo, J. E. Anthony, Y. T. Tao and V. Podzorov, *Phys. Chem. Chem. Phys.*, 2012, **14**, 14142–14151.

52 D. Braga and G. Horowitz, *Adv. Mater.,* 2009, **21**, 1473–1486.

53 I. N. Hulea, S. Fratini, H. Xie, C. L. Mulder, N. N. Iossad, G. Rastelli, S. Ciuchi and A. F. Morpurgo, *Nat. Mater.*, 2006, **5**, 982–986.

54 V. Podzorov, E. Menard, A. Borissov, V. Kiryukhin, J. A. Rogers and M. E. Gershenson, *Phys. Rev. Lett.*, 2004, **93**, 86602.

55 D. T. James, J. M. Frost, J. Wade, J. Nelson and J.-S. Kim, *ACS Nano*, 2013, **7**, 7983–7991.

56 J. E. Anthony, *Angew. Chem., Int. Ed. Engl.*, 2008, **47**, 452–483.

57 G. Giri, E. Verploegen, S. C. B. Mannsfeld, S. Atahan-Evrenk, D. H. Kim, S. Y. Lee, H. A. Becerril, A. Aspuru-Guzik, M. F. Toney and Z. Bao, *Nature*, 2011, **480**, 504–508.
58 K. Takimiya, S. Shinamura, I. Osaka and E. Miyazaki, *Adv. Mater.*, 2011, **23**, 4347–4370.
59 K. Takimiya, I. Osaka, T. Mori and M. Nakano, *Acc. Chem. Res.*, 2014, **47**, 1493–1502.
60 S. Colella, C. Ruzié, G. Schweicher, J. B. Arlin, J. Karpinska, Y. Geerts and P. Samorì, *Chempluschem.*, 2014, **79**, 371–374.
61 A. Tamayo, S. Hofer, T. Salzillo, C. Ruzié, G. Schweicher, R. Resel and M. Mas-Torrent, *J. Mater. Chem. C*, 2021, **9**, 7186–7193.
62 G. H. Roche, Y. T. Tsai, S. Clevers, D. Thuau, F. Castet, Y. H. Geerts, J. J. E. Moreau, G. Wantz and O. J. Dautel, *J. Mater. Chem. C*, 2016, **4**, 6742–6749.
63 G. Schweicher, V. Lemaur, C. Niebel, C. Ruzié, Y. Diao, O. Goto, W. Y. Lee, Y. Kim, J. B. Arlin, J. Karpinska, A. R. Kennedy, S. R. Parkin, Y. Olivier, S. C. B. Mannsfeld, J. Cornil, Y. H. Geerts and Z. Bao, *Adv. Mater.*, 2015, **27**, 3066–3072.
64 Y. Tsutsui, G. Schweicher, B. Chattopadhyay, T. Sakurai, J. B. Arlin, C. Ruzié, A. Aliev, A. Ciesielski, S. Colella, A. R. Kennedy, V. Lemaur, Y. Olivier, R. Hadji, L. Sanguinet, F. Castet, S. Osella, D. Dudenko, D. Beljonne, J. Cornil, P. Samorì, S. Seki and Y. H. Geerts, *Adv. Mater.*, 2016, **28**, 7106–7114.
65 R. Jouclas, J. Liu, M. Volpi, L. Silva de Moraes, G. Garbay, N. McIntosh, M. Bardini, V. Lemaur, A. Vercouter, C. Gatsios, F. Modesti, N. Turetta, D. Beljonne, J. Cornil, A. R. Kennedy, N. Koch, P. Erk, P. Samorì, G. Schweicher and Y. H. Geerts, *Adv. Sci.*, 2022, **9**, 2105674.
66 W. Xie, K. Willa, Y. Wu, R. Häusermann, K. Takimiya, B. Batlogg and C. D. Frisbie, *Adv. Mater.*, 2013, **25**, 3478–3484.
67 U. Zschieschang, F. Ante, D. Kälblein, T. Yamamoto, K. Takimiya, H. Kuwabara, M. Ikeda, T. Sekitani, T. Someya, J. B. Nimoth and H. Klauk, *Org. Electron*, 2011, **12**, 1370–1375.
68 R. Acharya, D. Günder, T. Breuer, G. Schmitz, H. Klauk and G. Witte, *J. Mater. Chem. C*, 2021, **9**, 270–280.
69 D. Loveland, B. Kailkhura, P. Karande, A. M. Hiszpanski and T. Y. J. Han, *J. Chem. Inf. Model*, 2020, **60**, 6147–6154.
70 C. C. Mattheus, G. A. de Wijs, R. A. de Groot and T. T. M. Palstra, *J. Am. Chem. Soc.*, 2003, **125**, 6323–6330.
71 V. C. Sundar, J. Zaumseil, V. Podzorov, E. Menard, R. L. Willett, T. Someya, M. E. Gershenson and J. A. Rogers, *Science (1979)*, 2004, **303**, 1644–1646.
72 F. Cozzi, S. Bacchi, G. Filippini, T. Pilati and A. Gavezzotti, *Chem. Eur. J.*, 2007, **13**, 7177–7184.
73 C. Wang, H. Dong, H. Li, H. Zhao, Q. Meng and W. Hu, *Cryst. Growth Des.*, 2010, **10**, 4155–4160.
74 H. C. Montgomery, J. H. Schön, C. Kloc and B. Batlogg, *J. Am. Chem. Soc*, 2001, **123**, 9482–9483.
75 G. R. Desiraju and A. Gavezzotti, *Acta. Crystallogr. B.*, 1989, **45**, 473–482.
76 S. Milita, F. Liscio, L. Cowen, M. Cavallini, B. A. Drain, T. Degousée, S. Luong, O. Fenwick, A. Guagliardi, B. C. Schroeder and N. Masciocchi, *J. Mater. Chem. C*, 2020, **8**, 3097–3112.

77 H. Ebata, T. Izawa, E. Miyazaki, K. Takimiya, M. Ikeda, H. Kuwabara and T. Yui, *J. Am. Chem. Soc.*, 2007, **129**, 15732–15733.
78 X. Liu, X. Su, C. Livache, L.-M. Chamoreau, S. Sanaur, L. Sosa-Vargas, J.-C. Ribierre, D. Kreher, E. Lhuillier, E. Lacaze and F. Mathevet, *Org. Electron*, 2020, **78**, 105605.
79 H. Minemawari, M. Tanaka, S. Tsuzuki, S. Inoue, T. Yamada, R. Kumai, Y. Shimoi and T. Hasegawa, *Chem. Mater.*, 2017, **29**, 1245–1254.
80 H. Chung, S. Chen, N. Sengar, D. W. Davies, G. Garbay, Y. H. Geerts, P. Clancy and Y. Diao, *Chem. Mater.,* 2019, **31**, 9115–9126.
81 H. Chung, D. Dudenko, F. Zhang, G. D'Avino, C. Ruzié, A. Richard, G. Schweicher, J. Cornil, D. Beljonne, Y. Geerts and Y. Diao, *Nat. Commun.*, 2018, **9**, 278.
82 P. Pandey, N. Demitri, L. Gigli, A. M. James, F. Devaux, Y. H. Geerts, E. Modena and L. Maini, *Cryst. Growth Des.*, 2022, **22**, 1680–1690.
83 Guangbin Dong, *C-C Bond Activation*, 1st edn., 2014.
84 C. Liu, K. Huang, W.-T. Park, M. Li, T. Yang, X. Liu, L. Liang, T. Minari and Y.-Y. Noh, *Mater. Horiz.*, 2017, **4**, 608–618.
85 V. Coropceanu, J. Cornil, D. A. da Silva Filho, Y. Olivier, R. Silbey and J.-L. Brédas, *Chem. Rev.*, 2007, **107**, 926–952.
86 P. M. Martin, *Introduction to Surface Engineering and Functionally Engineered Materials*, Wiley, 1st edn., 2011.
87 W. Andrew, *Handbook of Thin Film Deposition*, Elsevier, 3rd edn., 2012.
88 P. J. Kelly and R. D. Arnell, *Vacuum*, 2000, **56**, 159–172.
89 P. J. Kelly, R. D. Arnell and W. Ahmed, *Surf. Eng.*, 1993, **9**, 287–292.
90 O. O. Abegunde, E. T. Akinlabi, O. P. Oladijo, S. Akinlabi, A. U. Ude, O. O. Abegunde, E. T. Akinlabi, O. P. Oladijo, S. Akinlabi and A. U. Ude, *AIMS Mater. Sci., 2019 2:174*, 2019, **6**, 174–199.
91 Y. Diao, L. Shaw, Z. Bao and S. C. B. Mannsfeld, *Energy Environ. Sci.*, 2014, **7**, 2145–2159.
92 L. Fijahi, T. Salzillo, A. N. Tamayo, M. Bardini, C. Ruzié, C. Quarti, D. Beljonne, B. Simone D'agostino, Y. H. Geerts and M. Mas-Torrent, *J. Mater. Chem. C*, 2022, **10**, 7319–7328.
93 A. Campos, S. Riera-Galindo, J. Puigdollers and M. Mas-Torrent, *ACS Appl. Mater. Interfaces*, 2018, **10**, 15952–15961.
94 A. J. Lovinger and C. C. Gryte, *Macromolecules*, 1976, **9**, 247–253.
95 A. J. Lovinger, C. M. Lau and C. C. Gryte, *Polymer (Guildf)*, 1976, **17**, 581–586.
96 A. J. Lovinger, *J. Appl. Phys.*, 1978, **49**, 5003–5013.
97 G. Schweicher, G. Liu, P. Fastré, R. Resel, M. Abbas, G. Wantz and Y. H. Geerts, *Mater. Chem. Front*, 2021, **5**, 249–258.
98 P. Panini, B. Chattopadhyay, O. Werzer and Y. Geerts, *Cryst. Growth Des.*, 2018, **18**, 2681–2689.
99 N. Rodríguez-hornedo and D. Murphy, *J. Pharm. Sci.*, 1999, **88**, 651–660.
100 G. H. Nancollas and N. Purdie, *Chem. Soc. Rev.*, 1964, **18**, 1–20.
101 J. Bernstein, *Cryst. Growth Des.*, 2011, **11**, 632–650.
102 Z. Bao and J. Locklin, *Organic Field-Effect Transistors*, CRC Press, UK, 1st edn., 2007.
103 D. Braga and G. Horowitz, *Adv. Mater.,* 2009, **21**, 1473–1486.

Chapter 2

Discovering Crystal Forms of the Novel Molecular Semiconductor OEG-BTBT

Overview

In the first project of my Ph.D., I worked on a novel organic semiconductor OEG-BTBT, which was synthesised by Félix Devaux under the supervision of Prof. Yves Geerts from Université Libre de Bruxelles (ULB). While studying this system, I acquired knowledge of the polymorphic investigation and crystallography, in addition to learning characterization techniques like single-crystal X-ray diffraction (SCXRD), variable-temperature X-ray diffraction (VTXRD) and capillary transmission X-ray diffraction. I performed thorough research of OEG-BTBT that led to the finding of three crystal forms. I solved/indexed and analysed the crystal forms (low and high temperature crystal forms and a solvate) reported in this work. Nicola Demitri and Lara Gigli, scientists from Elettra Syncrotron, in collaboration with Ann Maria James, from Graz University of Technology, solved the room temperature crystal phase. To study the behaviour of the phase transition at high temperatures I submitted a proposal (ID proposal 20201790) to the PSI synchrotron for the MS-X04SA beamline and I was able to collect data at the beginning of 2021. I also performed further investigation to understand the kinetics of transformation of the polymorphic phases using the Avrami equation. Interestingly, the thermodynamic crystal form was found to exhibit plastic mechanical deformation when subjected to a three-point bending test.

We published these results in *Crystal Growth & Design-ACS publications*, in February 2022.

The link to the original publication is: **https://pubs.acs.org/doi/10.1021/acs.cgd.1c01203**

Supplementary information is reported in Appendix A.

CRYSTAL GROWTH & DESIGN

pubs.acs.org/crystal

Article

Discovering Crystal Forms of the Novel Molecular Semiconductor OEG-BTBT

Priya Pandey, Nicola Demitri, Lara Gigli, Ann Maria James, Félix Devaux, Yves Henri Geerts, Enrico Modena,* and Lucia Maini*

Cite This: *Cryst. Growth Des.* 2022, 22, 1680−1690

Read Online

ACCESS | Metrics & More | Article Recommendations | Supporting Information

ABSTRACT: This work is focused on a polymorphic and crystallographic study of a novel p-type organic semiconductor 2,7-bis(2-(2-methoxyethoxy)ethoxy)benzo[*b*]-benzo[4,5]thieno[2,3-*d*]thiophene (OEG-BTBT). The well-known BTBT core is functionalized by eight-atom-long oligoethylene glycol side chains. Our results demonstrate the discovery of three crystal forms of the OEG-BTBT molecule, namely, Form I, Form II, and Form III, in different experimental conditions. Crystal structures of Form I and Form III are reported, while only unit cell indexing of Form II could be determined. Form I and Form II are enantiotropically related, and Form II is stable at temperatures higher than 127 °C. The kinetics of transformation to Form II was studied by the Avrami equation. Form III is a solvate crystal form which is rarely observed in the field of organic electronics, and upon release of dichloromethane, it converts to Form I. Furthermore, we studied the mechanical properties of the Form I crystals, which exhibit plastic bending upon applying mechanical stress in the [100] direction. This distinct mechanical behavior is rationalized by the slip layer topology, the intermolecular interactions energies from energy frameworks, and the Hirshfeld surface analysis.

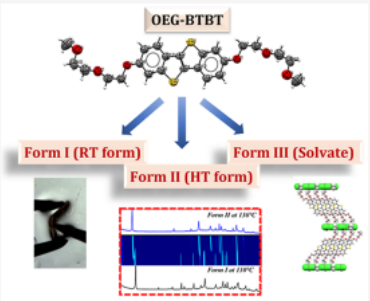

Chapter 3

From the Synthesis to the Device: Elucidating Structural and Electronic Properties of C7-BTBT-C7

Overview

My second project was dedicated to studying another p-type organic semiconductor, C7-BTBT-C7, which was synthesised by Christian Ruzié, under the supervision of Prof. Yves Geerts from Université Libre de Bruxelles (ULB). I selected this molecule to study and understand the odd-even effect, as a similar chain BTBT derivative - C8-BTBT-C8 has been widely studied for its crystal phases and device performance. I commenced with the bulk and thin-film polymorph screening with conventional methods, however, this molecule showed only one solid phase and a liquid crystal phase. To explore the non-conventional technique for directional crystallization using a thermal gradient, I did my secondment at ULB under the supervision of Prof. Yves Geerts and Dr. Guillaume Schweicher, where I examined multiple conditions to tailor the crystallization. In the last part of this project, my secondment was planned at Instituto de Ciencia de Materiales de Barcelona (ICMAB-CSIC), under the supervision of Prof. Marta Mas-Torrent. At ICMAB, with the help of Lamiaa Fijahi, I learnt to fabricate the organic field effect transistors (OFETs) using the solution shearing technique at different conditions. Finally, I recorded a high mobility value with this molecule.

In addition, these findings were also supported by the computational analysis of transfer integrals in collaboration with Nemo McIntosh, Marco Bardini, Dr. Samuele Giannini, Prof. Jérôme Cornil and Prof. David Beljonne at the University of Mons; Dr. Nicholas Turetta and Prof. Paolo Samorì from the University of Strasbourg for the measurement of the ionization energy of C7-BTBT-C7.

We published these results in *Journal of Materials Chemistry C - RSC Publishing*, in April 2023.

The link to the publication is: **https://doi.org/10.1039/D3TC00434A**

Supplementary information is reported in Appendix B.

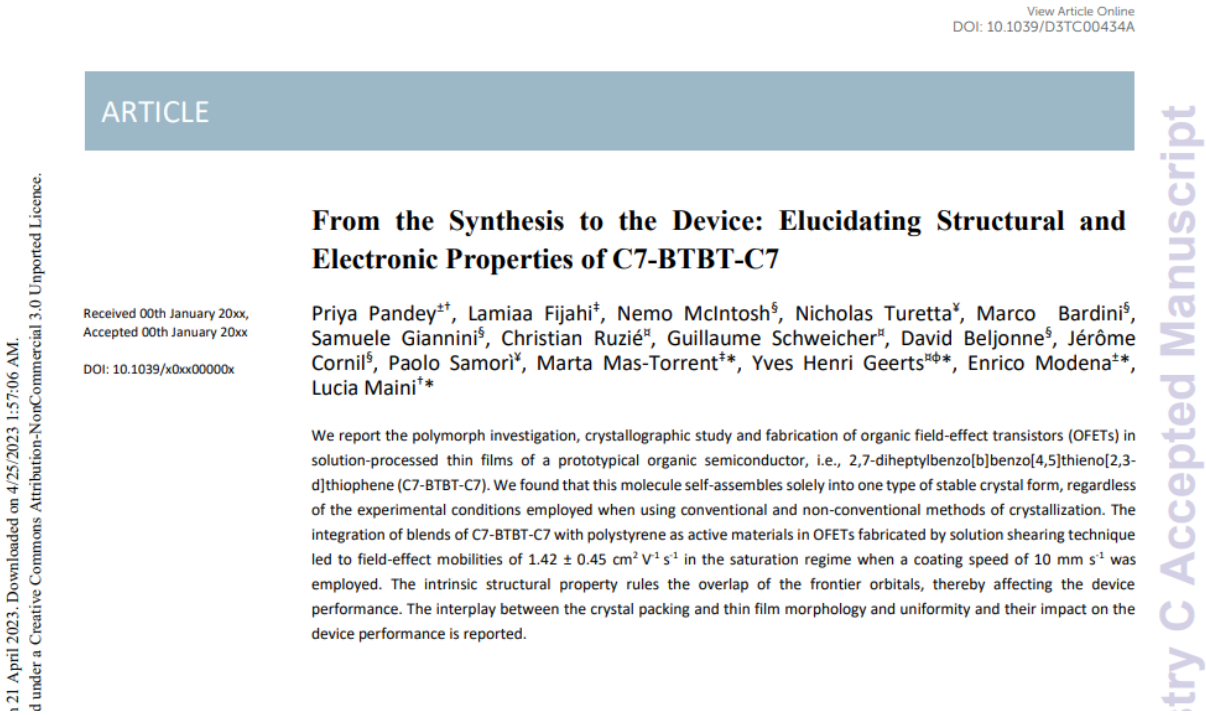

View Article Online
DOI: 10.1039/D3TC00434A

ARTICLE

From the Synthesis to the Device: Elucidating Structural and Electronic Properties of C7-BTBT-C7

Received 00th January 20xx,
Accepted 00th January 20xx

DOI: 10.1039/x0xx00000x

Priya Pandey[±†], Lamiaa Fijahi[‡], Nemo McIntosh[§], Nicholas Turetta[¥], Marco Bardini[§], Samuele Giannini[§], Christian Ruzié[¤], Guillaume Schweicher[¤], David Beljonne[§], Jérôme Cornil[§], Paolo Samorì[¥], Marta Mas-Torrent[‡*], Yves Henri Geerts[¤Φ*], Enrico Modena[±*], Lucia Maini[†*]

We report the polymorph investigation, crystallographic study and fabrication of organic field-effect transistors (OFETs) in solution-processed thin films of a prototypical organic semiconductor, i.e., 2,7-diheptylbenzo[b]benzo[4,5]thieno[2,3-d]thiophene (C7-BTBT-C7). We found that this molecule self-assembles solely into one type of stable crystal form, regardless of the experimental conditions employed when using conventional and non-conventional methods of crystallization. The integration of blends of C7-BTBT-C7 with polystyrene as active materials in OFETs fabricated by solution shearing technique led to field-effect mobilities of 1.42 ± 0.45 $cm^2 V^{-1} s^{-1}$ in the saturation regime when a coating speed of 10 mm s^{-1} was employed. The intrinsic structural property rules the overlap of the frontier orbitals, thereby affecting the device performance. The interplay between the crystal packing and thin film morphology and uniformity and their impact on the device performance is reported.

Chapter 4

Polymorphic landscape and device fabrication of ditbuC6-BTBT

Overview

The third project involved another novel p-type organic semiconductor molecule with a BTBT core and long alkyl chain capped with bulky tBu group- ditBuC6-BTBT, which was synthesised by Christian Ruzié and purified by Massimiliano Remigio This project was started simultaneously with the previous project of C7-BTBT-C7, and hence I performed the same experiments of bulk and thin films polymorph screening. However, this system presented another set of interesting results. From a polymorphic point of view, after a wide range of experiments, I found that this system exists in four crystalline forms under different conditions. During the experiments, an intriguing discovery of 'disappearing polymorphs' was witnessed and confirmed, as it was found that two of the polymorphs become unstable over time due to unintentional seeding of stable crystal form. Moreover, I also carried out a thorough crystallographic study, which presents thought-provoking results of uncommon packing arrangements and asymmetric units. I collaborated with Nemo McIntosh and Prof. Jérôme Cornil for computing the transfer integrals. Furthermore, I performed similar investigations, as for C7-BTBT-C7, directional crystallization at ULB under the supervision of Prof. Yves Geerts and Dr. Guillaume Schweicher, and OFET fabrication with the help of Lamiaa Fijahi and under the supervision of Prof. Marta Mas-Torrent, at ICMAB-CSIC. Fabrication of the working device of ditBuC6-BTBT was quite challenging and despite tuning

multiple parameters, it was not possible to obtain a good performance of the device due to its deep ionization potential (measured by Dr. Nicholas Turetta) and the issue with isolating one polymorph in the device. OFET fabrication using the thermal evaporation method was also performed by Federico Modesti under the supervision of Dr. Peter Erk from BASF. With the combination of all the analysis, we could conclude that this molecule has quite unique features from a crystallographic point of view and can be studied in detail in the future to improve the performance of the device.

Lastly, I managed all the collaborations, analysed the respective results to prepare a manuscript draft.

A research article with these results is going to be submitted to *Crystal Growth & Design - ACS Publications.*

Supplementary information is reported in Appendix C.

Polymorphic landscape and device fabrication of ditbuC6-BTBT

Priya Pandey[±†], Federico Modesti[Ψ], Lamiaa Fijahi[‡], Nemo McIntosh[§], Nicholas Turetta[¥], Christian Ruzié[¤], Massimiliano Remigio[¤], Guillaume Schweicher[¤], Peter Erk[Ψ], Jérôme Cornil[§], Paolo Samori[¥], Marta Mas-Torrent[‡]*, Yves Henri Geerts[¤ϕ]*, Enrico Modena[±]*, Lucia Maini[†]*

± PolyCrystalLine SPA, Via Della Cooperazione, 29 40059 Medicina, Bologna, Italy

†Dipartimento di Chimica "G. Ciamician", via Selmi 2 – Università di Bologna, I-40126, Bologna, Italy

ΨBASF SE, RCS – J542S, 67056 Ludwigshafen am Rhein, Germany

‡ Institut de Ciència de Materials de Barcelona (ICMAB-CSIC), Campus de la UAB, 08193, Bellaterra, Spain

§ Laboratory for Chemistry of Novel Materials, University of Mons, 7000 Mons, Belgium

¥University of Strasbourg, CNRS, ISIS UMR 7006, 8 Alleé Gaspard Monge, Strasbourg, F-67000 France

¤ Laboratoire de Chimie des Polymères, Faculté des Sciences, Université Libre de Bruxelles (ULB), CP 206/1 Boulevard du Triomphe, 1050 Bruxelles, Belgium

ϕ International Solvay Institutes, Université Libre de Bruxelles (ULB), CP 231 Boulevard du Triomphe, 1050, Bruxelles, Belgium

Abstract

We report the polymorphic investigation, crystallographic parameters, and charge transport properties by the fabrication of organic field-effect transistors (OFETs) of a novel molecular semiconductor, i.e. 2,7-bis(7,7-dimethyloctyl)benzo[b]benzo[4,5]thieno[2,3-d]thiophene (ditBuC6-BTBT). Four polymorphs of ditBuC6-BTBT we discovered, out of which three are room-temperature polymorphs (Form I, Ia, and II) while one is a high-temperature polymorph (Form III). We critically discuss the perplexing differences and similarities between Form I and Ia. Later on, we witnessed the disappearance of the metastable forms (Form I and Form Ia) as a consequence of the unintentional seeding of the thermodynamic stable form (Form II). Non-equilibrium crystallization techniques using thermal gradient and bar-assisted meniscus shearing methods were explored to gain improved control over polymorph selection. The intrinsic structural property ruled by the overlap of the frontier orbitals was studied by transfer integrals. Optimized devices fabricated out of solution shearing and vacuum evaporation deposited thin films led to maximum reproducible linear mobility around 0.048 $cm^2V^{-1}s^{-1}$. Results indicate that the final device performances were governed by the crystal structure features and ionization potential values.

Introduction

Polymorphism is the ability of a compound to exhibit more than one molecular packing.[1–3] Difference in molecular packing often leads to variation in the physical properties.[4–6] Multiple factors can guide the formation of polymorphs. The nucleation and growth are the two critical processes underlying the formation of polymorphs and they both depend on thermodynamic and kinetic aspects. A consequence of nucleation could be the occurrence of kinetic polymorphs that have a lifetime spanning from a few seconds to several years.[7] Another crucial point is the occurrence of concomitant polymorphs which may lead to difficulties in isolating polymorphs. There are several ways to tackle these issues and control the polymorph formation: (i) solvent-induced polymorph selectivity; the solvent may have a profound impact on the structure of nuclei through solvent–molecule interactions that govern the formation of a particular structure.[8] (ii) Temperature control; thermotropic polymorphs can be identified by investigating a wide range of temperatures[9] (iii) deposition control (for thin films); non-conventional crystallization techniques (like directional crystallization and solution shearing on substrates) can be explored for polymorph investigation, as a wide range of parameters can be optimized to drive the crystallization process towards one specific polymorph[9] (iv) post-deposition control; thermal- and solvent-vapour annealing can be used for increasing crystallinity and sometimes to alter the molecular packing in the OSC films.[10–12]

In organic electronics, the polymorphism of organic semiconductors (OSCs) may have severe consequences on the charge carrier mobility which brings us an opportunity to understand the importance of the packing on charge transport, in fact, the electronic properties can be directly related to the structural differences.[10,13,14] Within this context, studying substrate-induced and thin-film polymorphism is essential as interfacial phases can exhibit a molecular packing different from bulk phases.[9] This is even more important considering the fact that the zone actively involved in charge transport is the first few monolayers in contact with the dielectric. Aiming to control polymorphism in thin films, we explored different deposition techniques like directional crystallization using thermal gradient and solution shearing methods on glass and silicon substrates, respectively. Indeed, these non-conventional methods of polymorph screening have the potential to reproducibly generate non-equilibrium polymorphs by efficient control of process parameters.[15]

Some ideal candidates for solution-processed films of π-conjugated molecules for electronics are functionalized [1]Benzothieno[3,2-b][1]benzothiophene (BTBT) derivatives. This class of molecules is characterized by high solution-processability and chemical stability.[16,17] Numerous research groups have reported the study of BTBT derivatives with flexible alkyl side chains[14,18–21] or bulky groups.[22–25] In our study, we aim to investigate the structural changes occurring when we combine flexible alkyl chains and rigid bulky groups within the same molecule. We thus selected a BTBT derivative containing C6 alkyl chains ending with a bulky *tert*-butyl group- 2,7-bis(7,7-dimethyloctyl)benzo[b]benzo[4,5]thieno[2,3-d]thiophene (ditBuC6-BTBT) (Figure 1).

Herein, we report a wide bulk and thin-film polymorph screening and the study of thermodynamic stability and structural properties of the observed polymorphs. Conventional methods of recrystallizations led to the finding of three polymorphs at room temperature named Form I, Ia, and II, while another polymorph (Form III) is observed only at high temperatures. Both Form I and Form Ia can be described as 'disappearing polymorphs' because they become dramatically unstable in the presence of a thermodynamically stable polymorph in the surrounding. To attain more control over crystallization conditions and to investigate more polymorphs, we explored non-equilibrium processing techniques leading to the production of thin films using, namely the thermal gradient and solution shearing methods. We further calculated transfer integrals and evaluated the ionization energies of polymorphs Ia and II which show quite different crystal packing. Transfer integrals illustrates how a hole (HOMO-HOMO) or an electron (LUMO-LUMO) is delocalized between two molecules. Ionization energies (IE) represent the energy necessary to pull an electron out of your system and hence give insight into delocalization and polarization effects within the crystal packing. Ideally, the best-performing organic semiconductors (OSCs) in OFETs tend to have IEs ranging from 5.1–5.3 eV to guarantee ease of charge injection (to high work function electrodes) allied to stability versus oxidation.[14,26] Therefore, a good organic semiconductor

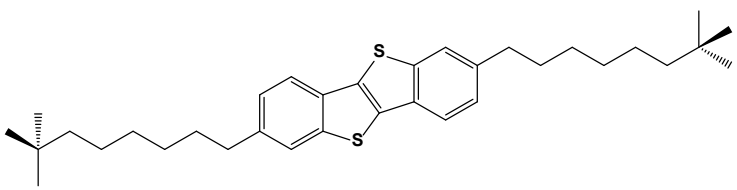

Figure 1 Chemical structure of ditBuC6-BTBT

candidate must present low reorganizational energy combined with large transfer integrals that are of similar amplitude and whose product is positive when considering herring-bone packing.. In our case, we observed extremely deep IE values. Electrical measurements are consistent with this result.

Experimental Section

Nuclear magnetic resonance (NMR).

The ^{1}H NMR spectra were recorded at 298 K on a Jeol 400 MHz (J400) Royal probe spectrometer. Chemical shifts are reported in parts per million (ppm) with TMS as the internal standard. The concentration of the solution in $CDCl_3$ is 9.8 mg mL^{-1}, and the number of scans was 32.

High-performance liquid chromatography (HPLC).

An Agilent HP 1100 system equipped with an HPLC column (Normal Phase, chiral, covalent bunded (Pirkle Covalent (R, R) Whelko-01 10/100 FEC 25cm x 4.6 mm)) and a UV detector were used to assess the purity of the analysed materials. Approximately 1 mg of the sample was dissolved in 1 mL of a mobile phase consisting of Hex-IPA 2:8 isocratic condition (both HPLC grade). The column temperature was set to 25˚C, and the chromatograms were analysed at 254 nm (see Figure S2).

Sublimation.

Severn Thermal oven equipped with TF50/7.5/3Z/F furnace (control unit: CU3Z330425660) was used to perform sublimation at 140˚C under 2.5 x 10^{-7} atm pressure.

Polymorph screening.

Solubility screening was performed for ditBuC6-BTBT using 22 different solvents prior to further study (Table S1). Solubility was examined at room temperature (RT), 50°C, and 75°C (depending on the solubility and the respective boiling point of solvents).

Recrystallization of ditBuC6-BTBT was carried out by solvent evaporation at RT in chloroform (CHF), dichloromethane (DCM), anisole (ANI), 1,2- dimethoxyethane (DMX), isopropyl acetate (IPA), isopropyl ether (IPE), methyl ethyl ketone (MEK), p-xylene (PXY), tetrahydrofuran (THF), toluene (TOL), at 50°C in diethyl carbonate (DEC), *N,N*-dimethylacetamide (DMA), *N,N*-dimethylformamide (DMF) and 1-methyl-2-pyrrolidone (MPY), and at 75°C in 2-propanol (2PR), benzyl alcohol (ABZ) and ethanol (ETH) (Table S1). Recrystallization by antisolvent addition was carried out by adding the antisolvent at RT to a saturated solution: the solvent systems used have been acetonitrile: p-xylene (1:1 v/v), chloroform: 2-propanol (1:1 v/v), chloroform: dimethyl sulfoxide (DMS) (1:1 v/v), tetrahydrofuran: ethanol (1:1 v/v) and toluene: ethanol (1:1 v/v). Prolonged slurry maturation experiments at RT were performed by stirring Form I in 2-methoxyethanol (2MX), acetonitrile (ACN), DMA, DMF, DMS, ETH, and H_2O. Slurry with solvent mixtures was also performed. Controlled recrystallization by temperature gradient has been performed using Crystal16, cooling a clear solution (5 mg mL^{-1}) in DMA, DMF, ETH, and TOL at a constant rate of 0.125°C/min from 70°C to RT. The starting material was also tested with mechanochemistry by dry grinding (Table S2).

Single crystal X-ray diffraction (SCXRD).

Crystals of Form Ia and Form II of ditBuC6-BTBT for Single crystal X-ray diffraction were obtained from CHF and DMA solutions obtained by gradient temperature (1 mg mL^{-1}), respectively.

All the crystal structures were collected with a Rigaku-Oxford Diffraction Xcalibur S diffractometer equipped with a Mo Kα (λ= 0.71073 Å) X-ray source, a graphite monochromator, and a Cryostream 800 cooler. Both Form Ia and II were collected at 100 K. Both the crystal structures were solved using WingX software-SHELXT codes and refined with SHELXL (version 2018/3). For better visualization, crystal structures were digitalized on CCDC Mercury 2020.3.0.[27,28]

Powder X-ray diffraction (PXRD).

Qualitative PXRD to identify the crystalline form was collected with a Rigaku MiniFlex 600 diffractometer with CuKα radiation from a copper-sealed tube operated at 40 kV voltage and

15 mA current using a Bragg−Brentano geometry. Diffraction patterns were measured over the 2θ range of 2−40° by step scanning with an increment of 0.01° per step.

Thin film X-Ray diffraction.

The XRD of ditBuC6-BTBT films was also collected with a Rigaku MiniFlex 600 diffractometer with Cu Kα radiation at room temperature.

The films prepared by directional crystallization were collected on a Panalytical diffractometer with 2D area detectors-PIXcel3D using parallel beam geometry, in the 2θ range between 2°- 40° with an increment of 0.02° per step.

The XRD ditBuC6-BTBT devices prepared by BAMS shearing technique were collected on a D-5000 model Siemens diffractometer with a secondary monochromator and scintillation detector.

Thin films obtained by evaporation were characterized by X-ray diffraction (Rigaku SmartLab) performed on 40 nm thick films deposited through vacuum deposition onto TDPA/Al_2O_3 substrates held at 25, 40, 70, 100, and 130°C. The diffractometer is equipped with a Cu Kα source. The measurements were carried out at a tube voltage of 40 kV (tube current of 50 mA), with scanning steps of 0.04° at a scanning speed of 1.5°/min.

Thermogravimetric Analysis-Evolved Gas Analysis (TGA-EGA).

TGA-EGA analysis was performed to determine the thermal stability and to obtain information about the purity of the ditBuC6-BTBT powder. The measurement was performed on approximately 6 mg of the sample on Mettler-Toledo TGA coupled with a Thermo Nicolet iS 10IR FT-IR spectrometer operated at a scan rate of 10°C min^{-1}, and the IR spectra were processed using STARe software.

Differential scanning calorimetry (DSC).

The DSC analysis for all the samples was performed on a Mettler-Toledo DSC1 instrument. Approximately 2−4 mg of samples were crimped in hermetic aluminium crucibles (40 µL) and scanned from room temperature to 200°C at a heating rate of 2°C min^{-1}, 5°C min^{-1} and 10°C

min^{-1} under a dry N_2 atmosphere (flow rate 80 mL min^{-1}). The data were treated with STARe software.

The ultra-fast DSC measurement was recorded using a Perkin-Elmer Diamond differential scanning calorimeter. Both samples of Forms I and II were placed in open Al-pans. All measurements were conducted in the 20-220°C temperature range at the scan rate of 300°C min^{-1}.

In-situ Variable temperature X-Ray Diffraction (VTXRD).

VTXRD was performed at the Paul Scherrer Institut (PSI) Synchrotron radiation facility (Switzerland). PXRD in capillary transmission mode at MS-X04SA beamline from 24°C to 148°C for the starting material (Form I) of ditBuC6-BTBT. The beam energy of 12.4 keV (1.0 Å) was used for data collection. The MS powder diffractometer is operated in Debye-Scherrer geometry, equipped with a solid-state silicon microstrip detector called MYTHEN (Microstrip sYstem for TimerEsolved experimeNts). Starting from room temperature, the XRD pattern was collected at various intervals until the complete conversion of Form I to Form III (138°C).[29]

Hot stage microscopy (HSM).

Crystals placed on a glass slide and covered with a cover slip were transferred to a heating chamber (hot stage) on an OLYMPUS BX41 stereomicroscope equipped with a LINKAM LTS350 stage for temperature control and VISICAM analyser. The heating chamber was capped with a sealable lid during heating and cooling cycles, and the rate was kept constant at 10°C min^{-1}. Time-lapse images were taken using a NIKON DS FI3 high-speed camera for all in situ experiments, and the images were analysed using software Nikon NIS Elements and Linksys32 data capture.

Temperature gradient apparatus.

The setup consists of a Linkam GS350 system presenting two distinct heating stages separated by a gap. One heating stage was set at a temperature above the melting point (T_h), and the other stage was at a temperature below the crystallization point (T_c) of ditBuC6-BTBT. The distance (gap) between the two stages, where the thermal gradient was generated, was 2

mm. A 76 mm × 26 mm × 1 mm microscope glass slide (Marienfeld Cat. No. 1000000) was intercalated between the stages and the sample to ensure a constant displacement velocity of the sample. During our thermal gradient experiments for ditBuC6-BTBT, the hot stage was set at a temperature T_h = 170°C, while the cold stage temperature T_c was varied from 70°C to 140°C. The system was covered by a hermetic lid so that the system remains thermally independent of the laboratory environment. This setup was mounted on a polarized optical microscope (POM) to take images before, during, and after the experiment.

Sample preparation: We used 20 × 20 × 0.16 mm^3 D263 Borosilicate cover glasses (Cat. No. 0101040, Marienfeld, Germany). The glass substrates were first washed with toluene and isopropanol and then dried with a nitrogen gun, followed by UV-ozone treatment for 20 min for all substrates. After this, 3-4 mg of ditBuC6-BTBT sample was deposited on the glass substrate, which was sandwiched and melted on the hot stage of the thermal gradient setup.

FKM treatment on the glass substrates was also performed to observe the influence of the substrate on the nucleation mechanism and, thus, on polymorphism. FKM is a fluorinated rubber $[(CH_2—CF_2)_{0.6}— (CF_2—CF(CF_3))_{0.4}]_n$ with molecular weight M_w = 70,000 g mol^{-1}. The FKM solution was prepared in acetone (60 mg mL^{-1}) and kept on overnight, stirring at 1000 RPM. The solution was then filtered using a 5 µm phobic filter. This FKM solution was then spin-coated at various amounts of FKM (µL) on the cleaned substrates at 6000 rpm spin-coating speed with a constant acceleration of 4000 s.

Calibration of the Magnitude of the Temperature Gradient Setup (G_{cal}). Previous work has shown that the effective magnitude of the temperature gradient (G_{exp}) that takes place between the hot and cold zones is less than the magnitude calculated by the equation $G = (T_h – T_c)/x$, where x = 2.0 mm (the gap between the hot and cold stages).[30] For our experiments, the temperature gradient was calculated to be G_{exp} ≈ 50°C mm^{-1} to G_{exp} ≈ 15°C mm^{-1} for the T_h–T_c couple 170-70°C to 170-140°C, respectively. The cooling rate C at the growth front was calculated by the equation $C=(T_h-T_c)V/x$, where V is the pulling velocity.[31]

Ionization energy (IE):

Photoelectron Yield Spectroscopy (PYS) in the air was used to determine IE values from the photoelectron emission yield of OSC samples in the form of powder. Photoelectron yield curves were collected within an energy range of 3.4 to 6.2 eV by using a Riken Keiki spectrophotometer (Japan) model AC-2 with an energy step of 0.05 eV and a UV spot intensity of 100 nW. The final estimate for IE values is known with an experimental error of ± 0.05 eV or less.

Transfer integrals.

Transfer integrals were computed with the ADF package using the B3LYP functional and the DZ basis set. We computed them for each pair in 3X3X3 supercell to assess the dimensionality of transport.

OFETs fabrication and characterization.

OFET fabrication with Bar-Assisted Menicus Shearing (BAMS). Bottom gate/bottom contact devices: Si/SiO_2 substrates presenting SiO_2 thickness 200 nm, C = 17.26 nF cm^{-2} were used. Interdigitated electrodes (made by photolithography) were fabricated consisting of Cr (5 nm) and gold (40 nm), deposited by thermal evaporation at deposition rates of 0.1–0.5 Å s^{-1} and 1–5 Å s^{-1}, respectively (Micro-Writer ML3 from Durham Magneto Optics). The channel lengths for bottom gate/bottom contact devices were 100 and 150 μm and the channel width/length ratio was always set to 100. The substrates were sonicated in acetone and isopropanol for 15 minutes, followed by 25 minutes of UV-Ozone treatment to avoid dewetting. The substrates were then immersed in a 15 mM solution of Penta-fluorobenzenethiol (PFBT) in isopropanol for 15 minutes to modify the work function of Au contacts. PFBT was purchased from Sigma-Aldrich. Finally, the substrates were rinsed with pure isopropanol and dried under a nitrogen flow.

Bottom gate /top contact devices: The silicon substrates were cleaned with acetone and isopropanol as mentioned above. After the solution shearing deposition, the films were mounted on the stage with shadow masks with a channel width W = 4000 μm and channel lengths L = 50–200 μm. The stage was carefully placed in the thermal evaporator and the chamber was kept under vacuum for 3 hours using the Leynold screen operator. After 3 hours,

the Au-deposition was started. The program was set for the Au-thickness of 25 nm. After evaporation, samples were kept in dark for 7 days prior measurement.

Organic semiconductor solution deposition: The pristine ink consisted of 2 wt.% solutions of ditBuC6-BTBT in chlorobenzene which was dissolved by heating overnight at 105°C. Polystyrene (PS) (M_w= 10,000 (10k) g mol^{-1} was purchased from Sigma–Aldrich and used without further purification. A blend solution of ditBuC6-BTBT and PS in chlorobenzene 2 wt.% was prepared at weight ratio ditBuC6-BTBT: PS 4:1. Both, pristine and blend films were deposited by the BAMS technique in ambient conditions at 105°C and a coating speed of 10 and 1-mm s^{-1}.

Electrical measurements: Transistor measurements were carried out with an Agilent B1500A semiconductor device analyser at ambient conditions. For all transfer measurements, the V_{DS} were -5 V (linear) and -40 V (saturation). The devices were characterized by extracting the field-effect mobility in linear and saturation regime and threshold voltage (V_{th}). μ was extracted using the following equation:

$$\mu^{lin} = \frac{\partial \mathrm{I_{DS}}}{\partial \mathrm{V_{GS}}} \frac{\mathrm{L}}{\mathrm{C\,W\,V_{DS}}} \qquad \text{Equation 1}$$

$$\mu^{\mathrm{Sat}} = \left(\frac{\partial \sqrt{\mathrm{I_{DS}}}}{\partial \mathrm{V_{GS}}}\right)^2 . \frac{2\mathrm{L}}{\mathrm{W}} . \frac{1}{\mathrm{C}} \qquad \text{Equation 2}$$

Where I_{DS} is the source-drain current, V_{GS} is the applied source-gate voltage, L is the channel length, W is the channel width, C is the specific capacitance of the dielectric, and V_{DS} the applied source-drain voltage.

OFETs fabricated by evaporation. OFETs were fabricated on the heavily doped silicon wafer, which serves as a gate electrode, covered by 30 nm of Al_2O_3 as provided by the manufacturer (Christian-Albrecht University of Kiel, Institute for Electrical Engineering, and Information Technology). The Al_2O_3 surface was pre-treated with oxygen plasma (Diener Electronic; oxygen flow rate 20 sccm, pressure 0.50 mbar, plasma power 100 W, duration 2 min) and then immersed overnight in a 1.5 mM solution of n-tetradecylphosponic acid (TDPA, Sigma Aldrich) in 2-propanol (Acros Organics). Afterwards, the substrates were rinsed with 2-

propanol, dried with N_2 flux, and put on a hot plate at 100°C for 10 min. This treatment leads to the formation of a self-assembled monolayer (SAM) of TDPA on the Al_2O_3 surface resulting in an additional dielectric thickness of ca. 1.5 nm. The TDPA/Al_2O_3 dielectric has a calculated capacitance of 185 nF cm^{-2}. Gold source and drain contacts were thermally deposited through a shadow mask onto the substrates held in a vacuum at room temperature (UNIVEX 300, Leybold GmbH; the pressure of ~10^{-5} mbar, the deposition rate of 0.7 Å s^{-1}, the nominal thickness of ca. 50 nm). Next, a SAM of pentafluorobenzenethiol (PFBT, Alfa Aesar) was obtained by immersing the substrates in a 10 mM solution of PFBT in 2-propanol for 30 min, then rinsed with 2-propanol and dried with an N_2 flux. The OSCs were deposited through a shadow mask onto the substrates (held at 25, 40, 70, 100, and 130°C) by thermal evaporation in a vacuum (UNIVEX 300, Leybold GmbH; the pressure of ≈ 9 × 10^{-7}/ 3 × 10^{-6} mbar, the deposition rate of 0.3 Å s^{-1}, the nominal thickness of ca. 25 or 40 nm). The nominal thickness of OSC films and gold electrodes were monitored via crystal quartz microbalance and confirmed by ellipsometer (OSC films) and profilometer (gold electrodes). The obtained OFETs present a channel width of 480 μm and a channel length of 215 μm. The electrical measurements were performed in ambient air and room temperature (Agilent 4155C Semiconductor Parameter Analyzer). Mobility values in linear (μ_{lin}) and in saturation regime (μ_{sat}) were calculated using the gradual channel approximation model as expressed in equations 1 and 2

Optical Microscopy.

Optical microscope pictures for OFETs fabricated with BAMS were taken using an Olympus BX51 equipped with a polarizer and analyser.

For OFETs fabricated by evaporation optical microscope images were taken with a Zeiss Axiotron equipped with Zeiss Mikroscope Objektiv Epiplan-Neofluar lenses and with AxioCam MRc.

Results and Discussions

Purity assessment by NMR and HPLC.

Purity of ditBuC6-BTBT was assessed by ^{1}H NMR. The sample was observed to be pure and no extra peaks were observed besides the expected water and $CDCl_3$ peaks (Figure S1). Therefore, the possibility of major contamination by another organic compound was ruled out. Further purity analysis with HPLC was performed to evaluate if any impurities that are lower than 5-6 % in weight are present. HPLC results showed two peaks with retention times 8.54 ± 0.01 min (area: 0.3 ± 0.1%) and 10.16 ± 0.02 min (area 99.6 ± 0.3%) (Figure S2a). We attempted to purify the compound by TLC using multiple solvent systems; however, the low concentration of the impurity and the close retention time between the impurity and the target molecule made it impossible to separate them by TLC. Thus, we performed sublimation of the material to purify it further, and post-sublimation HPLC resulted in only one peak with a retention time of 10.67 ± 0.02 min (Figure S2b). To analyse the phase of the pure compound, PXRD was performed.

Polymorph Screening.

The solubility assessment of ditBuC6-BTBT reveals that it is soluble in most of the organic solvents that were tested (see experimental section), and hence, it was recrystallized in various solvents. The explored methods were evaporation, anti-solvent addition, slurry maturation, recrystallization by temperature gradient, and mechanochemistry (Table S2).

The starting material powder is crystalline and was referred to as Form I. We observed two new polymorphs for ditBuC6-BTBT at room temperature by polymorph screening's recrystallization experiments. Solvents like ANI, CHF, DCM, IPE, PXY, THF, and TOL yielded Form Ia with flat-plate-like morphology. Thin hair-like long needle crystals of Form II resulted from controlled recrystallization in Crystal 16 by the temperature gradient in DEC and DMX solvents. In some solvents like DMA, DMF, IPA, etc., mixture of Form Ia and Form II was obtained as concomitant polymorphs, but after some days (the duration of days varied for each different solvent), the mixture eventually converted to Form II. The stability assessment of both the forms by slurry experiments suggests that Form II is the thermodynamic stable polymorph at room temperature. The pristine Form I is obtained only from the first recrystallization performed during the synthesis of the molecule.

Thermal properties and phase transitions.

Thermal gravimetric analysis results indicate that ditBuC6-BTBT is stable up to approximately 400°C (Figure S3), whereas DSC curves on the starting material (Form I) at 5°C min^{-1} showed only the melting at 145°C. DSC of Form II at 5°C min^{-1} shows an endothermic peak at 97°C, indicating a solid-solid phase transition to a high-temperature polymorph Form III then melting at around 145°C (Figure S4). Noteworthily, the melting temperatures in the two DSC curves were the same, hence, to verify temperature-dependent phase transitions, we also carried out variable-temperature X-ray diffraction at the PSI synchrotron.

The VTXRD measurement of Form I ditBuC6-BTBT disclosed an unexpected event, we observed a phase transition onset from 80°C, which underwent until 138°C and the high-temperature phase is ascribable to Form III (Figure 2).

This conversion observed in VTXRD explains the similar melting temperatures observed in DSCs, as both Form I and Form II undergo the transition to Form III. To detect the transition Form I→ Form III by DSC we ran measurements at different rates (2°C min^{-1}, 5°C min^{-1} and 10°C min^{-1}), but in all, the phase transition was not observed and the melting was ascribable to Form III. One possible explanation for the fact that no transition peak was observed in DSC of Form I, could be that the transition is extended in a very wide range of temperatures, so the peak almost appeared flat. However, later, with the DSC at an ultra-fast rate (300°C min^{-1}), we were able to capture the transition Form I→Form III at 79°C followed by the melting (Figure S5). We also carried out the DSC measurement at 300°C min^{-1} for Form II, the same

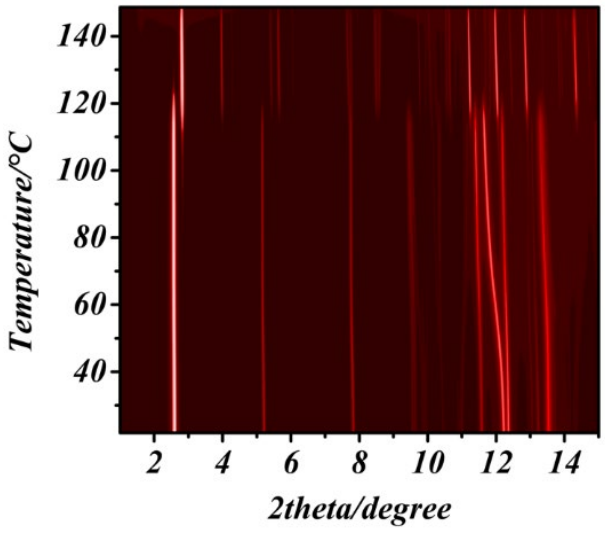

Figure 2 VTXRD (λ= 0.9999613 Å) showing transition of Form I to Form III.

transition of Form II→Form III was observed at 119 °C and melting at around 160°C (Figure S6).

All these thermal behaviours were also supported by hot-stage microscopy analysis on crystals of both polymorphs. The transition in crystals of Form Ia→Form III occurs in a very long temperature range, where the phase transition appears to swipe across the crystal from one end to another, changes albeit small are visible from the POM images (Figures S7 and S8). However, in the phase transition from Form II→Form III, the needle-like crystals of Form II appear like 'tail-wagging' as the crystal merely moves or changes the face orientation from one end of the needle (Figure S9). The temperature of transition for both polymorphs coincides with the results of DSC and VTXRD.

Table 1 Crystallographic parameters of all the polymorphs.

Parameters	**Form I**	**Form Ia**	**Form II**	**Form III**
Formula	$C_{68}H_{96}S_4$			
Molecular weight ($g.mol^{-1}$)	520.84			
Temperature (K)	293	100 (2)	100(2)	293
Crystal system	Monoclinic	Monoclinic	Triclinic	Triclinic
Space group	*C2*	*Cc*	$P\bar{1}$	$P\bar{1}$
a (Å)	14.3169	11.856(2)	5.9026(10)	8.0337
b (Å)	18.1198	11.8384(11)	19.606(2)	14.2968
c (Å)	6.22382	42.899(7)	27.750(3)	20.6208
α (°)	90	90	105.525(10)	103.24853
β (°)	107.90455	90.838(15)	94.938(12)	77.40277
γ (°)	90	90	98.078(11)	87.1292
V ($Å^3$)	1536.4	6020.5(17)	3037.7(7)	2237.4

Z/Z'	2/0.5	8/2	4/2	3/1.5
Density ($g \cdot cm^{-3}$)	-	1.149	1.139	-
F (000)	-	2272	1136	-
μ (mm^{-1})		0.197	0.196	-
GOF on F^2	-	1.059	0.981	-
R_1 (on F, I>2σ(I)/R_{ex}	-	0.1163	0.1115	-
WR_2 (F^2 all data) R_{wp}	-	0.2831	0.1768	-
R_{wp} (Pawley)	2.97	-	-	1.84

Structural characterization by Single-crystal X-ray diffraction.

We selected suitable single crystals of both Form Ia and Form II for SCXRD measurement. All the PXRD pattern comparisons of different polymorphs are presented in Figure S10.

The crystal quality of Form Ia was not ideal, and it was difficult to isolate a suitable single crystal for the SCXRD measurement, and the low diffracting power allowed to perform collection only at a low temperature (100 K). Form Ia was solved in monoclinic space group *Cc* with two full molecules in the asymmetric unit. This polymorph packs with 8 molecules in

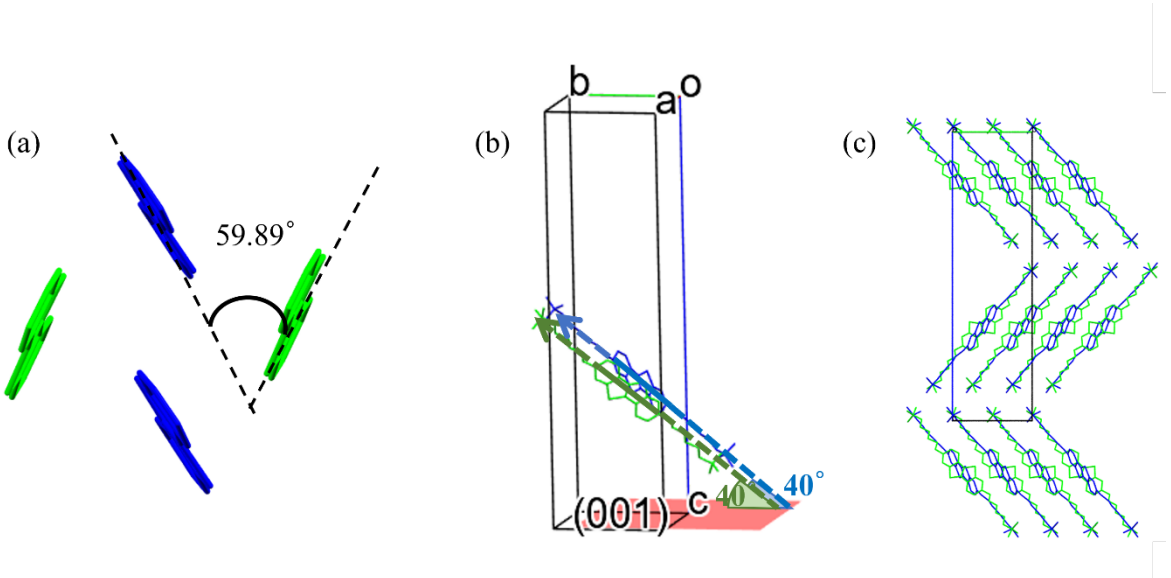

Figure 3 Crystal structure of Form Ia, showing (a) herringbone angle, (b) core-tilt angle and (c) packing. In figure (a) hydrogens and alkyl chains and in (b) and (c) only hydrogens are removed for the sake of clarity. The two independent molecules are highlighted with different colours- blue and green.

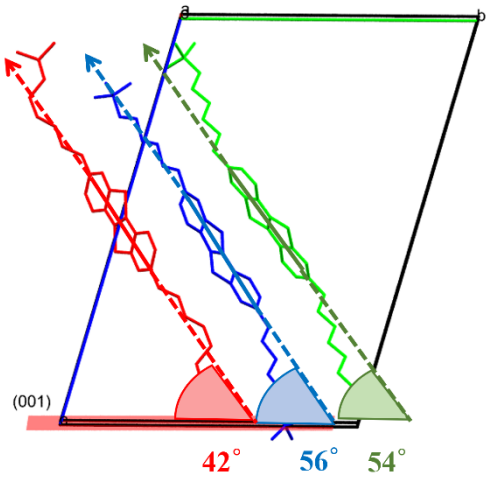

Figure 4 The three independent molecules in the unit cell (depicted by different colours of symmetry equivalence), the asymmetric unit consists of half red molecule, half green molecule, and a full blue molecule. The blue and the green molecules have almost the same tilt angle of 56˚ and 54° while the red molecule has a tilt angle of 42°.

the unit cell, comprising two anti-parallel layers. The anti-parallel layers are separated by 2.03 Å. Inside the layers, the molecules are arranged in a herringbone packing motif with an angle of 59.89° (Figure 3a). The molecules present a tilt angle of 40°. Previously, it has been observed that the core-tilt angle decreases with chain substitutions. For example, bare BTBT has almost an upright core with a tilt angle of 87°[22] and even the symmetrical substitution of BTBT core with the long alkyl chains like C6-diol,[20] C7 (Chapter 3), C8,[32] C12,[33] etc. does not significantly modify the tilt angle, whereas introduction to the bulky groups as side chains-like diiPr (67°), ditBu (50°) or diTMS (41°), significantly decreases the tilt angle.[23] Since, in our case, we have the combination of alkyl-C6 and bulky-tBu chains, the tilt-angle is expected to be decreased.

Form II crystals were less tricky to isolate as compared to Form Ia, however, the crystals were extremely flexible and thin needles, which led to difficulty in crystal mounting for data collection. Some good quality and collectible crystals were found in the recrystallization experiment from DMA solvent and the data collection was performed at low temperatures. Form II was found to crystalize in a triclinic system ($P\bar{1}$), with one full molecule and two half molecules placed on the inversion centre in the asymmetric unit (Z'=2) (see Figure 4). Two of the independent molecules have almost the same tilt angle with respect to the 0 0 1 plane (54˚ and 56°) while the third molecule forms a tilt angle of 42° (Figure 4).

The third molecule (indicated in red colour in Figure 4) is also shifted with respect to the other and it is not possible to describe it as a herringbone. The core of the fully independent molecule which does not lies on the inversion centre is slightly bent which could be related to the influence of the alkyl chain which shows different configurations Unlike Form Ia, Form II layers are interdigitated and not separated (see Figure 5c). This peculiar arrangement could be attributed to the presence of the bulky *t*Bu groups in the terminal positions which induce a smaller tilt angle as shown also in Form Ia, and higher Z'. It is worth noting that Form II is the thermodynamic stable form although it shows a more disordered packing.

Form III is only obtained by phase transition of Form I or Form II at a temperature higher than 138°C so no single-crystal data could be collected. The powder XRD pattern obtained at high temperature from the PSI synchrotron was indexed using TOPAS and was found to have a triclinic crystal structure ($P\ \bar{1}$), and a volume that corresponds to the presence of one and a half molecules in an asymmetric unit. We were able to get the low R_{wp} of 1.84 with Pawley

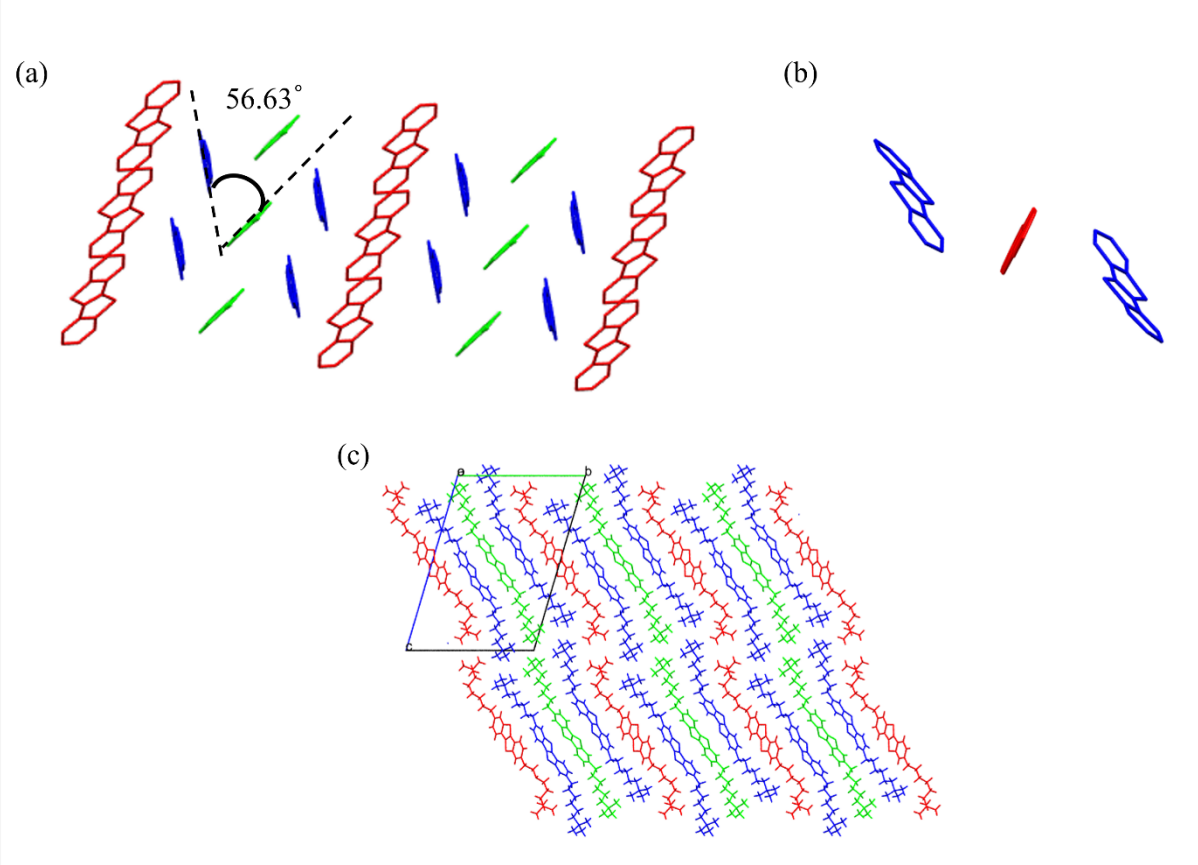

Figure 5 Crystal structure of Form II, showing (a) herringbone angle between blue and green molecules, (b) absence of herringbone with red molecules and (c) interdigitated packing. In figure (a) hydrogens and alkyl chains and in (b) only hydrogens are removed for the sake of clarity. The three independent molecules are highlighted with different colours- red, blue, and green.

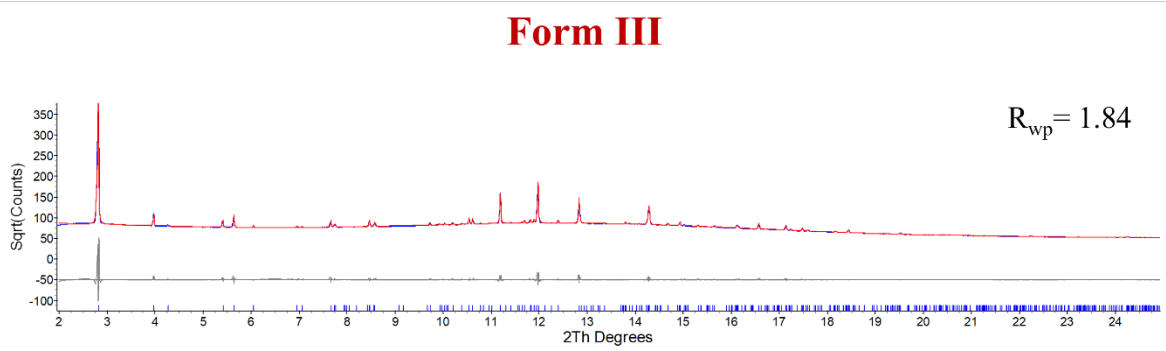

Figure 6 Pawley refinement plot with the corresponding unit cell parameters of Form III, measured at the PSI synchrotron. Experimental XRD powder pattern (blue curve) calculated one (red curve) and difference (grey curve) are presented.

refinement using these unit cell parameters. The strong peak at a low angle (2.80°, λ=0.9999613) suggests the presence of layers as observed in Form Ia. The distance between the layers decreases from 22.27 Å in Form I (at 76.5°) to 20.39 Å (at 2.8°) in Form III. This could be due to the core-tilt angle. Despite numerous attempts, it was not possible to solve the structure of Form III, due to the high number of degrees of freedom and/or the presence of disorder at elevated temperatures.

***Form I** vs **Form Ia**.* We struggled to identify the two different polymorphs Form I and Form Ia because they both possess a strong peak (0 0 1) at the same low angle and the PXRD pattern of both suffers from strong preferential orientation. Due to the preferential orientation of the recrystallized powder and crystals, the main peaks of both were ascribable to Form I. More accurate comparisons were done on the basis of the calculated pattern based on the structure collected at 100 K. When we tried to compare the calculated pattern with the high-quality

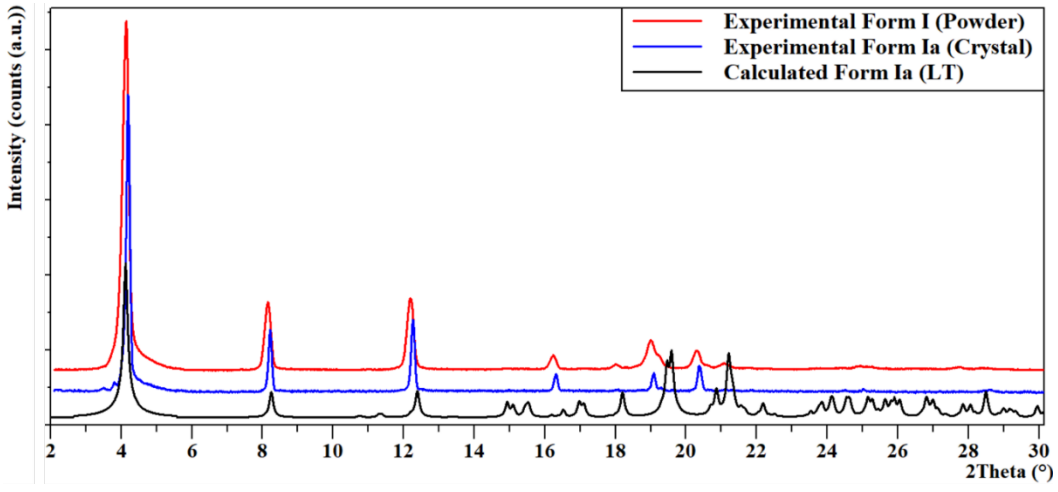

Figure 7 PXRD patterns of experimental Form I (red), Ia (blue) and calculated pattern of Form Ia (black) (λ=1.54 Å) in square root scale.

powder diffraction data at RT obtained from the PSI synchrotron there was a mismatch of peaks around and after 12˚ (Figure S12a), which we first assumed could be a result of the difference in temperature of collection (Figure 7). To confirm our hypothesis. we carried out a VTXRD experiment on the starting material (Form I) starting from RT down to 100 K. From the $VTXRD_{RT \rightarrow LT}$, we did not observe any thermotropic phase change or thermal contraction that could have been the reason for the mismatch of the XRD peaks (Figure S12b), which clearly means that there are two very similar polymorphs- starting material powder (Form I) and the crystals that were recrystallized from solvents (Form Ia) (Figure S12c).

We then indexed Form I from the PXRD pattern using TOPAS, which resulted in a monoclinic crystal system with a *C2* space group (which is similar to Form Ia) with half a molecule in an asymmetric unit. The Pawley refinement led to a low R_{wp} of 2.97 (Figure 8).

Are Form I and Form Ia disappearing polymorphs? Based on polymorph screening performed, it appeared that Form Ia often exhibits flat-sheet-like crystals. Form Ia is a kinetic form that is evident from the slurry maturation and solubility assessments. Yet, during the first recrystallization experiments where we observed only Form Ia, the crystals were found to be stable at RT and kept for several months. However, we witnessed a dramatic decrease in the stability of Form Ia when we performed more crystallization experiments for polymorph screening. The presence of seeds of Form II in the surroundings led to unintentional seeding which trigged the conversion of Form Ia→Form II in a matter of days. Upon conversion, the morphology also changed from sheets to needles. After a year of polymorph screening and the appearance of Form II, Form Ia got so unfavoured that even the recrystallization experiments that used to yield Form Ia (with sheet morphology), now result in Form II

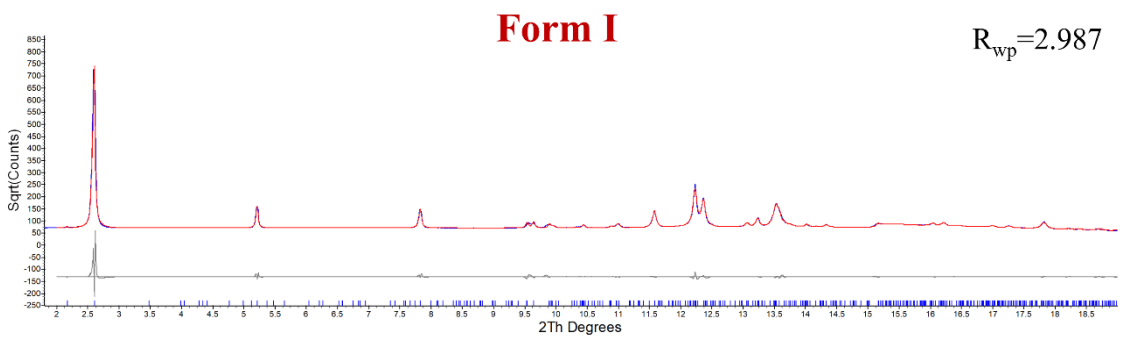

Figure 8 Pawley refinements plot with the corresponding unit cell parameters of Form I, measured at the PSI synchrotron (λ= 0.9999613 Å). Experimental XRD powder pattern (blue curve) calculated one (red curve) and difference (grey curve) are presented.

(needles) and we do not observe Form Ia crystals anymore from evaporation. A similar peculiar behaviour of vanishing polymorphs was witnessed and reported by Dunitz and Bernstein[34], Woodward and McCrone[35], and Webb and Anderson[36], where the metastable polymorph observed for a certain period was completely displaced by the stable polymorph due to the unintentional seeding. In our case, we found that the conversion of kinetic form to thermodynamic form was occurring only during the recrystallization or in the presence of residual solvent while there was no such transformation in the thin films or the vacuum-dried crystals. The thin films PXRD of Form Ia was found to be stable for 8 months (till date). However, in the latest fast recrystallizations at low temperature to obtain Form Ia we always observed concomitant polymorphs with an increasing amount of Form II.

It is worth noting that when it was possible to ascertain the presence of Form I vs Form Ia we always observed Form Ia except for the starting material, hence also Form I can be counted as a disappearing polymorph.

Directional crystallization using temperature gradient.

Bulk polymorph screening with conventional methods often suffers poor process control leading to elusive polymorphs. Therefore, we wanted to explore non-conventional crystallization, where we could control the crystallization parameters and follow both nucleation and growth mechanisms. Nucleation and kinetics play a decisive role in the crystallization process.[37] With the aid of the thermal gradient technique, we can produce films from the melt by tailoring the conditions responsible for nucleation and growth, like the temperature of hot and cold stages, the pulling rate of the substrate, the cooling rate, etc.

As shown in Figure 9, the nucleation of ditBuC6-BTBT occurs at the edge, or the corner of the substrate, and the nucleus grows quickly towards the vertical edge in the undercooled region, as the growth follows the coldest slice available and then propagates in the gradient direction.[38] For samples with higher pulling velocities like 50 µm s^{-1}, both primary and secondary nucleation sites were observed. We explored different conditions by varying the cold stage temperature (T_c=70-140˚C), hot stage temperature (T_h=170-180˚C), the pulling rate of the sample stage (5-50 µm s^{-1}), and the cooling rate at the growth front (Table S3). In all

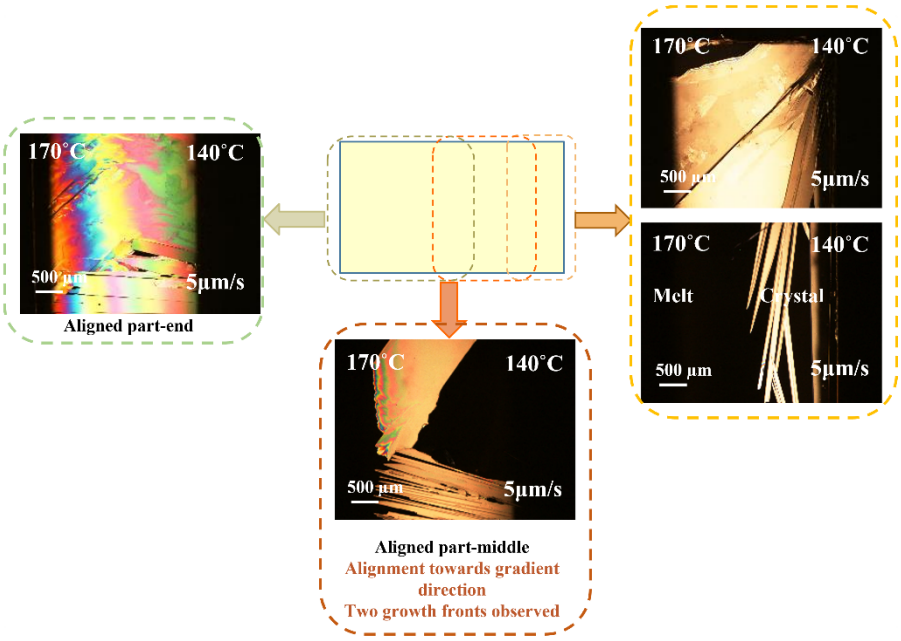

Figure 9 Polarized optical microscopy pictures recorded at room temperature after crystallization using the thermal gradient technique. Locations are indicated on the schematic representation of the sample. Sample conditions: T_h=170˚C, T_c=140˚C, and pulling velocity 5µm s^{-1}.

cases, we observed the needle-like morphology of the crystals, which aligned uniaxially in the direction of the thermal gradient until the formation of mm^2 size domains.

We also investigated the influence of the surface by treating the glass substrate with fluorinated rubber (FKM). The polymer was dissolved in acetone and spin-coated on the glass substrate prior to sample deposition. Aiming to induce different nucleation conditions, the FKM polymer layer was introduced between the ditBuC6-BTBT film and the glass substrate (Figure S13).

The XRD data of all the films indicate that when the crystallization occurred, predominantly Form III was observed. However, due to the instability of Form III at room temperature, it starts to transform to Form Ia immediately as the temperature is removed. This is evident from the small peak of Form Ia which is present in almost all the samples. This transformation and decreasing stability of Form III was monitored for a month, which illustrated that the kinetics of transformation was very slow. In some of the samples, where the low pulling rate was applied, we could also observe a very small peak of Form II (Figure S15).

Actually, we cannot be sure that we observed Form Ia instead of Form I because the strongest peaks of both, are at the same θ value, and the XRD of the films are highly preferentially

oriented. Since we always obtained Form Ia during our recrystallizations, we assumed that Form Ia is also obtained in the films.

Ionization potential

The ionization energy (IE) of the ditBuC6-BTBT powder and single-crystal samples has been determined via photoemission yield spectroscopy (PYS) in ambient air (Table S4). The IE values of isolated crystals of Form Ia (5.81 eV) and Form II (5.51 eV) significatively differ by 0.3 eV, thus highlighting the strong effect of structural order on the electronic properties of organic semiconductors.[39] The IEs of this bulky-end capped BTBT are larger than those typically observed for linear Cn-BTBT-Cn derivatives, typically around 5.3 eV for $5 < n < 14$[40] but in the same range as these achieved on previously reported bulky end-capped BTBT (around 5.7 eV)[23] Deeper IEs values like the ones observed for the polymorphs of ditBuC6-BTBT suggest that injections of charges will be more difficult in an OFET device.[23]

Transfer integral

The transfer integrals between the highest occupied molecular orbitals (HOMOs) of the individual units or dimers were calculated at the density functional theory (DFT) level (see the Experimental Section). Figure 10 illustrates the transfer integrals of Form Ia and Form II. The Form Ia crystal is made of two shifted herringbone planes that can barely exchange any charge but the charge transport within these herringbone planes should be rather good, though, as

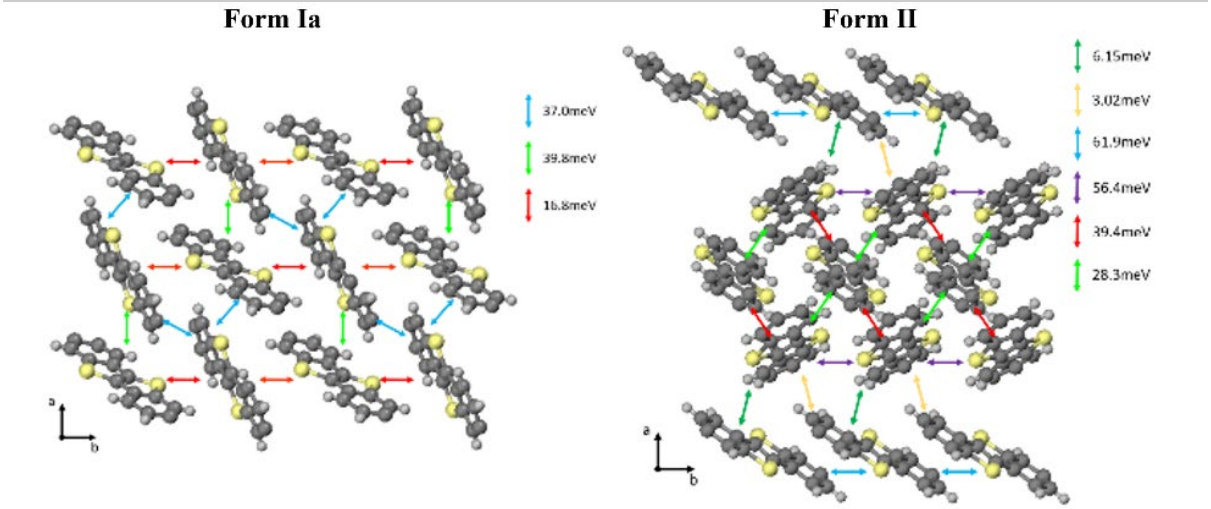

Figure 10 Spatial distribution of transfer integrals of Form Ia (left) and Form II (right).

they display transfer integrals around 40 meV in two directions and a third direction with integral of 16 meV. Also, for Form II the charge transport is expected within the planes parallel to (0 0 1) but it shows a 1D transport character with high HOMO couplings along two different stacks, one involving the molecules with the tilt angle of 42˚ which present a π-stacking, and the second involving the two molecules with 54˚ and 56˚ tilt angle and the herringbone motif.

Thin-Film polymorph screening.

Films of ditBuC6-BTBT were prepared by solution processing on silicon substrates by varying several parameters like solvents (CHF, TOL, DEC, DMA, and CLB), processing technique, (spin-coating, drop casting, and shear coating (see later)), temperature (pre- and post- thermal treatment up to 110˚C) and concentration (1 mg mL^{-1}, 3 mg mL^{-1}, and 22.6 mg mL^{-1} (2% w/w)).

The polymorphic tendency of ditbuC6-BTBT in thin films was the same as in bulk. As observed in bulk, Form Ia was observed in CHF and TOL while in DEC and DMA the mixture of Form Ia and Form II was observed which completely transformed into Form II in time. No other polymorph was obtained from spin-coating or drop-casting experiments.

Solution shearing and device fabrication.

For the fabrication of OFET we exploited the solution-shearing deposition technique, as it has appeared to be a promising approach for device fabrication with large area coverage and low production cost.[41] Moreover it allows better control the conditions of crystallization and can

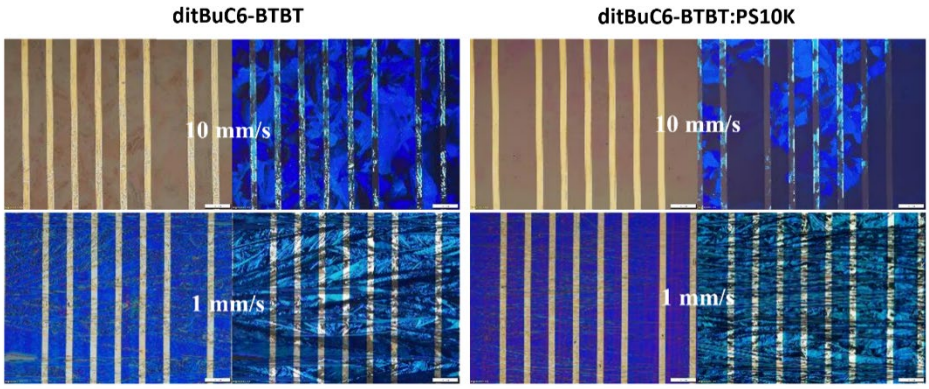

Figure 11 Polarised optical microscopy (POM) images of bottom gate/top contact devices of ditBuC6-BTBT and ditBuC6-BTBT:PS10K prepared with shearing speed of 10 mm s^{-1} (top) and 1 mm s^{-1} (bottom). Scale bar: 200 µm.

induce a polymorph formation different from the one's found in bulk or other conventional technique.

In this work, the films of ditbuC6-BTBT were prepared using the bar-assisted meniscus shearing (BAMS) technique. The organic field effect transistors (OFETs) were fabricated using the bottom gate/bottom contact (Figure S16) and bottom gate/top contact approach. The use of a polymeric blend of polystyrene (PS) was also carried out as the PS might promote homogeneity and an enhanced thin film crystallinity and electrical performance of the devices.[41]

Hence, we could investigate the impact of shearing deposition on crystalline property and phase behaviour of ditBuC6-BTBT. The POM images were recorded for pristine, and PS blended films fabricated via bottom contact and top contact at different coating rates (Figure 11). The films deposited with 1 mm s^{-1} shearing rate, show poor coverage, as the active layer was not homogenous to cover the electrodes. Also, the film morphology was found to be long needles which could be associated to the Form III, along with a few plate-like square crystals near the edges as observed in Form Ia.

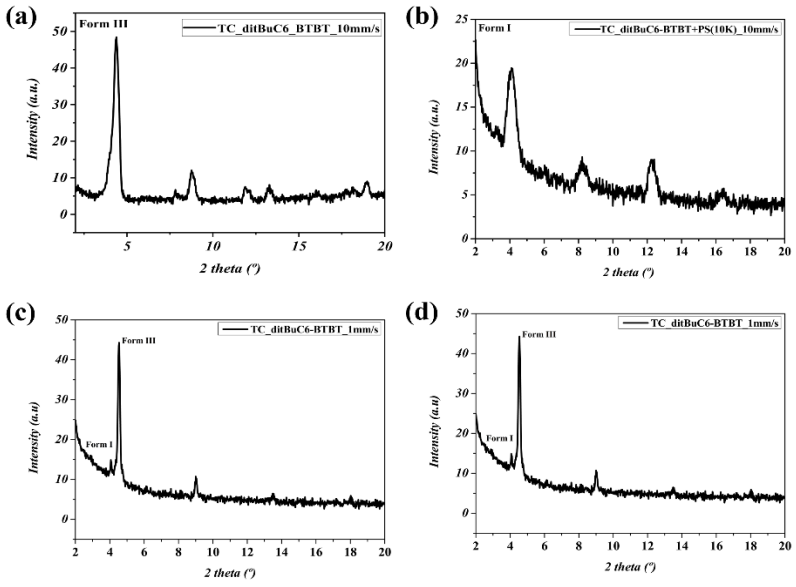

Figure 12 XRD patterns of (a) Pristine 10 mm s^{-1} (b) ditBuC6-BTBT:PS 10 mm s^{-1}(c) Pristine 1mm s^{-1}) and (d) ditBuC6-BTBT:PS 1 mm s^{-1}. In both (a) and (b) dominant peak of Form III, with a shoulder peak of Form Ia can be observed.

While the films with 10 mm s^{-1} were more homogeneous and isotropic, with complete coverage and larger crystalline domains. It was also observed that the film coverage was far improved with the PS blend.

From the structural characterization by PXRD of the thin films of all the samples, we always observed the mixture of Form III and Form Ia, with Form III in the dominance. Also, this result agrees with the morphology information obtained from directional crystallization technique, where we observed needle-like morphology for Form III while Form Ia crystals were sheets or plates.

The presence of two polymorphs in the films by solution shearing makes it even more difficult to isolate a polymorph for electrical measurements or to improve the device performance. Another critical issue associated with the devices of ditBuC6-BTBT is the extremely deep ionization potential values (reported above), which hampered the charge injection within the accumulation layer and led to our inability to record any FET response (either in the bottom or top contact configuration).[14] This was observed in the experimental outcomes of bottom gate/bottom contact and bottom gate/top contact devices with pristine molecule and ditBuC6-BTBTB: PS ink (Figure S16).

OFET fabrication by evaporation

Due to the inability to obtain operating devices through the BAMS technique, OFETs were fabricated through thermal evaporation in a high vacuum. Typically, ditBuC6-BTBT was deposited onto substrates consisting of a highly doped silicon wafer, which serves as a global gate electrode overgrown by atomic layer deposition with a 30-nm-thick layer of Al_2O_3. The dielectric was consequently treated with n-tetradecylphosphonic acid (TDPA), leading to the formation of a self-assembled monolayer (SAM). During the semiconductor deposition, the substrates were held at temperatures (T_{sub}) of 25, 40, 70, 100 and 130°C. Both bottom gate/top contact (BGTC) and bottom gate/bottom contact (BGBC) configurations were fabricated by thermal evaporation of source and drain gold electrodes, resulting in devices with a channel length (L) of 215 µm and channel width (W) of 480 µm. In the case of BGBC OFETs, the gold contacts were treated with pentafluorobenzenethiol (PFBT), which promotes a more uniform morphology of the organic layer across the contact-active channel interface.[42]

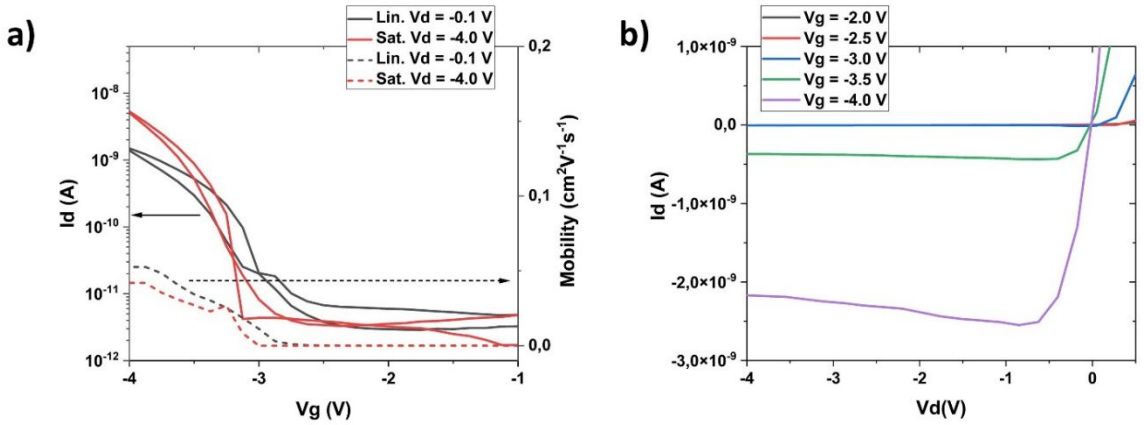

Figure 13 Representative (a) transfer and (b) output characteristics of BGBC OFETs based on ditBuC6-BTBT deposited at T_{sub} of 70 °C. In transfer characteristics, solid lines and dashed lines are referred to drain current and mobility respectively. TFTs have W/L = 480/215 µm.

The deposition of ca. 25 nm of ditBuC6-BTBT resulted in non-operating devices both in the case of BGTC and BGBC geometries at all substrate temperatures. By analysing the thin films with optical microscopy (Figure S17 and S18), we noted that, for all substrate temperatures, the 25-nm-thick layer of ditBuC6-BTBT is not enough to guarantee a uniform coverage of the active channel, giving discontinuous films characterized by pitted morphology. Moreover, thin films deposited at T_{sub} of 130°C were completely dewetted from the dielectric surface.

Therefore, BGTC and BGBC OFETs were fabricated by depositing a 40-nm-thick OSC layer, which results in complete coverage of the active channel at all substrate temperatures (except for T_{sub} of 130 °C which results again in total dewetting of the thin film from the dielectric surface). No drain current modulation upon the application of a gate bias was observed in BGTC devices at all substrate temperatures as well as for BGBC devices with T_{sub} of 25, 40 and 100°C. BGBC OFETs fabricated with T_{sub} of 70°C were the only ones to show field-effect response, allowing the collection of transfer and output characteristics, depicted in Figure 13. At first, it is clear that ditBuC6-BTBT shows poor performances due to the presence of hysteresis, high threshold voltage (V_{th}) and low on/off current ratio ($I_{ON/OFF}$). Particularly, OFETs exhibit V_{th} of -3.0 V and $I_{ON/OFF}$ of ≈ 6×10^2 along with hole mobility (µ) up to 0.057 $cm^2V^{-1}s^{-1}$ in a linear regime. The averaged V_{th}, $I_{ON/OFF}$ and µ values in linear and saturation regimes are reported in Table 2. As already mentioned, the main reason for poor electrical performances may be related to the deep ionisation potential of ditBuC6-BTBT, which leads to inefficient charge carrier injection which in turn is reflected in high V_{th}.

Table 2 Electrical performances of BC OFETs based on ditBuC6-BTBT in linear (V_d = -0.1 V) and saturation (V_d = -4.0 V). All the values are averaged over at least 5 devices.

T_{sub} (°C)		μ ($cm^2V^{-1}s^{-1}$)	V_{th}	$I_{ON/OFF}$
70	Linear	0.048 ± 0.008	-3.1 ± 0.1	≈ 6×10^2
	Saturation	0.034± 0.006	-3.0 ± 0.1	≈ 3×10^3

To understand the role of polymorphism in the electrical performances of ditBuC6-BTBT-based devices, XRD patterns of the thin films deposited through vacuum evaporation at T_{sub} of 25, 40, 70 and 100°C were recorded (Figure 14). The PXRD data reveals that we always obtain a mixture of polymorphs. For instance, at 25, 40 and 70˚C, Form Ia, II and III, are present, with the presence of Form Ia in dominant. Since the PXRD pattern are measured at RT and after some days we are not sure if the depositions lead to concomitant polymorphs and which ones or the transformation start in the second moment. The deposition at 100˚C, suggest that Form III is firstly obtained and the traces of Form Ia could be observed as a shoulder peak indicates that the transition to the Form Ia is starting (same as films produced by solution shearing at 105˚C). It is worth noting that the best-performing device was observed for samples at 70˚C, where we can distinctly observe the peaks of three polymorphs. Eventually, the OFETs fabricated by evaporation also resulted in the same problem of obtaining multiple polymorphs in the thin film, as we observed in the solution shearing method. Till now, it remains a challenge to isolate a single polymorph for a device to make

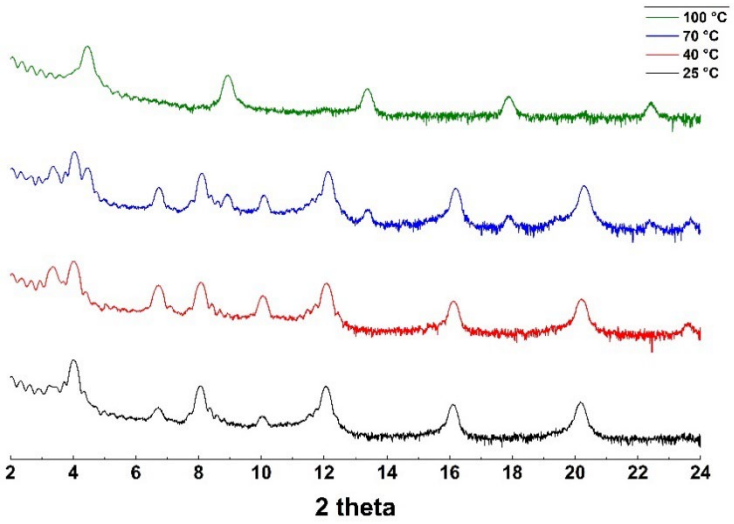

Figure 14 XRD patterns of ditBuC6-BTBT deposited at different substrate temperature onto Al_2O_3/TDPA substrate.

any conclusive statement about the hole mobility values. The co-existence of three different polymorphs in the OFETs implies the presence of grain boundaries, whose effect on charge transport is certainly detrimental but also renders comparison between polymorph performance impossible. For now, an observation can be made that the dominance of Form Ia, which has the best set of theoretical charge transport parameters is coherent with the fact that it's the only system that displays effective charge transport.

Conclusion.

In conclusion, we present a thorough study of the novel semiconductor ditBuC6-BTBT. Here, we emphasized the exhaustive polymorph screening in bulk and thin films which led to the finding of four polymorphs: Form I, Ia, II, and III. When we performed the polymorph screening of Form I, we found out that the recrystallization of the starting powder resulted in the thermodynamic stable Form II and a different polymorph named Form Ia, PXRD pattern of which is very close to Form I which makes it very challenging distinguish the two forms. Later on, both the metastable forms-Form I and Ia-, became dramatically unstable over time and converted to stable Form II due to an unintentional seeding effect. The crystallization experiments which used to result in Form Ia, now just yield Form II, and therefore, Form Ia and Form I can be remarked as a 'disappearing polymorph'. Form III is enantiotropically related to Form I, Ia, and Form II and it is stable at temperatures higher than 100°C. To expand the polymorph screening in view of the fabrication of devices, we explored the deposition of thin films by spin-coating and drop-casting and non-conventional techniques for directional crystallization using thermal gradient and solution shearing. However, in all the experiments we only observed the bulk phases, and no thin-film phase or non-equilibrium phase was observed. From the crystal structures of Form Ia and Form II, the transfer integrals were computed, and it was observed that Form II exhibits 1D charge transport, while Form Ia exhibits 2D charge transport within the plane parallel to (0 0 1). Furthermore, we fabricated bottom gate/bottom contact and bottom gate/top contact devices using solution shearing and evaporation methods. Different parameters like temperatures, shearing speed, and the blend of ditBuC6-BTBT with polystyrene were also varied in an attempt to improve mobility. We were able to extract the mobility values (μ_{lin} = 0.048 ± 0.008 $cm^2v^{-1}s^{-1}$ and μ_{sat} = 0.034± 0.006 $cm^2v^{-1}s^{-1}$) from the OFETs fabricated by evaporation at 70˚C, however, the deep

ionization potential values of both polymorphs (Form Ia and Form II) led to inefficient charge carrier injection and thus resulted in poor electrical performances. It was also observed that a mixture of polymorphs exists upon the deposition by both methods. Further attempts can be made in the future to isolate a single polymorph in the device and to improve the charge transport property.

References.

1 S. Aitipamula, R. Banerjee, A. K. Bansal, K. Biradha, M. L. Cheney, A. R. Choudhury, G. R. Desiraju, A. G. Dikundwar, R. Dubey, N. Duggirala, P. P. Ghogale, S. Ghosh, P. K. Goswami, N. R. Goud, R. R. K. R. Jetti, P. Karpinski, P. Kaushik, D. Kumar, V. Kumar, B. Moulton, A. Mukherjee, G. Mukherjee, A. S. Myerson, V. Puri, A. Ramanan, T. Rajamannar, C. M. Reddy, N. Rodriguez-Hornedo, R. D. Rogers, T. N. G. Row, P. Sanphui, N. Shan, G. Shete, A. Singh, C. C. Sun, J. A. Swift, R. Thaimattam, T. S. Thakur, R. Kumar Thaper, S. P. Thomas, S. Tothadi, V. R. Vangala, N. Variankaval, P. Vishweshwar, D. R. Weyna and M. J. Zaworotko, *Cryst. Growth Des.*, 2012, **12**, 2147–2152.

2 A. Gavezzotti, *J. Pharm. Sci.*, 2007, **96**, 2232–2241.

3 R. Purohit and P. Venugopalan, *Resonance*, 2009, **14**, 882–893.

4 K. B. Raju, S. Ranjan, V. S. Vishnu, M. Bhattacharya, B. Bhattacharya, A. K. Mukhopadhyay and C. M. Reddy, *Cryst. Growth Des.*, 2018, **18**, 3927–3937.

5 T. Matsukawa, M. Yoshimura, M. Uchiyama, M. Yamagishi, A. Nakao, Y. Takahashi, J. Takeya, Y. Kitaoka, Y. Mori and T. Sasaki, *Jpn. J. Appl. Phys.*, 2010, **49**, 085502.

6 L. Yu, *Acc. Chem. Res.*, 2010, **43**, 1257–1266.

7 J. D. Dunitz and J. Bernstein, *Acc. Chem. Res.*, 1995, **28**, 193–200.

8 P. Pandey, N. Demitri, L. Gigli, A. M. James, F. Devaux, Y. H. Geerts, E. Modena and L. Maini, *Cryst. Growth Des.*, 2022, **22**, 1680–1690.

9 A. O. F. Jones, B. Chattopadhyay, Y. H. Geerts, R. Resel, A. O. F. Jones, R. Resel, B. Chattopadhyay and H. Geerts, *Adv. Funct. Mater.*, 2016, **26**, 2233–2255.

10 H. Chung and Y. Diao, *J. Mater. Chem. C*, 2016, **4**, 3915–3933.

11 D. Mangin, F. Puel and S. Veesler, *Org. Process Res. Dev.*, 2009, **13**, 1241–1253.

12 Z.-P. Fan and H.-L. Zhang, in *Integrated Circuits/Microchips*, eds. K. H. Yeap and J. J. S. Hoyos, IntechOpen, Rijeka, 2020, p. Ch. 4.

13 G. Schweicher, Y. Olivier, V. Lemaur and Y. H. Geerts, *Isr. J. Chem.*, 2014, **54**, 595–620.

14 Y. Tsutsui, G. Schweicher, B. Chattopadhyay, T. Sakurai, J. B. Arlin, C. Ruzié, A. Aliev, A. Ciesielski, S. Colella, A. R. Kennedy, V. Lemaur, Y. Olivier, R. Hadji, L. Sanguinet, F. Castet, S. Osella, D. Dudenko, D. Beljonne, J. Cornil, P. Samorì, S. Seki and Y. H. Geerts, *Adv. Mater.,* 2016, **28**, 7106–7114.

15 S. Riera-Galindo, A. Tamayo and M. Mas-Torrent, *ACS Omega*, 2018, **3**, 2329–2339.

16 M. M. Torrent and C. Rovira, *Chem. Soc. Rev.*, 2008, **37**, 827–838.

17 M. Mas-Torrent and C. Rovira, *Chem Rev.*, 2011, **111**, 4833–4856.

18 H. Minemawari, M. Tanaka, S. Tsuzuki, S. Inoue, T. Yamada, R. Kumai, Y. Shimoi and T. Hasegawa, *Chem. Mater.*, 2017, **29**, 1245–1254.

19 A. O. F. Jones, Y. H. Geerts, J. Karpinska, A. R. Kennedy, R. Resel, C. Röthel, C. Ruzié, O. Werzer and M. Sferrazza, *ACS Appl. Mater. Interfaces*, 2015, **7**, 1868–1873.
20 G. H. Roche, Y. T. Tsai, S. Clevers, D. Thuau, F. Castet, Y. H. Geerts, J. J. E. Moreau, G. Wantz and O. J. Dautel, *J. Mater. Chem. C*, 2016, **4**, 6742–6749.
21 C. Ruzié, J. Karpinska, A. Laurent, L. Sanguinet, S. Hunter, T. D. Anthopoulos, V. Lemaur, J. Cornil, A. R. Kennedy, O. Fenwick, P. Samorì, G. Schweicher, B. Chattopadhyay and Y. H. Geerts, *J. Mater. Chem. C*, 2016, **4**, 4863–4879.
22 H. Chung, S. Chen, B. Patel, G. Garbay, Y. H. Geerts and Y. Diao, *Cryst. Growth Des.*, 2020, **20**, 1646–1654.
23 G. Schweicher, V. Lemaur, C. Niebel, C. Ruzié, Y. Diao, O. Goto, W. Y. Lee, Y. Kim, J. B. Arlin, J. Karpinska, A. R. Kennedy, S. R. Parkin, Y. Olivier, S. C. B. Mannsfeld, J. Cornil, Y. H. Geerts and Z. Bao, *Adv. Mater.*, 2015, **27**, 3066–3072.
24 H. Chung, S. Chen, N. Sengar, D. W. Davies, G. Garbay, Y. H. Geerts, P. Clancy and Y. Diao, *Chem. Mater.*, 2019, **31**, 9115–9126.
25 H. Chung, D. Dudenko, F. Zhang, G. D'Avino, C. Ruzié, A. Richard, G. Schweicher, J. Cornil, D. Beljonne, Y. Geerts and Y. Diao, *Nat. Commun., 2018 9:1*, 2018, **9**, 1–12.
26 G. Schweicher, G. Garbay, R. Jouclas, F. Vibert, F. Devaux and Y. H. Geerts, *Adv. Mater.*, 2020, **32**, 1905909.
27 C. F. MacRae, I. Sovago, S. J. Cottrell, P. T. A. Galek, P. McCabe, E. Pidcock, M. Platings, G. P. Shields, J. S. Stevens, M. Towler and P. A. Wood, *J. Appl. Crystallogr.*, 2020, **53**, 226–235.
28 C. F. Macrae, I. J. Bruno, J. A. Chisholm, P. R. Edgington, P. McCabe, E. Pidcock, L. Rodriguez-Monge, R. Taylor, J. van de Streek and P. A. Wood, *J. Appl. Crystallogr.*, 2008, **41**, 466–470.
29 P. R. Willmott, D. Meister, S. J. Leake, M. Lange, A. Bergamaschi, M. Böge, M. Calvi, C. Cancellieri, N. Casati, A. Cervellino, Q. Chen, C. David, U. Flechsig, F. Gozzo, B. Henrich, S. Jäggi-Spielmann, B. Jakob, I. Kalichava, P. Karvinen, J. Krempasky, A. Lüdeke, R. Lüscher, S. Maag, C. Quitmann, M. L. Reinle-Schmitt, T. Schmidt, B. Schmitt, A. Streun, I. Vartiainen, M. Vitins, X. Wang and R. Wullschleger, *J. Synchrotron Radiat.*, 2013, **20**, 667–682.
30 G. Schweicher, G. Liu, P. Fastré, R. Resel, M. Abbas, G. Wantz and Y. H. Geerts, *Mater. Chem. Front*, 2021, **5**, 249–258.
31 G. Schweicher, G. Liu, P. Fastré, R. Resel, M. Abbas, G. Wantz and Y. H. Geerts, *Mater. Chem. Front*, 2021, **5**, 249.
32 T. Izawa, E. Miyazaki and K. Takimiya, *Adv. Mater.*, 2008, **20**, 3388–3392.
33 H. Minemawari, M. Tanaka, S. Tsuzuki, S. Inoue, T. Yamada, R. Kumai, Y. Shimoi and T. Hasegawa, *Chem. Mater.*, 2017, **29**, 1245–1254.
34 J. D. Dunitz and J. Bernstein, *Acc. Chem. Res.*, 1995, **28**, 193–200.
35 G. Woodard, W. M.-J. of A. Crystallography and undefined 1975, *scripts.iucr.org*, 1975, **8**, 342–342.
36 J. Webb and B. F. Anderson, *J. Chem. Educ.*, 1978, **55**, 644.
37 N. Rodríguez-hornedo and D. Murphy, *J. Pharm. Sci.*, 1999, **88**, 651–660.
38 S. S. Lee, S. B. Tang, D. M. Smilgies, A. R. Woll, M. A. Loth, J. M. Mativetsky, J. E. Anthony and Y. L. Loo, *Adv. Mater.*, 2012, **24**, 2692–2698.

39 K. R. Graham, G. O. N. Ndjawa, S. M. Conron, R. Munir, K. Vandewal, J. J. Chen, S. Sweetnam, M. E. Thompson, A. Salleo, M. D. McGehee and A. Amassian, *Adv. Energy Mater.*, 2016, **6**, 1601211.
40 K. Takimiya, I. Osaka, T. Mori and M. Nakano, *Acc. Chem. Res.*, 2014, **47**, 1493–1502.
41 A. Tamayo, S. Hofer, T. Salzillo, C. Ruzié, G. Schweicher, R. Resel and M. Mas-Torrent, *J. Mater. Chem. C*, 2021, **9**, 7186–7193.
42 M. R. Niazi, R. Li, M. Abdelsamie, K. Zhao, D. H. Anjum, M. M. Payne, J. Anthony, D. M. Smilgies and A. Amassian, *Adv. Funct. Mater.*, 2016, **26**, 2371–2378.

Chapter 5

Bulk Polymorphic Study of BTBT Systems

Overview

In addition to the previous three main projects, I also studied other BTBT systems like BTBT (bare), ditBu-BTBT and C2F5C6-BTBT. Out of which, BTBT and ditBu-BTBT were previously reported in the literature and C2F5C6-BTBT was a novel organic semiconductor. My findings in polymorph investigations coincided with the literature for both BTBT and ditBu-BTBT. Although to add to the literature, I also examined the mechanical properties of both these molecules. BTBT exhibits a brittle response to mechanical stress, and ditBu-BTBT bends plastically. These results were supported by discussions on the intermolecular energies of the two. C2F56-BTBT is rather an interesting system to study as in the initial experiments I observed multiple thermotropic polymorphs and one polymorph from bulk polymorph screening.

The supporting information is reported in Appendix D.

Bulk Polymorphic Study of BTBT Systems

Introduction

The rise of small-molecule organic semiconductors (OSCs) has escalated largely in the past few decades.[1] With the increasing number of OSCs being studied, an increasing number of polymorphs is recorded, proving the enhanced interest in polymorphism among research groups and industries.[2] Polymorphism is a vital phenomenon, which is popular in active pharmaceutical ingredients (APIs), and OSCs.[3–9] A molecule can adopt more than one packing arrangement owing to the supramolecular synthons, which critically determine the physical properties of the material.[10] In OSCs, the packing arrangement primarily defines the charge transport mechanism, *ergo*, the great impact of molecular packing or the presence of polymorphs on electrical properties has been witnessed previously.[11,12] Similarly, mechanical properties are also narrated by the crystal packing and studied for addressing solid-state issues in pharmaceutical processes and the design of smart materials.[13,14] To exploit the vast possibilities of tuning the properties with polymorphs, one must overcome the hurdle of understanding the molecular origin of polymorphism that is required for controlling polymorph formation, which remains a challenge for each unique system, to date.[15]

In this work, we have performed a systematic study of three OSC systems. A common conjugated core, [1]benzothieno[3,2-b]benzothiophene (BTBT), was selected for all the systems. We varied the substitution in the BTBT core with bulky and linear groups and investigated the polymorphic behaviour. The molecular scheme of the systems studied (1) BTBT, (2) 2,7-di-tert-butyl-4b,9b-dihydrobenzo[b]benzo [4,5]thieno[2,3-d]thiophene (ditBu-BTBT) and, (3) 2,7-bis (7,7,8,8,8-pentafluorooctyl)-46,9b-dihydrobenzo [b]benzo[4,5]thieno[2,3-d]thiophene (C2F5C6-BTBT) are illustrated in Figure 1. Interestingly, the polymorphic response of all three systems was observed to be completely different from one another. We noticed that the BTBT core without any substitution does not possess any polymorph, the system with bulky substitution (ditBu-BTBT) undergoes a polymorphic transition due to dynamic rotational disorder in the bulky group at elevated temperatures, while the system with linear substitution functionalised by fluorination in the terminal

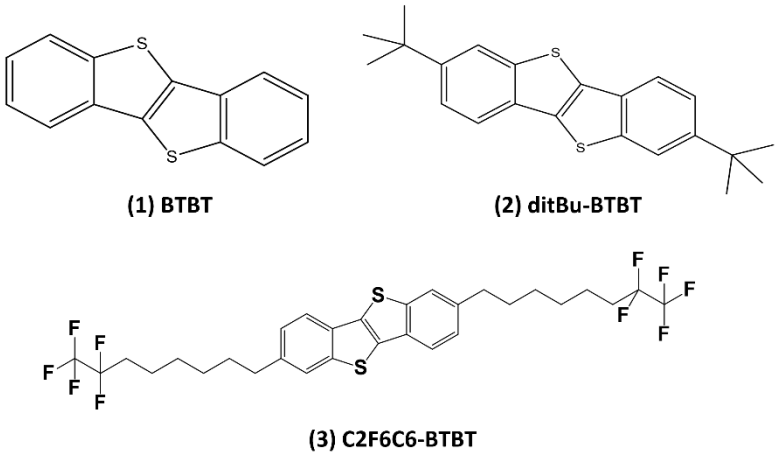

Figure 1 Molecular scheme of compounds studied (1) BTBT, (2) ditBu-BTBT and (3) C2F5C6-BTBT

carbons, a large number of thermotropic polymorphic transitions are observed. These systems were explored and characterized for changes in molecular structures.

Furthermore, we have also examined the mechanical bending properties of BTBT and ditBu-BTBT crystals. The three pillars for predicting the mechanical response of molecular crystals to external stress are (i) facile slip layers, (ii) topology of slip layers and (iii) interaction energies among molecules in different directions.[13,16] For example, generally the brittle crystals are found to exhibit interdigitated packing with a zipper-type arrangement of molecules which leads to mechanical interlocking. This packing corrugation and absence of slip can also be observed and verified from the interaction energy maps, where the molecules are interlocked with isotropic interactions in all three dimensions of the structure.[17] However, in the case of plastic or elastic crystals, typically there is a layer separation which acts as a facile slip plane, orthogonal to the stacking direction. With the help of interaction energy maps, a further distinction between elastic and plastic crystals can be made, where the intertape interaction energy in elastic crystals is expected to be higher than that of plastic crystals. Typically, plastic bending occurs in molecular crystals when the packing is anisotropic in such a way that strong and weak interaction patterns occur in nearly perpendicular directions. It has been established up until now that plastic deformation is a permanent change in crystal shape, which typically occurs by delamination and sliding of crystal slabs.[18] However, the accurate prediction of the crystal's response to mechanical stress remains a

challenge. In this work, we elaborately discuss the mechanical reconfiguration of BTBT and ditBu-BTBT crystals. The distinct mechanical deformation response of the two molecules was attributed to the crystal structure and molecular packing that dictates the layer topology and the intermolecular interaction energy contributions.

Experimental Section

Polymorph screening.

Solubility screening for (1) BTBT, (2) ditBu-BTBT and (3) C2F2C6-BTBT was performed using different solvents (Table S1).

BTBT: 24 different solvents were screened for solubility assessment of BTBT. Recrystallization from solvent evaporation (10 mg mL^{-1}) at RT was performed in Toluene (TOL), p-Xylene (PXY), Mesitylene (MST), N,N-dimethylacetamide (DMA), N,N-dimethylformamide (DMF) and 1-Methyl-2-Pyrrolidone (MPY), at 50°C in 2-Methoxyethanol (2MX), and at 75°C in Benzyl Alcohol (ABZ), Dimethyl Sulfoxide (DMS), 1,4-Dioxane (DIX) and Isopropyl Acetate (IPA). Prolonged slurry maturation experiments at RT were performed by stirring the starting material in 2-Propanol (2PR), Chloroform (CHF), N,N-dimethylacetamide (DMA), N,N-dimethylformamide (DMF), Dimethyl Sulfoxide (DMS), Ethanol (ETH), Isopropyl Ether (IPE), Nitromethane (NMT) and water (H_2O). Slurry with solvent mixtures was also performed. The slurry samples were monitored by PXRD in intervals of 4, 7 and 15 days. The solvothermal method was also adopted using the Teflon-lined autoclave filled with a super-saturated solution of BTBT at elevated temperatures of 80˚C.

ditBu-BTBT: 24 solvents were screened for solubility assessment of ditbu-BTBT. Crystals of (2) were obtained by slow evaporation (10 mg mL^{-1}) at RT in Chloroform (CHF), Dichloromethane (DCM), Diethyl Carbonate (DEC), N,N-dimethylacetamide (DMA), 1,2- Dimethoxyethane (DMX), Methyl ethyl ketone (MEK), 1-Methyl-2-Pyrrolidone (MPY), Mesitylene (MST), p-Xylene (PXY), Tetrahydrofuran (THF) and Toluene (TOL). Recrystallization at 50°C was performed in 1,4-Dioxane (DIX), N,N-dimethylformamide (DMF), Isopropyl Acetate (IPA), Isopropyl ether (IPE), while at 75°C Benzyl Alcohol (ABZ) solubilized (2). Prolonged slurry maturation experiments at RT

were performed by stirring the starting material in 2-Methoxyethanol (2MX), 2-Propanol (2PR), Acetonitrile (ACT), Anisole (ANI), Dimethyl Sulfoxide (DMS), Ethanol (ETH), Nitromethane (NMT) and water (H_2O). Slurry with solvent mixtures was also performed. The slurry samples were monitored by PXRD in intervals of 4, 7 and 15 days. The solvothermal method was also adopted using the Teflon-lined autoclave filled with a super-saturated solution of ditBu-BTBT at elevated temperatures of 80˚C.

C2F5C6-BTBT: Since the amount of starting material was very limited, we restricted our solubility screening to 9 different solvents. Recrystallization by slow evaporation of C2F5C6-BTBT at RT was carried out in N,N-dimethylformamide (DMF), p-Xylene (PXY), Tetrahydrofuran (THF), and Toluene (TOL) (10 mg mL^{-1}), while for 2- Propanol (2PR) and Acetonitrile (ACN) the evaporation was performed at 50°C.

Powder X-ray diffraction (PXRD).

Qualitative PXRD to identify the crystalline form was collected with a Rigaku MiniFlex 600 diffractometer with CuKα radiation from a copper-sealed tube operated at 40 kV voltage and 15 mA current using a Bragg–Brentano geometry. Diffraction patterns were measured over the 2θ range of 2–40° by step scanning with an increment of 0.01° per step at a rate of 10°(2θ) min^{-1}.

Single crystal X-ray diffraction (SCXRD).

Suitable crystals of BTBT and ditBu-BTBT for SCXRD were obtained from TOL solutions (1 mg mL^{-1}). The crystal structure was collected with a Rigaku-Oxford Diffraction Xcalibur S diffractometer with Mo Ka radiation (λ= 0.71073 Å) and graphite monochromator. The data collection was performed at room temperature. The crystal structure was solved using WingX software-SHELXT codes and refined with SHELXL (version 2018/3). For visualization of the crystal structure, CCDC Mercury 2020.3.0 was used.[19,20]

Hirshfeld surface analysis.

The CrystalExplorer 17.5 package was used for the Hirshfeld surface analysis which was carried out based on the crystal geometry. The corresponding 2D fingerprint plots were also generated using CrystalExplorer 17.5 in the d_{norm} range of 0.0033 to 1.4654.

Thermo-Gravimetric Analysis-Evolved Gas analysis (TGA-EGA).

TGA-EGA analysis was performed to determine the thermal stability and to obtain information about the purity of the starting material powders of all three systems. The measurement was performed on approximately 3-6 mg (accurately weighted) of each sample with Mettler-Toledo TGA coupled with a Thermo Nicolet iS 10IR FT-IR spectrometer operated at a scan rate of 10°C min^{-1} and analysed using STARe software.

Differential scanning calorimetry (DSC).

The DSC for all the samples was performed on a Mettler-Toledo DSC1 instrument. Approximately 2−4 mg of samples (accurately weighted) were crimped in hermetic aluminium crucibles (40 μL) and scanned from room temperature to 200°C at a heating/cooling rate of 5°C min^{-1} under a dry N_2 atmosphere (flow rate 80 mL min^{-1}). The data were analysed with STARe software.

In-situ Variable temperature X-Ray Diffraction (VTXRD).

X-ray powder diffractograms in the 3−40° 2θ range were collected for BTBT and ditBu-BTBT samples on a PANalytical X'Pert PRO automated diffractometer, equipped with an X'Celerator detector and an Anton Paar TTK 450 system for measurements at controlled temperature. Data were collected in the open air in Bragg–Brentano geometry using Cu Kα radiation without a monochromator. Thermal programs were selected based on TGA results.

Hot stage microscopy (HSM).

Crystals on a glass- slide and covered with a cover slip were placed in a heating chamber (hot stage) on OLYMPUS BX41 stereomicroscope equipped with a LINKAM LTS350 platinum plate for temperature control and VISICAM analyser. The heating chamber was capped with a sealable lid during heating and cooling cycles, and the rate was kept constant at 10°C min^{-1}. Time-lapse images were taken using a NIKON DS FI3 high-speed camera for all in situ experiments and the images were analysed using software Nikon NIS Elements and Linksys32 data capture.

Mechanical Deformation Tests

Mechanical bending tests on the single crystals of BTBT and ditBu-BTBT were performed on a stereo-microscope equipped with cross polarizers and a Nikon DS-Fi3 camera using a needle and forceps.

Results and Discussion

Polymorph screening

We performed polymorph screening for all three molecules by adopting various methods of recrystallizations like slow evaporation and slurry maturation at RT and HT depending on the solubility assessment (see Table S1, S2 and S3). We also adopted the solvothermal method with super-saturated solutions at elevated temperatures (80˚C) for BTBT and ditBu-BTBT

BTBT and ditBu-BTBT are well-studied in the literature and our experiments, we did not observe any other polymorph for both. While system C2F5C6-BTBT is a novel p-type organic semiconductor with long and flexible symmetrical peripheral chains. Out of all the solvents tested for C2F5C6-BTBT, we observed a second polymorph (labelled Form II) in a mixture of

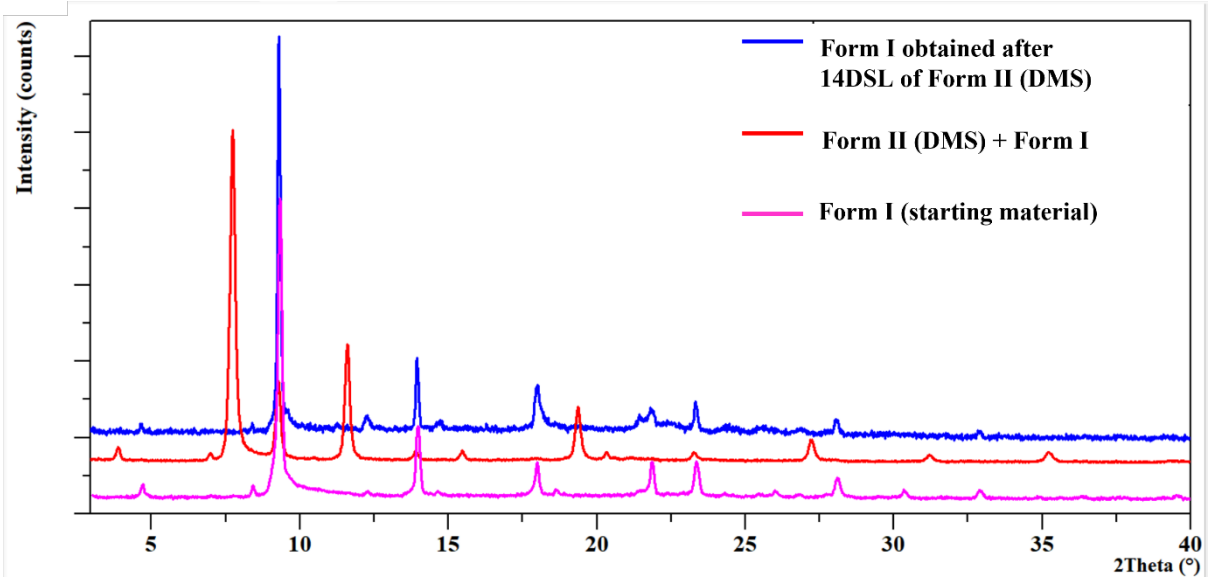

Figure 2 PXRD pattern comparison of Form I+II mixture (red) and pure Form I after 14 days slurry at room temperature (blue), λ=1.54 Å.

the starting material form (Form I) in DMS solvent by evaporation and slurry experiments at room temperature. We performed further stability assessment of this mixture and observed that the PXRD peaks of the new polymorph (Form II) disappeared after 14 days of slurry experiment at room temperature, resulting in a conversion of the bulk into Form I (Figure 2).

Thermal properties and phase transitions

Investigation of temperature dependant phase transitions by Differential Scanning Calorimetry (DSC) revealed that BTBT does not undergo any phase transition until melting (peak at 185˚C) where two events take place simultaneously: recrystallization and melting as witnessed by hot-stage microscopy (HSM).

In the case of ditBu-BTBT, from the results of DSC, we observed a phase transition taking place at 72˚C as reported by Chung *et al.*[21] We employed DSC, HSM, and variable temperature XRD (VTXRD) to have a detailed analysis of the high-temperature phase transition in ditBu-BTBT. We witnessed a cooperative transition taking place. The DSC shows the reversibility of the transition, which is one important aspect of a cooperative transition to occur. From the result of HSM, we see a distinct phase boundary line sweeping from one to the other end of the crystal in a matter of a second or even less (Figure 3). The ultrafast kinetics of transition is another characteristic of a cooperative transition. We tested several crystals to compute the reversibility of this transition, and in all the crystals, the same transition was observed. With

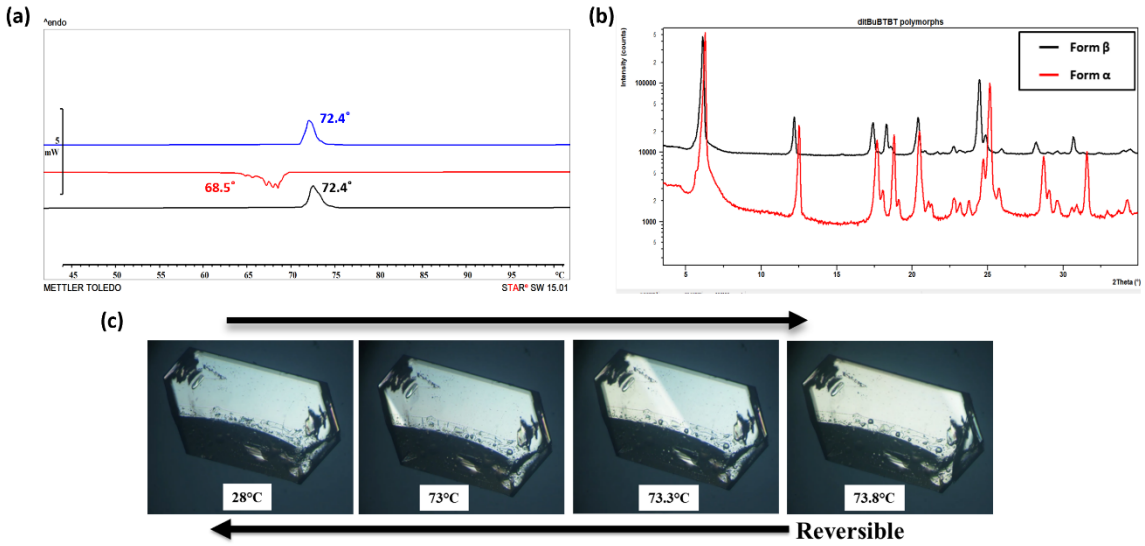

Figure 3 Thermal properties of ditBu-BTBT (a) DSC at 10˚C min^{-1}, (b) VTXRD at RT and at 75˚C, showing two polymorphs (α and β), and (c) HSM images from RT to HT, showing the phase boundary line sweep across the crystal undergoing cooperative transition.

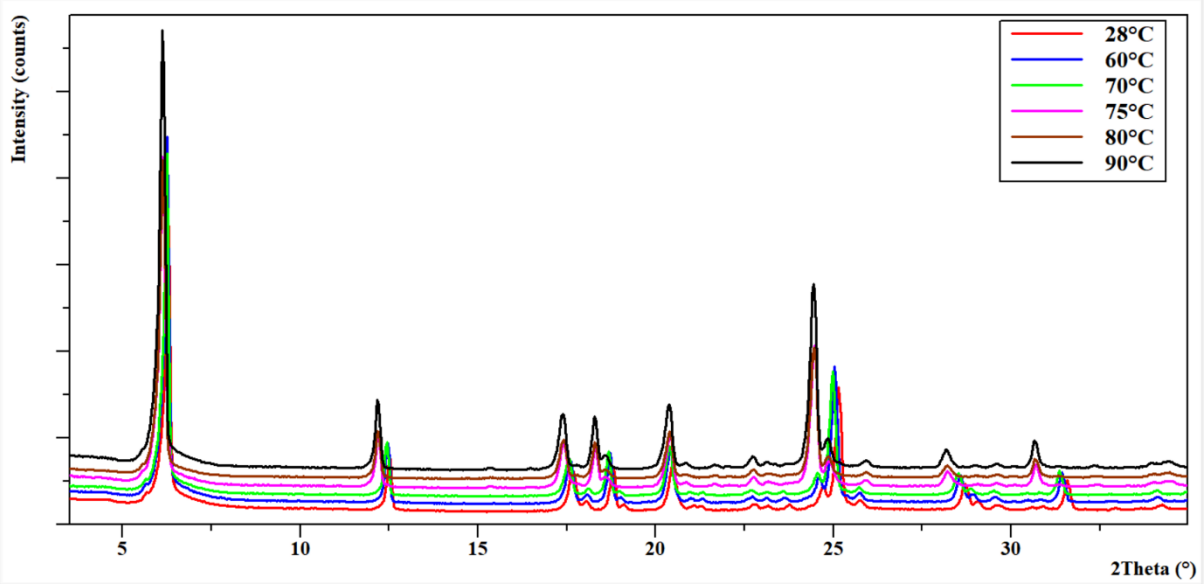

Figure 4 ditBu-BTBT VTXRD showing the XRD pattern at different temperature and highlighting the phase transition at 75˚C.

the aid of VTXRD, we confirmed this transition, which looks rather like a thermal expansion; however, as a matter of fact, the unit cell modification in cooperative transitions' phases is very small. All these results coincide with the previous work by Chung *et al*[21] (Figures 4 and 6).

The thermal properties of C2F5C6-BTBT led to the finding of multiple thermotropic transitions. In the first heating, the material undergoes three solid-solid transitions (at 72˚C, 85˚C and 113˚C) before melting at 160˚C. During cooling, the melt cools down to give a liquid crystal (155˚C) at first which further transitions to a crystalline phase at 83˚C followed by another solid-solid transition at 60˚C. The second heating led to another set of transitions at 110˚C and 115˚C (transition at 115˚C was only observed in HSM, not in DSC) followed by melting at 160˚C (Figure 5). All these thermal behaviours were confirmed by DSC and HSM. It was worth noting that the melting temperature of all the cycles was the same, indicating a consistent high-temperature phase after 115˚C. The other course of transition for 1st and 2nd heating were not coinciding. The number of transitions taking place in this molecule as a function of temperature required much more detailed analysis and characterisations. However, as stated above the amount of material was limited and it was not possible to move ahead with further studies on this molecule. Deeper investigations on the polymorphic properties of this molecule with the identification of temperature dependant phases by XRD can be interesting for future studies. Up till now, it is indeed difficult to say if Form II obtained

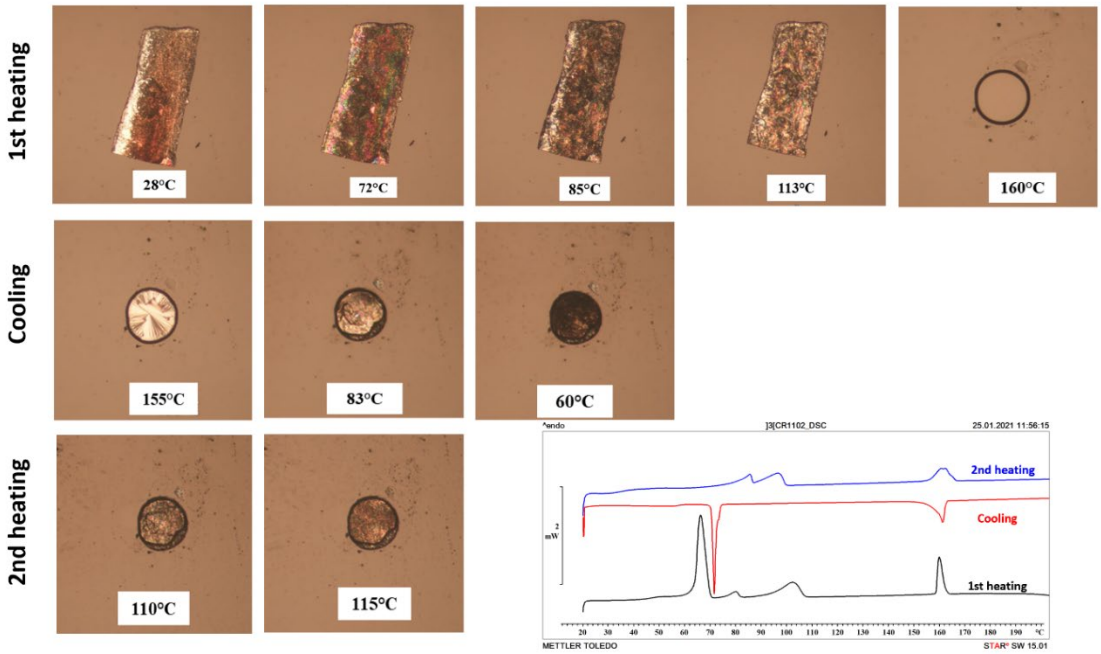

Figure 5 HSM and DSC images of C2F5C6-BTBT showing transitions during heating-cooling-heating cycle.

in the recrystallization experiments at RT corresponds to any of the phases identified with thermal characterizations.

Crystal structure study

For having a complete understanding of the crystal structure, we carried out single-crystal X-ray diffraction (SCXRD) measurements on the samples. From our analysis, we discovered that the structure of BTBT and ditBu-BTBT were coinciding with the literature (Table S4). However,

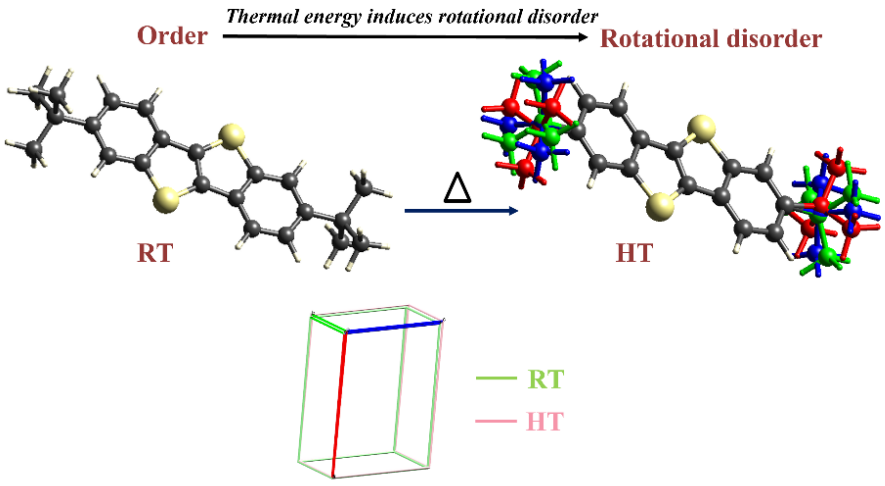

Figure 6 ditBu-BTBT polymorphs and unit cell comparison.

despite several attempts, it was not possible to grow single crystals of C2F5C6-BTBT with sufficient quality to allow the elucidation of its crystal structure. Therefore, here on, we will focus our structural analysis on BTBT and ditBu-BTBT.

The crystals of BTBT, recrystallized in toluene by slow evaporation, were selected for the SCXRD. The structure was resolved in the monoclinic $P2_1/c$ space group. The molecules are packed in a herringbone-packing motif with a herringbone angle of 56.9˚. The core-tilt angle of 87.1˚ indicates that the BTBT core stays almost upright (Figure 7).

While in ditBu-BTBT, also recrystallisation in toluene was selected for SCXRD measurement at room temperature and the structure was resolved in the monoclinic $P2_1/c$ space group with half a molecule in the asymmetric unit (Form α). Like BTBT, ditBu-BTBT also adopts herringbone packing with a herringbone angle of 54.1˚, while the core-tilt angle was observed to be 50.6˚, clearly indicating that the tilt angle decreases drastically with the introduction of bulky tBu group to the BTBT molecule (Figure 7).

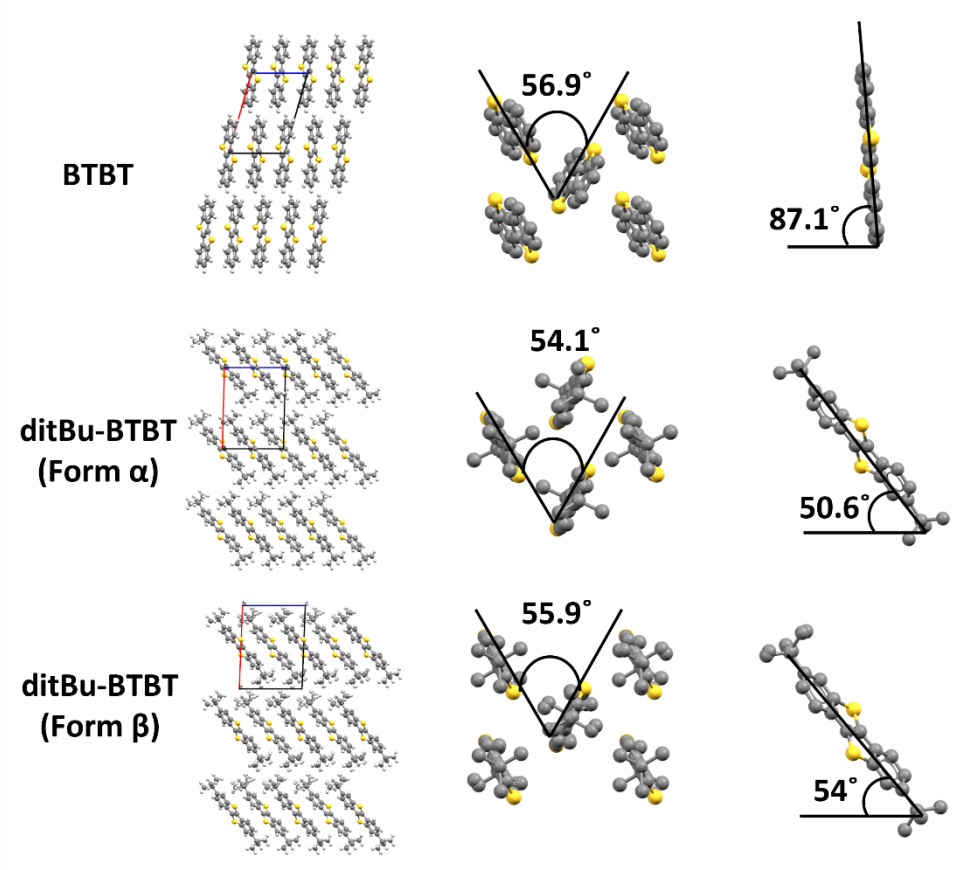

Figure 7 Packing, herringbone angles and core-tilt angles from BTBT and ditBu-BTBT polymorphs single crystal structure data.

Chung *et al.*[21] have also reported the high-temperature polymorph of ditBu-BTBT. This polymorph (Form β) is a result of cooperative transition taking place as a function of temperature, as discussed above. Form β exhibit dynamic disorder at high temperature. The molecules of Form α undergo order-to-disorder transition at high temperatures, triggering the tBu group to rotate keeping the core intact. This does not cause a major change in the unit cell, and the herringbone packing also remains preserved causing the change in herringbone angle (55.9˚) (Figure 7). These changes, albeit small, are enough to impact the transfer integrals and the charge transport.

Hirshfeld surface analysis

For 3D visualization and a clear understanding of intermolecular interactions, Hirshfeld surfaces and their respective 2D fingerprint plots were calculated using the Crystal Explorer package. The electron density Hirshfeld surface plot of BTBT was mapped over d_{norm} (Figure 8). The d_{norm} plots were chosen for mapping since they combine both the distance from the point to the nearest nucleus external to the surface (d_e) and the distance to the nearest nucleus internal to the surface (d_i), each normalized by the van der Waals radius for the particular atoms involved in the close contact to the surface.

From the plots, we can identify the dominant interactions. In the case of BTBT, short contact interactions are present between S—C, C—H and S—S. However, 2D fingerprint plots illustrate that the overall contribution of interactions is dominated by H—H and C—H

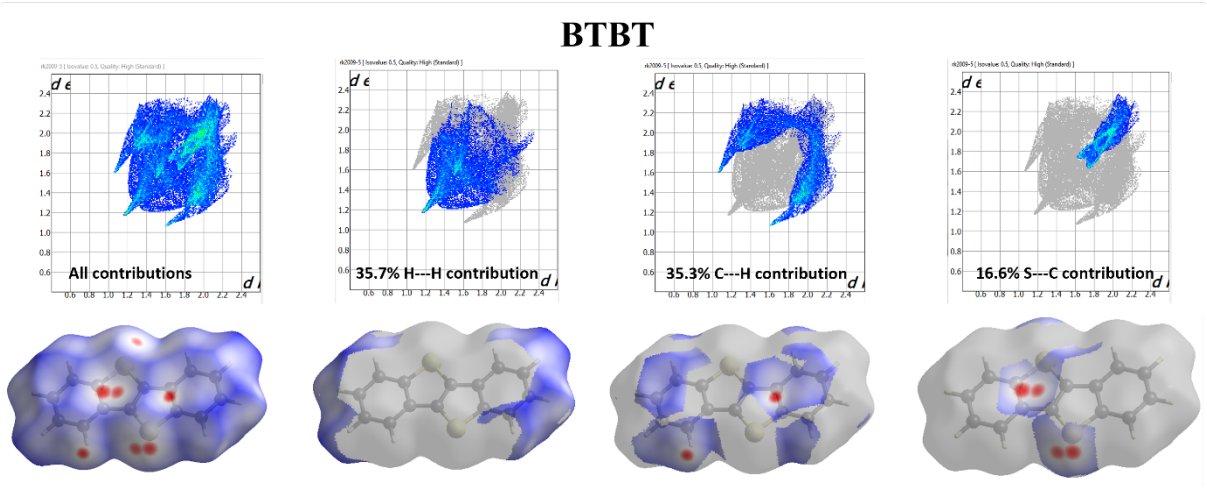

Figure 8 Hirshfeld surface plots of dnorm and their respective fingerprint plots for BTBT molecule.

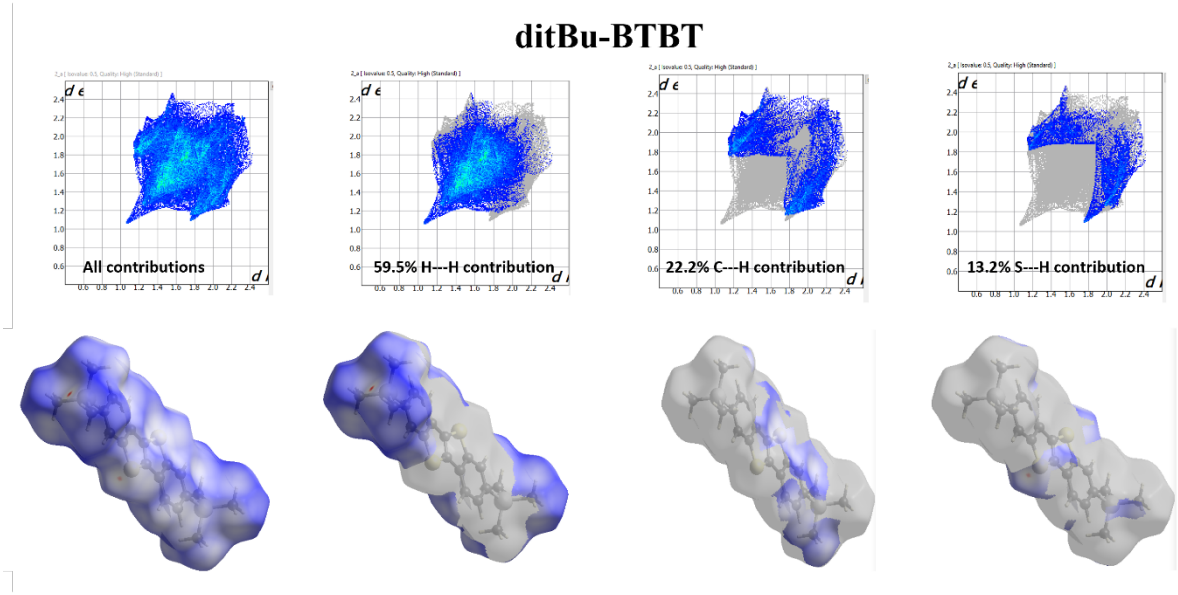

Figure 9 Hirshfeld surface plots of dnorm and their respective fingerprint plots for ditBu-BTBT.

interactions leading by approximately 35% for both. The map of the percentage contribution of each interaction is presented in Figure 8.

In system ditBu-BTBT, the fingerprint plots reveal that the packing environment is completely different than BTBT due to the influence of tBu groups. In this case, the major contribution of interactions is ruled by H—H interactions with 59.5% while C—H interactions are less than half (22.2%). It is also worth noting that the short contact interactions in ditBu-BTBT are much lesser compared to BTBT, which are present only with H—H and S—H interactions (Figure 9).

Energy framework analysis and mechanical properties

To visualize the intermolecular interactions in a precise and quantitative manner we calculated the pair-wise intermolecular interaction energies called ''Energy frameworks'' using the CrystalExplorer tool which allows us to visualize the 3D topology of the molecules.

In BTBT, the aggregate of total energy in the 1D tape was -25 kJ mol^{-1} which includes the interaction responsible for the herringbone packing of the molecule, while in the stacking direction, the aggregate of total energy was found to be -18.5 kJ mol^{-1}. By looking at the tubes corresponding to the interaction strength, it is clear that the intratape interactions are making a 2D network, and thus are much stronger than the intertape interactions (-5.7 kJ mol^{-1}) (Figure 10).

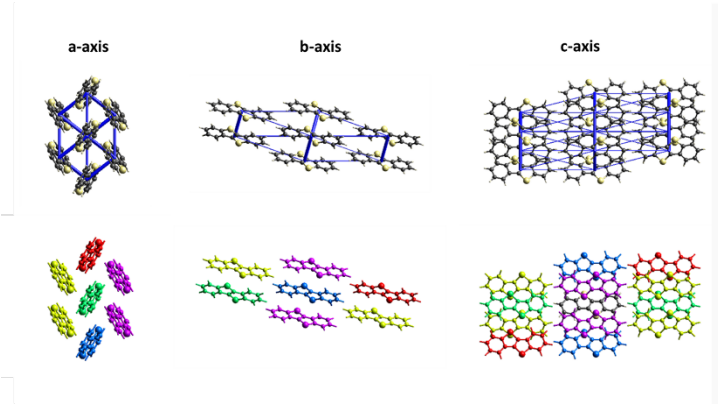

Interaction Energies (kJ/mol)
R is the distance between molecular centroids (mean atomic position) in Å.

Total energies, only reported for two benchmarked energy models, are the sum of the four energy components, scaled appropriately (see the scale factor table below)

N	Symop	R	Electron Density	E_ele	E_pol	E_dis	E_rep	E_tot
1	x, y, z	13.19	B3LYP/6-31G(d,p)	0.6	-0.1	-1.4	0.1	-0.6
1	-x, y+1/2, -z+1/2	11.76	B3LYP/6-31G(d,p)	-1.1	-0.3	-9.2	6.0	-5.7
1	x, y, z	11.81	B3LYP/6-31G(d,p)	-2.3	-0.3	-9.6	6.5	-7.1
1	x, y, z	5.87	B3LYP/6-31G(d,p)	-12.2	-1.0	-28.3	32.1	-18.5
1	-x, y+1/2, -z+1/2	4.93	B3LYP/6-31G(d,p)	-10.8	-1.4	-41.3	37.8	-25.0

Scale factors for benchmarked energy models
See Mackenzie et al. IUCrJ (2017)

Energy Model	k_ele	k_pol	k_disp	k_rep
CE-HF ... HF/3-21G electron densities	1.019	0.651	0.901	0.811
CE-B3LYP ... B3LYP/6-31G(d,p) electron densities	1.057	0.740	0.871	0.618

Figure 10 Energy framework analysis of BTBT showing total intermolecular energies with blue tubes and colours, each colour denoting unique pairwise intermolecular energies in 3.8 Å radius to the central molecule.

In RT polymorph of ditBu-BTBT-Form α, the intralayer aggregate intermolecular energies are much larger than that of the interlayer (Figure 11). Like in BTBT, the highest energy contribution is present in the herringbone direction (-40.6 kJ mol^{-1}) while the next highest intermolecular energy was -26.8 kJ mol^{-1} in the stacking direction. The intertape interaction energy (-5.9 kJ mol^{-1}) was 5 times lower than the intratape interaction energies, which suggests that (0 0 1) is the weakest plane which may act as an active slip plane (as shown in the indexing of Figure 12).

The intratape intermolecular energy contribution of ditBu-BTBT-Form α was found to be much higher than that of BTBT, while the intertape energies for both are comparable. This suggests that ditBu-BTBT-Form α is more likely to exhibit an active slip plane than BTBT. The layer separation in BTBT and ditBu-BTBT-Form α was observed to be 0.56 Å and 0.68 Å, respectively. Further experimental studies on mechanical properties highlighting the

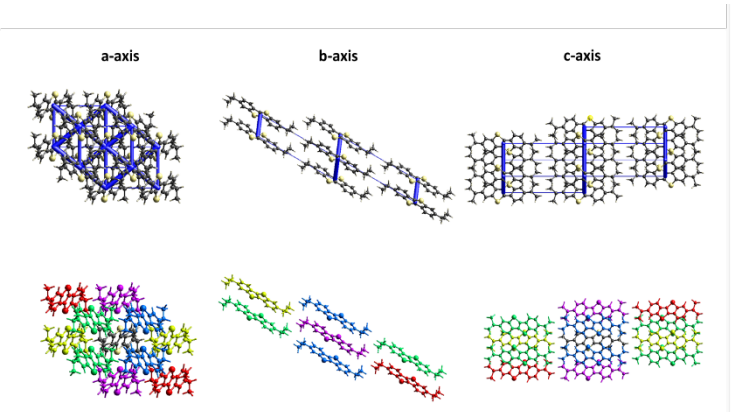

Interaction Energies (kJ/mol)
R is the distance between molecular centroids (mean atomic position) in Å.

Total energies, only reported for two benchmarked energy models, are the sum of the four energy components, scaled appropriately (see the scale factor table below)

N	Symop	R	Electron Density	E_ele	E_pol	E_dis	E_rep	E_tot
1	x, y, z	18.12	B3LYP/6-31G(d,p)	-0.0	-0.0	-1.2	0.0	-1.0
1	x, y, z	17.05	B3LYP/6-31G(d,p)	-1.0	-0.2	-9.8	6.1	-5.9
1	-x, y+1/2, -z+1/2	16.33	B3LYP/6-31G(d,p)	-0.6	-0.0	-6.9	3.2	-4.6
1	-x, y+1/2, -z+1/2	5.12	B3LYP/6-31G(d,p)	-11.4	-2.0	-66.4	49.7	-40.6
1	x, y, z	6.13	B3LYP/6-31G(d,p)	-13.0	-1.2	-43.1	41.1	-26.8

Scale factors for benchmarked energy models
See Mackenzie et al. IUCrJ (2017)

Energy Model	k_ele	k_pol	k_disp	k_rep
CE-HF ... HF/3-21G electron densities	1.019	0.651	0.901	0.811
CE-B3LYP ... B3LYP/6-31G(d,p) electron densities	1.057	0.740	0.871	0.618

Figure 11 Energy framework analysis of ditBu-BTBT showing total intermolecular energies with blue tubes and colours, each colour denoting unique pairwise intermolecular energies in 3.8 Å radius to the central molecule.

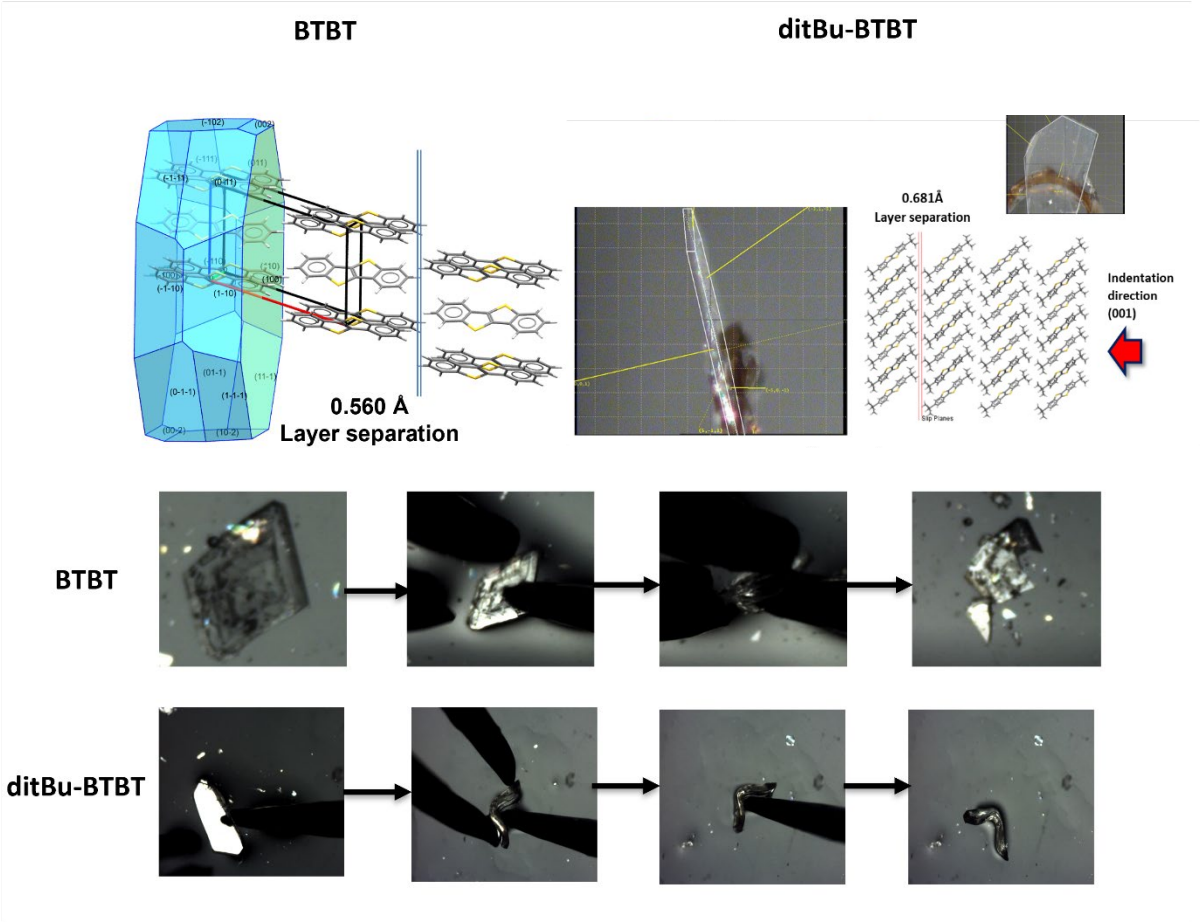

Figure 12 Slip layer topology and mechanical bending tests on BTBT and ditBu-BTBT-Form α

deformation mechanics were carried out using a three-point bending test on the respective single crystals using a pair of forceps and a needle under a polarized optical microscope.

The indentation direction on the major face of both the molecules is perpendicular to the slip layers along (0 0 1). The crystals of BTBT were broken as soon as the indentation was initiated and thus, it was found to exhibit brittle mechanical properties. However, the crystals of ditBu-BTBT-Form α were found to undergo plastic bending along the (0 0 1) plane. Several crystals were tested to confirm the reproducibility, and the results coincided. The major reason behind the plastic bending in ditBu-BTBT-Form α is the presence of the van der Waals group (tBu) which tends to act as a shape synthon which behaves as lubricated planes and allows molecular motions with minimal friction between molecular sheets. In addition, the much higher ratio of intratape to intertape intermolecular energy and the larger layer separation in ditBu-BTBT-Form α altogether contributes to this plastic bending behaviour of the crystals.

Conclusions

While focusing on [1]benzothieno[3,2-b]benzothiophene (BTBT) derivatives in our previous works, here, we presented the detailed bulk polymorphic investigation on three BTBT systems- bare BTBT, ditBu-BTBT and C2F5C6-BTBT. Out of these three, BTBT and ditBu-BTBT were well-studied in the literature while the latter was a novel p-type organic semiconductor with long and flexible alkyl chain and terminal fluorinated carbons. All the systems set forth unique polymorphic properties depending on the side-chain substitutions. While bare BTBT was found to be extremely stable in only one crystal form, ditBu-BTBT exhibits a polymorph due to cooperative transition at high temperatures. The system C2F5C6-BTBT presents a large number of polymorphs and liquid crystalline phases. These polymorphic and crystallographic studies serve a great advantage in understanding each system and that the key factor governing the existence of multiple phases is the side chains. For example, the two polymorphs in ditBu-BTBT exist due to the rotational disorder arising due to the rotation of the tBu group when external thermal energy is provided. Similarly, in C2F5C6-BTBT, the long chain gives the molecule more degree of freedom and the termination of the chain with the fluorinated group can form multiple supramolecular synthons giving rise to multiple polymorphs.

Furthermore, we also attempted to illustrate the structure-mechanical property relationship in the BTBT and ditBu-BTBT crystals. ditBu-BTBT exhibits plastic bending behaviour which is attributed to the facile slip plane and the tBu groups which facilitates the slippage of layers. Such mechanical property aids in promising applications of ditBu-BTBT which can be explored in detail in future.

References

1 L. A. Stevens, K. P. Goetz, A. Fonari, Y. Shu, R. M. Williamson, J. L. Brédas, V. Coropceanu, O. D. Jurchescu and G. E. Collis, *Chem. Mater.*, 2015, **27**, 112–118.

2 D. Mangin, F. Puel and S. Veesler, *Org. Process Res. Dev.*, 2009, **13**, 1241–1253.

3 T. Matsukawa, M. Yoshimura, M. Uchiyama, M. Yamagishi, A. Nakao, Y. Takahashi, J. Takeya, Y. Kitaoka, Y. Mori and T. Sasaki, *Jpn. J. Appl. Phys.*, 2010, **49**, 085502.

4 C. Cappuccino, S. Canola, G. Montanari, S. G. Lopez, S. Toffanin, M. Melucci, F. Negri and L. Maini, *Cryst. Growth Des.*, 2019, **19**, 2594–2603.

5 P. Pandey, N. Demitri, L. Gigli, A. M. James, F. Devaux, Y. H. Geerts, E. Modena and L. Maini, *Cryst. Growth Des.*, 2022, **22**, 1680–1690.

6 C. C. Mattheus, G. A. de Wijs, R. A. de Groot and T. T. M. Palstra, *J. Am. Chem. Soc.*, 2003, **125**, 6323–6330.

7 I. de Oliveira Martins, F. Marin, E. Modena and L. Maini, *Faraday Discuss.*, 2022, **235**, 490–507.
8 J. Bernstein, *Cryst. Growth Des.*, 2011, **11**, 632–650.
9 J. Bernstein, *Polymorphism in Molecular Crystals*, 2007, **9780199236565**, 1–424.
10 S. Aitipamula, R. Banerjee, A. K. Bansal, K. Biradha, M. L. Cheney, A. R. Choudhury, G. R. Desiraju, A. G. Dikundwar, R. Dubey, N. Duggirala, P. P. Ghogale, S. Ghosh, P. K. Goswami, N. R. Goud, R. R. K. R. Jetti, P. Karpinski, P. Kaushik, D. Kumar, V. Kumar, B. Moulton, A. Mukherjee, G. Mukherjee, A. S. Myerson, V. Puri, A. Ramanan, T. Rajamannar, C. M. Reddy, N. Rodriguez-Hornedo, R. D. Rogers, T. N. G. Row, P. Sanphui, N. Shan, G. Shete, A. Singh, C. C. Sun, J. A. Swift, R. Thaimattam, T. S. Thakur, R. Kumar Thaper, S. P. Thomas, S. Tothadi, V. R. Vangala, N. Variankaval, P. Vishweshwar, D. R. Weyna and M. J. Zaworotko, *Cryst. Growth Des.*, 2012, **12**, 2147–2152.
11 S. Riera-Galindo, A. Tamayo and M. Mas-Torrent, *ACS Omega*, 2018, **3**, 2329–2339.
12 I. Temiño, F. G. del Pozo, M. R. Ajayakumar, S. Galindo, J. Puigdollers and M. Mas-Torrent, *Adv. Mater. Technol.*, 2016, **1**, 1600090.
13 K. B. Raju, S. Ranjan, V. S. Vishnu, M. Bhattacharya, B. Bhattacharya, A. K. Mukhopadhyay and C. M. Reddy, *Cryst. Growth Des.*, 2018, **18**, 3927–3937.
14 P. Naumov, S. Chizhik, M. K. Panda, N. K. Nath and E. Boldyreva, *Chem. Rev.*, 2015, **115**, 12440–12490.
15 H. Chung, S. Chen, B. Patel, G. Garbay, Y. H. Geerts and Y. Diao, *Cryst. Growth Des.*, 2020, **20**, 1646–1654.
16 S. Das, A. Mondal and C. M. Reddy, *Chem. Soc. Rev.*, 2020, **49**, 8878–8896.
17 C. M. Reddy, G. Rama Krishna and S. Ghosh, *CrystEngComm.*, 2010, **12**, 2296–2314.
18 E. Ahmed, D. P. Karothu and P. Naumov, *Angew. Chem., Int. Ed. Engl.*, 2018, **57**, 8837–8846.
19 C. F. MacRae, I. Sovago, S. J. Cottrell, P. T. A. Galek, P. McCabe, E. Pidcock, M. Platings, G. P. Shields, J. S. Stevens, M. Towler and P. A. Wood, *J. Appl. Crystallogr.*, 2020, **53**, 226–235.
20 C. F. Macrae, I. J. Bruno, J. A. Chisholm, P. R. Edgington, P. McCabe, E. Pidcock, L. Rodriguez-Monge, R. Taylor, J. van de Streek and P. A. Wood, *J. Appl. Crystallogr.*, 2008, **41**, 466–470.
21 H. Chung, D. Dudenko, F. Zhang, G. D'Avino, C. Ruzié, A. Richard, G. Schweicher, J. Cornil, D. Beljonne, Y. Geerts and Y. Diao, *Nat. Commun.*, 2018, **9**, 278.

Chapter 6

Understanding the solid-state packing and the influence of bulky substituents in the series of rylene molecules

Overview

The last project of my PhD research represents the collaborative work with Rahul Meena, who is an early-stage-researcher (ESR) in the UHMob project. My contribution to this work was collecting the crystal structures with SCXRD, solving them, and analysing the crystal structures. This project involves six molecules of the rylene family, which are polynuclear aromatic hydrocarbons like naphthalene, perylene and terrylene derivatives with methyl group substitutions. I studied each molecule for all the crystallographic parameters and packing descriptors.

The supporting information is reported in Appendix E.

Understanding the solid-state packing and the influence of bulky substituents in the series of rylene molecules

Introduction

Crystal engineering is rationally designing and synthesizing molecular solid-state structures by fine-tuning the intermolecular interactions.[1,2] In the solid state, molecules self-assemble owing to a complex combination of chemical and geometrical factors and complementary contributions of a number of intermolecular interactions, like π-π and van der Waals interactions.[3–5] The supramolecular arrangement of the molecules is significantly impacted by these types of interactions, which attributes to molecular packing in one or more crystal forms and thus influencing characteristic physical properties of the molecule.[6]

Extensive research on the packing motif has highlighted four major possible packing motifs in organic crystals: (1) typical herringbone (C—H···π) without the π- π overlap between neighbouring molecules[7]; (2) slipped π-stacking or non-classical herringbone packing with π- π overlap between neighbouring molecules[8]; (3) one dimensional (1D) π-stacking, lamellar packing[9]; and (4) two dimensional (2D) π-stacking, lamellar packing.[2,10] Physical properties like electrical, mechanical, or optical properties are critically mediated by the crystal packing motifs. It is also well known that the symmetric or asymmetric substitutions in the π- electron skeleton of the rigid core can be detrimental to the structural modifications, and it is intriguing to study the characteristic properties of the molecular packing.[11]

The critical study of organic crystals for structural comparison is often complex. However, an approach based on the molecular structure depending on the size and shape and substitution of symmetric and asymmetric groups might reveal a relationship between the crystal structures. Pioneer research on the series of polynuclear aromatic hydrocarbons was well-studied by Desiraju and Gavezzoti[12] in

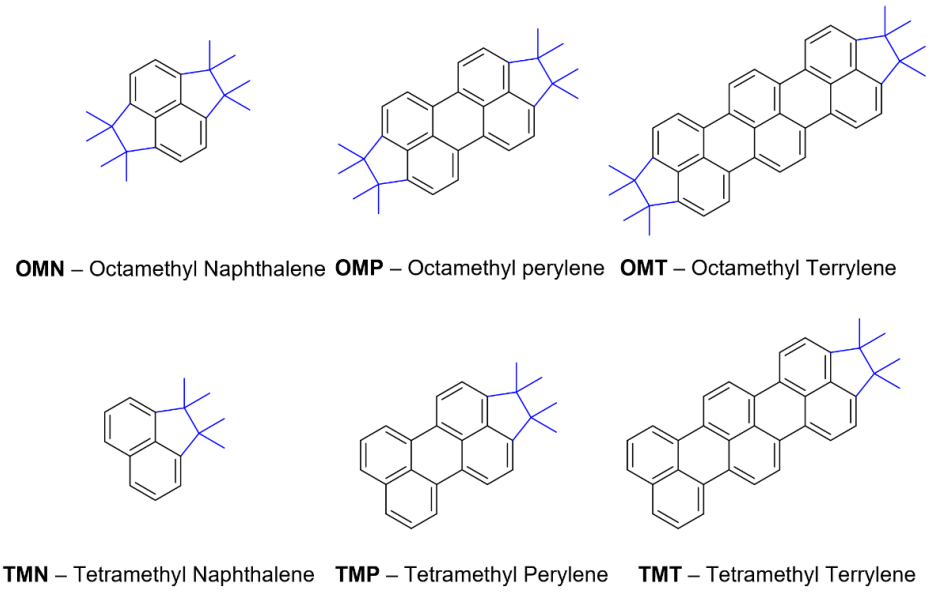

Figure 1 Molecular schemes of the molecules studied.

1989, which thoroughly illustrates the type of packing motifs adapted by the series of selected molecules. Herein, we have also studied a series of polynuclear aromatic hydrocarbons like naphthalene, perylene, and terrylene derivatives with methyl group substitutions. These molecules are prone to undergo dimer formation,[13,14] we attempted to introduce bulky substituents to the core to study the potential restriction of the crystal packing to monomers due to steric hindrance.

Another important aspect considered is polymorphism. Distinct polymorphs can arise due to differences in the crystallization conditions depending on the nucleation, growth, and dissolution mechanisms.[14,15] Different polymorphs might render completely different packing motifs, and it is paramount to examine the structural attributes of all the kinetic and thermodynamic crystal forms isolated. In one of our systems, we observed concomitant polymorphs, which we have thoroughly analysed in the later sections.

Experimental Section

Synthesis.

Crystals of Octamethyl Naphthalene (OMN), Octamethyl perylene (OMP), Octamethyl Terrylene (OMT), Tetramethyl Naphthalene (TMN), Tetramethyl Perylene (TMP) and Tetramethyl Terrylene (TMT) have been provided by ULB.

Single crystal X-ray diffraction (SCXRD).

Suitable crystals of all the molecules for SCXRD were obtained by slow evaporation from DCM: Heptane solution (1 mg ml^{-1}). The crystal structure was collected with a Rigaku-Oxford Diffraction Xcalibur S diffractometer with Mo Ka radiation (λ= 0.71073 Å) and graphite monochromator. The data collection was performed at room temperature and also at low temperatures for TMP crystals. The crystal structure was solved using WingX software-SHELXT codes and refined with SHELXL (version 2018/3). For visualization and analysis of the crystal structure and calculation of unified intermolecular interaction energies between neighbouring molecules, CCDC Mercury 2020.3.0 was used.[16,17] After data collection, reduction, and solution, all the crystallographic files were checked with PLATON and IUCR checkcif, and no significant alerts were found.

Results and discussions

Design and synthesis.

Molecules from the rylene family with octa-and tetra-methyl substitutions were synthesised to understand the impact of varying rigid cores and the substitutions on the crystal packing.

Structural characterization by Single-crystal X-ray diffraction.

The synthesized molecules were recrystallized by slow evaporation, mostly in the solvent mixture of DCM: Heptane (3:7), and the crystals obtained were selected for single crystal X-ray diffraction (SCXRD) analysis. Hereby, we report the crystal structure analysis of five rylene molecules and an attempt to understand the crystal packing behavioural trend with increased aromatic core and the introduction of tetra- and octa-methyl group substitutions.

Octamethyl Naphthalene (OMN): Single crystals with thick block-like morphology obtained by recrystallization were selected for data collection by SCXRD. The structure was resolved in a monoclinic space group $P2_1/n$ with half molecule in the asymmetric unit. Analysis of the crystal packing revealed that the molecules are present in a *T*-

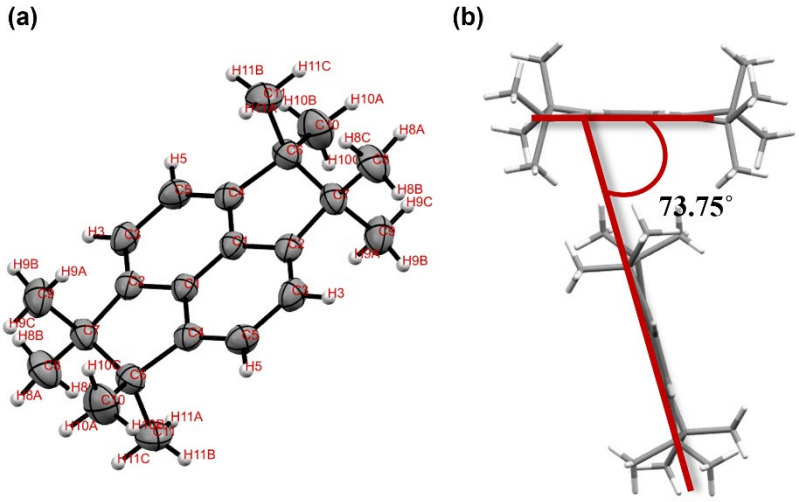

Figure 2 (a) ORTEP figure of OMN molecule and (b) herringbone angle of 73.75˚

shape like a herringbone motif; however, it cannot be regarded as the 'traditional herringbone' since the herringbone motif is typically formed by the edge-to-face C—H···π interaction with C—H being the atoms of the aromatic core. In our case of OMN crystals, the C—H atoms of the terminal methyl substituents are involved in the interaction with the π-cloud of the aromatic core. The angle between the two closest

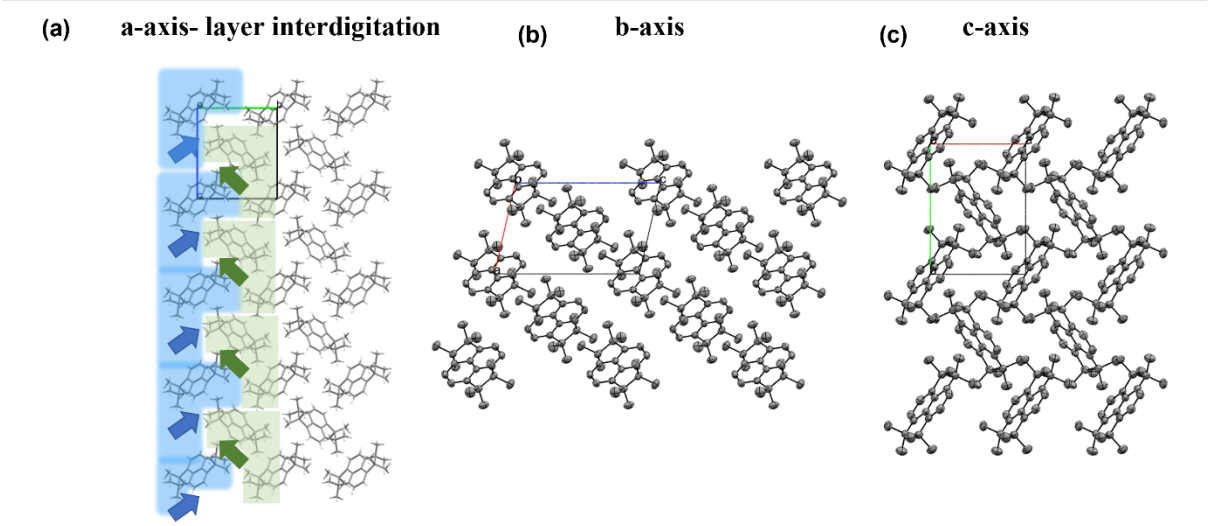

Figure 3 Packing of OMN in a, b, and c axis. (a) shows the layer topology and interdigitated molecules inside a-axis

neighbouring molecules (in the *T*-shape) is 73.75° (Figure 2b) and the core-tilt angle is 29.4˚. The molecules involved in the π-stacking direction are shifted in both x- and y-axis, exhibiting pitch and roll angles of 32.2˚ and 46.5˚, respectively (Table 2). The molecule packs in interdigitated fashion with 1D tapes along a-axis organised in an antiparallel arrangement (Figure 3a). The intermolecular interactions calculated by mercury software were found to be quite isotropic with -28.7 and -22.0 kJ/mol (Figure 14).[18,19]

Octamethyl perylene (OMP): Recrystallization of OMP molecule resulted in concomitant polymorphs with different morphologies, namely OMP-I, with 3D block-

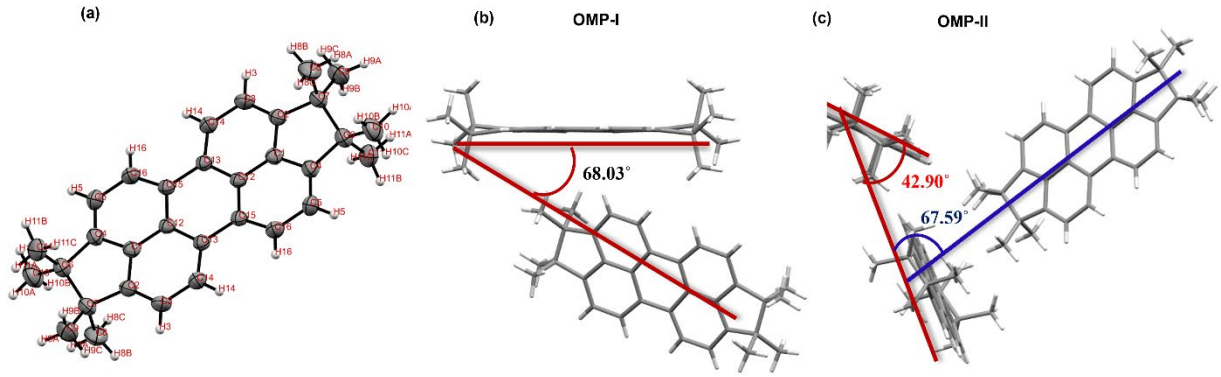

Figure 4 (a) ORTEP figure of OMP molecule (b) herringbone angle in OMP-I, and (c) intralayer (red) and interlayer (blue) herringbone angles in OMP-II.

like morphology and OMP-II, with needle-like morphology.

OMP-I. The structure from the SCXRD collection of OMP-I was resolved in a monoclinic space group $P2_1/c$ with half molecule in the asymmetric unit. This polymorph shows a herringbone packing by the interaction of terminal methyl group C—H with the π-cloud of the aromatic core, and the angle between the two molecules is 68.03° (Figure 4b). The tilt angle decreased to 28.1˚ compared to OMN, while the pitch angle increased significantly from OMN to OMP (P= 63.8˚ and R= 39.9˚). From the molecular packing, we can clearly see the 1D tapes forming layers arranged in an antiparallel fashion along the a-axis, like in OMN (Figure 5a). The unified intermolecular potential values are higher in the direction of the herringbone (-46.2 kJ/mol) than in the π-stacking direction (-22.6 kJ/mol) (Figure 14).

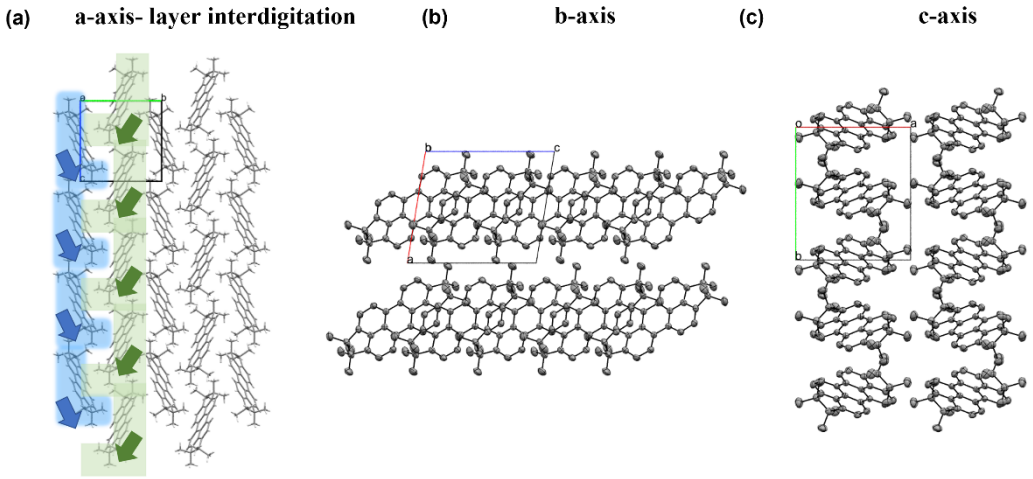

Figure 5 Packing of OMP-I in a, b, and c axis. (a) shows the layer topology and interdigitated molecules inside a-axis

OMP-II. The crystal of OMP-II was observed only once by recrystallization from DCM: Heptane solution (1 mg ml^{-1}). Because of this low frequency of appearance of OMP-II, minor stability with respect to OMP-I was supposed. The structure of OMP-II was resolved in P*bca* space group with half molecule in the asymmetric unit. This polymorph exhibits two kinds of herringbone packing motifs, intralayer and interlayer, with an angle of 42.90° and 67.59° (indicated by different colours in Figure 4c), respectively. The intermolecular potential value does not follow OMP-I, as the strongest interaction is present in the π-stacking direction (-37.2 kJ/mol) while in the herringbone direction, the interaction potential was found to be -28.5 kJ/mol (Figure 14).

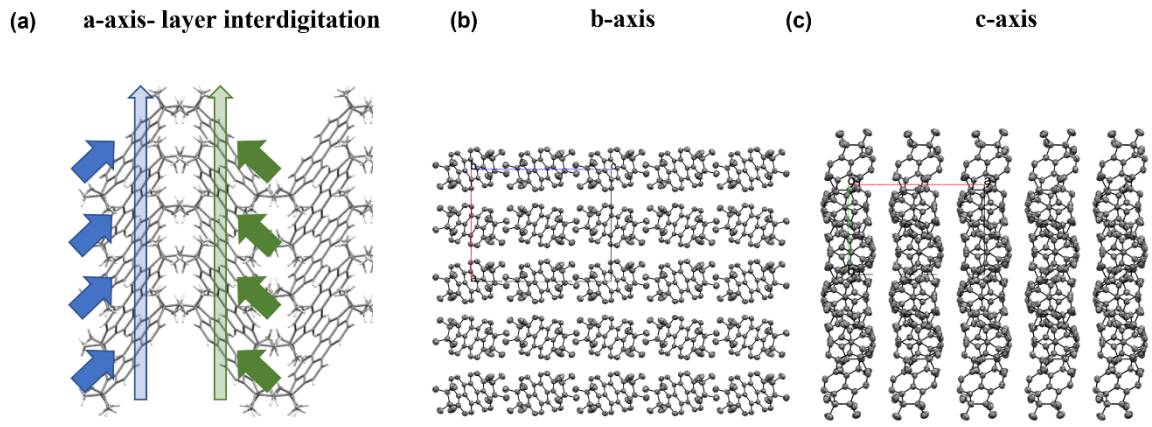

Figure 6 Packing of OMP-II in a, b, and c axis. (a) shows the layer topology and interdigitated molecules inside a-axis

Octamethyl Terrylene (OMT): OMT was recrystallized by slow evaporation in chloroform. Even though the crystals were not qualitatively ideal, and the morphology was found to be very thin needles, suitable crystals were selected, and SCXRD was measured at 298 K, 160 K, and 100 K and data reduction was performed, and finally, we were able to solve the structure of all the temperatures. The best quality data was observed at 160 K, and the solution led to a low R-factor of 4.8%, and this data has been used further to analyse the structural properties. OMT was resolved in a monoclinic space group with $P2_1/n$ with half molecule in the asymmetric unit. The crystals were found to be disordered at all temperatures. The disorder is present in the terminal methyl groups and the end-carbon atoms of the ring to which the methyl groups are attached. The disordered atoms were defined over two sites, each with 0.5:0.5 occupancies.

The packing analysis reveals that OMT exists in a non-classical herringbone packing with π- π overlap between neighbouring molecules. Yet again, like OMN and OMP, the OMT molecules involved in the herringbone are connected by the C—H of terminal methyl groups of one molecule to the π-cloud of the other with an angle of 57.74° (Figure 7b). It was observed that OMT showcased the least core-tilt angle of 22.7˚. The core-tilt angle decreased systematically from OMN> OMP-I> OMT (29.4˚>28.1˚>22.7˚) as the number of aromatic rings increased in these molecules. OMT exhibits high pitch and roll angles of 65.8˚ and 70.1˚, respectively, indicating that the two molecules in π-stacking were shifted with great extent. Significant systematic increase in pitch angles

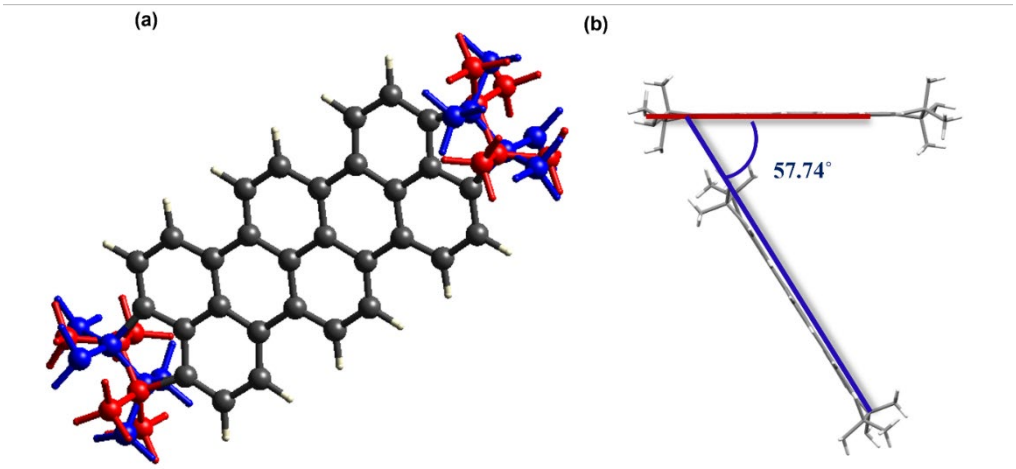

Figure 7 (a) OMT molecule with disorder represented in red and blue colours (b) interlayer herringbone angle of 57.74˚

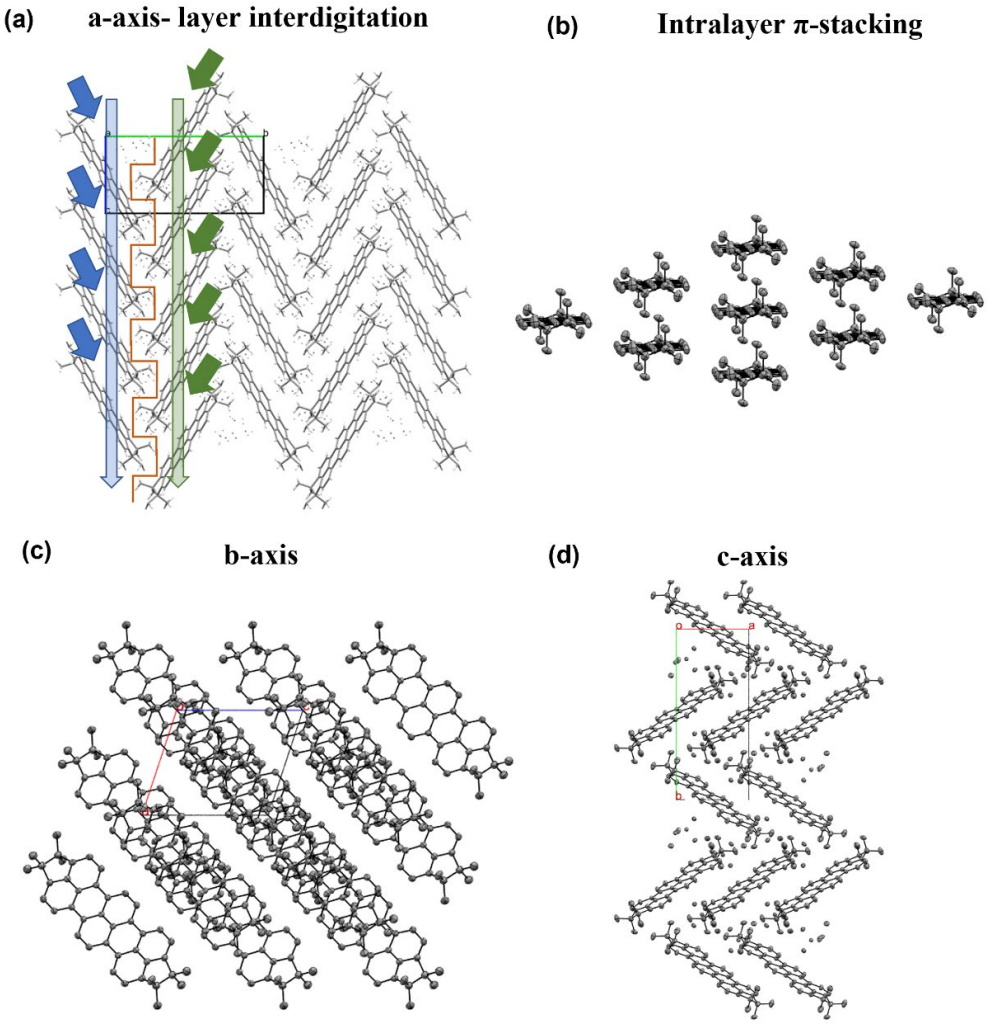

Figure 8 Packing of OMT (a) shows the layer topology and interdigitated molecules inside a-axis (b) interlayer pi-stacking, and (c) and (d) shows packing along b and c axes, respectively.

from OMN<OMP-I<OMT was observed. Pitch angle distortions typically retain large intermolecular spatial overlaps, whereas roll angle inclinations ≥45° essentially destroy overlap between the π-orbitals of adjacent molecules.

Looking at the unified intermolecular potential contributions, we can observe that the strongest intermolecular interactions are present in the π-stacking directions (-51.5 and -39.8 kJ/mol) while in the herringbone direction, the intermolecular energies are a bit lower (-34.9 kJ/mol) indicating predominance of π- π stacking (Figure 14).

Tetramethyl Naphthalene (TMN): The structure of TMN was resolved in a monoclinic space group $P2_1/n$ with one full molecule in the asymmetric unit cell. The molecule

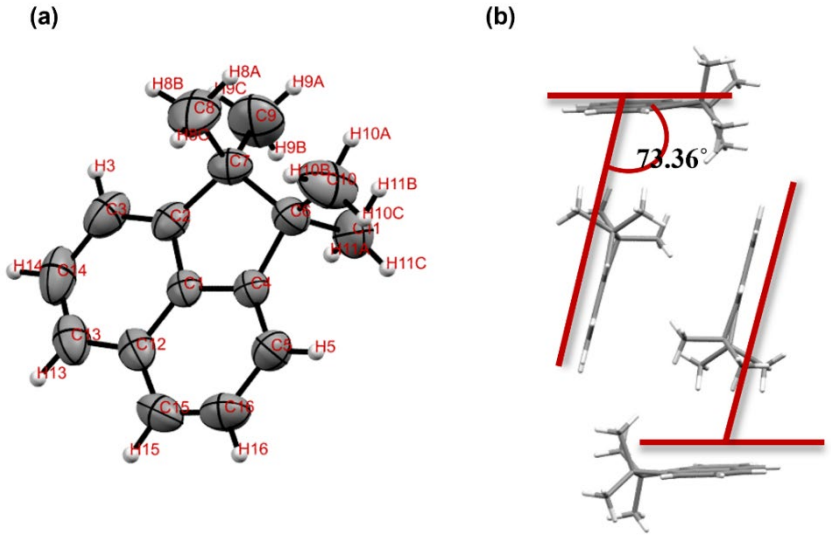

Figure 9 (a) ORTEP figure of TMN molecule and (b) herringbone angle of 73.36˚ in the sandwiched herringbones motif.

exhibits a sandwich herringbone packing, with a herringbone angle of 73.36° (Figure 9b). This packing arises due to the formation of dimers arranged in the reverse fashion with methyl groups facing opposite directions to minimize the steric hindrance (Figure 10a).

The crystal packing of TMN confirms our hypothesis that asymmetric substitution on small aromatic cores like naphthalene might result in the formation of dimers and sandwiched herringbone motif, as it is evident that mono substitution is not sufficient to break the dimer formation. Therefore, we attempted to tune the packing by crystal engineering for better charge transport properties by introducing larger aromatic cores and symmetric substitution of the methyl groups.

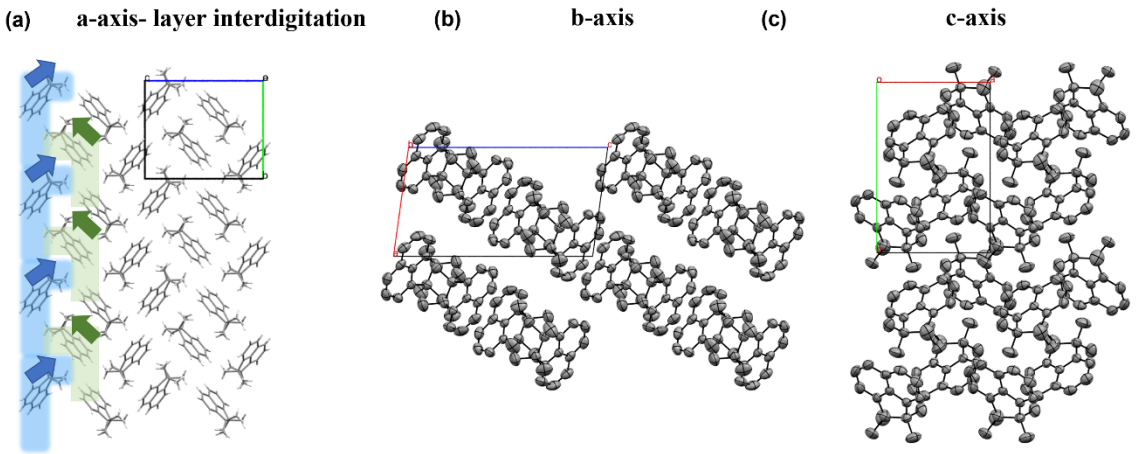

Figure 10 Packing of TMN a, b, and c axis. (a) shows the layer topology and interdigitated molecules inside a-axis.

The naphthalene core in TMN was observed to be slightly tilted by around 16˚. The final pitch and roll angle values, were found to be 28.1˚ and 4.8˚, respectively, indicating larger molecular slipping along x-axis compared to the y-axis

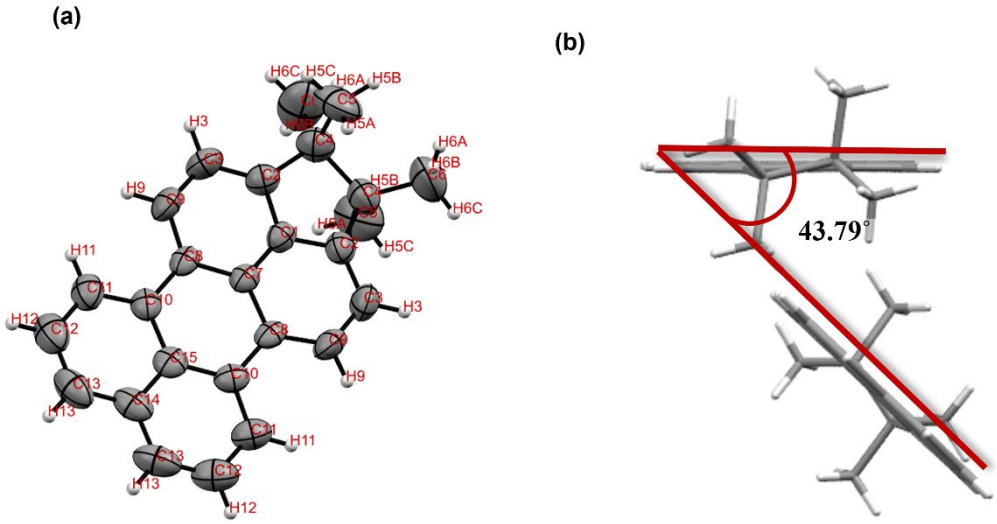

Figure 11 (a) ORTEP figure of TMP molecule and (b) herringbone angle 43.79°

Tetramethyl Perylene (TMP): The data collection of TMP resulted in an orthorhombic space group $P2_12_12$ with half molecule in the asymmetric unit. It is interesting to note that the asymmetric unit in the TMP molecule lies on the two-fold axis, unlike the other systems where usually the asymmetric unit lies on the inversion centre. TMP forms layers, but the molecules in a layer are shifted along the long axis (Figure 12a). The molecules at different depths along the long molecular axis are arranged in a face-to-

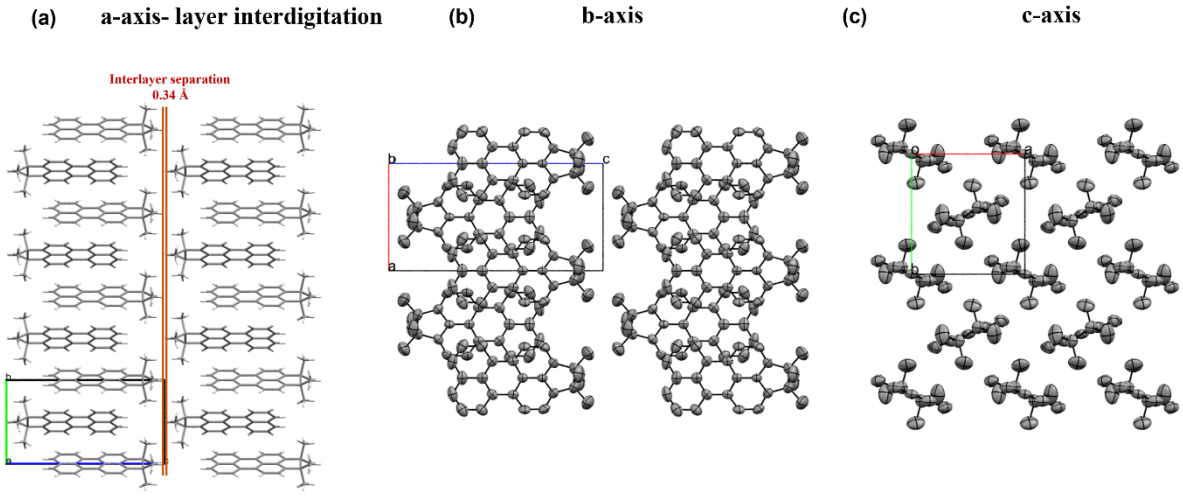

Figure 12 Packing of TMP a, b, and c axis. (a) shows the layer topology and layer separation inside a-axis

edge fashion forming a typical herringbone packing motif with a herringbone angle of 43.79° (Figure 11b). The further analysis illustrates that the molecule stands upright with the core-tilt angle of 0˚. This is also evident from the interplanar distance (d-spacing), which is equal to the length of the c-axis. Interestingly, it is worth noting that there is no molecular slipping along the axis, implying the pitch angle to be 0˚, which seems to be compensated by the large roll angle of 68.1˚. The large roll angle indicates that overlap between the π-orbitals of adjacent molecules is destroyed.

The intermolecular potential is -48.4 kJ/mol in the herringbone direction, while almost half (-26.8 kJ/mol) is in the π-stacking direction (Figure 14).

Tetramethyl Terrylene (TMT): Despite several attempts, it was not possible to grow single crystals of TMT with sufficient quality to allow the elucidation of its crystal structure. The measurement will be performed once suitable crystals of TMT are formed.

Table 1 Cell parameters of all the crystal systems

Parameters	**OMN**	**OMP**		**OMT**	**TMN**	**TMP**
		Form I	**Form II**			
Formula	$C_{22}H_{28}$	$C_{16}H_{16}$		$C_{42}H_{36}$	$C_{16}H_{18}$	$C_{26}H_{22}$
Molecular weight (g.mol^{-1})	292.44	208.29		538.99	210.30	334.459
Temperature (K)	293	293		160	293	293
Crystal system	Monoclinic	Monoclinic	Orthorhombic	Monoclinic	Monoclinic	Orthorhombic
Space group	*P 2$_1$/n*	*P 2$_1$*/c (14)	*Pbca* (62)	*P 2$_1$/n*	*P 2$_1$/n*	*P2$_1$2$_1$2* (18)
a (Å)	7.6046(6)	9.6846(5)	14.112(2)	8.41240(10)	7.7744(7)	7.5439(8)
b (Å)	10.1262(9)	11.0235(7)	9.306(2)	18.7148(2)	11.5631(7)	7.9920(12)
c (Å)	11.8110(9)	11.0493(6)	17.683(4)	9.59720(10)	14.0906(10)	15.094(3)
β (°)	103.015(7)	9.257(5)	90	108.2790(10)	97.887(7)	90
V (Å^3)	886.15	1164.24 (12)	2322.2(8)	1434.71(3)	1254.71(16)	910.03

Z/Z'	2/0.5	4/0.5	8/0.5	2/0.5	4/1	2/0.5
Density ($g \cdot cm^{-3}$)	1.096	1.188	1.192	1.248	1.113	1.220
F (000)	320	448	896	572	456	356
μ (mm^{-1})	0.061	0.067	0.067	0.530	0.062	0.069
GOF on F^2	0.679	0.910	0.939	1.057	1.034	1.067
R_1 (on F, $I>2\sigma(I)/R_{ex}$	0.0585	0.0830	0.0910	0.0480	0.0819	0.0787
WR_2 (F^2 all data) R_{wp}	0.1469	0.1992	0.1843	0.1494	0.2204	0.1739

Comparison with packing descriptors: For a refined and elaborative understanding of the molecular packing arrangement, we studied the packing descriptors that might describe the core in a wider aspect. The crystal structures and all the features can be elaborately described by two kinds of descriptors: crystallographic and packing parameters.[20] The crystallographic parameters include space group, cell parameters, the volume of the cell, multiplicity, asymmetric unit, and the temperature of data collection. All these crystallographic parameters for our systems have been discussed above (Table 1). Packing descriptors are the variables describing the stacking arrangement, for example, the distance between the centroids of the aromatic cores

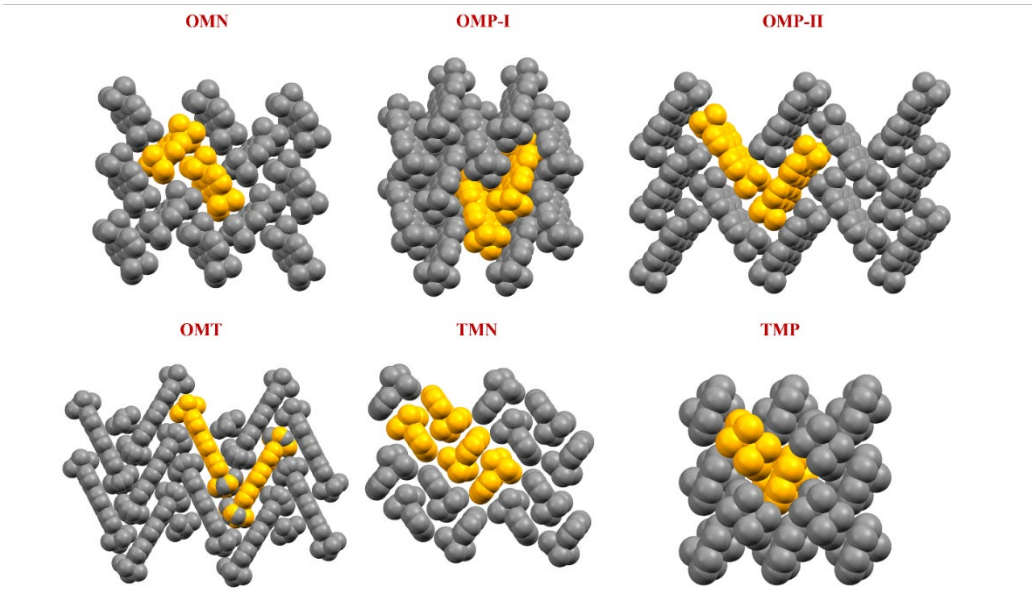

Figure 13 Space fill packing highlighting the herringbone motifs in all the molecules.

(SV), the interplanar distance between the aromatic planes (dπ-π), the displacement of the aromatic units along the long (χ) and short (ψ) molecular axis; the directions cosines of the SV (Δx with the x-axis and Δy with the y-axis); the angles of the aromatic unit slipping along the x (pitch)- and y (roll)-direction (P and R, respectively) (see Table 2). All the descriptors can be later combined to result in a multivariate Principle Component Analysis (PCA), which helps in viewing and comparing multiple variables at the same time to find a correlation between packing arrangements, which can render guidelines for predicting the likely packing families or clusters depending on the substituents used.

From the analysis of packing parameters, we observe a cumulative trend in the core-tilt angle which decreases from OMN>OMP-I>OMT>TMN>TMP. Other trends observed can be separated into two groups of octa-and tetra-methyl substitutions. For example, the herringbone angle is observed to decrease from OMN>OMP>OMT and similarly TMN>TMP, indicating that the face-to-edge intermolecular interactions can potentially increase with the increasing number of rings in the core. Pitch angles are found to increase from OMN<OMP-I<OMT, which shows that the molecules in the π-direction are facing more slippage in x-axis; while pitch angle decreases from TMN>TMP, where in TMP there is absolutely no slippage in x-axis. However, it would be more precise to analyse the true nature of these trends along with the last molecule of the series – TMT, which we expect to report in the future work once the crystal structure is obtained.

Table 2 Packing descriptors of selected molecules.

Descriptors	**OMN**	**OMP- I**	**OMP- II**	**OMT**	**TMN**	**TMP**
HB (°)	73.8	68.0	67.6	57.7	73.4	43.8
Core-tilt angle (°)	29.4	28.1	33.8	22.7	16.1	0
Stacking dist. (Å)	7.6	11.1	9.3	9.6	5.834	7.5
Interplanar distance, d(Å)	4.8	4.6	5.2	2.6	5.135	2.8

χ (°)	66.6	32.3	34.7	52.4	62.0	90
Ψ (°)	48.3	69.8	83.0	41.6	85.8	22.7
Δ x	3.0	9.3	7.7	5.8	2.74	0
Δ y	5.1	3.8	1.2	7.2	0.4	7.0
Pitch (°)	32.2	63.9	55.9	65.8	28.1	0
Roll angle (°)	46.5	39.9	12.4	70.1	4.8	68.1

Conclusions

In summary, we have systematically outlined a thorough crystal structure study of a series of polynuclear aromatic hydrocarbons. We examined different systems with variations in molecular size, shape, and substitutions. It was observed that the

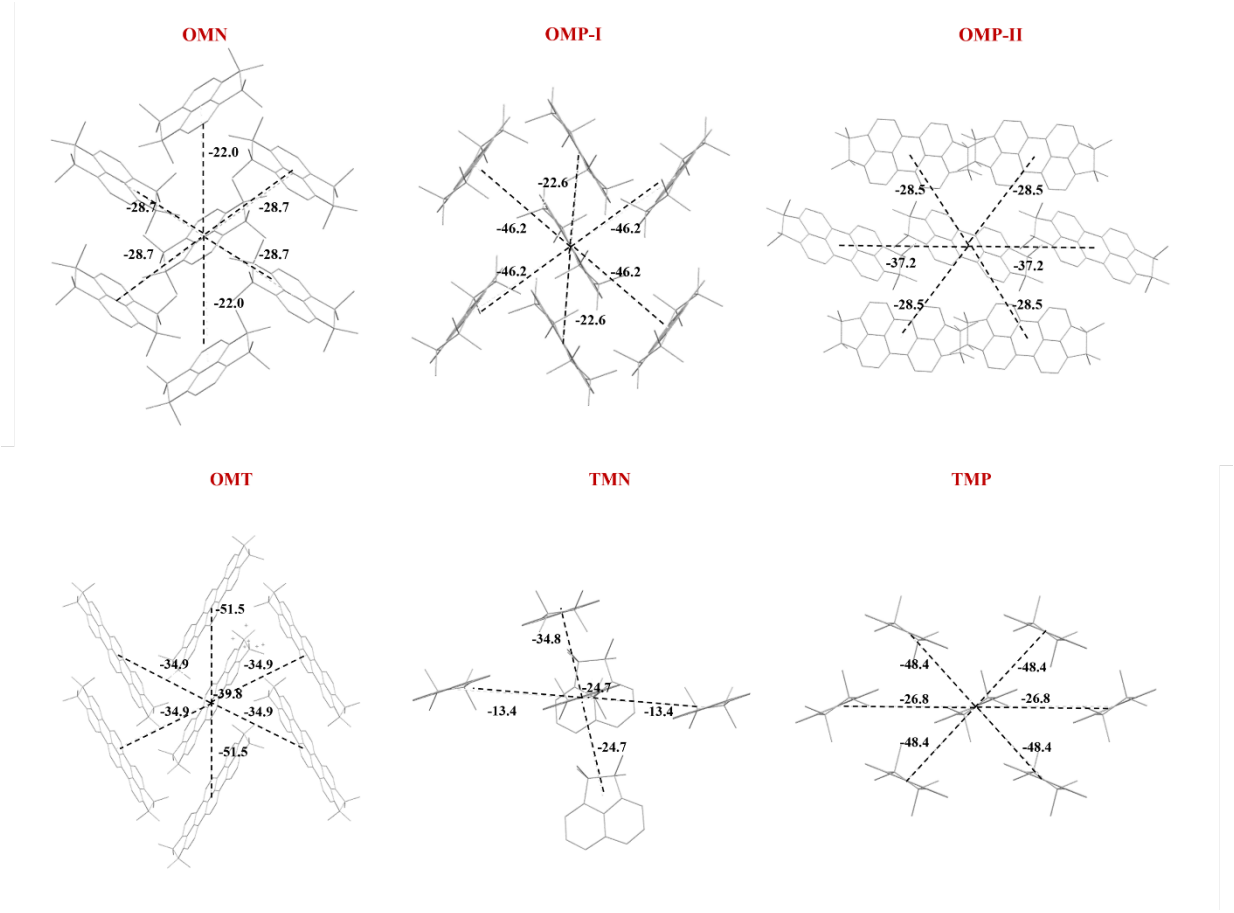

Figure 14 Unified intermolecular potentials (kJ/mol) of all the molecules, calculated by mercury software.

molecular packing behaviour is significantly impacted by the number of aromatic rings and whether the substitution is symmetric or asymmetric. It is pre-established that typically naphthalene, perylene, and terrylene molecules crystallise into sandwiched herringbone by the formation of dimers.[12] Crystal engineering was done by the introduction of peripheral methyl groups that might influence the monomer-driven crystal packing for better electrical performances.

Beginning from the symmetrical substitution and increasing the aromatic core size from naphthalene to perylene to terrylene, we observed a non-classical herringbone packing motif. The non-classical term was used since the *T*-shape of the herringbone is present. However, supramolecular interactions exist between the methyl C—H with the π-electron cloud. We witnessed this packing in all the symmetrically substituted molecules. It was also interesting to note that two crystal forms were obtained for the OMP molecule, and in OMP-II, there two herringbone motifs were present- both intralayer and interlayer. In contrast, the OMT resulted in interlayer herringbone with intralayer π-π stacking. Ultimately, we succeeded in achieving monomer packing by symmetrical substitution.

We further attempted to study the impact on the crystal packing by asymmetric substitution of methyl groups. However, we discovered that asymmetric substitution in the naphthalene aromatic core led to the formation of dimers, packing in sandwiched herringbone motif. By increasing the number of aromatic carbons in TMP, the molecules were found to be arranged in traditional herringbone packing. Thus, we can conclude that asymmetric substitution and sufficient aromatic rings in the core together promote better/desired packing amongst all the systems by arranging the neighbouring molecules in a head-to-toe manner.

From molecule-based organic chemistry to supramolecule-based crystal engineering, it is evident that the crystal packing arrangement of a molecule is driven by geometrical notions in a chemical context. The goal was set to understand and tailor the crystal packing by effective design strategies. We studied a family of rylene molecules, and

our results established that these molecules were engineered to attain the desired packing for potential electrical applications in the future.

References

1 G. R. Desiraju, *Curr. Opin. Solid State Mater. Sci.*, 1997, **2**, 451–454.
2 C. Wang, H. Dong, H. Li, H. Zhao, Q. Meng and W. Hu, *Cryst. Growth De.s*, 2010, **10**, 4155–4160.
3 R. Taylor, *CrystEngComm.*, 2014, **16**, 6852–6865.
4 G. R. Desiraju, *J. Chem. Sci.,* 2010, **122**, 667–675.
5 A. Nangia and G. R. Desiraju, in *Design of Organic Solids*, eds. E. Weber, Y. Aoyama, M. R. Caira, G. R. Desiraju, J. P. Glusker, A. D. Hamilton, R. E. Meléndez and A. Nangia, Springer Berlin Heidelberg, Berlin, Heidelberg, 1998, pp. 57–95.
6 M. Waqas Alam, M. Farhan, B. Souayeh, M. Aamir and M. S. Khan, *Crystals (Basel)*, 2021, **11**, 1070.
7 C. C. Mattheus, G. A. de Wijs, R. A. de Groot and T. T. M. Palstra, *J. Am. Chem. Soc.*, 2003, **125**, 6323–6330.
8 V. C. Sundar, J. Zaumseil, V. Podzorov, E. Menard, R. L. Willett, T. Someya, M. E. Gershenson and J. A. Rogers, *Science (1979)*, 2004, **303**, 1644–1646.
9 F. Cozzi, S. Bacchi, G. Filippini, T. Pilati and A. Gavezzotti, *Chem. Eur. J.*, 2007, **13**, 7177–7184.
10 H. C. Montgomery, J. H. Schön, C. Kloc and B. Batlogg, *J. Am. Chem. Soc*, 2001, **123**, 9482–9483.
11 H. Minemawari, M. Tanaka, S. Tsuzuki, S. Inoue, T. Yamada, R. Kumai, Y. Shimoi and T. Hasegawa, *Chem. Mater.*2017, **29**, 1245–1254.
12 G. R. Desiraju and A. Gavezzotti, *Acta. Crystallogr. B.,* 1989, **45**, 473–482.
13 C. L. Hall, I. Andrusenko, J. Potticary, S. Gao, X. Liu, W. Schmidt, N. Marom, E. Mugnaioli, M. Gemmi and S. R. Hall, *ChemPhysChem.*, 2021, **22**, 1631–1637.
14 A. Pick, M. Klues, A. Rinn, K. Harms, S. Chatterjee and G. Witte, *Cryst. Growth Des.*, 2015, **15**, 5495–5504.
15 P. Pandey, N. Demitri, L. Gigli, A. M. James, F. Devaux, Y. H. Geerts, E. Modena and L. Maini, *Cryst. Growth Des.*, 2022, **22**, 1680–1690.
16 C. F. MacRae, I. Sovago, S. J. Cottrell, P. T. A. Galek, P. McCabe, E. Pidcock, M. Platings, G. P. Shields, J. S. Stevens, M. Towler and P. A. Wood, *J. Appl. Crystallogr.*, 2020, **53**, 226–235.
17 C. F. Macrae, I. J. Bruno, J. A. Chisholm, P. R. Edgington, P. McCabe, E. Pidcock, L. Rodriguez-Monge, R. Taylor, J. van de Streek and P. A. Wood, *J. Appl. Crystallogr.*, 2008, **41**, 466–470.
18 A. Gavezzotti and G. Filippini, *J. Phys. Chem.*, 1994, **98**, 4831–4837.
19 A. Gavezzotti, *Acc. Chem. Res.*, 1994, **27**, 309–314.
20 M. D. Curtis, J. Cao and J. W. Kampf, *J. Am. Chem. Soc.*, 2004, **126**, 4318–4328.

Chapter 7

Conclusions and Outlook

Conclusions and Outlook

The overall goal of this thesis was the study of polymorphism of organic semiconductors (OSCs) like [1]Benzothieno[3,2-b][1]benzothiophene (BTBT) derivatives.

From the initial study of bulk polymorphism, I discovered several polymorphs for some compounds, confirming that the molecule's ability to self-assemble into different packing arrangements can vary from molecule to molecule. It was observed that multiple parameters like the method of crystallization, the peripheral chains attached to the core, the type of substrate used (if any), temperature, pressure, and the role of solvent, strongly influence the emergence of different polymorphs.

During this Ph.D., I acquired adequate skills and competence in polymorphic investigation and solid-state characterizations like single-crystal X-ray diffraction (SC-XRD), variable-temperature X-ray diffraction (VT-XRD) and capillary transmission X-ray diffraction. I learnt to perform comprehensive analysis on the crystallographic features of obtained crystal phases. I also successfully submitted a proposal (ID proposal 20201790) to the PSI synchrotron for the MS-X04SA beamline and I was able to collect and analyse the data at the beginning of 2021.

In the framework of UHMob project, I did my first secondment in ULB to explore the utility of thermal gradient technique for obtaining polymorphs under non-equilibrium conditions. The results obtained from thermal gradient crystallization experiments highlighted the ability of this technique for achieving preferentially aligned crystals along the thermal gradient direction based on the nucleation rate, undercooling, maximal growth rate, and adequate gradient parameters.

The second secondment was planned to learn solution-shearing technique for OFET fabrication. I explored multiple parameters for achieving the optimum conditions to get improved device performance. The electrical properties in terms of charge carrier mobility were assessed for two OSC molecules discussed in Chapter 3 and 4.

The UHMob project also promoted networking and collaborations amongst the early-stage-researchers (ESRs). As a result of which, I also received contribution from the some ESRs in

the projects – Nemo McIntosh, Marco Bardini, Nicholas Turetta and Lamiaa Fijahi (Chapter 3 and 4). Likewise, I also collaborated to contribute for solving and analysing several crystal structures for other ESR – Rahul Meena, as discussed in Chapter 6.

The experimental activity reported in this thesis was targeted at contributing to addressing the key role of polymorphism and crystal structure in organic electronics. As the strategic design of OSC is fundamental, the detailed study of polymorphs of an OSC and the crystallographic investigation of the phases are also critically significant. It is paramount to identify the different polymorphs that an OSC system can generate as well as the conditions that promote their formation with the goal to control the desired phase isolation. Investigation of polymorphs is a common activity for pharmaceutical compounds (*e.g.,* APIs), while in organic electronics it is still an emerging field. To this end, a multi-technique approach for investigating equilibrium and non-equilibrium polymorphs to understand and harness the structure-property relationships is essential. In this thesis, we strove to recognize the vital role of crystal packings as a consequence of varying the side chains, on the charge transport properties.

In the future, concerted pathways of supramolecular chemistry and crystal engineering to optimize the charge transport in OFETs will help to extend our current understanding of the relationship between a supramolecular solid-state organization and the electronic properties. This thesis finally proposes diverse solutions that enclose all the above-mentioned approaches towards the progress of the field.

APPENDIX A

Discovering Crystal Forms of Novel Molecular Semiconductor OEG-BTBT

Priya Pandey[†§], Nicola Demitri[⊥], Lara Gigli[⊥], Ann Maria James[‖], Félix Devaux[#], Yves Henri Geerts[#‡], Enrico Modena[†], Lucia Maini*[§]

[†]PolyCrystalLine SPA, Via Della Cooperazione, 29 40059 – Medicina (BO) Italy

[§]Dipartimento di Chimica "G. Ciamician", via Selmi 2 −Università di Bologna, I-40126, Bologna, Italy

[⊥]Elettra Sincrotrone Trieste, I-34149 Basovizza, Trieste, Italy

[‖]Institute of Solid-State Physics, Graz University of Technology, 8010 Graz, Austria

[#]Laboratoire de Chimie des Polymères, Faculté des Sciences, Université Libre de Bruxelles (ULB), CP 206/1 Boulevard du Triomphe, 1050, Bruxelles, Belgium

[‡]International Solvay Institutes, Université Libre de Bruxelles (ULB), CP 231 Boulevard du Triomphe, 1050, Bruxelles, Belgium

Table S1 List of Solvents used for solubility screening.

S. No.	Solvents	Soluble (Yes/No)
1	1-Propanol	No
2	2-Butanol	No
3	2-Methoxyethanol	No
4	2-Propanol	No
5	Acetonitrile	No
6	Acetone	No
7	Chloroform	**Yes**
8	Cyclohexanone	**Yes**
9	Dichloromethane	**Yes**
10	1,4-Dioxane	No
11	N,N-Dimethylacetamide	**Yes**
12	N,N-Dimethylformamide	**Yes**
13	Dimethyl Sulfoxide	No
14	Ethyl Acetate	No
15	Ethanol	No
16	Water	No
17	Heptane	No
18	Isopropyl ether	No
19	Methyl ethyl Ketone	No
20	Methanol	No
21	Nitromethane	No
22	Propyl acetate	No
23	p-Xylene	No
24	Tetrahydrofuran	**Yes**
25	Toluene	**Yes**

Table S2 Short contacts list of Form I (RT), Form I (LT) and Form III (LT)

Contacts	Form I (RT)	Form I (LT)	Form III (LT)
C---S	3.416 (6) *(C12---S1)* 3.490 (6) *(C6---S1)*	3.374 (2) *(C12---S1)* 3.441 (2) *(C6---S1)*	3.371 (3) *(C1---S1)* 3.406 (3) *(C4---S1)*

O---H	2.533 *(O3---H12)* 2.673 *(O1---H11)* 2.684 *(O2---H3)*	2.502 *(O3---H12)* 2.549 *(O1---H11)* 2.690 *(O2---H11)* 2.625 *(O2---H3)* 2.709 *(O1---H8)*	2.454 *(O3---H12)* 2.509 *(O1---H11)* 2.596 *(O2---H3)* 2.674 *(O1---H8)* *2.464 (DCM) (O3---H16)*
C---H	-	2.882 *(C3---H4)* 2.889 *(C4---H8)*	2.827 *(C6---H4)* 2.866 *(C3---H6)* 2.891 *(C2---H6)* *2.872 (DCM) (C10---H16)*
C---O	3.18 (1) *(O3---C10)*	3.135 (4) *(O3---C10)*	3.140 (4) *(O3---C10)*

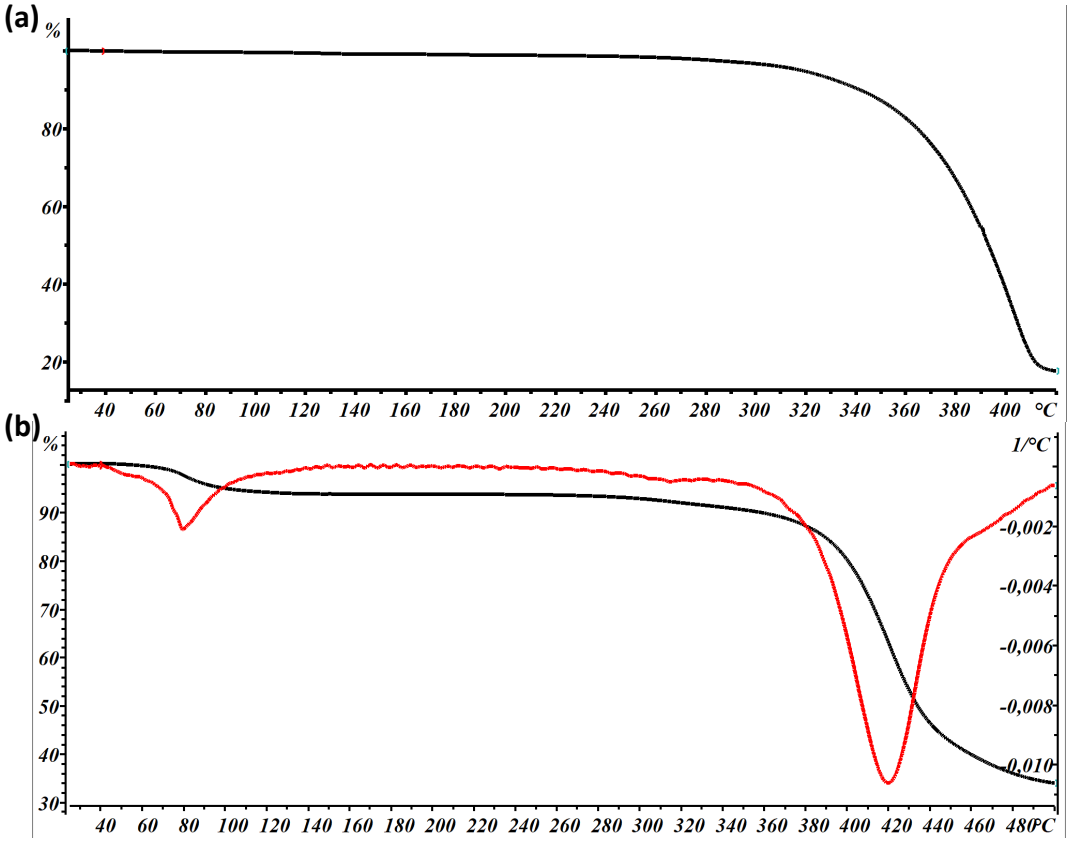

Figure S1 TGA plots of (a) Form I and (b) Form III. The red line in Form III represents the 1st derivative showing solvent loss around 70°C.

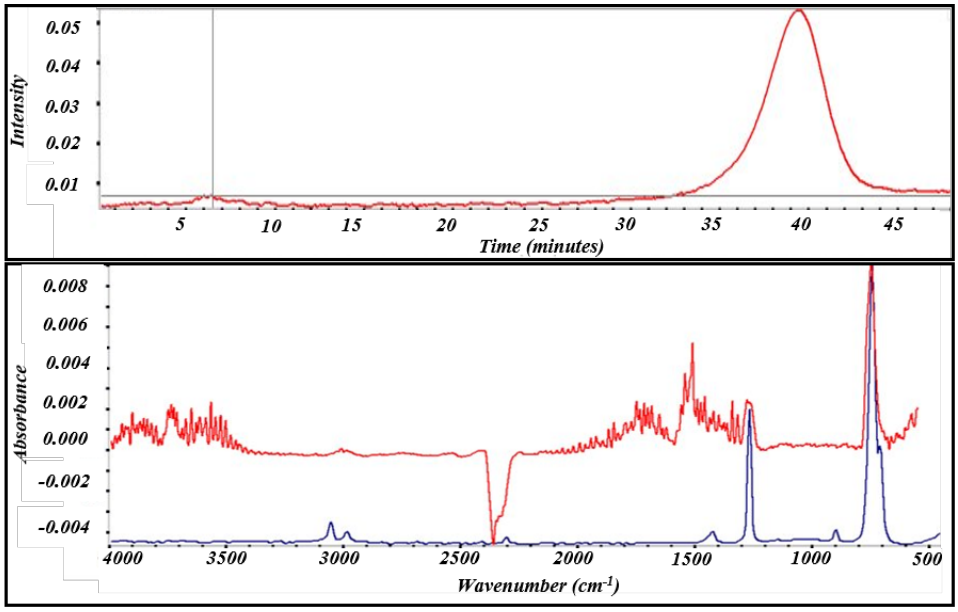

Figure S2 EGA of Form III indicting a loss of DCM at 6.93 minutes and degradation of OEG-BTBT at around 40 minutes

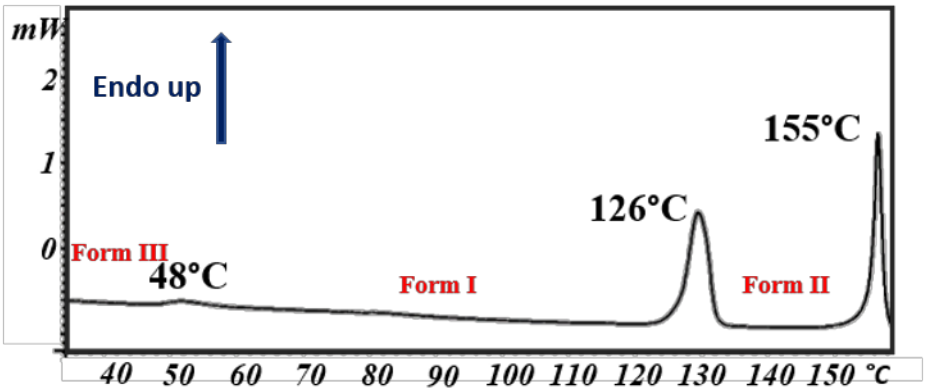

Figure S3 DSC of Form III crystals showing transition from Form III →Form I→Form II followed by melting (onset temperatures indicated; endo UP). The heating rate was 10°C/min.

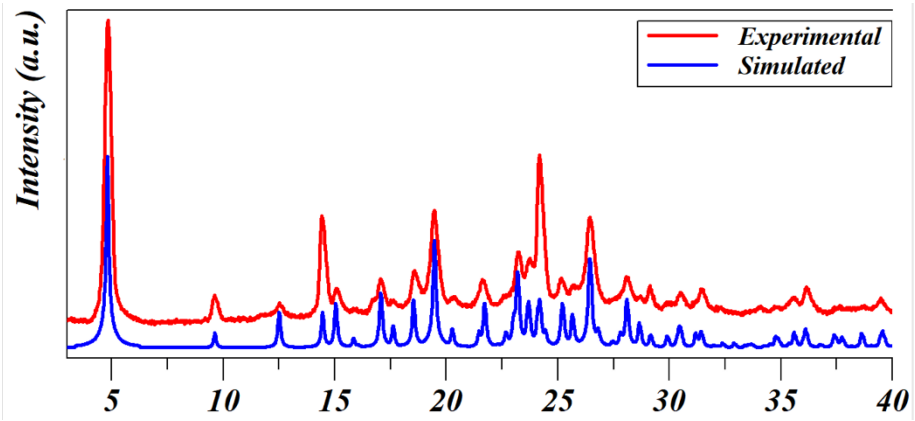

Figure S4 Comparison of simulated and experimental pXRD of bulk Form I

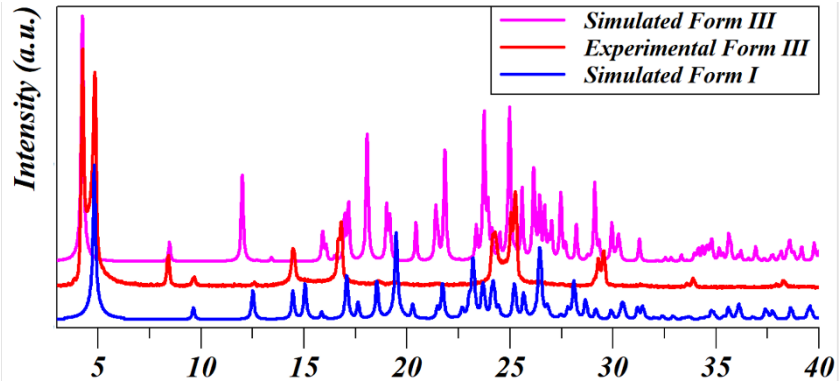

Figure S5 Comparison of Form III experimental pattern with simulated pattern of Form III and Form I, showing that the experimental diffractogram contains the peaks of both Form I and Form III and exists as a mixture.

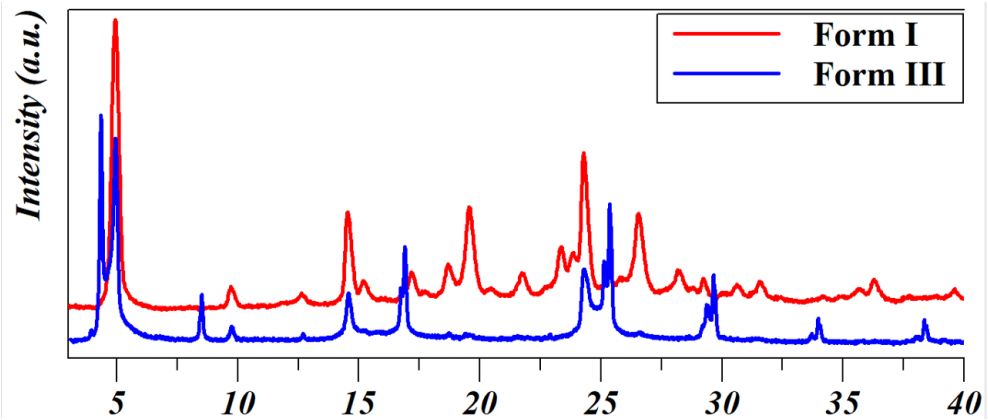

Figure S6 PXRD of Form I (red) and Form III (blue). Form III is a mixture of Form I and Form III (λ=1.54Å)

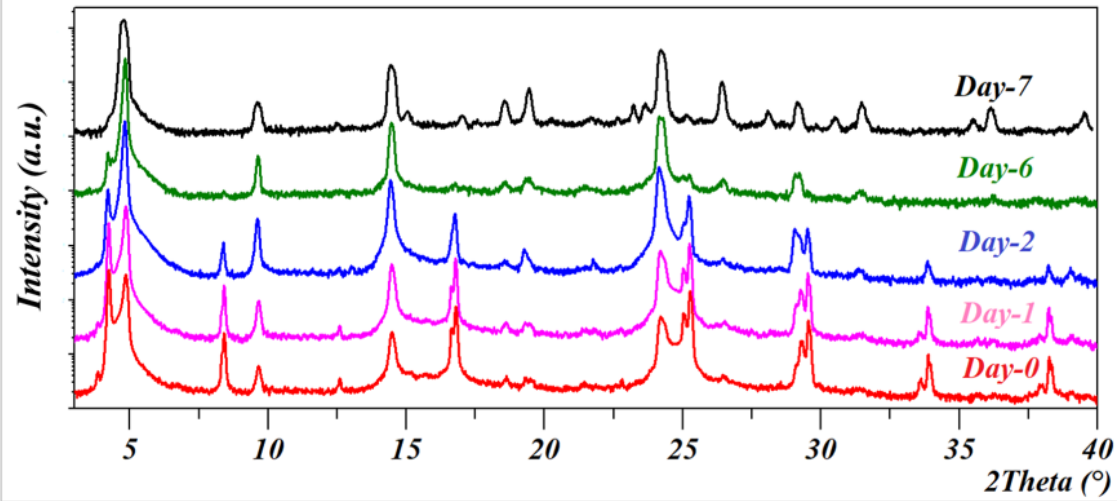

Figure S7 Stability assessment of Form III. Powder XRD of Form III crystals of Day-0 (red), Day-1(Pink), Day-2 (Blue), Day-6 (Green) and Day-7(Black) was measured. (λ=1.54Å) Form III completely converts to Form I in 7 days at room temperature and pressure.

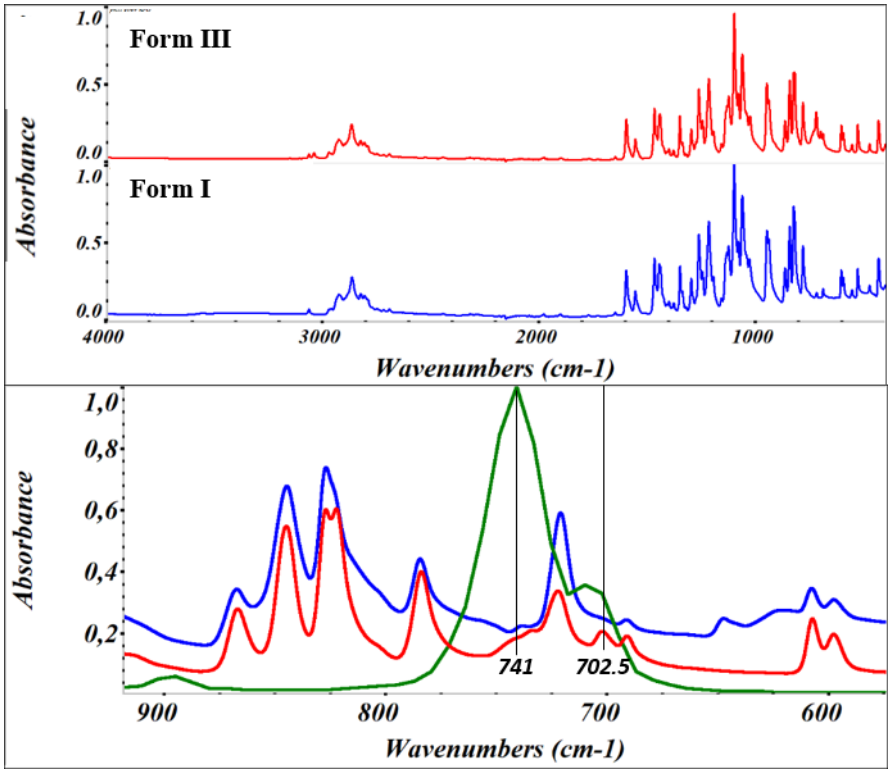

Figure S8 FTIR spectrum of (a) Form I (blue) and Form III (red) and (b) Comparison of both Forms with DCM (Green). Form III shows a shoulder band at 741 cm^{-1} and a band at 702.5 cm^{-1} which is ascribable to the presence of DCM.

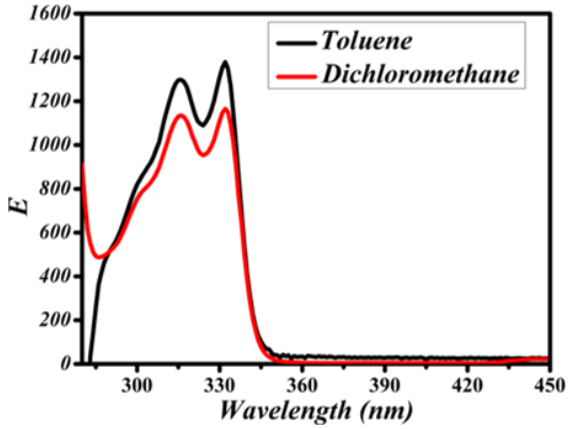

Figure S9 UV spectra of OEG-BTBT in Toluene and dichloromethane solutions

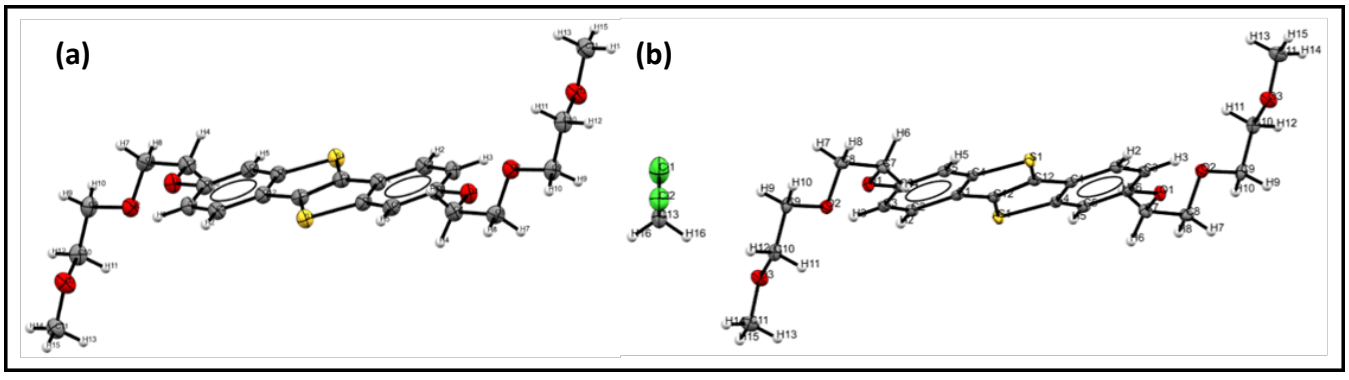

Figure S10 ORTEP ellipsoid representation of OEG-BTBT (a) Form I and (b) Form III

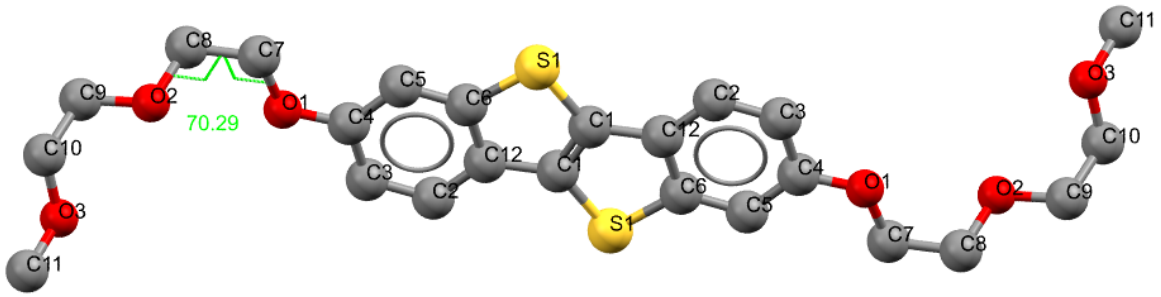

Figure S11 OEG-BTBT Form I (RT) O1-C7-C8-O2 torsion (70.29). Hydrogen atoms are deleted for simplicity.

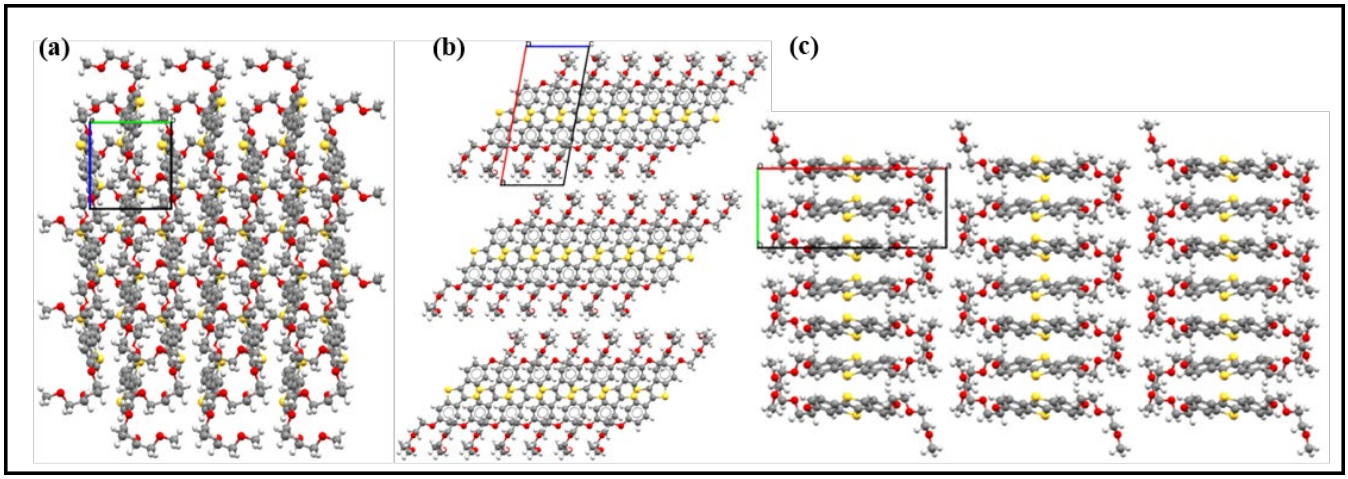

Figure S12 Packing of OEGBTBT Form I along (a) a-axis (b) b-axis and (c) c-axis.

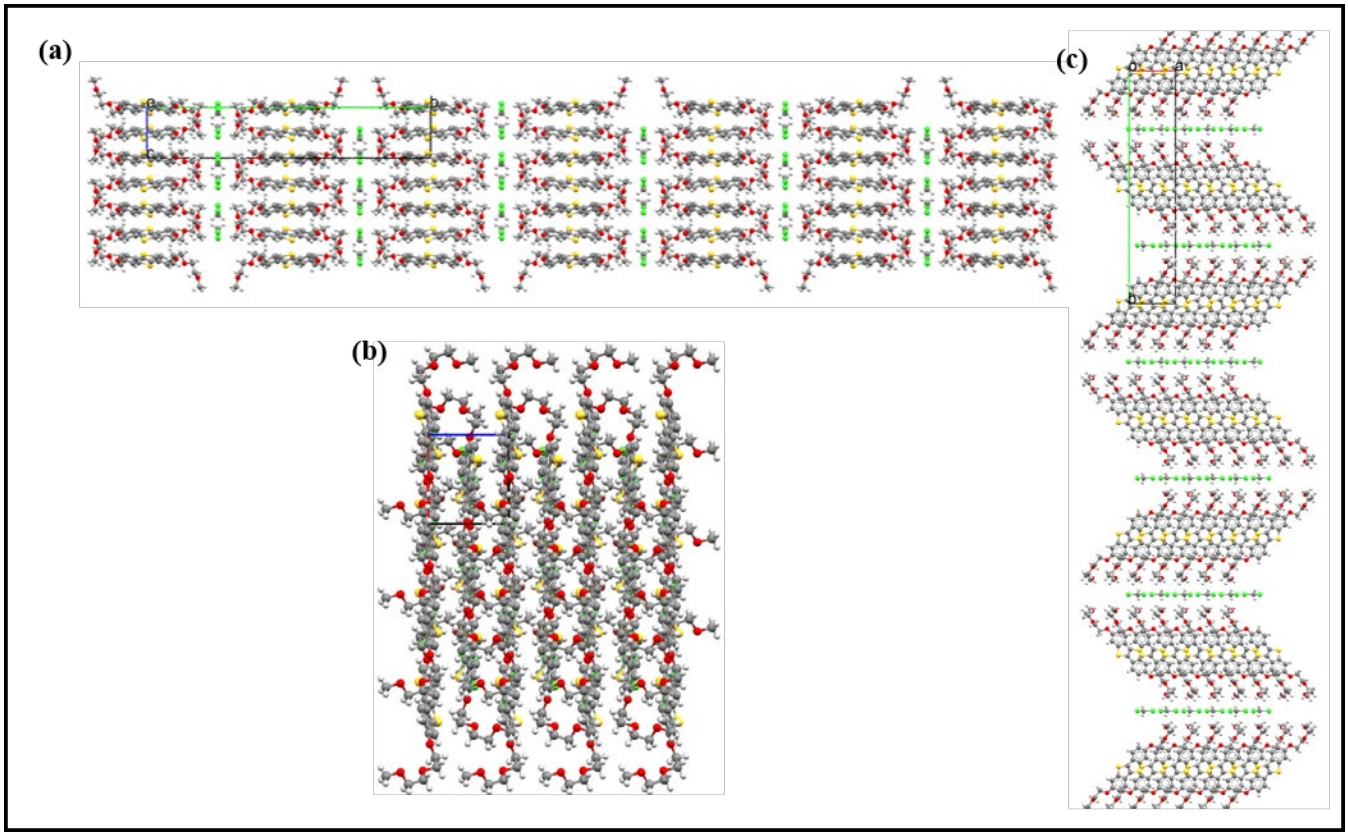

Figure S13 Packing of OEGBTBT Form III along (a) a-axis (b) b-axis and (c) c-axis.

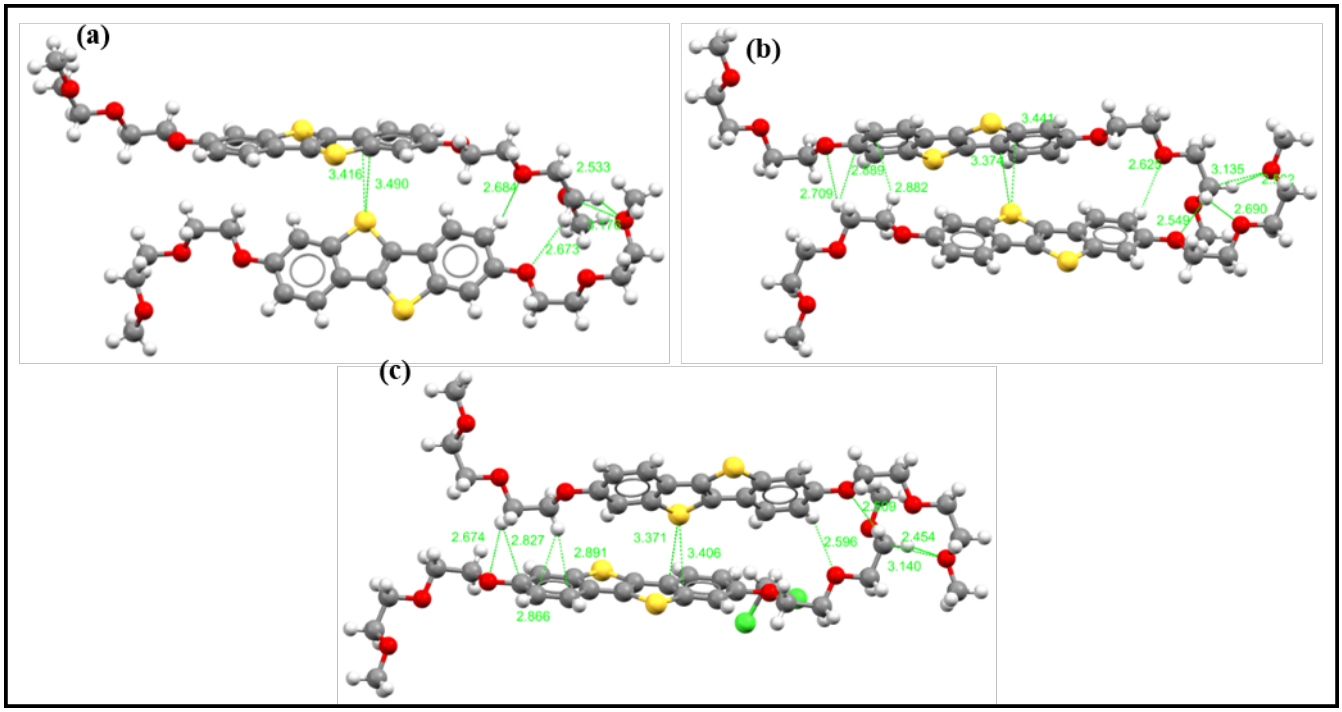

Figure S14 Short contacts of (a) Form I (RT) (b) Form I (LT) and (c) Form III (LT).

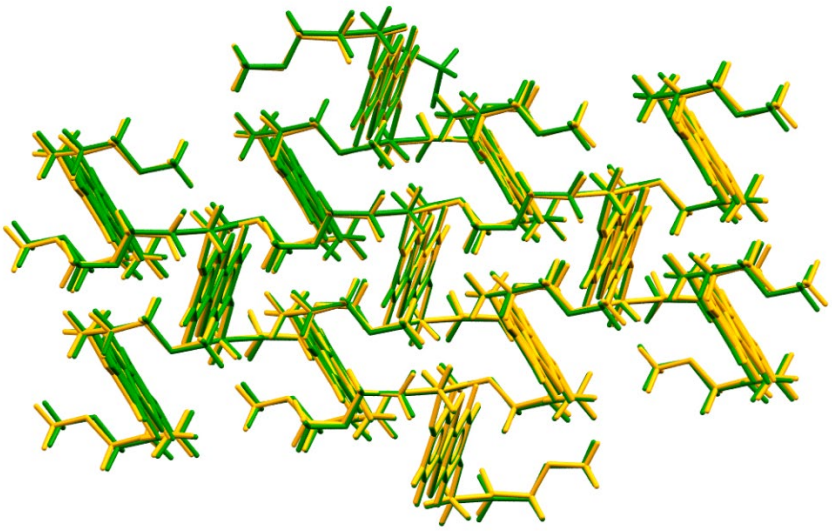

Figure S15 Crystal packing similarity of Form I and Form III with RMSD15 0.141Å. This value is comparable to the RMSD15 of Form I-LT and RT with the value 0.132Å.

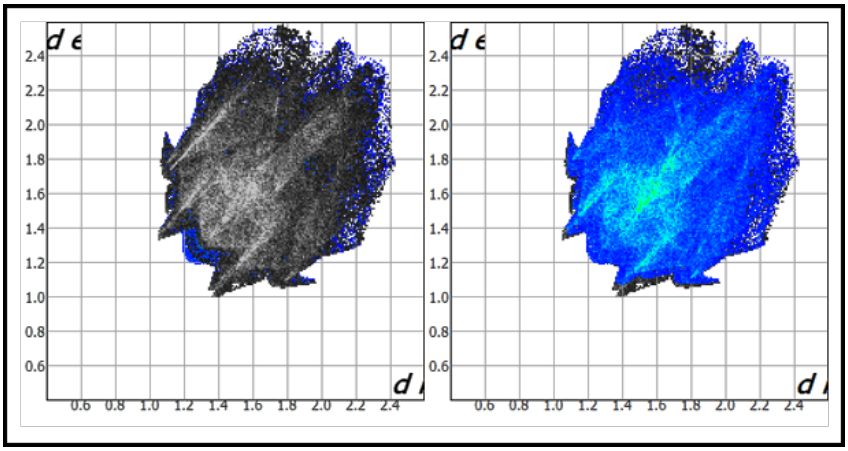

Figure S16 Superimposition of Hirshfeld surface fingerprint plots of Form I (Blue) and Form III (Black)

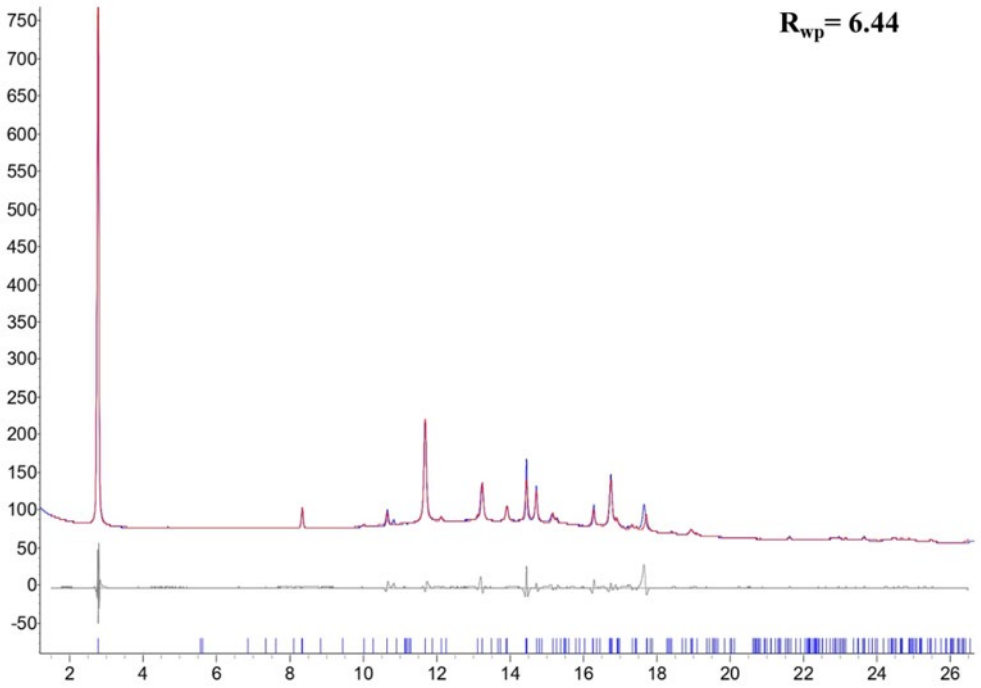

Figure S17 Indexing of Form II with R_{wp}= 6.44 (λ=0.9999613Å).

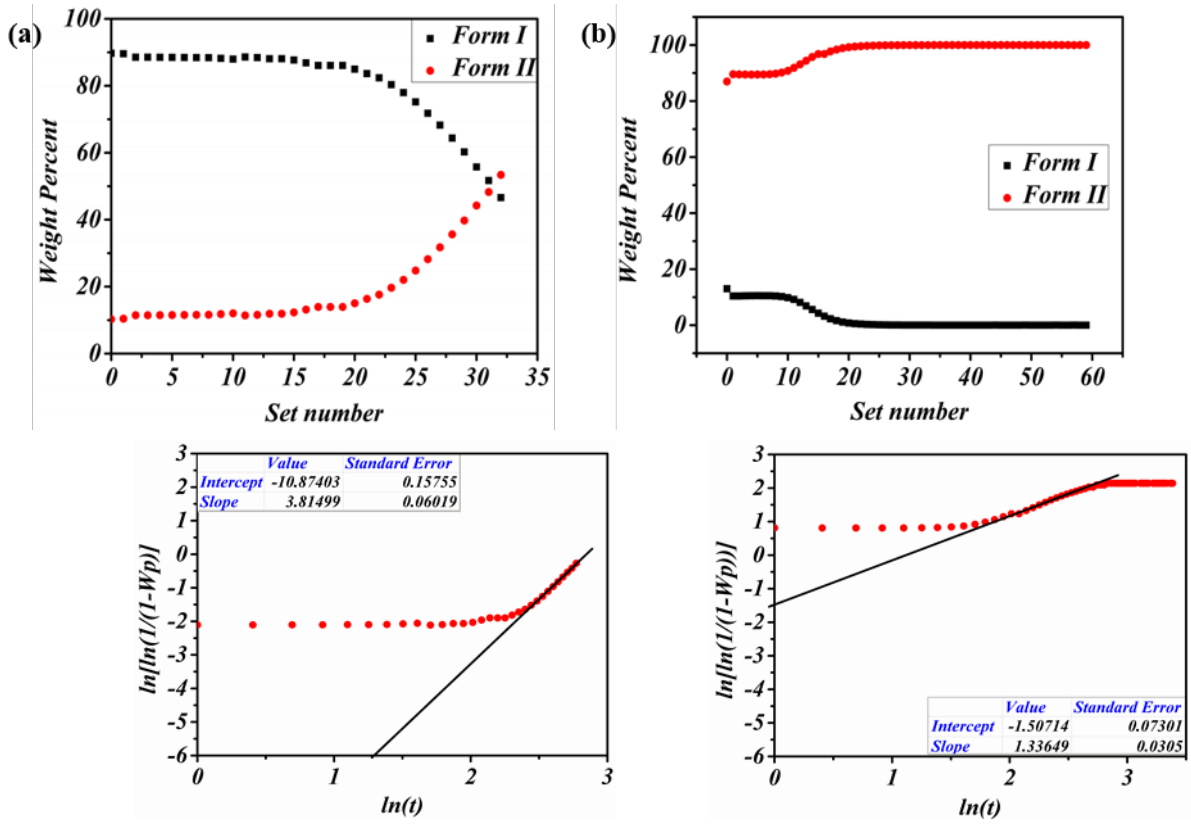

Figure S18 Kinetics of transformation of Form I to Form II at (a) 117°C and (b) 124°C and Avrami plots at (c) 117°C and (d) 124°C.

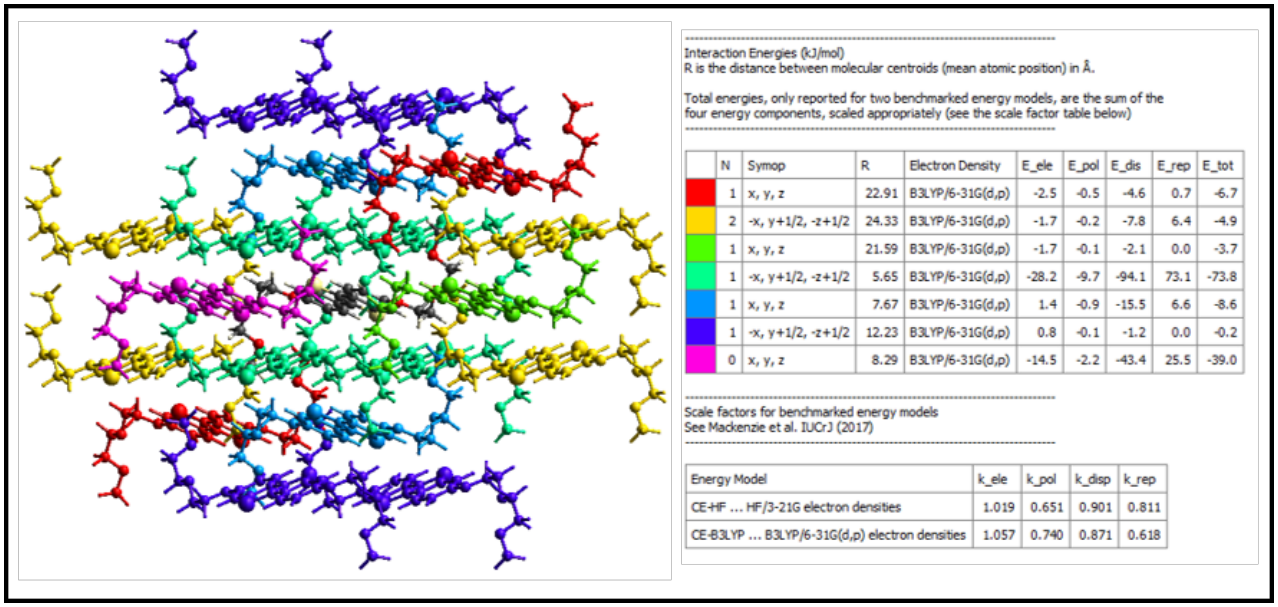

Interaction Energies (kJ/mol)
R is the distance between molecular centroids (mean atomic position) in Å.

Total energies, only reported for two benchmarked energy models, are the sum of the four energy components, scaled appropriately (see the scale factor table below)

	N	Symop	R	Electron Density	E_ele	E_pol	E_dis	E_rep	E_tot
	1	x, y, z	22.91	B3LYP/6-31G(d,p)	-2.5	-0.5	-4.6	0.7	-6.7
	2	-x, y+1/2, -z+1/2	24.33	B3LYP/6-31G(d,p)	-1.7	-0.2	-7.8	6.4	-4.9
	1	x, y, z	21.59	B3LYP/6-31G(d,p)	-1.7	-0.1	-2.1	0.0	-3.7
	1	-x, y+1/2, -z+1/2	5.65	B3LYP/6-31G(d,p)	-28.2	-9.7	-94.1	73.1	-73.8
	1	x, y, z	7.67	B3LYP/6-31G(d,p)	1.4	-0.9	-15.5	6.6	-8.6
	1	-x, y+1/2, -z+1/2	12.23	B3LYP/6-31G(d,p)	0.8	-0.1	-1.2	0.0	-0.2
	0	x, y, z	8.29	B3LYP/6-31G(d,p)	-14.5	-2.2	-43.4	25.5	-39.0

Scale factors for benchmarked energy models
See Mackenzie et al. IUCrJ (2017)

Energy Model	k_ele	k_pol	k_disp	k_rep
CE-HF ... HF/3-21G electron densities	1.019	0.651	0.901	0.811
CE-B3LYP ... B3LYP/6-31G(d,p) electron densities	1.057	0.740	0.871	0.618

Figure S19 Energies associated with all the molecules in the radius 3.80 Å from the centered molecule (depicted by different colors).

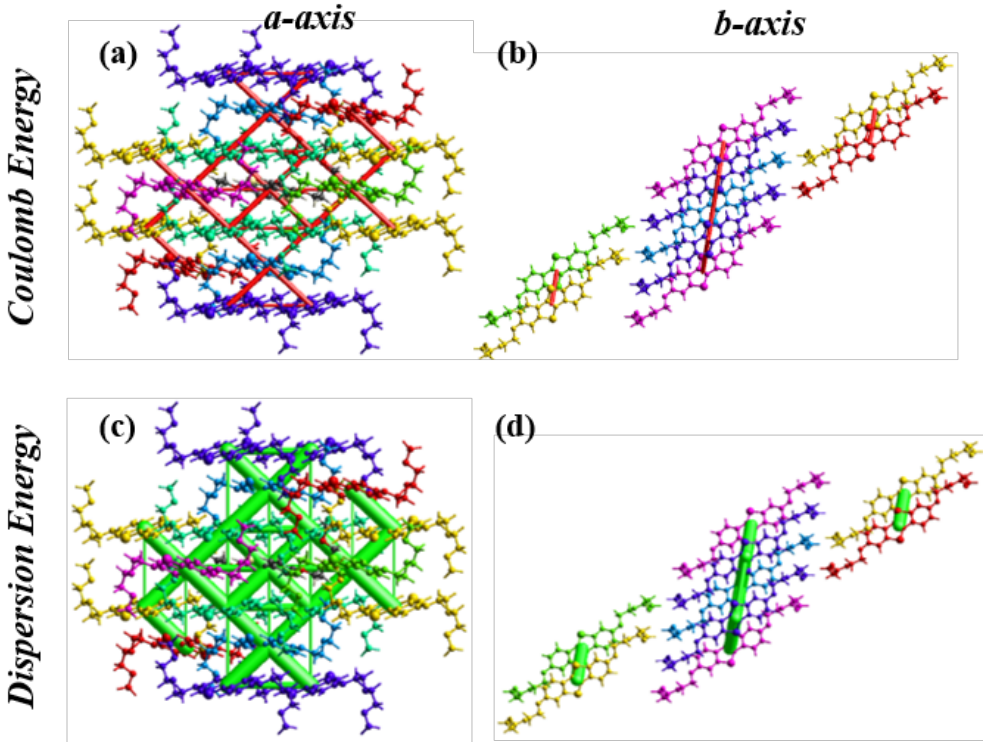

Figure S20 Energy frameworks corresponding to the different energy components (Coulomb and dispersion) in Form I along a and b crystallographic axes. The energy scale factor is 25 and the energy threshold is 5 kJ mol^{-1}. Energy framework shown along (a,c) a-axis and (b,d) b-axis; and Coulomb energy (a,b; red), Dispersion energy (c,d; green). Dispersion energy cutoff is set to 10KJ/mol.

APPENDIX B

From the Synthesis to the Device: Elucidating Structural and Electronic Properties of C7-BTBT-C7

Priya Pandey[±†], Lamiaa Fijahi[‡], Nemo McIntosh[§], Nicholas Turetta[¥], Marco Bardini[§], Samuele Giannini[§], Christian Ruzié[¤], Guillaume Schweicher[¤], David Beljonne[§], Jérôme Cornil[§], Paolo Samorì[¥], Marta Mas-Torrent[‡]*, Yves Henri Geerts[¤ϕ]*, Enrico Modena[±]*, Lucia Maini[†]*

[±] PolyCrystalLine SPA, Via Della Cooperazione, 29 40059 Medicina, Bologna, Italy

[†]Dipartimento di Chimica "G. Ciamician", via Selmi 2 − Università di Bologna, I-40126, Bologna, Italy

[‡] Institut de Ciència de Materials de Barcelona (ICMAB-CSIC), Campus de la UAB, 08193, Bellaterra, Spain

[§] Laboratory for Chemistry of Novel Materials, University of Mons, 7000 Mons, Belgium

[¥]University of Strasbourg, CNRS, ISIS UMR 7006, 8 Alleé Gaspard Monge, Strasbourg, F-67000 France

[¤] Laboratoire de Chimie des Polymères, Faculté des Sciences, Université Libre de Bruxelles (ULB), CP 206/1 Boulevard du Triomphe, 1050, Bruxelles, Belgium

[ϕ] International Solvay Institutes, Université Libre de Bruxelles (ULB), CP 231 Boulevard du Triomphe, 1050, Bruxelles, Belgium

Table S 1 Solubility test results using 21 different solvents for 5 mg of C7-BTBT-C7 starting material powder. “X”: suspension, “YES”: clear solution, “-”: not performed.

	Temperature	**RT (20-25°C)**					**50°C**	**75°C**
	Volume added to 5 mg	**50µL**	**100µL**	**250µL**	**500µL**	**1mL**	**1mL**	**1mL**
	Concentration (mg mL^{-1})	**100**	**50**	**20**	**10**	**5**	**5**	**5**
2MX	2-Methoxyethanol	X	X	X	X	X	X	X
2PR	2-Propanol	X	X	X	X	X	X	Yes
ABZ	Benzyl Alcohol	X	X	X	X	X	Yes	-
ACN	Acetonitrile	X	X	X	X	X	X	X
ANI	Anisole	X	Yes	-	-	-	-	-
CHF	Chloroform	Yes	-	-	-	-	-	-
CLB	Chlorobenzene	Yes	-	-	-	-	-	-
DCM	Dichloromethane	Yes	-	-	-	-	-	-
DEC	Diethyl Carbonate	X	X	X	X	Yes	-	-
DMA	*N,N*-dimethylacetamide	X	X	X	X	X	Yes	-
DMF	*N,N*-dimethylformamide	X	X	X	X	X	Yes	-
DMS	Dimethyl Sulfoxide	X	X	X	X	X	X	X
DMX	1,2- Dimethoxyethane	X	X	Yes	-	-	-	-
ETH	Ethanol	X	X	X	X	X	X	Yes
H2O	Water	X	X	X	X	X	X	X
IPA	Isopropyl Acetate	X	X	X	X	Yes	-	-
IPE	Isopropyl Ether	X	X	X	Yes	-	-	-
MEK	Methyl ethyl Ketone	X	X	X	Yes	-	-	-
MPY	1-Methyl-2-Pyrrolidone	X	X	X	X	Yes	-	-
PXY	p-Xylene	Yes	-	-	-	-	-	-

THF	Tetrahydrofuran	Yes	-	-	-	-	-	-
TOL	Toluene	Yes	-	-	-	-	-	-

Table S 2 Crystallographic parameters of C7-BTBT-C7 from SCXRD.

Parameters	**C7-BTBT-C7**
Formula	$C_{28}H_{36}S_2$
Molecular weight (g.mol^{-1})	218.34
Temperature (K)	293 (2)
Crystal system	Monoclinic
Space group	*P 2$_1$/*c
a (Å)	27.260(6)
b (Å)	7.9879(9)
c (Å)	5.9104(6)
β (°)	92.662(16)
V (Å^3)	1285.59
Z/Z'	2/0.5
Density (g·cm^{-3})	1.128
F (000)	472
μ (mm^{-1})	0.219
GOF on F^2	1.037
R_1 (on F, I>2σ(I)/R_{ex}	0.0819
WR_2 (F^2 all data) R_{wp}	0.1525
CCDC number	2225078

Table S 3 Structural and packing descriptors for BTBT cores of C7-BTBT-C7, C8-BTBT-C8 and C12-BTBT-C12

Descriptors	**C7**	**C8**	**C12**

	$P2_1/c$		
	Monoclinic		
a (Å)	27.26(6)	29.18(4)	37.91(3)
b (Å)	7.988(9)	7.88(1)	7.74(7)
c (Å)	5.910(6)	5.927(7)	5.86(5)
α (°)	90	90	90
β (°)	92.66(16)	92.44(4)	90.59(3)
γ (°)	90	90	90
V (Å³)	1285.60(4)	1361.61	1721.00(3)
Z/Z'	2/0.5	2/0.5	2/0.5
HB (°)	56.48	54.85	53.86
Stacking vector, SV (Å)	5.91	5.93	5.86
Interplanar distance, d(Å)	2.84	2.79	2.71
X (°)	88.52	88.58	88.45
Ψ (°)	28.19	27.38	26.88
Δx	0.15	0.15	0.16
Δy	5.21	5.27	5.23
Pitch (°)	3.08	3.02	3.35
Roll angle (°)	61.40	62.10	62.61
Core tilt angle (°)	87.66	87.87	87.9

Table S 4 Ionization energy (IE) values of C7-BTBT-C7 and other BTBT compounds that are structurally similar as determined by PYS from powder samples.

Compound	**IE (eV)**
C7-BTBT-C7	5.28 ± 0.02
C8-BTBT-C8	5.33 ± 0.05
C12-BTBT-C12	5.31 ± 0.05

Table S 5 Charge transport parameters and experimental mobilities of C7-, C8- and C12-BTBT.

X-BTBT	J_P (meV)	J_{T1} (meV)	J_{T2} (meV)	λ (meV)	μ_{exp} ($cm^2/V.s$)
C7	+51.1	-23.4	-23.4	243.9	1.4

C8	+45.2	-7.1	-7.1	243.6	1.3[1], 6.2[2], 10[3]
C12	+65.1	-47.2	-47.2	243.1	1.6[4]

Table S 6 Electrical characteristics of pristine and PS blended devices of C7-BTBT-C7 with different channel lengths.

Condition	**Channel width (μm)**	**V^{th}_{Sat} (V)**	**μ_{Sat} ($cm^2V^{-1}s^{-1}$)**
Pristine	200	-21.64±0.54	0.19±0.02
	100	-22.46±1.28	0.06±0.00
	50	-23.76±1.85	0.04±0.01
PS10K	200	-31.99±1.45	1.42±0.46
	100	-31.81±1.92	1.28±0.46
	50	-34.22±2.28	0.92±0.03
PS280K	200	-32.78±1.43	0.39±0.09
	100	-36.20±0.57	0.32±0.12
	50	-37.08±0.62	0.25±0.03

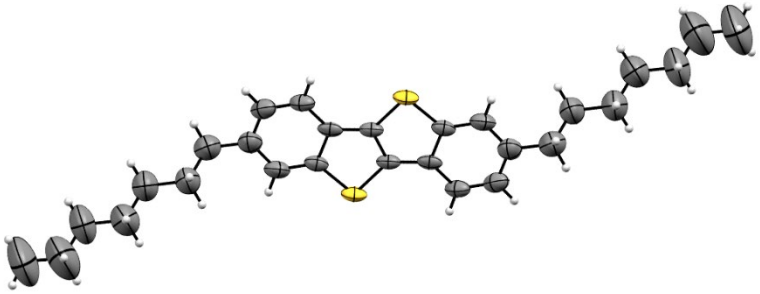

Figure S 1 Crystal structure of C7-BTBT-C7 at room temperature. The atomic displacement parameters (ADPs) of carbons in the end of the chain are bigger as there is more degree of freedom in the chains.

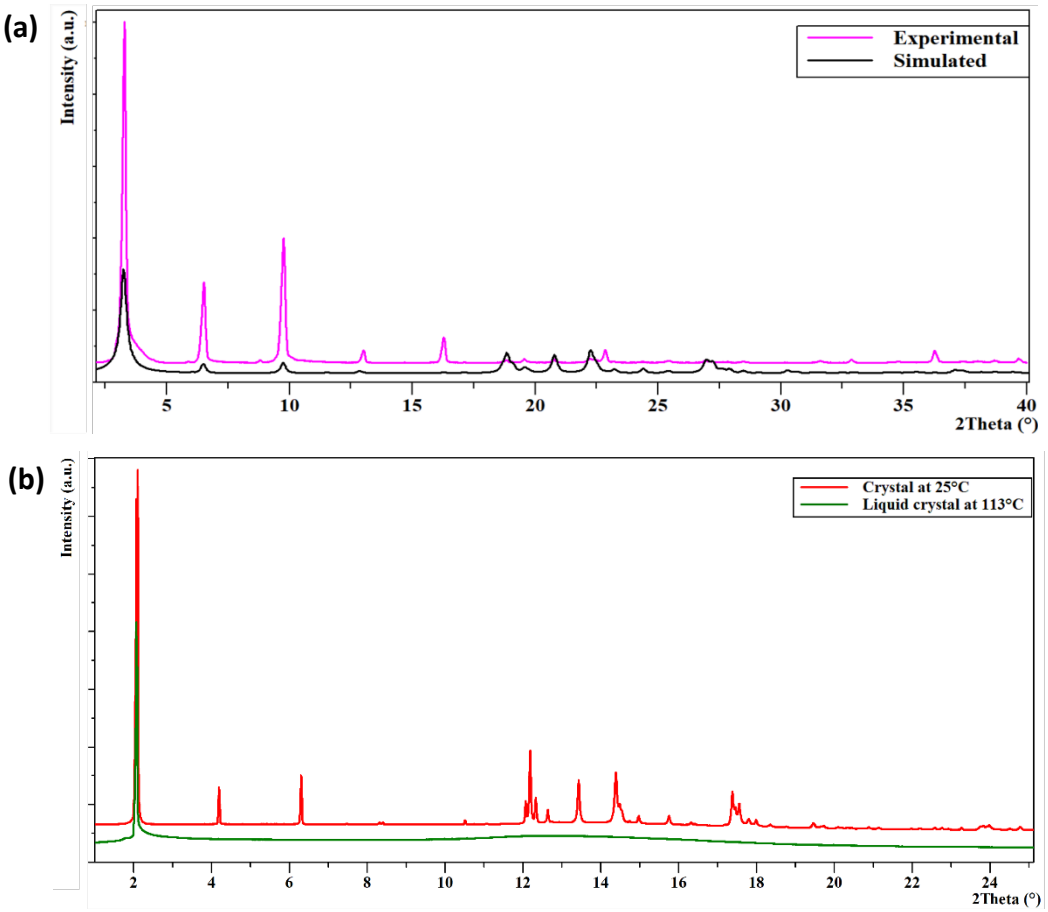

Figure S 2 (a) XRD comparison of simulated (black) and experimental (pink) patterns collected with Bragg-Brentano geometry (λ=1.54 Å) at 25˚C. The real sample dramatically suffers of preferential orientation, and (b) XRD of crystal at 25˚C (red) and liquid crystal at 113˚C (green) for C7-BTBT-C7 collected with transmission geometry (λ=0.9999613 Å). In both cases square root scale was used to emphasize the weak peaks.

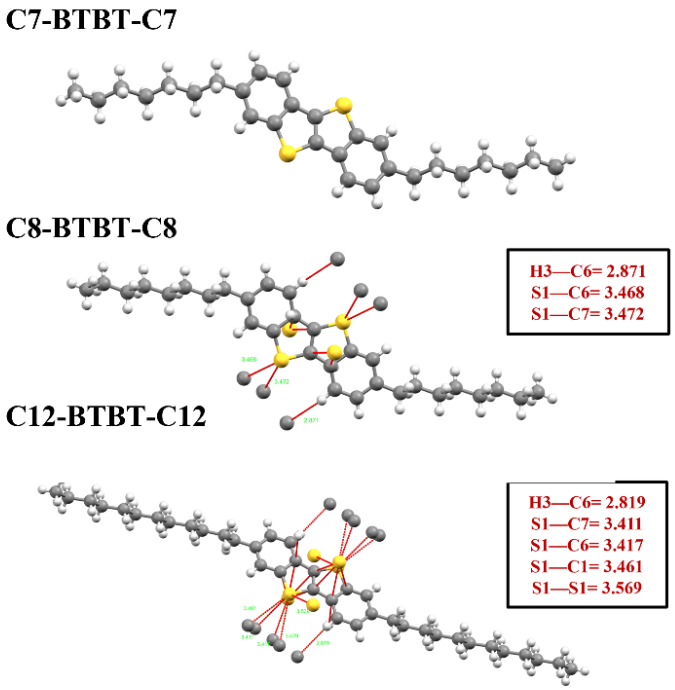

Figure S 3 Short contact interaction in C7-BTBT-C7, C8-BTBT-C8 and C12-BTBT-C12.

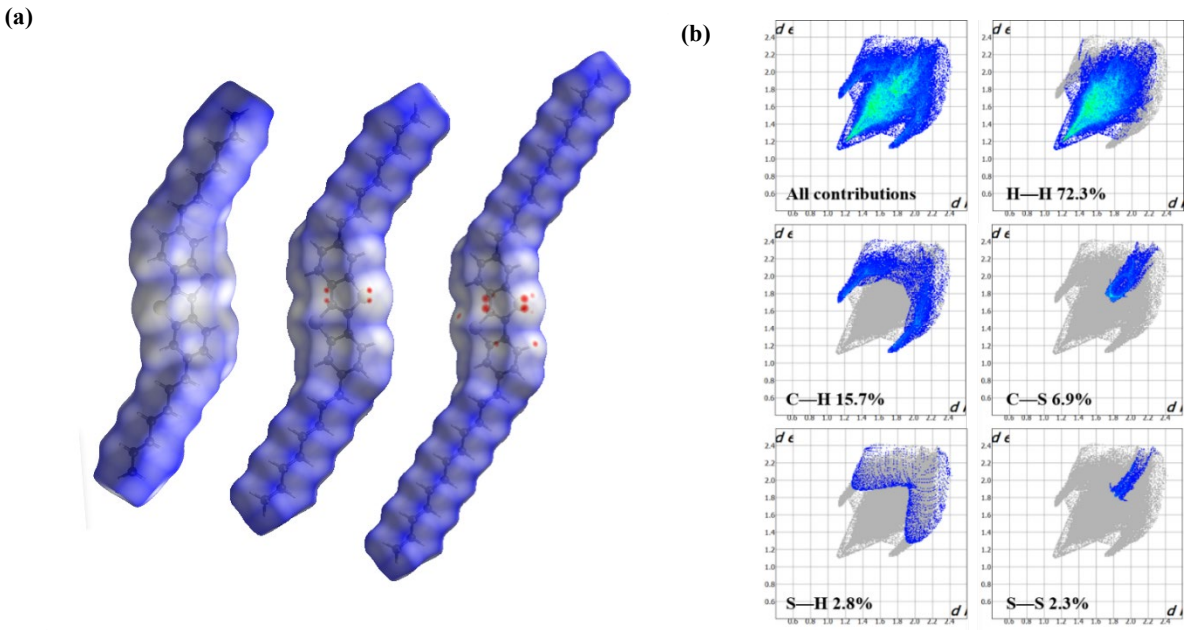

Figure S 4 Hirshfeld surfaces (a) d_{norm} electron density map for C7-BTBT-C7, C8-BTBT-C8 and C12-BTBT-C12 (left to right). Red dots white regions and blue regions are indicative of distances that are shorter, equal, and greater than the van der Waals radii, respectively. (b) 2D fingerprint plots of C7-BTBT-C7 indicating the percentage of contribution of each interaction present in the molecule.

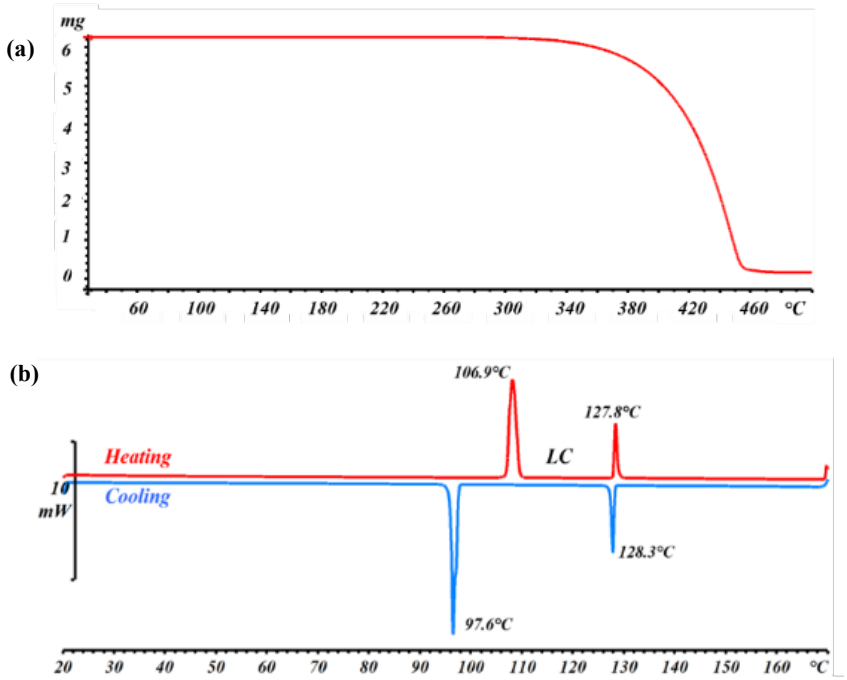

Figure S 5 (a) TGA at a scan rate of 10°C min^{-1} and (b) DSC at a scan rate of 5°C min^{-1} of C7-BTBT-C7.

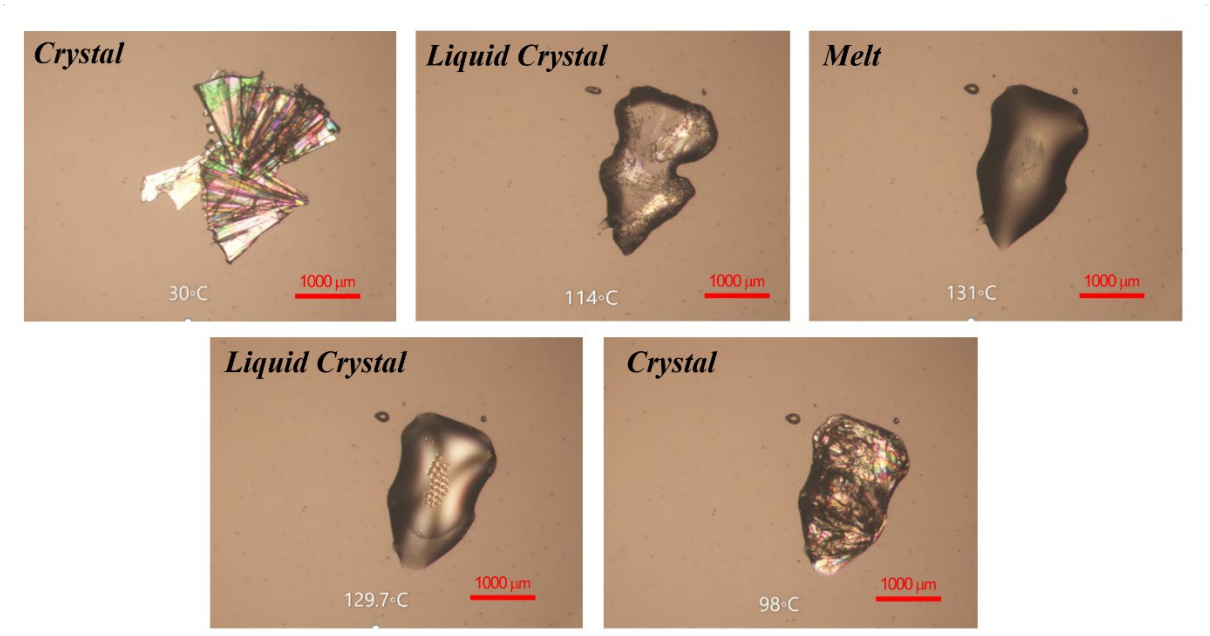

Figure S 6 Hot-stage microscopy images of phase transitions from crystal to liquid crystal, liquid crystal to melt, melt to liquid crystal and liquid crystal to crystal in C7-BTBT-C7. Heating and cooling rates were maintained at 10°C min^{-1}.

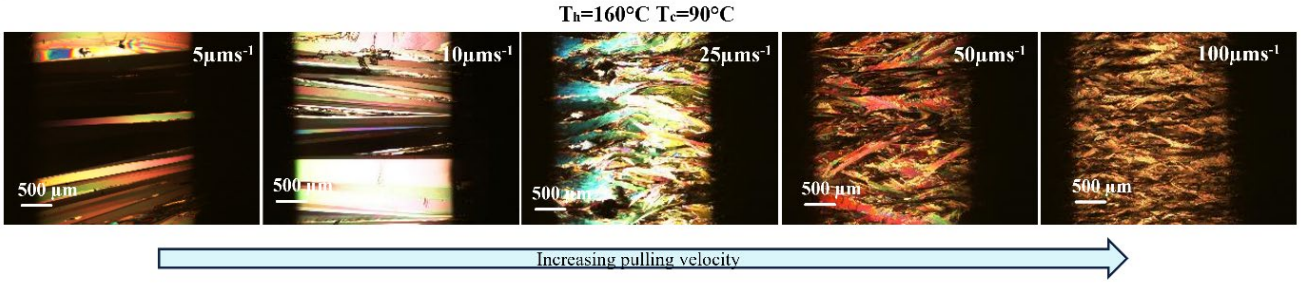

Figure S 7Polarized optical microscopy images recorded at room temperature after crystallization showing the alignment region with different pulling velocities. The entangled ribbon/needle-like morphology was observed. The entanglement increases with increasing pulling velocity.

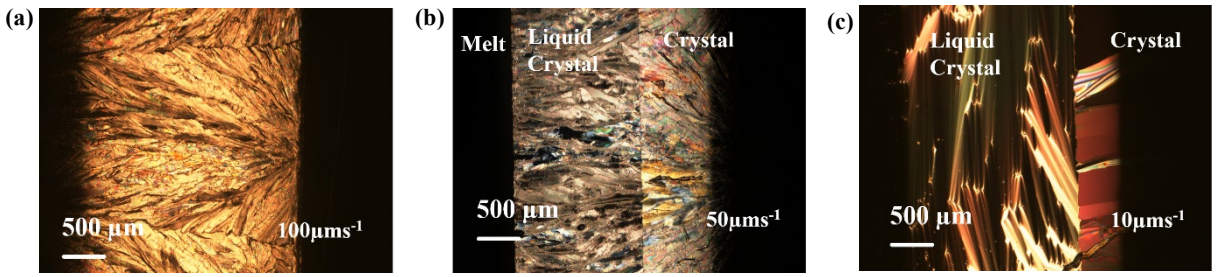

Figure S 8 (a) Multiple nucleation sites (T_h-T_c: 160-90˚C) at 100 µm s^{-1}.(b) Growth Fronts (T_h-T_c: 160-70˚C) at 50 µm s^{-1}. (c) liquid crystal phase was separated by a crystal growth front. The crystal growth front is parallel to the thermal gradient.

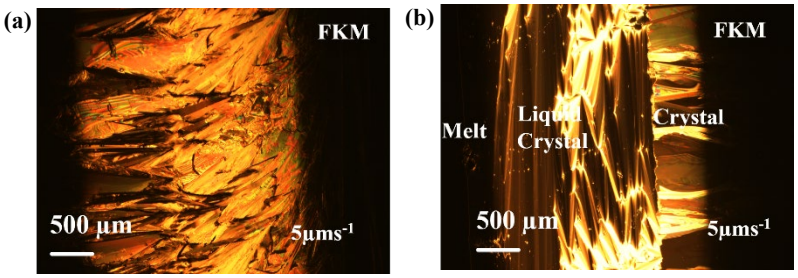

Figure S 9 Polarized optical microscopy images on FKM coated films (pulling velocity 5 µm s^{-1}) showing (a) nucleation and alignment and (b) growth fronts. The morphology follows the same trend as the films without FKM, and no significant differences in the POM images were observed.

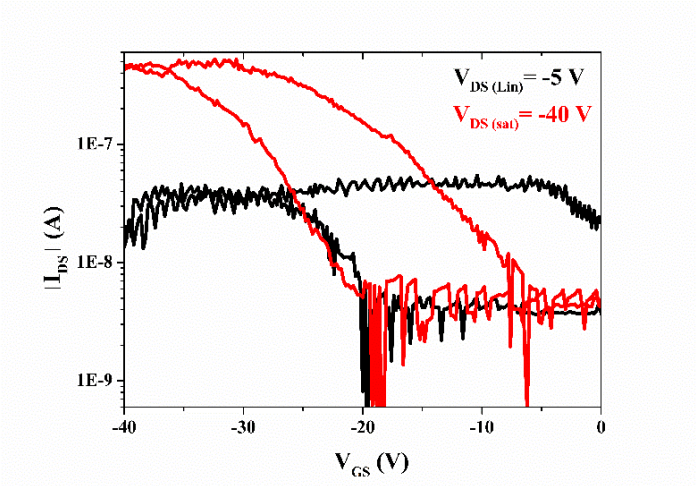

Figure S 10 Representative transfer characteristics showing linear and saturation curves of bottom gate/bottom contact device of C7-BTBT-C7. Channel length 150 µm and channel width/length ratio is 100.

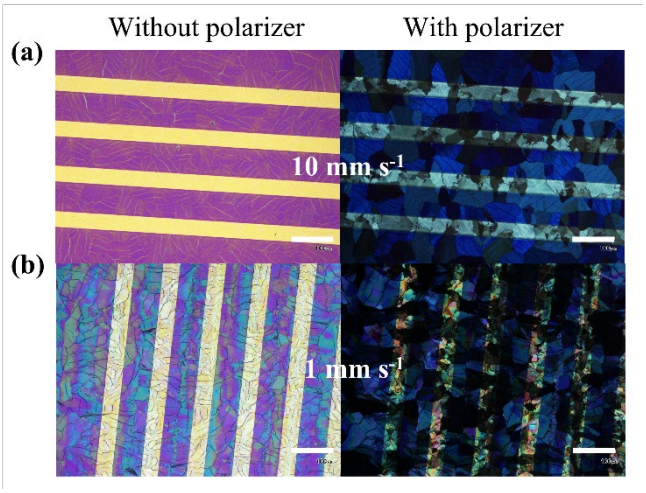

Figure S 11 Polarised optical microscopy (POM) images of bottom gate/bottom contact devices of C7-BTBT-C7 prepared with shearing speed of (a) 10 mm s^{-1} and (b) 1 mm s^{-1}. Scale bar: 200 µm.

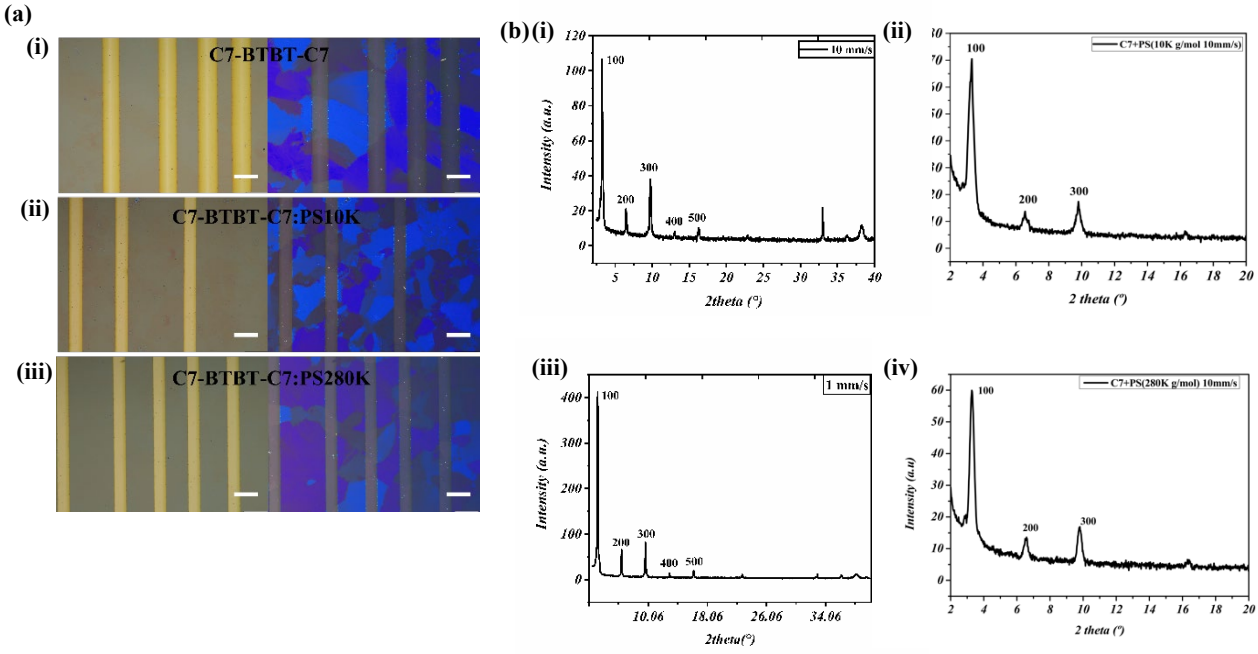

Figure S 12 (a) POM images of bottom gate/top contact devices at 10 mm s^{-1} (i) Pristine (ii) C7-BTBT-C7:PS10K (iii) C7-BTBT-C7:PS280K (The 1 mm s^{-1} films were not homogeneous and did not have full coverage on the electrodes) (b) XRD patterns of (i) Pristine 10 mm s^{-1} (ii) Pristine 1 mm s^{-1} (iii) C7-BTBT-C7:PS10K (10mm s^{-1}) and (iv) C7-BTBT-C7:PS280K 10 mm s^{-1}. Scale bar: 200 µm.

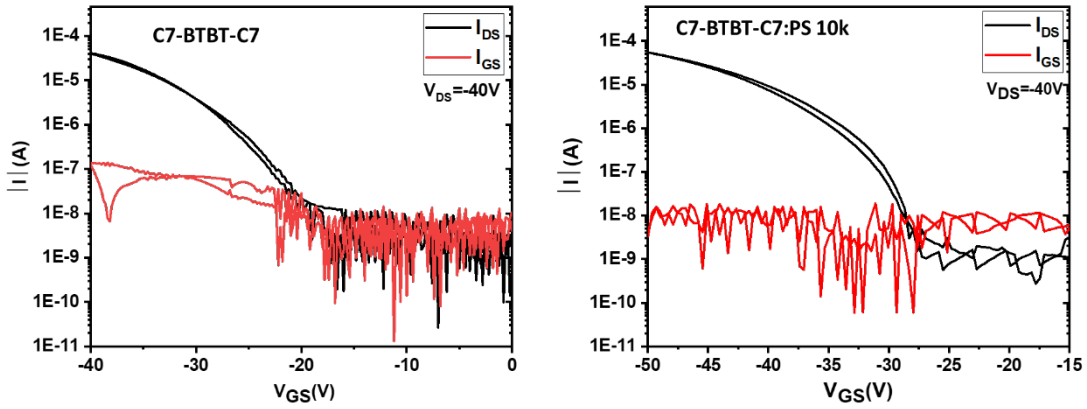

Figure S 13 Transfer characteristics of a representative pristine-based OFET and a blend-based OFET showing the source-gate current (I_{GS}).

References

1 J. Li, A. Babuji, I. Temiño, T. Salzillo, F. D'Amico, R. Pfattner, C. Ocal, E. Barrena and M. Mas-Torrent, *Adv. Mater. Technol.*, 2022, **7**, 2101535.

2 L. Jiang, J. Liu, X. Lu, L. Fu, Y. Shi, J. Zhang, X. Zhang, H. Geng, Y. Hu, H. Dong, L. Jiang, J. Yu and W. Hu, *J. Mater. Chem. C*, 2018, **6**, 2419–2423.
3 R. Janneck, N. Pilet, S. P. Bommanaboyena, B. Watts, P. Heremans, J. Genoe and C. Rolin, *Adv. Mater.*, 2017, **29**, 1703864.
4 S. Colella, C. Ruzié, G. Schweicher, J.-B. Arlin, J. Karpinska, Y. Geerts and P. Samorì, *Chempluschem.*, 2014, **79**, 371–374.

APPENDIX C

Polymorphic landscape and device fabrication of a novel organic semiconductor: ditbuC6-BTBT

Priya Pandey[±†], Federico Modesti[Ψ], Lamiaa Fijahi[‡], Nemo McIntosh[§], Nicholas Turetta[¥], Christian Ruzié[¤], Massimiliano Remigio[¤], Guillaume Schweicher[¤], Peter Erk[Ψ], Jérôme Cornil[§], Paolo Samorì[¥], Marta Mas-Torrent[‡*], Yves Henri Geerts[¤ϕ*], Enrico Modena[±*], Lucia Maini[†*]

± PolyCrystalLine SPA, Via Della Cooperazione, 29 40059 Medicina, Bologna, Italy

†Dipartimento di Chimica "G. Ciamician", via Selmi 2 – Università di Bologna, I-40126, Bologna, Italy

ΨBASF SE, RCS – J542S, 67056 Ludwigshafen am Rhein, Germany

‡ Institut de Ciència de Materials de Barcelona (ICMAB-CSIC), Campus de la UAB, 08193, Bellaterra, Spain

§ Laboratory for Chemistry of Novel Materials, University of Mons, 7000 Mons, Belgium

¥University of Strasbourg, CNRS, ISIS UMR 7006, 8 Alleé Gaspard Monge, Strasbourg, F-67000 France

¤ Laboratoire de Chimie des Polymères, Faculté des Sciences, Université Libre de Bruxelles (ULB), CP 206/1 Boulevard du Triomphe, 1050 Bruxelles, Belgium

ϕ International Solvay Institutes, Université Libre de Bruxelles (ULB), CP 231 Boulevard du Triomphe, 1050, Bruxelles, Belgium

Table S 1 Solubility test results using 21 different solvents for 5 mg of ditBuC6-BTBT starting material powder. “X”: suspension, “YES”: clear solution, “-”: not performed, and SS*: sparingly soluble.

	Temperature	**RT (20-25°C)**					**50°C**	**75°C**
	Solvent	**50µL**	**100µL**	**250µL**	**500µL**	**1mL**	**1mL**	**1mL**
	Volume added to 5 mg	**50µL**	**100µL**	**250µL**	**500µL**	**1mL**	**1mL**	**1mL**
	Concentration (mg mL^{-1})	**100**	**50**	**20**	**10**	**5**	**5**	**5**
2MX	2-Methoxyethanol	X	X	X	X	X	X	X
2PR	2-Propanol	X	X	X	X	X	X	Yes
ABZ	Benzyl Alcohol	X	X	X	X	X	X	Yes
ACN	Acetonitrile	X	X	X	X	X	X	X
ANI	Anisole	X	X	Yes	-	-	-	-
CHF	Chloroform	Yes	-	-	-	-	-	-
CLB	Chlorobenzene	Yes	-	-	-	-	-	-
DCM	Dichloromethane	X	X	X	X	X	Yes	-
DEC	Diethyl Carbonate	X	X	X	X	X	Yes	-
DMA	*N,N*-dimethylacetamide	X	X	X	X	X	Yes	-
DMF	*N,N*-dimethylformamide	X	X	X	X	X	X	X
DMF	Dimethyl Sulfoxide	X	X	X	Yes	-	-	-
ETH	Ethanol	X	X	X	X	X	X	SS*
H2O	Water	X	X	X	X	X	X	X
IPA	Isopropyl Acetate	X	X	X	X	Yes	-	-
IPE	Isopropyl Ether	X	X	X	X	Yes	-	-
MEK	Methyl ethyl Ketone	X	X	X	X	Yes	-	-
MPY	1-Methyl-2-Pyrrolidone	X	X	X	X	X	Yes	-

PXY	p-Xylene	X	Yes	-	-	-	-	-
THF	Tetrahydrofuran	Yes	-	-	-	-	-	-
TOL	Toluene	X	Yes	-	-	-	-	-

Table S 2 Polymorph screening experiments and the respective polymorphs obtained.

Experiment	**Solvent/ Solvent mixture**	**Form I**	**Form II**	**Form I + Form II mixture**
Evaporation	2-Propanol	-	-	Yes
	Benzyl Alcohol	-	-	Yes
	Anisole	Yes	-	-
	Chloroform	Yes	-	-
	Dichloromethane	Yes	-	-
	Diethyl Carbonate	-	Yes	-
	N,N-dimethylacetamide	-	-	Yes
	N,N-dimethylformamide	-	-	Yes
	1,2- Dimethoxyethane	-	Yes	-
	Isopropyl Acetate	-	-	Yes
	Isopropyl Ether	Yes	-	-
	Methyl ethyl Ketone	-	-	Yes
	1-Methyl-2-Pyrrolidone	-	-	Yes
	p-Xylene	Yes	-	-
	Tetrahydrofuran	Yes	-	-
	Toluene	Yes	-	-
	THF+Toluene (1:1)	-	-	Yes
Anti-solvent addition (1:1)	Acetonitrile: p-Xylene	Yes	-	-

	Chloroform: 2-Propanol	-	-	Yes
	Chloroform: Dimethyl Sulfoxide	Yes	-	-
	Tetrahydrofuran: Ethanol	Yes	-	-
	Toluene: Ethanol	-	-	Yes
Slurry maturation	2-Methoxyethanol			
	4-days	Yes	-	-
	7-days		-	-
	20-days		-	-
	Acetonitrile			
	4-days	-	-	Yes
	7-days	-	-	
	20-days	-	-	
	N,N-dimethylacetamide			
	4-days	-	-	Yes
	7-days	-	-	Yes
	20-days	-	Yes	-
	N,N-dimethylformamide			
	4-days	-	-	Yes
	7-days	-	-	Yes
	20-days	-	Yes	-
	Dimethyl Sulfoxide			
	4-days	Yes	-	-
	7-days		-	-
	20-days		-	-
	Ethanol			
	4-days	-	-	Yes
	7-days	-	-	Yes
	20-days	-	Yes	-

	Water 4-days 7-days 20-days	Yes	- - -	- - -
Slurry maturation (Solvent mixtures)	2-Methoxyethanol + *N,N*-dimethylformamide 4-days 7-days 20-days	Yes	- - -	- - -
	2-Methoxyethanol + 2-Propanol 4-days 7-days 20-days	- - -	Yes	- - -
	2-Methoxyethanol + 1,2-Dimethoxyethane (50°C) 4-days 7-days 20-days	- - -	Yes	- - -
	Acetonitrile + p-Xylene 4-days 7-days 20-days	- - -	Yes	- - -
	Toluene + Ethanol 4-days 7-days 20-days	- - -	Yes	- - -
Crystal16: temperature gradient crystallization	*N,N*-dimethylacetamide	Yes	-	-
	N,N-dimethylformamide	Yes	-	-
	Ethanol	-	Yes	-
Mechanochemistry	Dry grinding	Yes	-	-

Table S 3 Summary of the different gradient conditions applied in the present study.

Entry	T_h (˚C)	T_c (˚C)	Pulling Velocity *V* (μm s^{-1})	Gradient Magnitude *G* (˚C mm^{-1})	Cooling rate (˚C s^{-1})
TG_{111}	170	70	25	50	1.25
TG_{112}	170	70	50	50	2.5
TG_{121}	170	80	25	45	1.125
TG_{122}	170	80	50	45	2.25
TG_{131}	170	90	25	40	1
TG_{132}	170	90	50	40	2
TG_{141}	170	100	5	35	0.175
TG_{142}	170	100	10	35	0.35
TG_{143}	170	100	25	35	0.875
TG_{144}	170	100	50	35	1.75
TG_{151}	170	120	25	25	0.625
TG_{152}	170	120	50	25	1.25
TG_{161}	170	140	5	15	0.075
TG_{162}	170	140	10	15	0.15
TG_{163}	170	140	20	15	0.3
TG_{164}	170	140	25	15	0.375
TG_{165}	170	140	50	15	0.75
TG_{211}	180	140	5	20	0.1
TG_{212}	180	140	10	20	0.2
TG_{213}	180	140	25	20	0.5
TG_{214}	180	140	50	20	1

Table S 4 Ionization energy (IE) values of ditBuC6-BTBT as determined by PYS from powder (IEp) and single-crystalline (IESC) samples. SC samples lied on the substrate with the short axis perpendicular to the substrate plane.

Compound	**IE_p (eV)**	**IE_{SC} (eV)**
ditBuC6-BTBT (I)	5.78 ± 0.03	5.81 ± 0.05
ditBuC6-BTBT (II)	5.57 ± 0.03	5.51 ± 0.05
C7-BTBT-C7	5.28 ± 0.02	-
diC7tBu-BTBT	5.59 ± 0.04	-

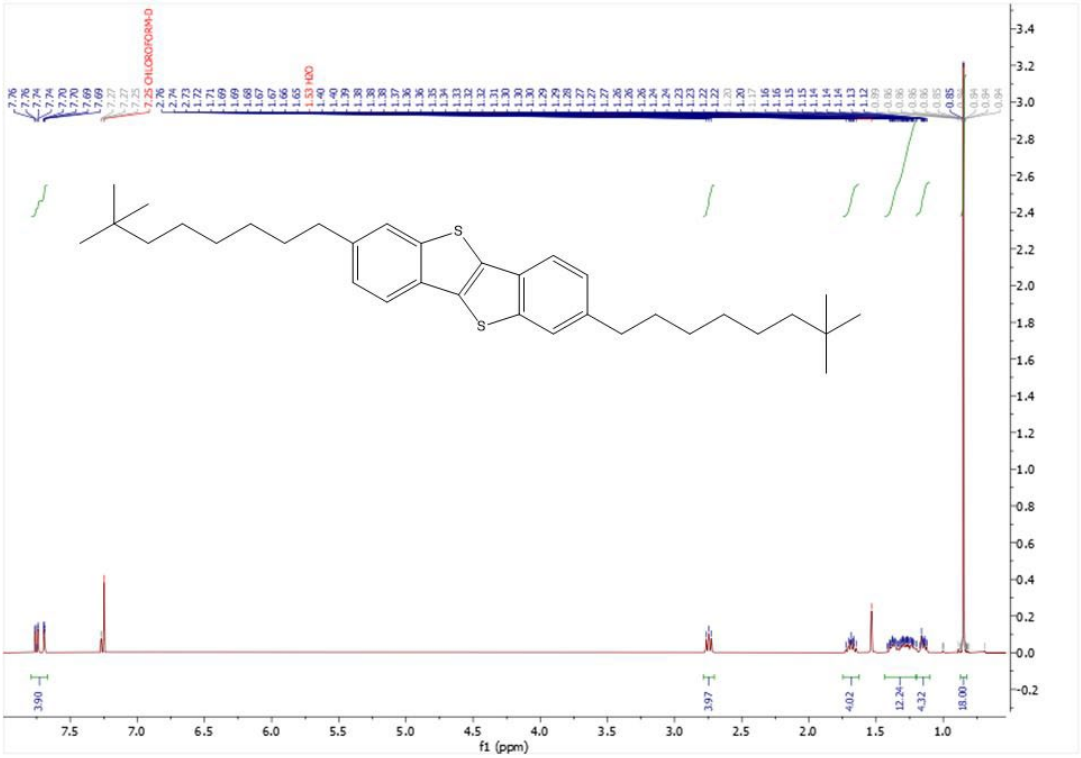

Figure S 1 ^{1}H NMR of ditBuC6-BTBT

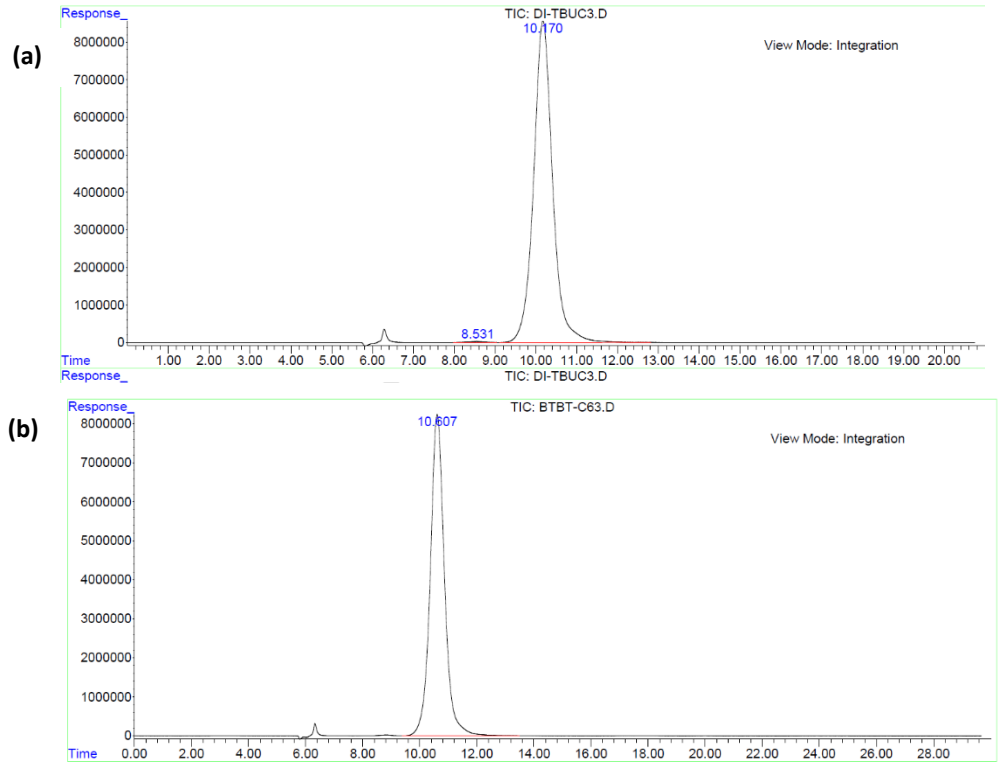

Figure S 2 High performance liquid chromatography (HPLC) spectra of ditBuC6-BTBT sample (a) before and (b) after sublimation.

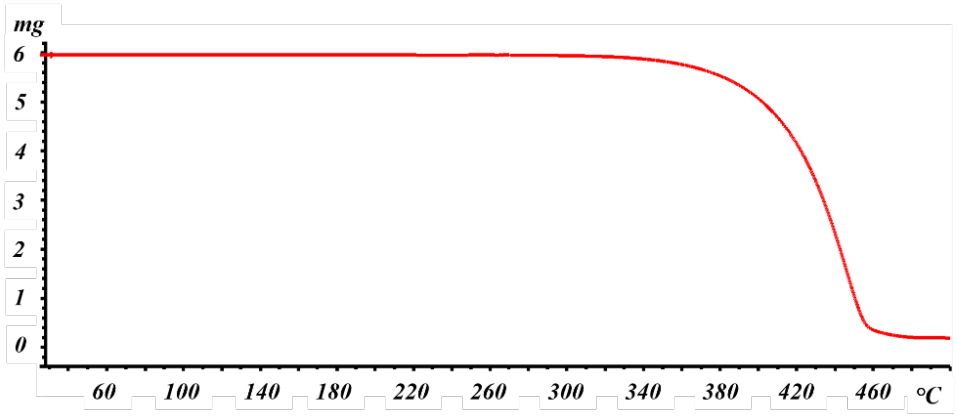

Figure S 3 Thermo Gravimetric analysis (TGA) of ditBuC6-BTBT at 10˚C min^{-1}.

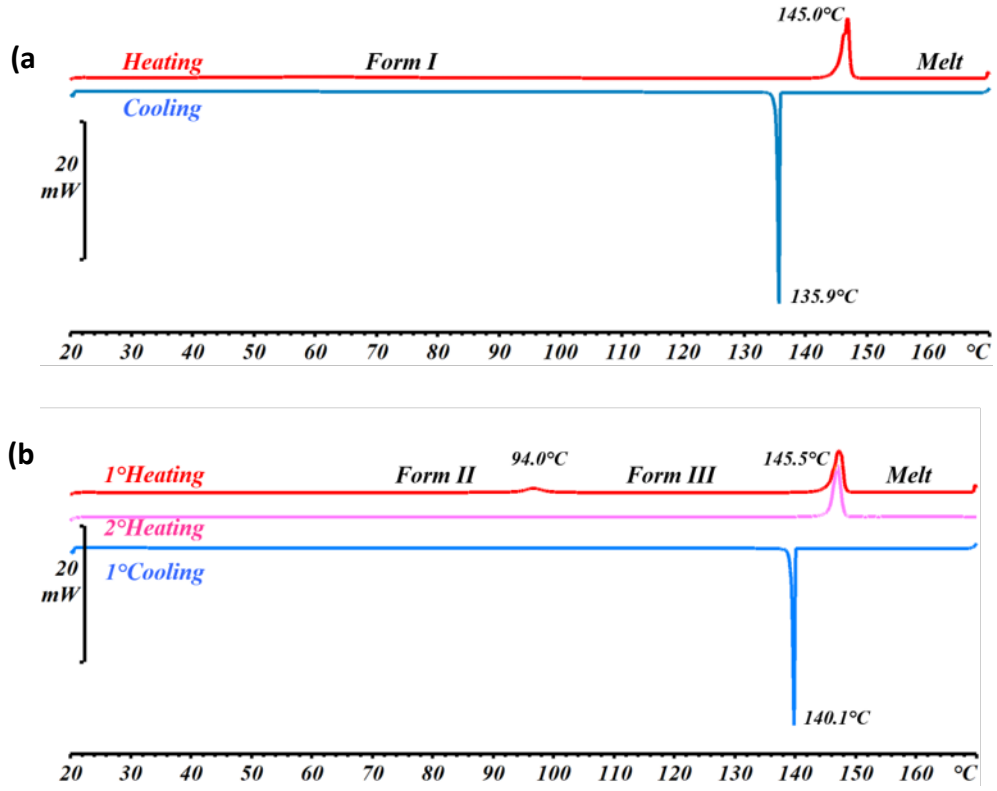

Figure S 4 Differential scanning calorimetry (DSC) of (a) Form I and (b) Form II, at 5˚C min^{-1}.

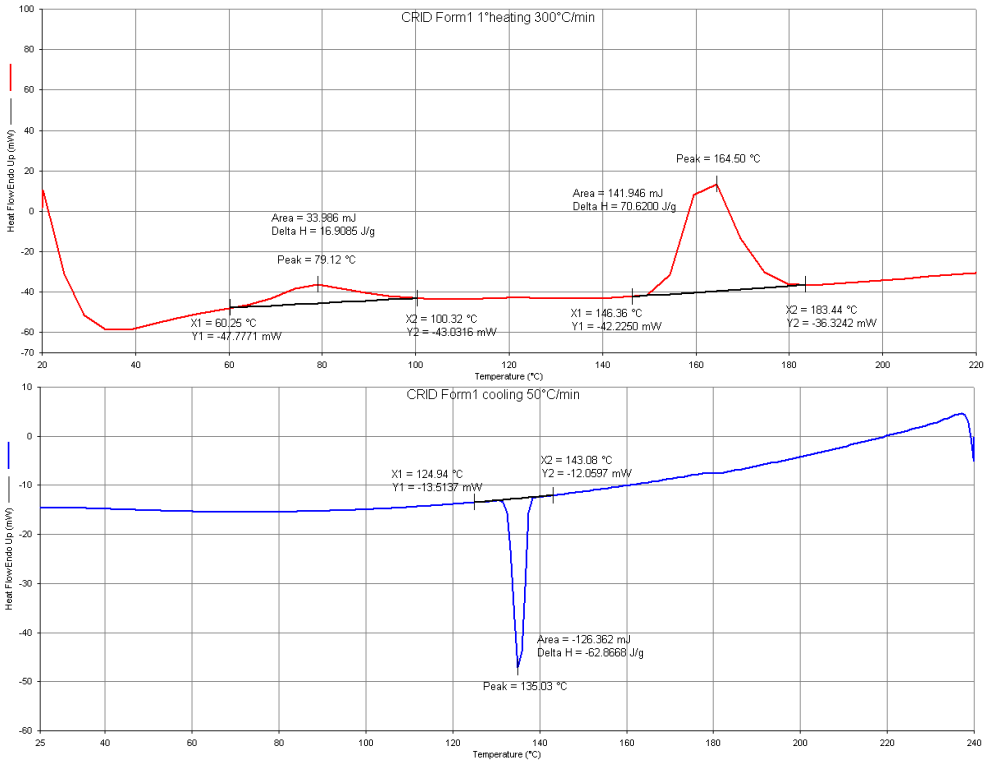

Figure S 5 DSC of Form I at 300˚C min^{-1}, showing the transition to Form III at 79˚C.

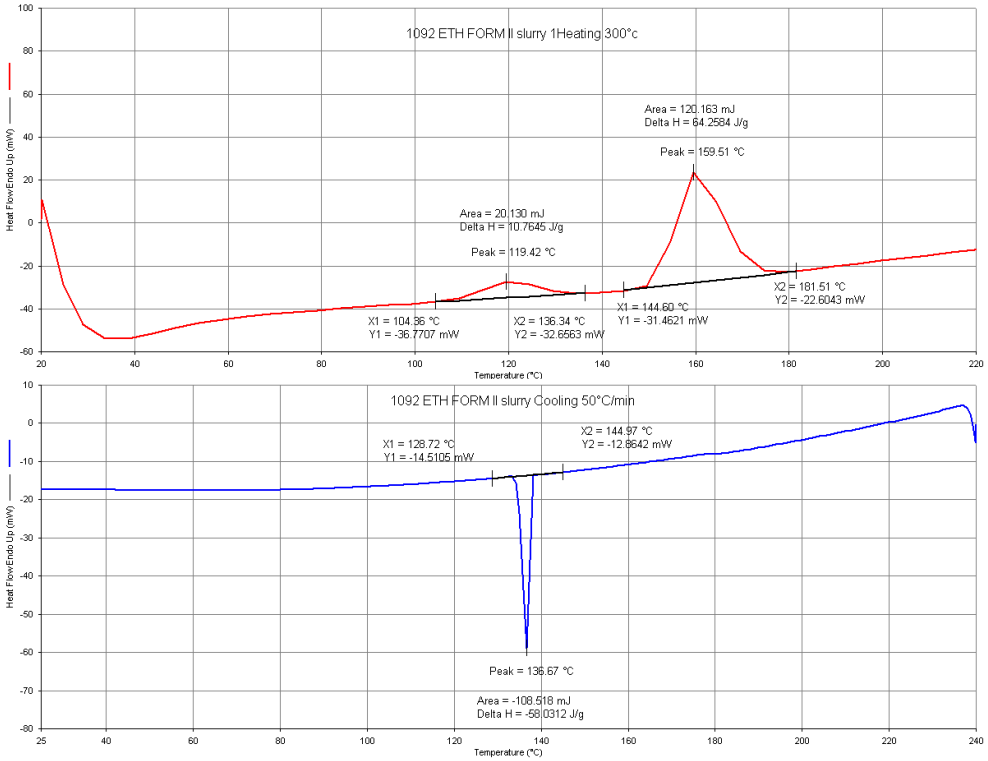

Figure S 6 DSC of Form II at 300˚C min^{-1}, showing the transition to Form III at 119˚C.

From all the three DSC figures S4, S5 and S6, it appears that the transitions from Form I→Form III and Form II→Form III are irreversible. However, during the stability analysis we observed that Form III is only stable at high temperatures, as the slow conversion to Form I and then later to Form II was observed using XRD. The kinetics of transformation is very slow and thus undetected in DSC. Refer to Figure S15.

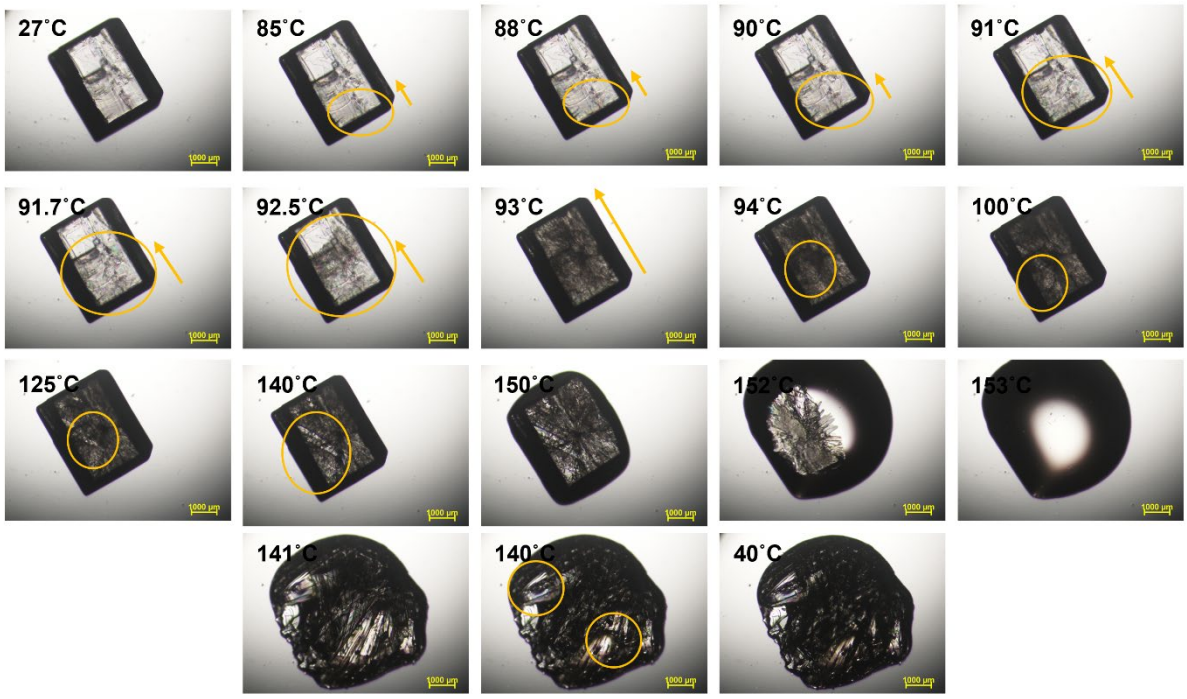

Figure S 7 Hot-stage microscope (HSM) images of crystal of Form Ia crystal, showing the transition starting from the bottom edge of the crystal at 85˚C and propagating to the top edge and complete transition to Form III at 140˚C, followed by melting at 153˚C. Recrystallization from melt occurred at 141˚C, further small changes were observed throughout cooling until 40˚C. Scale bar 1000 µm.

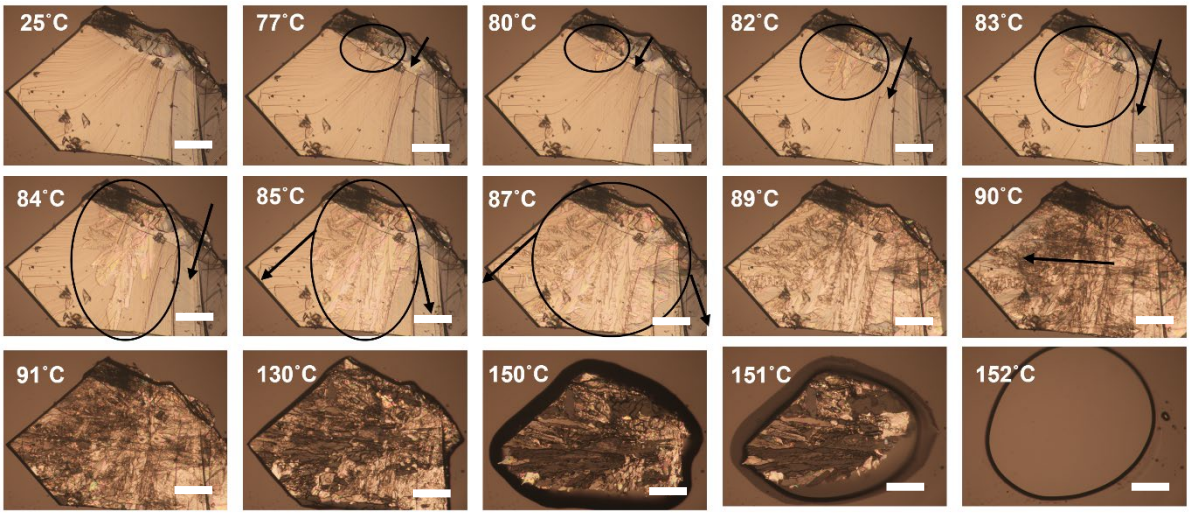

Figure S 8 HSM images of crystal of Form Ia crystal, showing the transition starting from the top edge of the crystal at 77˚C and propagating to the bottom edge and complete transition to Form III at 130˚C, followed by melting at 152˚C. Scale bar 500 µm.

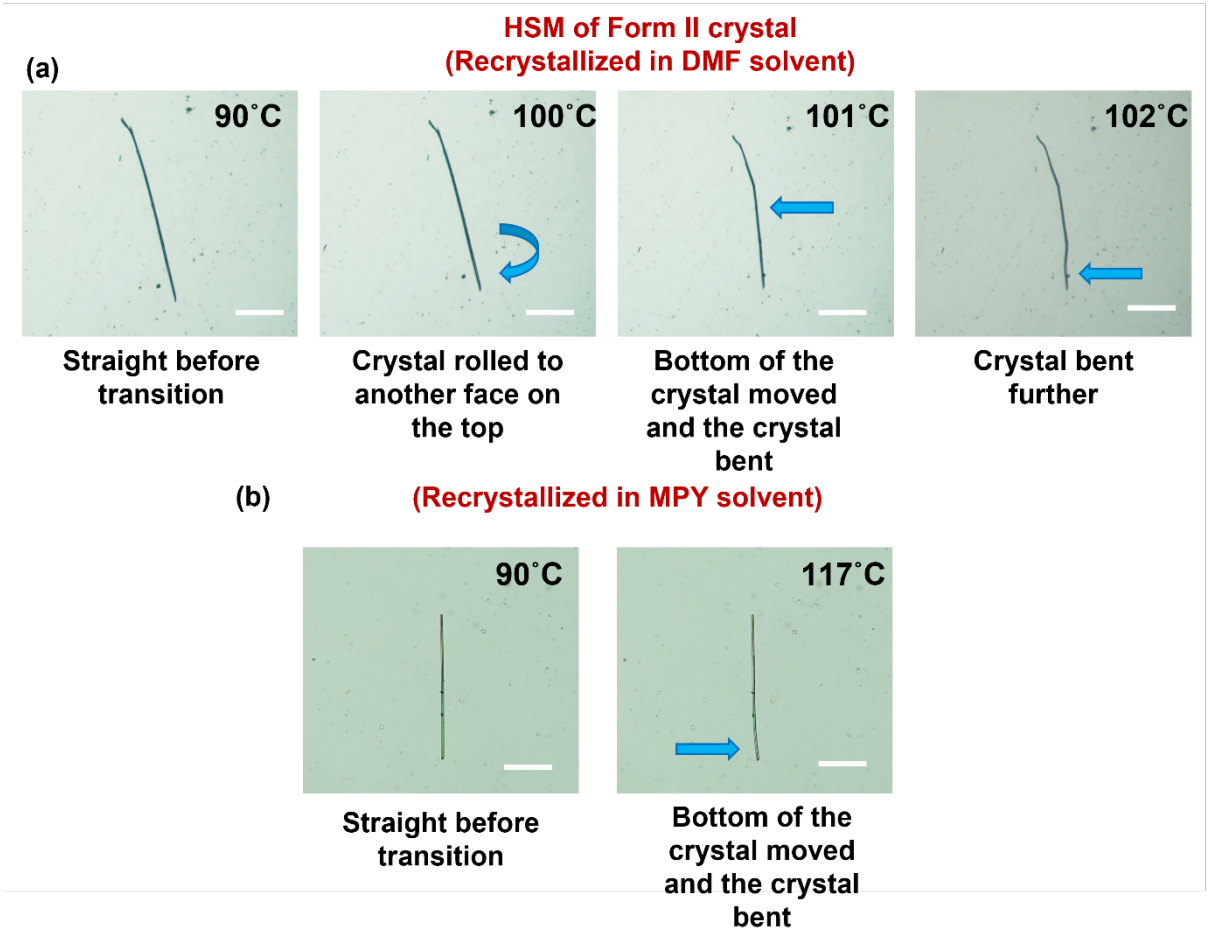

Figure S 9 HSM images of Form II crystals in (a) DMF solvent and (b) MPY solvent, showing the transition to Form III by slight movement at the bottom of the needle crystals. Scale bar 500 µm.

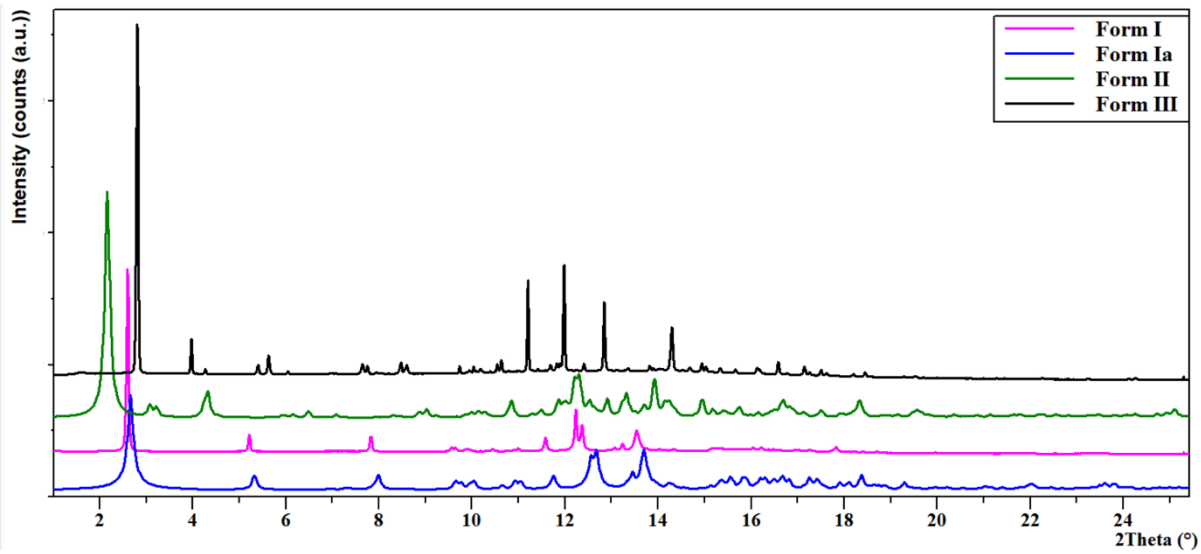

Figure S 10 Powder X-Ray Diffraction (PXRD) patterns of all the polymorphs.

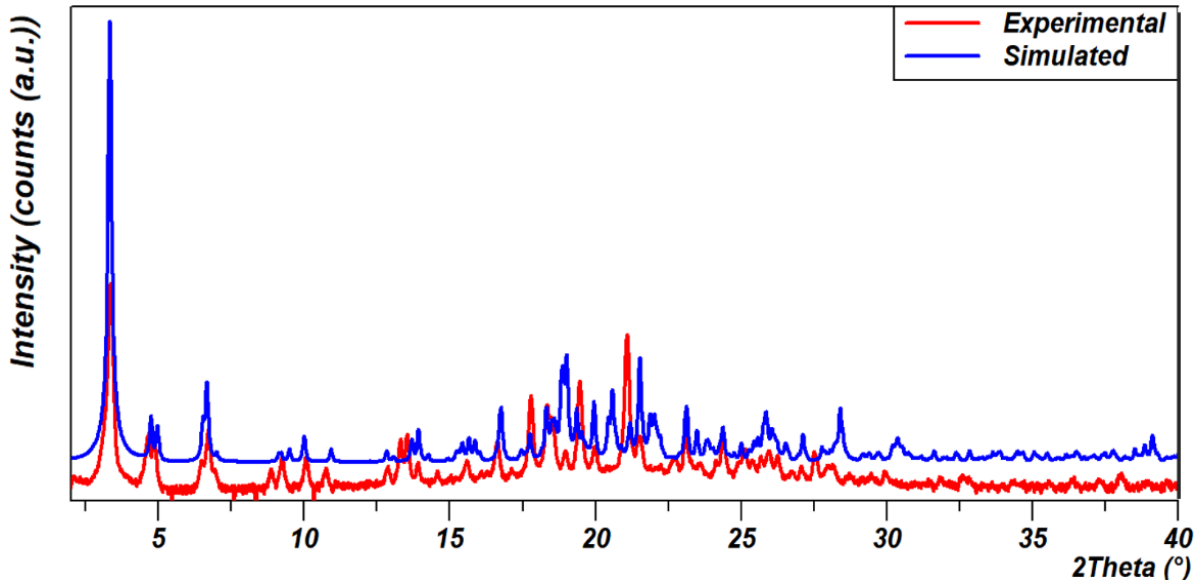

Figure S 11 Comparison of experimental and simulated PXRD patterns of Form II, showing exact match.

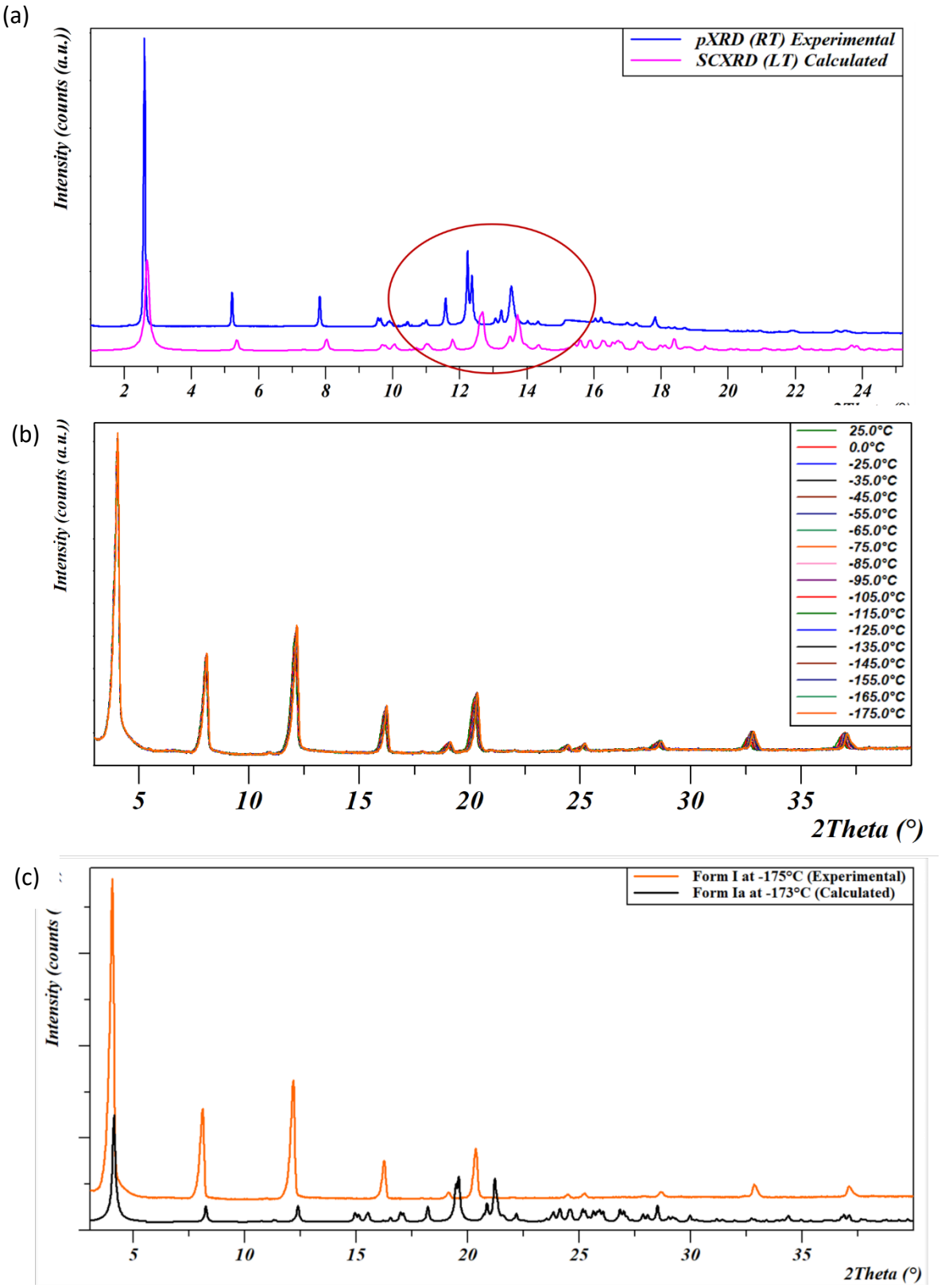

Figure S 12 (a) Comparison of experimental (from PSI synchrotron) and simulated PXRD patterns of Form I and Form Ia, highlighting the slight difference in the patterns (top) (λ=0.9999613 Å) (b) variable temperature XRD (VTXRD) of Form I (starting material) down until -175˚C (λ=1.54 Å) and (c) comparison of experimental and calculated PXRD at low temperature (λ=1.54 Å). The VTXRD shows that there is neither any transition from RT to LT nor thermal contraction in Form I.

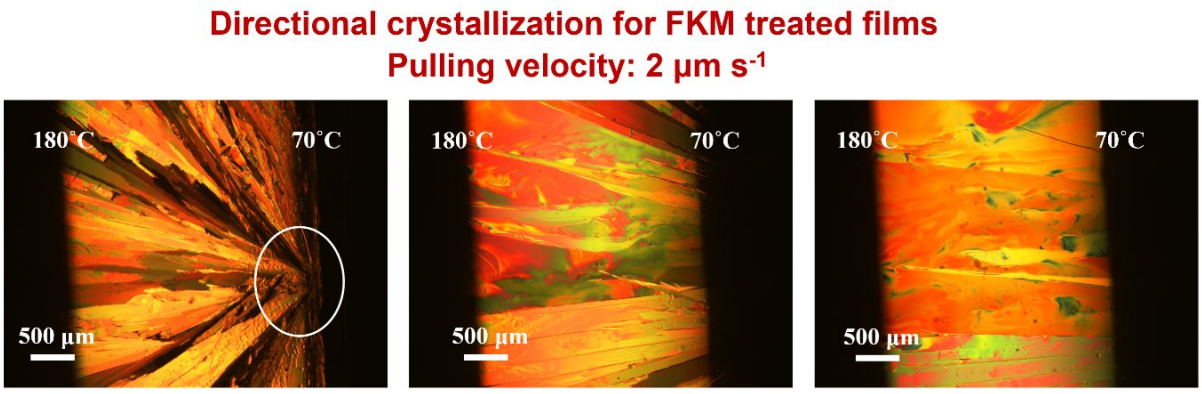

Figure S 13 Polarized Optical Microscope (POM) images at RT of directional crystallization of ditBuC6-BTBT using thermal gradient after surface treatment by FKM polymer, showing nucleation in undercooling region, alignment region and the growth region. T_h = 180˚C, T_c=70˚C, v= 2 µm s^{-1}, spin-coating of FKM by 6000 RPM and 4000 acceleration.

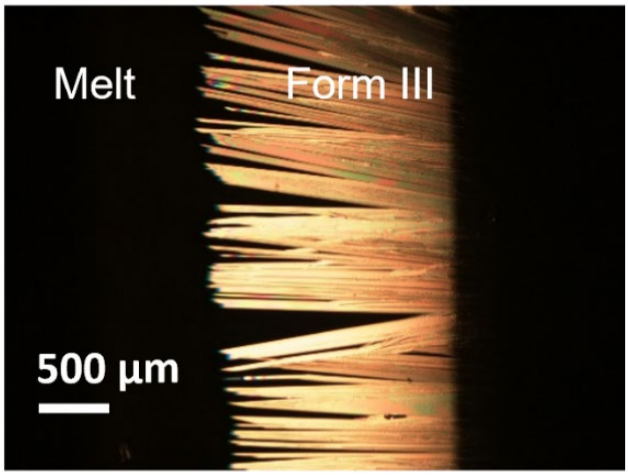

Figure S 14 In-situ POM image of Form III crystal alignment by thermal gradient technique, showing the melt and the crystal phase. T_h = 170˚C, T_c=70˚C, v= 25 µm s^{-1}.

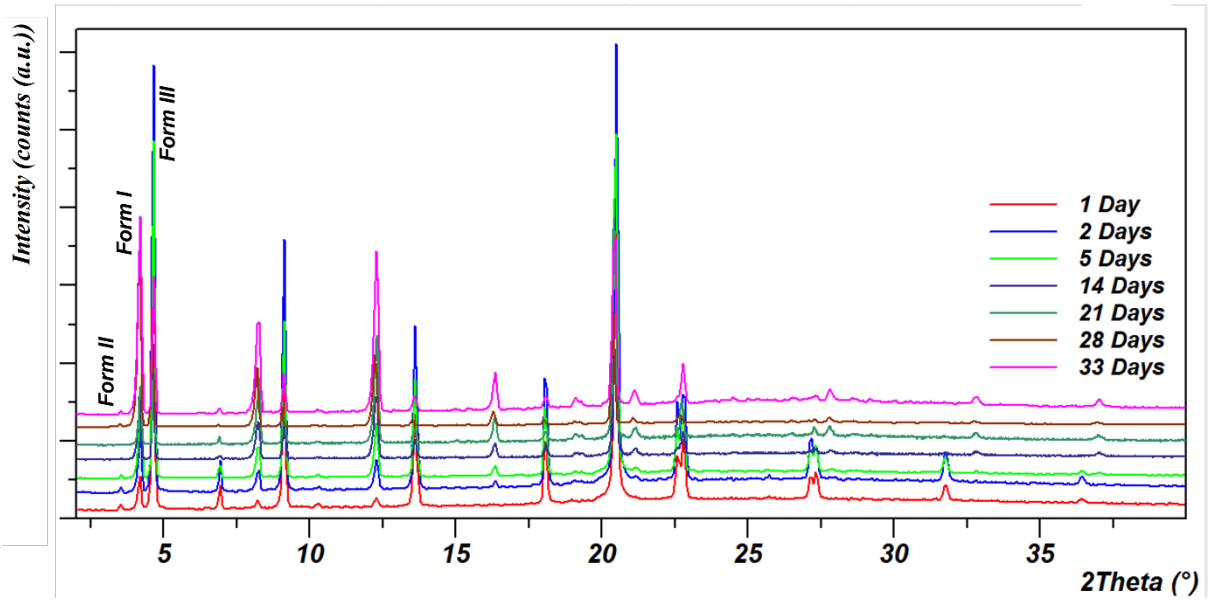

Figure S 15 PXRD pattern of films by thermal gradient representing the stability test, which reveals that Form III converts to Form I over time, which, in turn, starts to convert to Form II. However, the kinetics of transformation is very slow and the conversion to Form I was taking more than a month time.

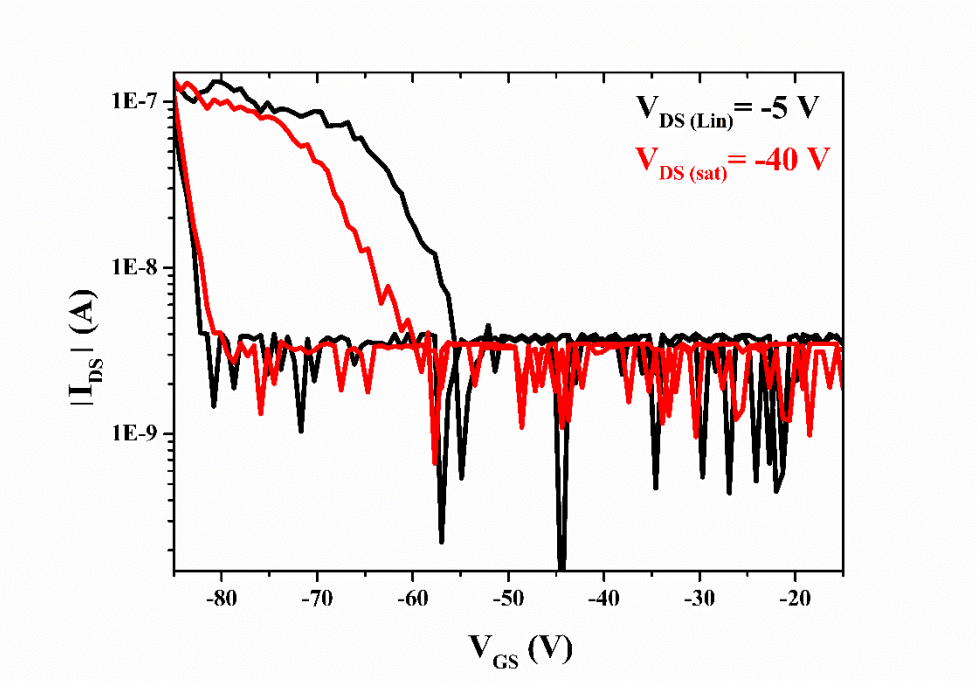

Figure S 16 Transfer characteristics of bottom gate bottom contact OFET on pristine dittBuC6-BTBT deposited by solution shearing at 105˚C temperature and 10 mm s^{-1} shearing speed, showing saturation curve. W/L = 100.

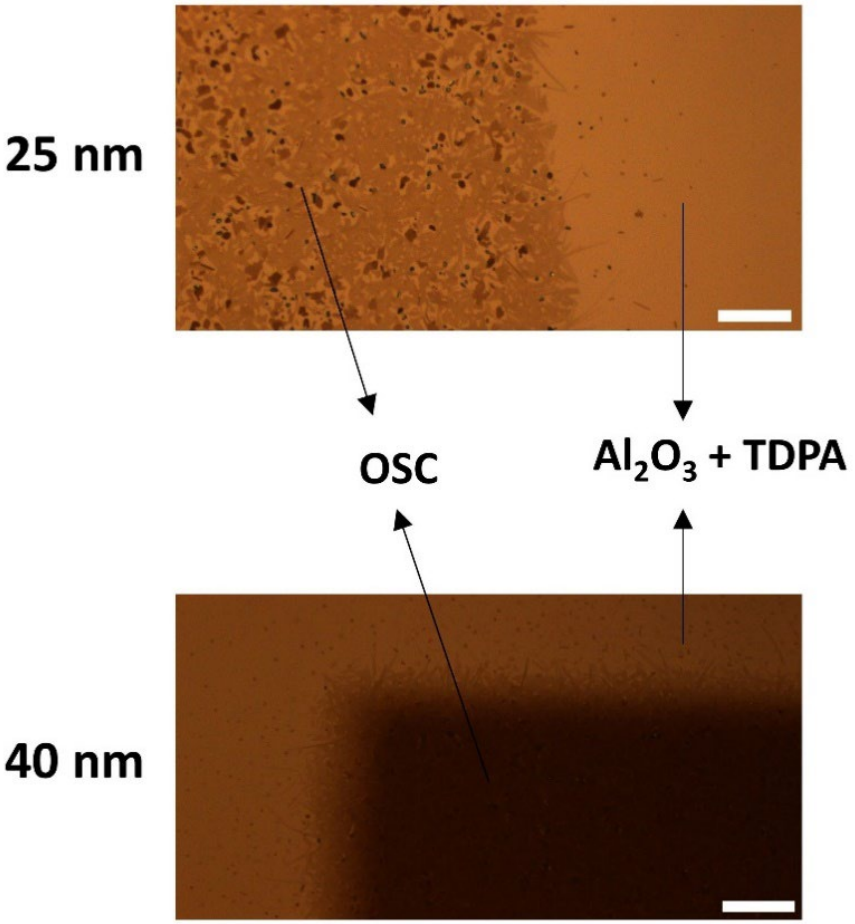

Figure S 17 Optical micrographs of ditBuC6-BTBT deposited with a nominal thickness of 25 nm (on the top) and 40 nm (on the bottom) onto Al_2O_3/TDPA at T_{sub} 40°C. Scale bar = 20 µm.

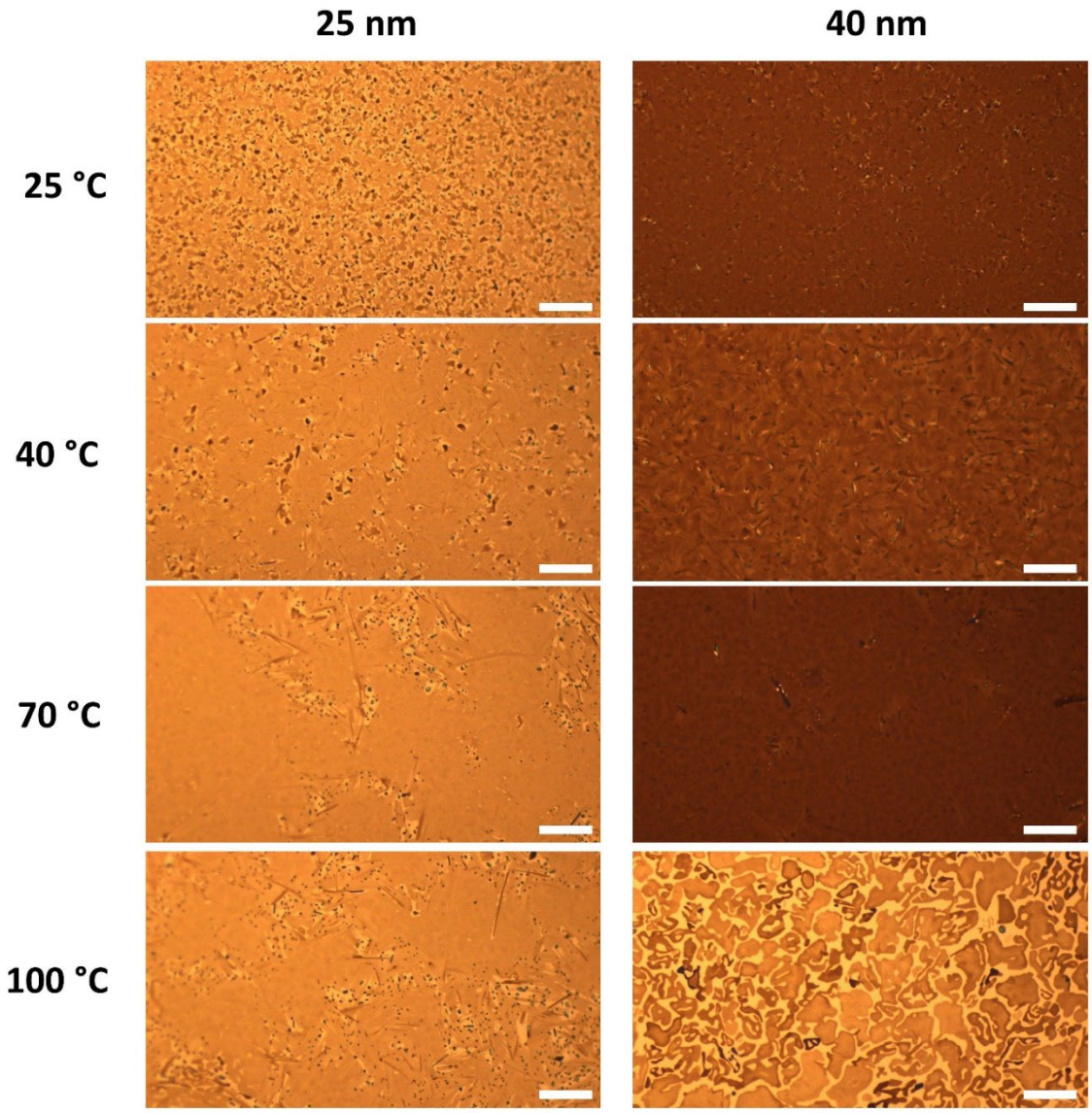

Figure S 18 Optical micrographs of ditBuC6-BTBT deposited with a nominal thickness of 25 nm (on the left) and 40 nm (on the right) onto Al_2O_3/TDPA at T_{sub} 25, 40, 70 and 100°C. Scale bar = 20 µm.

APPENDIX D

Bulk Polymorphic Study of BTBT Systems

Table S 1 Solubility test results using 24 different solvents for 5 mg of BTBT starting material powder. "X": suspension, "YES": clear solution, "-": not performed, ''SS'': Sparingly soluble.

	Temperature	**RT (20-25°C)**					**50°C**	**75°C**
	Volume added to 5 mg	**50µL**	**100µL**	**250µL**	**500µL**	**1mL**	**1mL**	**1mL**
	Concentration (mg mL^{-1})	**100**	**50**	**20**	**10**	**5**	**5**	**5**
2MX	2-Methoxyethanol	X	X	X	X	X	Yes	-
2PR	2-Propanol	X	X	X	X	X	X	X
ABZ	Benzyl Alcohol	X	X	X	X	X	X	Yes
ACN	Acetonitrile	X	X	X	X	X	X	Yes
ANI	Anisole	X	X	X	X	X	X	Yes
CHF	Chloroform	X	X	X	X	X	X	X
DCM	Dichloromethane	X	X	X	X	X	X	X
DEC	Diethyl Carbonate	X	X	X	X	X	X	Yes
DIX	1,4-Dioxane	X	X	X	X	X	X	Yes
DMA	*N,N*-dimethylacetamide	X	X	X	X	X	X	X
DMF	*N,N*-dimethylformamide	X	X	X	X	X	X	X
DMS	Dimethyl Sulfoxide	X	X	X	X	X	X	X
DMX	1,2- Dimethoxyethane	X	X	X	X	X	X	Yes
ETH	Ethanol	X	X	X	X	X	X	X
H2O	Water	X	X	X	X	X	X	X
IPA	Isopropyl Acetate	X	X	X	X	X	X	Yes

IPE	Isopropyl Ether	X	X	X	X	X	X	X
MEK	Methyl ethyl Ketone	X	X	X	X	X	X	X
MPY	1-Methyl-2-Pyrrolidone	X	X	X	X	Yes	-	-
MST	Mesitylene	X	X	X	X	Yes	-	-
NMT	Nitromethane	X	X	X	X	X	X	SS
PXY	p-Xylene	X	X	X	X	Yes	-	-
THF	Tetrahydrofuran	X	X	X	X	Yes	-	-
TOL	Toluene	X	X	X	X	Yes	-	-

Table S 2 Solubility test results using 24 different solvents for 5 mg of ditBu-BTBT starting material powder. “X”: suspension, “YES”: clear solution, “-”: not performed, ‘’SS’’: Sparingly soluble.

	Temperature	**RT (20-25°C)**					**50°C**	**75°C**
	Volume added to 5 mg	**50µL**	**100µL**	**250µL**	**500µL**	**1mL**	**1mL**	**1mL**
	Concentration (mg mL^{-1})	**100**	**50**	**20**	**10**	**5**	**5**	**5**
2MX	2-Methoxyethanol	X	X	X	X	X	X	SS
2PR	2-Propanol	X	X	X	X	X	X	SS
ABZ	Benzyl Alcohol	X	X	X	X	X	SS	Yes
ACN	Acetonitrile	X	X	X	X	X	X	SS
ANI	Anisole	X	X	X	X	X	X	SS
CHF	Chloroform	X	X	X	X	Yes	-	-
DCM	Dichloromethane	X	X	X	X	Yes	-	-
DEC	Diethyl Carbonate	X	X	X	X	Yes	-	-
DIX	1,4-Dioxane	X	X	X	X	X	Yes	-
DMA	*N,N*-dimethylacetamide	X	X	X	X	Yes	-	-
DMF	*N,N*-dimethylformamide	X	X	X	X	X	Yes	-
DMS	Dimethyl Sulfoxide	X	X	X	X	X	X	SS
DMX	1,2- Dimethoxyethane	X	X	X	X	Yes	-	-
ETH	Ethanol	X	X	X	X	X	X	X
H2O	Water	X	X	X	X	X	X	X
IPA	Isopropyl Acetate	X	X	X	X	X	Yes	-
IPE	Isopropyl Ether	X	X	X	X	X	Yes	-
MEK	Methyl ethyl Ketone	X	X	X	X	Yes	-	-
MPY	1-Methyl-2-Pyrrolidone	X	X	X	X	Yes	-	-
MST	Mesitylene	X	X	X	X	Yes	-	-
NMT	Nitromethane	X	X	X	X	X	X	SS

PXY	p-Xylene	X	X	X	X	Yes	-	-
THF	Tetrahydrofuran	X	X	X	X	Yes	-	-
TOL	Toluene	X	X	X	X	Yes	-	-

Table S 3 Solubility test results using 9 different solvents for 5 mg of C2F5C6-BTBT starting material powder. "X": suspension, "YES": clear solution, "-": not performed, ''SS'': Sparingly soluble.

	Temperature	**RT (20-25°C)**					**50°C**	**75°C**
	Volume added to 5 mg	**50µL**	**100µL**	**250µL**	**500µL**	**1mL**	**1mL**	**1mL**
	Concentration (mg mL^{-1})	**100**	**50**	**20**	**10**	**5**	**5**	**5**
2PR	2-Propanol	X	X	X	X	X	Yes	-
ACN	Acetonitrile	X	X	X	X	X	Yes	-
CHF	Chloroform	Yes	-	-	-	-	-	-
DCM	Dichloromethane	Yes	-	-	-	-	-	-
DMF	*N,N*-dimethylformamide	X	X	X	X	Yes	-	-
DMS	Dimethyl Sulfoxide	X	X	X	X	X	Yes	-
PXY	p-Xylene	Yes	-	-	-	-	-	-
THF	Tetrahydrofuran	Yes	-	-	-	-	-	-
TOL	Toluene	Yes	-	-	-	-	-	-

Table S 4 Crystallographic data of BTBT[1] and ditBu-BTBT[2]

	BTBT	**ditBu-BTBT: α Form**	**ditBu-BTBT: βForm**
Empirical formula	C_{14} H_8 S_2	$C_{22}H_{24}S_2$	
Formula weight	240.32	352.53	
Temperature / K	100(2)	298(2)	370(2)
Crystal system	Monoclinic	Monoclinic	Monoclinic

Space group	$P2_1/c$	$P2_1/c$	$P2_1/c$
Unit cell dimensions	a = 11.8009(18) Å b = 5.8622(9) Å c = 7.9331(12) Å β = 105.974(3)	a = 14.1772(6) Å b = 6.1547(3) Å c = 10.6485(5) Å β = 92.2098(16)°	a = 14.6338(12) Å b = 6.3264(6) Å c = 10.4185(9) Å β = 93.755(3)°
Volume / A³	527.615	928.46(7)	962.47(15)
Z	2	2	2
R-factor/ %	2.63	3.39	4.48

References

1 V. S. Vyas, R. Gutzler, J. Nuss, K. Kern and B. v. Lotsch, *CrystEngComm.*, 2014, **16**, 7389–7392.

2 H. Chung, D. Dudenko, F. Zhang, G. D'Avino, C. Ruzié, A. Richard, G. Schweicher, J. Cornil, D. Beljonne, Y. Geerts and Y. Diao, *Nat. Comm.,* 2018, **9**, 1–12.

APPENDIX E

Understanding the solid-state packing and the influence of bulky substituents in the series of rylene molecules

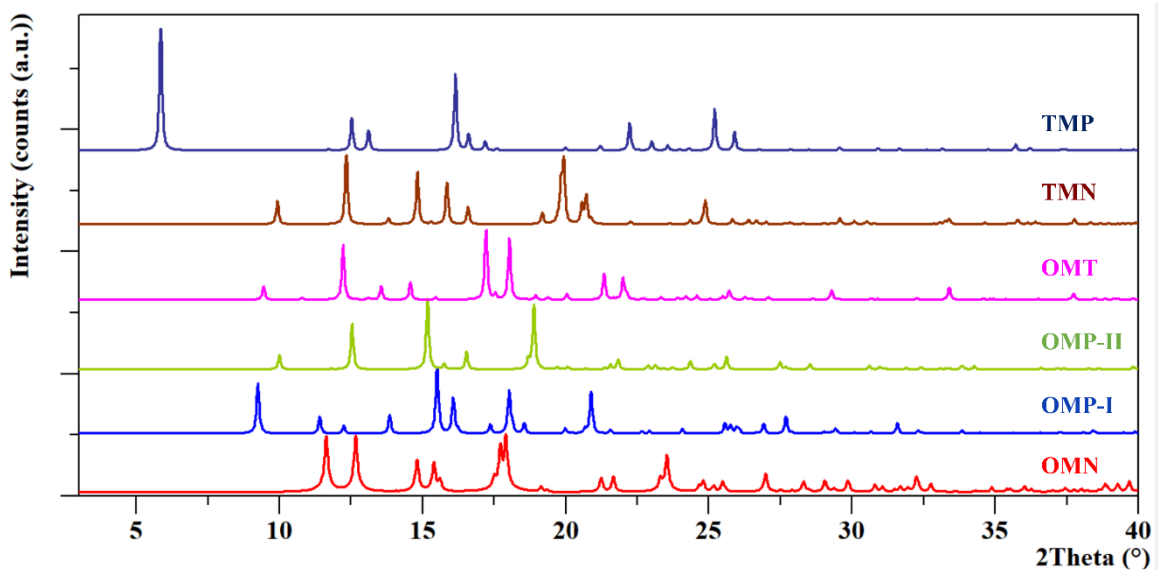

Figure S 1 Simulated PXRD patterns of all the molecules.

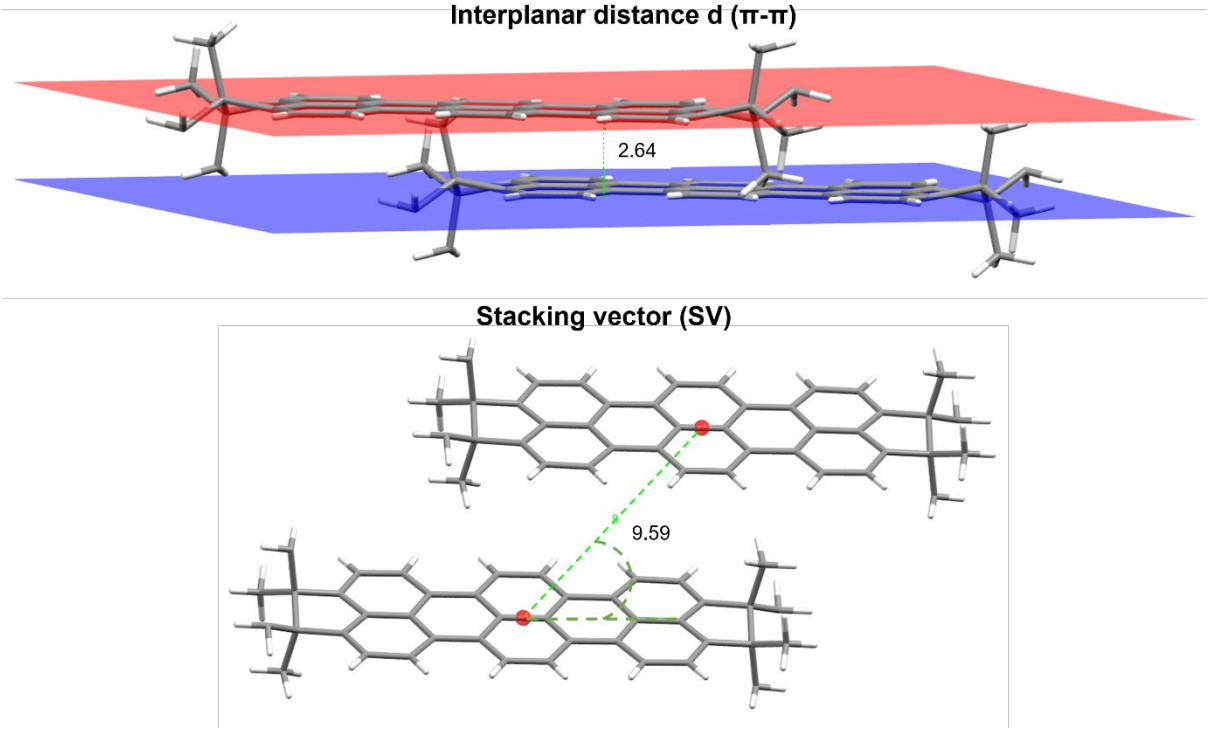

Figure S 2 Measurement of packing parameters- interplanar distance and stacking vector.

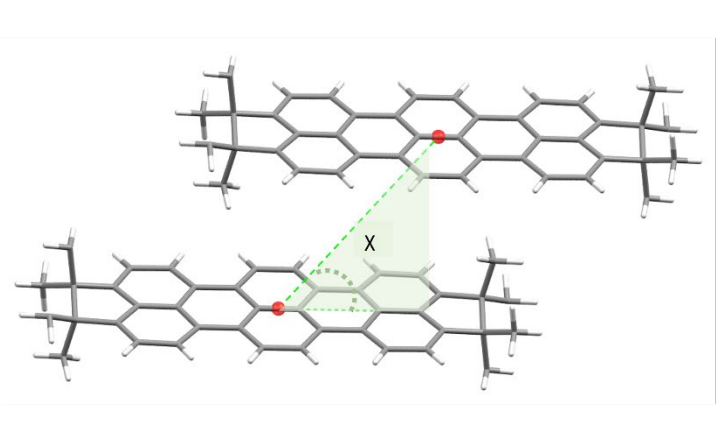

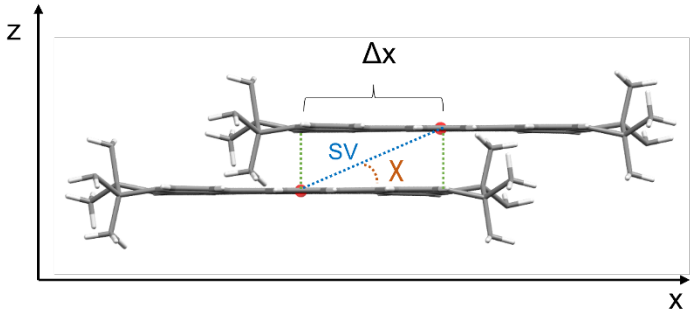

$$\Delta x = SV \cdot cos\, \chi$$

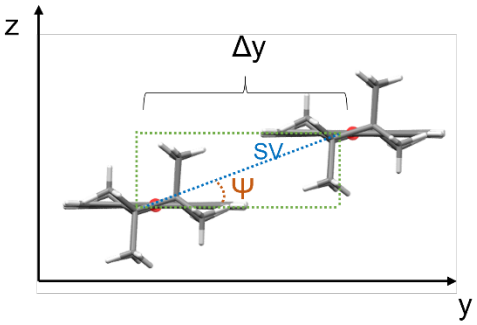

$$\Delta y = SV \cdot cos\, \psi$$

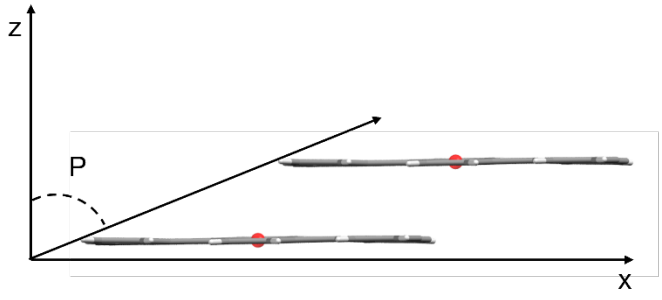

$$\Delta x = d(\pi - \pi) \times \tan P$$

$$P = \arctan\left(\frac{\Delta x}{d(\pi - \pi)}\right)$$

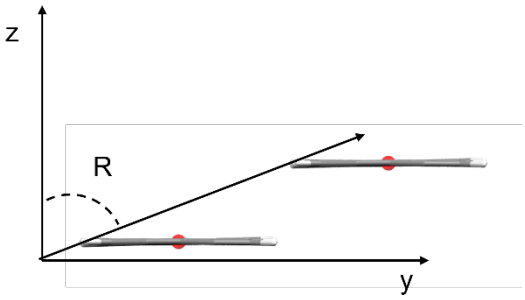

$$\Delta y = d(\pi - \pi) \times \tan R$$

$$R = \arctan\left(\frac{\Delta y}{d(\pi - \pi)}\right)$$

Figure S 3 Measurement and calculations of displacement of the aromatic units along the long (χ) and short (ψ) molecular axis; the directions cosines of the SV (Δx with the x-axis and Δy with the y-axis); the angles of the aromatic unit slipping along the x (pitch)- and y (roll)-direction.

Table S 1 Crystal data and structure refinement for OMN.

Identification code	OMN	
Empirical formula	C22 H28	
Formula weight	292.44	
Temperature	293(2) K	
Wavelength	0.71073 Å	
Crystal system	Monoclinic	
Space group	P 21/n	
Unit cell dimensions	a = 7.6046(6) Å	a= 90°.
	b = 10.1262(9) Å	b= 103.015(7)°.
	c = 11.8110(9) Å	g = 90°.
Volume	886.15(13) $Å^3$	
Z	2	
Density (calculated)	1.096 Mg/m^3	
Absorption coefficient	0.061 mm^{-1}	
F(000)	320	
Theta range for data collection	3.407 to 29.380°.	
Index ranges	-9<=h<=10, -13<=k<=7, -15<=l<=16	
Reflections collected	3926	
Independent reflections	2035 [R(int) = 0.0174]	
Completeness to theta = 25.000°	99.9 %	
Refinement method	Full-matrix least-squares on F^2	
Data / restraints / parameters	2035 / 0 / 100	
Goodness-of-fit on F^2	1.061	
Final R indices [I>2sigma(I)]	R1 = 0.0587, wR2 = 0.1347	
R indices (all data)	R1 = 0.0784, wR2 = 0.1467	
Extinction coefficient	n/a	
Largest diff. peak and hole	0.214 and -0.163 $e.Å^{-3}$	

Table S 2 Atomic coordinates (x 10^4) and equivalent isotropic displacement parameters ($Å^2$x 10^3) for OMN. U(eq) is defined as one third of the trace of the orthogonalized U^{ij} tensor.

	x	y	z	U(eq)
C(1)	5453(2)	5539(2)	5273(1)	36(1)
C(2)	5160(2)	6013(2)	6324(1)	38(1)

C(4)	6727(2)	6223(2)	4815(1)	39(1)
C(3)	3945(2)	5336(2)	6805(1)	46(1)
C(6)	7615(2)	7233(2)	5732(1)	44(1)
C(5)	7004(2)	5789(2)	3768(1)	46(1)
C(7)	6217(2)	7311(2)	6575(1)	43(1)
C(8)	7104(3)	7510(2)	7861(2)	63(1)
C(9)	4840(3)	8434(2)	6193(2)	60(1)
C(11)	9424(2)	6622(2)	6369(2)	62(1)
C(10)	8010(3)	8558(2)	5223(2)	69(1)

Table S 3 Anisotropic displacement parameters ($Å^2 x\ 10^3$) for OMN. The anisotropic displacement factor exponent takes the form: $-2p^2[\ h^2a^{*2}U^{11} + ... + 2\ h\ k\ a^*\ b^*\ U^{12}\ ]$

	U^{11}	U^{22}	U^{33}	U^{23}	U^{13}	U^{12}
C(1)	37(1)	38(1)	33(1)	-1(1)	7(1)	5(1)
C(2)	38(1)	43(1)	32(1)	-2(1)	3(1)	8(1)
C(4)	36(1)	39(1)	39(1)	3(1)	5(1)	5(1)
C(3)	49(1)	57(1)	34(1)	-5(1)	14(1)	7(1)
C(6)	43(1)	38(1)	47(1)	-1(1)	3(1)	1(1)
C(5)	43(1)	54(1)	44(1)	5(1)	16(1)	-1(1)
C(7)	48(1)	40(1)	37(1)	-5(1)	1(1)	5(1)
C(8)	71(1)	68(1)	43(1)	-12(1)	-1(1)	-5(1)
C(9)	69(1)	50(1)	58(1)	-8(1)	7(1)	17(1)
C(11)	42(1)	67(1)	70(1)	-7(1)	-3(1)	3(1)
C(10)	83(2)	47(1)	79(1)	2(1)	21(1)	-10(1)

Table S 4 Crystal data and structure refinement for OMP-I.

Identification code	OMP-I	
Empirical formula	C16 H16	
Formula weight	208.29	
Temperature	293(2) K	
Wavelength	0.71073 Å	
Crystal system	Monoclinic	
Space group	P 21/c	
Unit cell dimensions	a = 9.6846(5) Å	a= 90°.
	b = 11.0235(7) Å	b= 99.257(5)°.
	c = 11.0493(6) Å	g = 90°.
Volume	1164.24(12) $Å^3$	
Z	4	
Density (calculated)	1.188 Mg/m^3	
Absorption coefficient	0.067 mm^{-1}	
F(000)	448	
Theta range for data collection	3.568 to 25.046°.	
Index ranges	-11<=h<=11, -13<=k<=13, -13<=l<=11	
Reflections collected	4530	
Independent reflections	2057 [R(int) = 0.0573]	
Completeness to theta = 25.046°	99.8 %	
Refinement method	Full-matrix least-squares on F^2	
Data / restraints / parameters	2057 / 0 / 146	
Goodness-of-fit on F^2	1.193	
Final R indices [I>2sigma(I)]	R1 = 0.0822, wR2 = 0.1789	
R indices (all data)	R1 = 0.0904, wR2 = 0.1877	
Extinction coefficient	1.76(10)	
Largest diff. peak and hole	0.380 and -0.506 e.$Å^{-3}$	

Table S 5 Atomic coordinates (x 10^4) and equivalent isotropic displacement parameters ($Å^2$x 10^3) for OMP-I. U(eq) is defined as one third of the trace of the orthogonalized U^{ij} tensor.

	x	y	z	U(eq)
C(6)	1808(2)	388(2)	8235(2)	43(1)
C(7)	2908(2)	1422(2)	8712(2)	42(1)
C(8)	2319(2)	2691(2)	8358(2)	63(1)
C(9)	3422(2)	1405(2)	10094(2)	61(1)

C(11)2067(2)	-763(2)	9033(2)	58(1)
C(10)277(2)	766(3)	8184(2)	63(1)
C(12)4278(2)	234(2)	5969(1)	30(1)
C(15)3575(2)	-470(2)	4966(1)	31(1)
C(13)5657(2)	720(2)	6054(1)	31(1)
C(4) 2189(2)	63(2)	6987(2)	37(1)
C(3) 5392(2)	1666(2)	8026(2)	41(1)
C(14)6175(2)	1403(2)	7084(2)	38(1)
C(1) 3542(2)	489(2)	6934(2)	34(1)
C(16)2230(2)	-862(2)	5023(2)	40(1)
C(2) 4064(2)	1211(2)	7949(2)	36(1)
C(5) 1526(2)	-608(2)	6021(2)	44(1)

Table S 6 Anisotropic displacement parameters ($Å^2 x\ 10^3$) for OMP-I. The anisotropic displacement factor exponent takes the form: $-2p^2[\ h^2a^{*2}U^{11} + ... + 2\ h\ k\ a^*\ b^*\ U^{12}\ ]$

	U^{11}	U^{22}	U^{33}	U^{23}	U^{13}	U^{12}
C(6)	44(1)	45(1)	42(1)	-3(1)	17(1)	0(1)
C(7)	48(1)	41(1)	40(1)	-5(1)	16(1)	2(1)
C(8)	72(1)	44(1)	80(2)	-6(1)	30(1)	10(1)
C(9)	71(1)	74(2)	42(1)	-13(1)	19(1)	-10(1)
C(11)	74(1)	53(1)	51(1)	5(1)	23(1)	-6(1)
C(10)	48(1)	80(2)	66(1)	-12(1)	24(1)	4(1)
C(12)	34(1)	25(1)	32(1)	1(1)	5(1)	2(1)
C(15)	34(1)	27(1)	32(1)	-1(1)	5(1)	1(1)
C(13)	34(1)	28(1)	33(1)	0(1)	5(1)	0(1)
C(4)	38(1)	37(1)	39(1)	-1(1)	11(1)	2(1)
C(3)	47(1)	40(1)	36(1)	-10(1)	5(1)	-5(1)
C(14)	36(1)	39(1)	39(1)	-4(1)	5(1)	-5(1)
C(1)	37(1)	29(1)	36(1)	1(1)	8(1)	3(1)
C(16)	38(1)	41(1)	40(1)	-7(1)	5(1)	-7(1)
C(2)	44(1)	32(1)	33(1)	-2(1)	8(1)	2(1)
C(5)	33(1)	48(1)	51(1)	-3(1)	12(1)	-7(1)

Table S 7 Crystal data and structure refinement for OMP-II.

Identification code	OMP-II	
Empirical formula	C16 H16	
Formula weight	208.29	
Temperature	293(2) K	
Wavelength	0.71073 Å	
Crystal system	Orthorhombic	
Space group	P b c a	
Unit cell dimensions	a = 14.112(2) Å	a= 90°.
	b = 9.306(2) Å	b= 90°.
	c = 17.683(4) Å	g = 90°.
Volume	2322.2(8) $Å^3$	
Z	8	
Density (calculated)	1.192 Mg/m^3	
Absorption coefficient	0.067 mm^{-1}	
F(000)	896	
Crystal size	? x ? x ? mm^3	
Theta range for data collection	3.491 to 29.461°.	
Index ranges	-18<=h<=19, -12<=k<=7, -22<=l<=22	
Reflections collected	6541	
Independent reflections	2721 [R(int) = 0.1378]	
Completeness to theta = 25.242°	99.8 %	
Refinement method	Full-matrix least-squares on F^2	
Data / restraints / parameters	2721 / 0 / 146	
Goodness-of-fit on F^2	0.975	
Final R indices [I>2sigma(I)]	R1 = 0.0912, wR2 = 0.1737	
R indices (all data)	R1 = 0.2635, wR2 = 0.2515	
Extinction coefficient	0.106(9)	
Largest diff. peak and hole	0.303 and -0.276 e.$Å^{-3}$	

Table S 8 Atomic coordinates (x 10^4) and equivalent isotropic displacement parameters ($Å^2$x 10^3) for OMP-II. U(eq) is defined as one third of the trace of the orthogonalized U^{ij} tensor.

x	y	z	U(eq)
C(13)4112(2)	821(4)	5031(2)	45(1)
C(1) 4776(2)	2461(4)	4120(2)	47(1)
C(15)5765(2)	488(4)	4506(2)	45(1)

C(12)4885(2)	1218(4)	4563(2)	43(1)
C(14)3313(3)	1663(4)	5025(2)	53(1)
C(2) 3940(3)	3285(4)	4103(2)	48(1)
C(3) 3216(3)	2882(4)	4569(2)	55(1)
C(16)6449(3)	1036(4)	4028(2)	52(1)
C(5) 6314(3)	2296(5)	3593(2)	56(1)
C(4) 5471(3)	3015(4)	3642(2)	49(1)
C(6) 5131(3)	4425(4)	3303(3)	53(1)
C(7) 4027(3)	4397(5)	3486(3)	61(1)
C(11)5387(3)	4597(5)	2478(3)	81(2)
C(10)5616(3)	5621(5)	3755(3)	90(2)
C(9) 3463(3)	3790(6)	2790(3)	86(2)
C(8) 3582(4)	5814(5)	3671(3)	106(2)

Table S 9 Anisotropic displacement parameters ($Å^2 x\ 10^3$) for OMP-II. The anisotropic displacement factor exponent takes the form: $-2p^2[\ h^2a^{*2}U^{11} + ... + 2\ h\ k\ a^*\ b^*\ U^{12}\ ]$

	U^{11}	U^{22}	U^{33}	U^{23}	U^{13}	U^{12}
C(13)	42(2)	47(2)	45(2)	-6(2)	1(2)	2(2)
C(1)	41(2)	49(2)	49(2)	-5(2)	-3(2)	-1(2)
C(15)	40(2)	55(3)	41(2)	-5(2)	0(2)	-2(2)
C(12)	40(2)	47(2)	43(2)	-5(2)	-4(2)	0(2)
C(14)	45(2)	60(3)	54(3)	1(3)	6(2)	1(2)
C(2)	48(2)	46(2)	51(3)	-3(2)	-3(2)	0(2)
C(3)	47(2)	53(3)	65(3)	-2(3)	-1(2)	4(2)
C(16)	44(2)	59(3)	53(3)	-2(3)	2(2)	7(2)
C(5)	45(2)	66(3)	58(3)	3(3)	6(2)	-3(2)
C(4)	47(2)	51(3)	50(3)	-5(2)	-1(2)	-3(2)
C(6)	55(2)	47(2)	57(3)	0(2)	-4(2)	-2(2)
C(7)	57(3)	56(3)	69(3)	7(3)	1(2)	5(2)
C(11)	77(3)	94(4)	72(3)	23(3)	9(3)	14(3)
C(10)	91(4)	66(3)	112(5)	-6(3)	-31(3)	-15(3)
C(9)	71(3)	112(4)	76(3)	23(3)	-19(3)	-12(3)
C(8)	101(4)	65(3)	152(6)	26(4)	49(4)	29(3)

Table S 10 Crystal data and structure refinement for OMT.

Identification code	rm-316_cu	
Empirical formula	C42.03 H34	
Formula weight	538.99	
Temperature	160(2) K	
Wavelength	1.54184 Å	
Crystal system	Monoclinic	
Space group	P 21/n	
Unit cell dimensions	a = 8.41240(10) Å	α= 90°.
	b = 18.7148(2) Å	β= 108.2790(10)°.
	c = 9.59720(10) Å	γ = 90°.
Volume	1434.71(3) $Å^3$	
Z	2	
Density (calculated)	1.248 Mg/m^3	
Absorption coefficient	0.530 mm^{-1}	
F(000)	572	
Crystal size	0.360 x 0.100 x 0.020 mm^3	
Theta range for data collection	4.726 to 79.206°.	
Index ranges	-9<=h<=10, -23<=k<=23, -12<=l<=12	
Reflections collected	15243	
Independent reflections	3061 [R(int) = 0.0192]	
Completeness to theta = 67.684°	100.0 %	
Refinement method	Full-matrix least-squares on F^2	
Data / restraints / parameters	3061 / 40 / 265	
Goodness-of-fit on F^2	1.101	
Final R indices [I>2sigma(I)]	R1 = 0.0480, wR2 = 0.1472	
R indices (all data)	R1 = 0.0505, wR2 = 0.1497	
Extinction coefficient	0.0010(5)	
Largest diff. peak and hole	0.336 and -0.251 e.$Å^{-3}$	

Table S 11. Atomic coordinates (x 10^4) and equivalent isotropic displacement parameters ($Å^2$x 10^3) for OMT. U(eq) is defined as one third of the trace of the orthogonalized U^{ij} tensor.

x	y	z	U(eq)	
C(18)	7834(1)	5413(1)	9468(1)	25(1)
C(17)	9432(1)	5182(1)	9388(1)	23(1)
C(21)	10096(1)	4689(1)	11904(1)	26(1)

C(12)	7171(1)	5899(1)	6955(1)	25(1)
C(13)	6656(1)	5778(1)	8209(1)	26(1)
C(1) 6066(1)	6262(1)	5765(1)	27(1)	
C(15)	8745(1)	5685(1)	6841(1)	26(1)
C(2) 4481(1)	6502(1)	5734(1)	30(1)	
C(16)	9099(2)	5860(1)	5555(1)	32(1)
C(4) 6435(1)	6436(1)	4480(1)	31(1)	
C(20)	8550(1)	4929(1)	11931(1)	33(1)
C(19)	7448(2)	5281(1)	10742(1)	34(1)
C(5) 7965(2)	6235(1)	4377(1)	36(1)	
C(3) 3981(2)	6382(1)	6946(1)	34(1)	
C(14)	5081(1)	6024(1)	8175(1)	31(1)
C(6) 4798(3)	6720(1)	3401(4)	35(1)	
C(7) 3570(5)	6753(1)	4164(2)	25(1)	
C(8) 2535(3)	6135(1)	3294(2)	29(1)	
C(10A)	4726(3)	6828(2)	1905(2)	38(1)
C(11A)	5693(3)	7718(1)	3943(3)	48(1)
C(11)	5140(4)	7288(2)	2364(4)	53(1)
C(6A)	5105(3)	6951(1)	3549(3)	26(1)
C(7A)	3788(4)	6996(2)	4408(3)	38(1)
C(9) 2422(3)	7389(1)	4146(3)	31(1)	
C(8A)	1875(4)	6973(2)	3781(3)	53(1)
C(10)	3849(4)	6099(2)	2438(3)	47(1)
C(9A)	4284(5)	7766(2)	4915(4)	41(1)

Table S 12 Anisotropic displacement parameters ($Å^2x\ 10^3$) for OMT. The anisotropic displacement factor exponent takes the form: $-2\pi^2[\ h^2a^{*2}U^{11} + ... + 2\ h\ k\ a^*\ b^*\ U^{12}\ ]$

	U^{11}	U^{22}	U^{33}	U^{23}	U^{13}	U^{12}
C(18)	25(1)	25(1)	25(1)	1(1)	7(1)	1(1)
C(17)	24(1)	21(1)	24(1)	-1(1)	6(1)	-2(1)
C(21)	26(1)	27(1)	25(1)	2(1)	8(1)	0(1)
C(12)	25(1)	23(1)	25(1)	0(1)	6(1)	-1(1)
C(13)	25(1)	25(1)	26(1)	1(1)	7(1)	0(1)
C(1) 28(1)	25(1)	26(1)	0(1)	6(1)	0(1)	
C(15)	27(1)	27(1)	25(1)	1(1)	7(1)	0(1)

C(2) 27(1)	30(1)	30(1)	3(1)	5(1)	2(1)	
C(16)	29(1)	41(1)	28(1)	5(1)	11(1)	5(1)
C(4) 33(1)	32(1)	25(1)	4(1)	6(1)	3(1)	
C(20)	32(1)	45(1)	27(1)	8(1)	13(1)	7(1)
C(19)	27(1)	44(1)	32(1)	7(1)	12(1)	9(1)
C(5) 37(1)	45(1)	26(1)	8(1)	12(1)	6(1)	
C(3) 26(1)	41(1)	33(1)	6(1)	9(1)	7(1)	
C(14)	28(1)	37(1)	28(1)	5(1)	10(1)	4(1)
C(6) 36(1)	34(1)	36(1)	7(1)	9(1)	2(1)	
C(7) 23(1)	23(1)	25(1)	4(1)	3(1)	0(1)	
C(8) 29(1)	28(1)	24(1)	-1(1)	1(1)	-3(1)	
C(10A)	35(1)	54(2)	22(1)	8(1)	6(1)	7(1)
C(11A)	42(1)	36(1)	58(2)	15(1)	4(1)	-1(1)
C(11)	47(2)	66(2)	47(2)	25(2)	15(1)	11(2)
C(6A)	25(1)	25(1)	26(1)	7(1)	7(1)	2(1)
C(7A)	35(2)	42(2)	37(1)	9(1)	8(1)	2(2)
C(9) 32(1)	28(1)	29(1)	3(1)	4(1)	7(1)	
C(8A)	38(2)	77(2)	41(2)	12(2)	8(1)	17(2)
C(10)	45(2)	51(2)	41(1)	-6(1)	7(1)	3(1)
C(9A)	54(2)	28(2)	33(2)	2(1)	4(1)	10(1)

Table S 13 Crystal data and structure refinement for TMN.

Identification code	TMN	
Empirical formula	C16 H18	
Formula weight	210.30	
Temperature	293(2) K	
Wavelength	0.71073 Å	
Crystal system	Monoclinic	
Space group	P 21/n	
Unit cell dimensions	a = 7.7744(7) Å	a= 90°.
	b = 11.5631(7) Å	b= 97.887(7)°.
	c = 14.0906(10) Å	g = 90°.
Volume	1254.71(16) $Å^3$	
Z	4	
Density (calculated)	1.113 Mg/m^3	
Absorption coefficient	0.062 mm^{-1}	
F(000)	456	
Theta range for data collection	3.646 to 29.043°.	
Index ranges	-10<=h<=5, -14<=k<=15, -18<=l<=17	
Reflections collected	5627	
Independent reflections	2883 [R(int) = 0.0168]	
Completeness to theta = 25.000°	99.6 %	
Refinement method	Full-matrix least-squares on F^2	
Data / restraints / parameters	2883 / 0 / 146	
Goodness-of-fit on F^2	1.028	
Final R indices [I>2sigma(I)]	R1 = 0.0796, wR2 = 0.2196	
R indices (all data)	R1 = 0.1170, wR2 = 0.2518	
Extinction coefficient	0.015(7)	
Largest diff. peak and hole	0.532 and -0.216 e.$Å^{-3}$	

Table S 14 Atomic coordinates (x 10^4) and equivalent isotropic displacement parameters ($Å^2$x 10^3) for TMN. U(eq) is defined as one third of the trace of the orthogonalized U^{ij} tensor.

x	y	z	U(eq)
C(1) 6127(3)	6865(2)	6036(2)	44(1)
C(4) 7627(3)	6198(2)	6086(2)	45(1)
C(12)5790(3)	7826(2)	5426(2)	54(1)

C(2)	5012(3)	6468(2)	6656(2)	50(1)
C(15)	7077(4)	8084(2)	4839(2)	65(1)
C(5)	8829(3)	6478(2)	5505(2)	60(1)
C(6)	7621(3)	5300(2)	6866(2)	55(1)
C(7)	5711(3)	5356(2)	7126(2)	54(1)
C(16)	8526(4)	7428(3)	4888(2)	70(1)
C(13)	4218(4)	8401(2)	5471(2)	69(1)
C(3)	3493(4)	7069(3)	6687(2)	73(1)
C(14)	3135(4)	8038(3)	6073(3)	81(1)
C(11)	8922(4)	5753(3)	7736(2)	82(1)
C(8)	4568(5)	4379(3)	6638(3)	97(1)
C(9)	5558(6)	5314(4)	8188(2)	100(1)
C(10)	8235(6)	4134(3)	6607(3)	99(1)

Table S 15 Anisotropic displacement parameters ($Å^2 x\ 10^3$) for TMN. The anisotropic displacement factor exponent takes the form: $-2p^2[\ h^2a^{*2}U^{11} + ... + 2\ h\ k\ a^*\ b^*\ U^{12}\ ]$

	U^{11}	U^{22}	U^{33}	U^{23}	U^{13}	U^{12}
C(1)	46(1)	39(1)	44(1)	-8(1)	-1(1)	-2(1)
C(4)	47(1)	45(1)	42(1)	-4(1)	4(1)	-1(1)
C(12)	62(2)	42(1)	54(1)	-9(1)	-11(1)	-1(1)
C(2)	45(1)	50(1)	55(1)	-12(1)	6(1)	-7(1)
C(15)	90(2)	51(1)	53(2)	7(1)	4(1)	-9(2)
C(5)	53(2)	65(2)	64(2)	1(1)	16(1)	4(1)
C(6)	55(2)	50(1)	61(2)	8(1)	10(1)	5(1)
C(7)	64(2)	49(1)	51(1)	-4(1)	13(1)	-9(1)
C(16)	81(2)	73(2)	59(2)	6(1)	23(1)	-13(2)
C(13)	69(2)	52(2)	81(2)	-8(1)	-14(2)	12(1)
C(3)	51(2)	75(2)	94(2)	-16(2)	20(2)	-4(1)
C(14)	55(2)	72(2)	112(3)	-23(2)	-9(2)	20(2)
C(11)	71(2)	98(2)	70(2)	15(2)	-12(2)	-5(2)
C(8)	87(2)	60(2)	141(3)	-8(2)	1(2)	-23(2)
C(9)	108(3)	128(3)	70(2)	14(2)	33(2)	8(2)
C(10)	127(3)	56(2)	123(3)	8(2)	51(2)	25(2)

Table S 16 Crystal data and structure refinement for TMP.

Identification code	TMP	
Empirical formula	C13 H11	
Formula weight	167.22	
Temperature	293(2) K	
Wavelength	0.71073 Å	
Crystal system	Orthorhombic	
Space group	P 21 21 2	
Unit cell dimensions	a = 7.5439(8) Å	a= 90°.
	b = 7.9920(12) Å	b= 90°.
	c = 15.094(3) Å	g = 90°.
Volume	910.1(2) $Å^3$	
Z	4	
Density (calculated)	1.220 Mg/m^3	
Absorption coefficient	0.069 mm^{-1}	
F(000)	356	
Theta range for data collection	3.713 to 29.331°.	
Index ranges	-10<=h<=9, -8<=k<=10, -10<=l<=19	
Reflections collected	2754	
Independent reflections	1891 [R(int) = 0.0278]	
Completeness to theta = 25.000°	99.2 %	
Refinement method	Full-matrix least-squares on F^2	
Data / restraints / parameters	1891 / 0 / 120	
Goodness-of-fit on F^2	1.107	
Final R indices [I>2sigma(I)]	R1 = 0.0787, wR2 = 0.1611	
R indices (all data)	R1 = 0.1183, wR2 = 0.1868	
Absolute structure parameter	10.0(10)	
Extinction coefficient	n/a	
Largest diff. peak and hole	0.162 and -0.189 e.$Å^{-3}$	

Table S 17 Atomic coordinates (x 10^4) and equivalent isotropic displacement parameters ($Å^2$x 10^3) for TMP. U(eq) is defined as one third of the trace of the orthogonalized U^{ij} tensor.

x	y	z	U(eq)
C(15)5000	5000	5630(4)	52(2)
C(14)5000	5000	6573(4)	64(2)
C(10)3453(5)	5581(5)	5166(3)	51(1)

C(8)	3456(4)	5582(4)	4190(3)	44(1)
C(9)	2057(5)	6100(5)	3665(3)	60(1)
C(7)	5000	5000	3755(4)	43(1)
C(13)	3490(8)	5571(6)	7025(3)	79(2)
C(2)	3594(5)	5559(5)	2312(3)	54(1)
C(3)	2107(6)	6103(6)	2743(3)	66(1)
C(11)	2035(6)	6128(5)	5654(3)	66(1)
C(12)	2045(8)	6124(6)	6571(4)	80(2)
C(1)	5000	5000	2832(4)	46(1)
C(4)	4131(6)	5570(7)	1346(3)	68(1)
C(5)	4621(9)	7393(8)	1122(3)	108(2)
C(6)	2706(8)	5023(11)	711(4)	127(3)

Table S 18 Anisotropic displacement parameters ($Å^2 x\ 10^3$) for TMP. The anisotropic displacement factor exponent takes the form: $-2p^2[\ h^2a^{*2}U^{11} + ... + 2\ h\ k\ a^*\ b^*\ U^{12}\ ]$

	U^{11}	U^{22}	U^{33}	U^{23}	U^{13}	U^{12}
C(15)	62(3)	30(3)	64(4)	0	0	-3(3)
C(14)	97(5)	39(3)	55(4)	0	0	-8(4)
C(10)	57(2)	36(2)	59(3)	0(2)	9(2)	0(2)
C(8)	42(2)	27(2)	63(3)	-2(2)	3(2)	1(2)
C(9)	45(2)	59(3)	77(3)	-3(2)	3(2)	15(2)
C(7)	43(3)	31(3)	55(4)	0	0	-1(2)
C(13)	126(5)	56(3)	54(3)	-3(2)	21(3)	0(4)
C(2)	54(2)	53(3)	55(3)	-3(2)	-7(2)	-2(2)
C(3)	51(2)	74(3)	74(4)	3(3)	-15(2)	11(3)
C(11)	69(3)	55(3)	73(3)	-2(2)	15(3)	7(3)
C(12)	102(4)	60(3)	77(4)	-1(3)	25(3)	10(3)
C(1)	39(3)	42(3)	55(4)	0	0	-4(2)
C(4)	72(2)	79(3)	54(3)	-4(2)	-11(2)	-2(3)
C(5)	155(5)	89(4)	80(4)	33(3)	3(4)	8(4)
C(6)	99(4)	198(8)	85(4)	-38(5)	-24(3)	2(4)